Body-Centric Wireless Communications: Wearable Antennas, Channel Modelling, and Near-Field Antenna Measurements

Final Thesis

submitted to the faculty of Loughborough University
in partial fulfilment of the requirements for the degree of
Doctor of Philosophy

under a Joint PhD Programme of Loughborough University with National Center for Scientific Research "Demokritos"

Anastasios Paraskevopoulos

Supervisors

Y. Vardaxoglou, A. Alexandridis

The Wolfson School of

Mechanical, Electrical and Manufacturing Engineering

Loughborough University

July 2016

Loughborough University

Abstract

This thesis provides novel contribution to the field of body-centric wireless communications (BCWC) with the development of a measurement methodology for wearable antenna characterisation on the human body, the implementation of fully-textile wearable antennas and the on-body channel modelling considering different antenna types and user's dynamic effects.

More specifically, a measurement methodology is developed for characterising wearable antennas on different locations of the human body. A cylindrical near-field (CNF) technique is employed, which facilitates wearable antenna measurements on a full-body solid anthropomorphic mannequin (SAM) phantom. This technique allows the fast extraction of the full spherical radiation pattern and the corresponding radiation efficiency, which is an important parameter for optimising wearable system design. It appears as a cost- effective and easy to implement solution that does not require expensive positioning systems to rotate the phantom, in contrast to conventional roll-over-azimuth far-field systems.

The CNF measurement method is evaluated by using a printed dipole antenna in vertical and horizontal polarisation in three on-body locations, namely on chest, head and shoulder, at 2.4 and 5.8 GHz ISM band. Moreover, two textile wearable patch antennas are examined with distinct radiation characteristics, which are suitable for on-body and off-body communications. Apart from the 3D far-field antenna performance, the measured near-field is graphically presented on the human body outline, which gives an insight of the on-body propagation. The accuracy of the available measurement results is validated with EM simulations using an equivalent numerical phantom. Hence, this measurement system can be used as a repeatable test-bed for evaluating the performance of wearable antennas.

Furthermore, a flexible fully-textile wearable antenna is designed, fabricated and measured at 2.4 GHz that can be easily integrated in smart clothing.

It supports surface wave propagation and exhibits an omni-directional radiation pattern that makes it suitable for on-body communications. It is based on a multilayer low-profile higher-mode patch antenna (HMMPA) design with embroidered shorting vias. Emphasis is given to the fabrication process of the textile vias with conductive sewing thread that play an important role in generating the optimal mode for on-body radiation. The radiation pattern shape of the proposed fully-textile antenna was found to be similar to a copper rigid antenna, exhibiting a high on-body radiation efficiency of $\approx$ 50%. The potential of the embroidery technique for creating wearable antennas is also demonstrated with the fabrication of a circularly polarised spiral antenna that achieves a broadband performance from 0.9-3 GHz, which is suitable for off-body communications. By testing the textile spiral antenna on the SAM phantom, the antenna-body interaction is examined in a wide frequency range.

Finally, a statistical characterisation of on-body communication channels is undertaken both with EM simulations and channel measurements including user's dynamic movement (walking and running). By using antenna types of different polarisation, the on-body channels are examined for different propagation conditions. Four on-body channels are examined with the one part fixed on the waist of the human body while the other part located on the chest, back, wrist and foot. Channel path gain is derived, while large-scale and small-scale fading are modelled by best-fit statistical distributions.

Acknowledgements

First of all, I want to express my deep gratitude to my supervisors Prof. Yiannis Vardaxoglou and Dr. Antonis Alexandridis for their ongoing guidance and valuable advices throughout my PhD studies. I am also grateful to Dr. William Whittow for providing the full-size body SAM phantom and for his helpful suggestions during the preparation of my scientific publications.

I am also lucky to be surrounded from colleagues with high scientific and ethical values. I want to express my appreciation to dear colleagues: Duarte, Federico, Shiyu, Isaac, Chinwe, Yunfei, Abraham, Alford and Kostas from Loughborough University and Aris, Asimina, Martin, Kostas, Lefteris, Fotis and Thodoris from NCSR "Demokritos" for exchanging knowledge, but also for their continuous support and friendship.

Finally, I am grateful to my family (Vaya, Stefanos, Kostas, Nikos, Georgina) and my girlfriend Milly for all the years of encouragement, patience and support that helped me reach my personal goals.

List of publications

Journals:

- **A. Paraskevopoulos**, A. Tsolis, J. Vardaxoglou, A. A. Alexandridis, "Cylindrical near-field assessment of wearable antennas for body-centric communications", in IET Microwaves, Antennas & Propagation, Accepted in November 2016.
- **A. Paraskevopoulos**, D. d. S. Fonseca, R. D. Seager, W. G. Whittow, J. C. Vardaxoglou, A. A. Alexandridis, "Higher-mode textile patch antenna with embroidered vias for on-body communication", in IET Microwaves, Antennas & Propagation, vol. 10, no. 7, pp. 802-807, 15 May 2016.
- A. Tsolis, **A. Paraskevopoulos**, W. G. Whittow, A. Alexandridis, J. C. Vardaxoglou, "Design, realisation and evaluation of a liquid hollow torso phantom appropriate for wearable antenna assessment", in IET Microwaves, Antennas & Propagation, Accepted in December 2016.
- S. Zhang, **A. Paraskevopoulos**, C. Luxey, J. Pinto, W. Whittow, "Broad-band embroidered spiral antenna for off-body communications", in IET Microwaves, Antennas & Propagation, vol. 10, no. 13, pp. 1395-1401, 27 October 2016.

Conferences:

- **A. Paraskevopoulos**, A. Alexandridis, F. Lazarakis, T. Zervos, A. Michalopoulou, J.C. Vardaxoglou, "Investigation of wearable antennas performance in static LOS and NLOS on-body channels", Antennas & Propagation Conference (LAPC), 2014 Loughborough, November 2014, pp. 355-358.

- **A. Paraskevopoulos**, A. Alexandridis, T. Zervos, A. Michalopoulou, F. Lazarakis, J.C. Vardaxoglou, "Modelling of dynamic on-body channels using different types of wearable antennas", The 8th European Conference on Antennas and Propagation (EuCAP 2014), The Hague, April 2014, pp. 852-856.
- **A. Paraskevopoulos**, A. Alexandridis, F. Lazarakis, J.C. Vardaxoglou,"Modelling of dynamic on-body waist-foot channel at 2.45 GHz", Antennas & Propagation Conference (LAPC), 2013 Loughborough, November 2013, pp. 155-160.
- S. Zhang, D. Speight, **A. Paraskevopoulos**, D. Fonseca, C. Luxey, W. Whittow, J. Pinto, "On-body measurements of embroidered spiral antenna", Antennas & Propagation Conference (LAPC), 2015 Loughborough, November 2015, pp. 1-5.

Contents

List of Figures

List of Tables

List of Acronyms

AUT Antenna under test

BAN Body Area Networks

BCWC Body Centric Wireless Communications

BER Bit Error Rate

CDF Cumulative Distribution Function

CM Channel Model

CNF Cylindrical near-field

CW Continuous wave

dB Decibel

dBi Decibel in respect to an isotropic radiator

ECG Electrocardiogram

EIRP Equivalent Isotropic Radiated Power

EM Electromagnetic

EMG Electromyography

ERP Effective Radiated Power

ETSI European Telecommunications Standards Institute

FCC Federal Communications Commission

HF High frequency

HMMPA Higher mode microstrip patch antenna

HR Heart rate

IFA Inverted-F antenna

ISM Industrial Scientific Medical

LOS Line of sight

MICS Medical Device Radiocommunications Service

MPA Microstrip patch antenna

NFC Near-field coupling

NF-FF Near-field to far-field

NLOS Non Line of sight

PCB Printed circuit board

PEC Perfect Electric Conductor

PG Path Gain

RMS Root mean square

Rx Receiving

SAM Specific anthropomorphic mannequin

SAR Specific absorption rate

SMA Sub-miniature adapter

SNR Signal-to-noise ratio

TM Transverse Magnetic

Tx Transmitting

UHF Ultra high frequency

UWB Ultra-wideband

VHF Very high frequency

VNA Vector Network Analyser

WBAN Wireless Body Area Networks

WLAN Wireless Local Area Network

WMTS Wireless Medical Telemetry Services

List of Symbols

A_{eff} Effective antenna aperture

AR Axial ratio (dB)

BW Bandwidth (Hz)

δ Penetration depth (m)

D Directivity of the antenna (dBi)

e Efficiency of the antenna (%)

ϵ_{r} Relative permittivity

f_{r} Resonance frequency (Hz)

G Gain of the antenna (dBi)

HPBW Half-power (3 dB) beam width (^{o})

θ Azimuth angle (^{o})

λ Wavelength (m)

λ_{g} Guided Wavelength (m)

μ Mean

MEG Mean effective gain (dB)

σ Conductivity (S/m)

S_{11} Reflection coefficient

S_{21} Propagation/ transmission coefficient

σ Standard deviation

$\tan\delta$ Loss tangent

ϕ Elevation angle (^{o})

ϕ_{ff} Far-field angle of validity (^{o})

XPR Cross polarisation ratio (dB)

Chapter 1

Introduction

Body-centric wireless communications is an area of increasing interest due to the proliferation of wearable devices. These devices serve various functionalities in a broad range of applications making our everyday life more comfortable. They can communicate with a mobile terminal to exchange information related to the user's interests or connect with a number of sensors attached or implanted in the human body and sense vital signs about the user's health condition. Numerous wearable devices of different shape and frequency of operation have been released during the last decade.

Wearable devices can be found in medical sensor networks applied in healthcare and patient monitoring, in sports performance monitoring, in security and military usage, in personal entertainment and communications, where data among a number of transceivers are exchanged.

Concerning medical applications, there is a large variety serving various needs, from smart diagnosis to treatment. Body sensors are carefully attached on specific body parts. Physiological parameters such as blood pressure, heart beat rate or electrocardiogram (ECG), body temperature, respiratory rate, insulin levels can be recorded and transmitted to hospital and doctor databases enabling close monitoring and early prevention. Patients and elderly people can be monitored in their home environment. Monitoring during the daily routine gives an opportunity to spot episodic abnormalities that are not likely to occur in hospital bed, achieving better diagnostic and prognostic values. The feasibility of non-invasive monitoring of heart beat rate and breathing rate by simply recording the phase of the reflection coefficient ($\angle S_{11}$) of an on-body antenna, affected by the human chest movement, is presented in [1].

Sport monitoring research can be also considerably benefited from wireless connectivity. A close study of body functions can be performed under physiological states during active training. Observing heart-rate, breathing, calories burnt and function of muscles and joints, performances of elite sportsmen could be improved. These sensors can measure and send real-time information on a connected device of the athlete's smartwatch or even to the trainer's terminal.

Security and military applications are favoured by wearable technology in smart suits for fire fighters, soldiers and support personnel incorporating unobtrusive communication in battlefields. Smart clothes use special sensors to detect bullet wounds or to monitor the body's vital signals during combat conditions. Space applications include biosensors for monitoring the physiological parameters of astronauts during space flights. In a recent research study textile antennas are designed and fabricated especially for spacesuits [2].

In the business environment, BAN devices can be used in numerous ways, such as touch-based authentication services using the human body as a transmission channel (e.g. data deliver on handshake). Several applications are possible, like electronic payment, e-business card, auto-lock, or login systems. User identification/authentication, associated with biometrics, plays a key role in here. Recently, the ability to make payments through the near-field coupling (NFC) capability of smart phones and smart watches showed a big potential of this technology to become fully integrated on the human body in the next few years.

In entertainment, wireless applications are multimedia oriented, examples being personal audio and video such as wearable bluetooth headphones and head mounted displays.

The rapid growth of wearable devices in the market is reported from the research analyst firm Gartner, Inc. [3], which forecasts that in 2016, 274.6 million wearable electronic devices will be sold worldwide, an increase of 18.4 % from 232.0 million units in 2015 (Fig. 1.1). For 2017, more than 322 million wearable devices are expected to be sold. Sales of wearable electronic devices will generate revenue of $28.7 billion (£20.1 billion) in 2016, showing the fast development in this technology segment. From the same report, it is also worth to highlight (Fig. 1.1) that "smart" clothing will grow from 1 million units this year to 5.3 million units in 2017 [3], presenting a remarkable growth of 430 %.

Wearable devices are transformed from protruding external devices to low-profile conformal devices incorporated into clothing. To achieve this, textile materials with

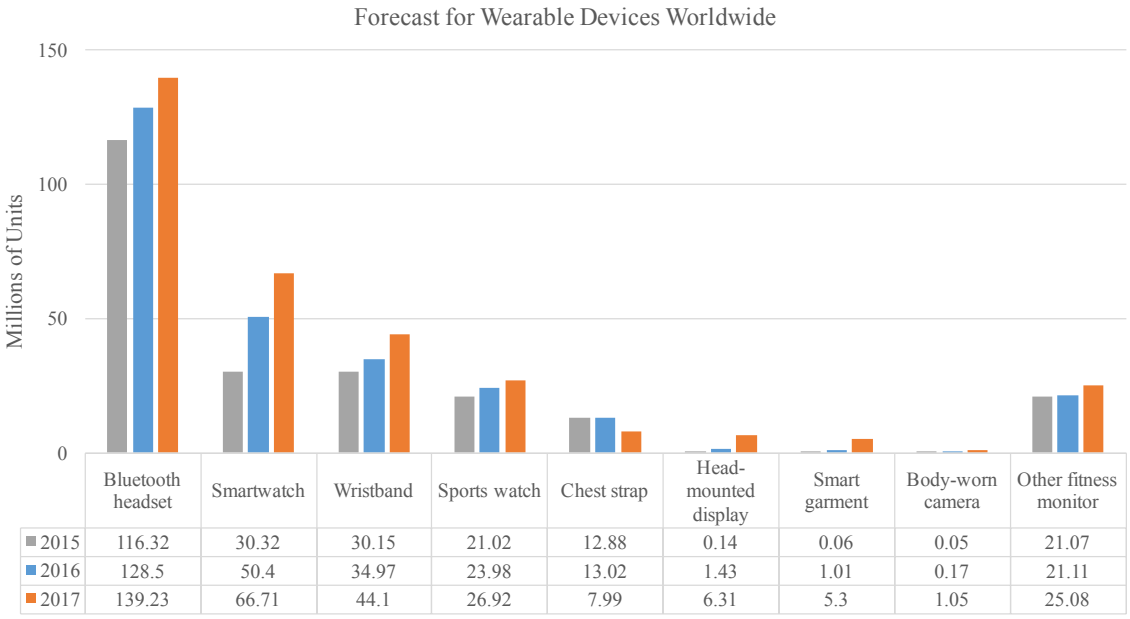

	Bluetooth headset	Smartwatch	Wristband	Sports watch	Chest strap	Head-mounted display	Smart garment	Body-worn camera	Other fitness monitor
2015	116.32	30.32	30.15	21.02	12.88	0.14	0.06	0.05	21.07
2016	128.5	50.4	34.97	23.98	13.02	1.43	1.01	0.17	21.11
2017	139.23	66.71	44.1	26.92	7.99	6.31	5.3	1.05	25.08

Figure 1.1 Predicted growth of wearable devices worldwide by Gartner Inc. [3].

conductive properties ("e-textiles") have been demonstrated as possible materials to create lightweight and flexible wearable devices that can be seamlessly integrated in clothing. Hence, physical cables and bulky circuits are replaced by flexible electronics, making the wearable system lighter and more flexible to be easily adopted by the user. The potential of "smart" clothing has been demonstrated in a broad range of applications, from biomedical applications for health monitoring to military and even space applications. Professional athletes and soldiers already take advantage of these type of garments.

The increasing amount of wearable devices closely attached on the human body surface creates the need for optimising their on-body communication performance by minimising the antenna/ body interaction as well as by thoroughly characterising the dynamic on-body communication channel. So far, a small amount of data in comparison to the plethora of wearable devices has been available in the literature for body-centric communications.

1.1 Overview of Body-Centric Wireless Communications (BCWC)

Wearable devices have evolved the last decade in a variety of applications making everyday life more comfortable and activities less time consuming. By constant monitoring of user's everyday activities and health condition, wearable devices enhance quality of living. A BCWC system can be consisted of either a star or star mesh hybrid topology. In star, several on-body nodes communicate with a central hub node that routes all the data to an off-body node. In the second topology, each on-body node can communicate directly with the destination node without the need for relaying (peer-to-peer).

In BCWC there are 3 types of nodes placed on the human body, forming three types of communication links:

1. *In-body communication (Implant node):* A node that is placed inside the human body, below the skin or further deeper inside the body tissue. The implant node communicates with a node on the body surface.

2. *On-body communication (Body-surface node):* A node that is placed directly on the surface of the human body or at most 2 cm away, and communicates with another body-surface node.

3. *Off-body communication (External node):* A node that is not in contact with human body (from a few centimeters up to several meters away from the body) and communicates with a node on the body surface.

For *on-body* communication, the path between transmitting and receiving nodes should be considered the path around the body curvature rather than a straight line through the body, due to the increased propagation losses in the body tissue. For this reason apart from space waves, propagation through surface waves should also be considered. For *off-body* communication, the distance between transmitter and receiver is not fixed and depends on the type of external node, such as a computer, smart phone, base station or other wearable device mounted on a different user. In Fig. 1.2 all the possible communication links between devices for BANs are shown. Four channel models (CM) occur; Implant node to Implant node (CM1), Implant node to Body Surface node (CM2), Body Surface to Body surface node (CM3) and Body Surface to External node (CM4). The CM3 channel models that will be discussed

in Chapter 2 characterise the path loss of BAN devices taking into account possible shadowing effects due to human body different postures and movement or obstacles near the human body.

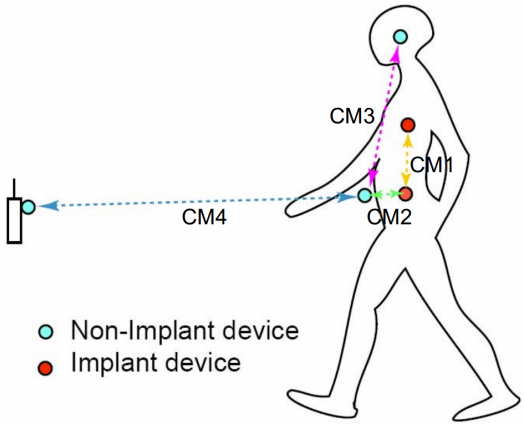

Figure 1.2 Possible communication links for Body Area Networks [4].

A range of operating frequencies is likely to be used in such body area networks, including low frequencies, such as 10 MHz using body coupling mechanism; the industrial, scientific, and medical (ISM) band, at 915 MHz, 2.45 GHz and 5.8 GHz, and the ultra-wideband (UWB) standard, between 3.1 and 10.6 GHz . Much attention has been recently paid to the ISM band due to the increasing number of applications using Bluetooth and Wi-Fi standards.

In Fig. 1.3, the frequency bands commonly used for WBAN are schematically shown.

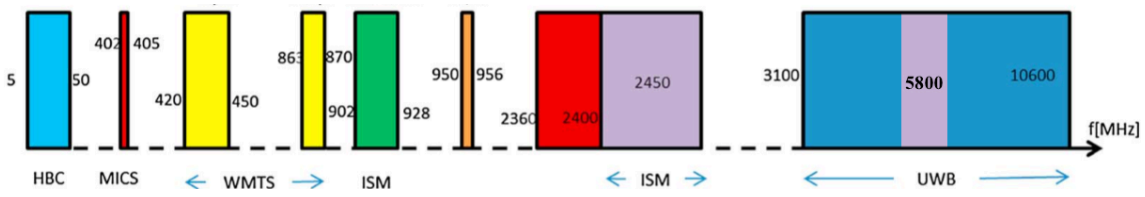

Figure 1.3 Commonly used frequency bands for WBAN [5].

Wearable devices should comply with the health and safety standards concerning the amount of the radiated power towards the human body, while, at the same time, they should operate efficiently and unobstructed inside or on the body surface. The Federal Communications Commission (FCC) in United States and the European Telecommunications Standards Institute (ETSI) organisations set regulations for the compliance/ limitations of short range devices (SRD) that operate in the ISM band

in respect of the operating frequencies, output power, spurious emissions, modulation methods, and transmit duty cycles, among other things.

The frequency bands that cover the majority of applications in BCWC are the Medical Implant Communications Service (MICS) band and the Industrial, Scientific, and Medical (ISM) band.

The MICS band was adopted by FCC on October 10, 1999, and has been developed for use in medical implant communication systems by FCC (47 C.F.R. Part 95) [6] and ETSI (ETSI EN 301 839) [7]. Example applications include heart pacemakers and defibrillators, while, in the future, wireless medical implant systems might include automated drug delivery devices and real-time patient monitoring. The MICS band uses the frequency range between 402 and 405 MHz and gives an implantable medical device the ability to be controlled and monitored from outside. Due to SAR limitations and interference issues, MICS band systems have an upper limit of 25 μW equivalent isotropic radiated power (EIRP) (as the signal level measured outside of the body), which is 2.15 dB lower than the effective radiated power (ERP) level. EIRP is the product of the maximum output power available at the antenna terminal of the transmitter and the antenna gain. Accordingly, the output power is set to a maximum of 25 μW Effective Radiated Power (ERP). A better penetration through the human tissue compared to higher frequencies is achieved. However, electromagnetic waves transmitted from medical implant devices experience high attenuation inside the human body due to the high conductivity of human tissue. Due to the limited bandwidth available (300 kHz), MICS systems exhibit low bit rates as compared to systems using the higher frequency WiFi or Bluetooth technologies.

The ISM band has been created in the early 1990s by FCC for unlicensed communication equipment, which operates in the following frequency ranges:

- 902–928 MHz
- 2400–2483.5 MHz
- 5725–5875 MHz

As compared to the MICS band, the ISM bands provides (a) an easier antenna design due to the higher operation frequency and the expanded expertise obtained through the use of WiFi and Bluetooth systems in recent years, (b) better SAR distributions, and (c) wider bandwidth. However, signals at higher frequencies are attenuated considerably faster inside the human body, thus making the band useful

for on-body and off-body devices while difficult to adopt for in-body (implantable) devices.

The guidelines given by FCC (part 15) [8] according to the maximum allowed EIRP levels regarding on-body devices are:

- A maximum permitted EIRP level of 0.3 W (or 24.7 dBm) for devices operating at 915 MHz.
- A maximum permitted EIRP level of 0.2 W (or 23 dBm) for devices operating at 2.45 GHz and 5.8 GHz.

Accordingly, the European standard, given by ETSI (EN 300 400-1) [9] and by European Commission Decision (2013/752/EU) [10], denotes a maximum EIRP level of 0.01 W (or 10 dBm) at 2.4 GHz. For 5.8 GHz, the same standard denotes a maximum EIRP level of 0.025 W (or 14 dBm).

In this work, the ISM band is thoroughly studied that is considered ideal for short-range over-the-body surface communication due to the extremely low power that minimises SAR and high data rates up to 10 Mbps obtained while simultaneously complying with non-interference guidelines between different devices. For this reason, most of the wearable devices that exist in the market and their respective on-body applications operate using the well-established Wi-Fi and bluetooth standards. Moreover, the majority of the available literature on wearable antennas and on-body channel modelling is focused in this specific frequency band. Hence, there is an increasing interest to understand and improve the current wearable technology in ISM band in order to become a key part of everyday life.

1.2 Research Challenges & Motivation

The human body is considered as a lossy dielectric, which, when located in the near field of a radiating antenna, influences the antenna's input impedance and radiation characteristics significantly. Radiation to some directions is reduced because of the body shadowing, multipath fading and electromagnetic wave absorption in the tissues. The amount of absorption typically depends strongly on the antenna location with respect to the body and the distance from the body surface. The body absorption results to an overall reduction of the transmitted power and consequently to antenna radiation efficiency. This effect forces a wearable device to operate at higher output

power levels to maintain the required link quality and meet the demand for high data rates, hence shortening the battery life.

To overcome the restrictions and limitations due to antenna/ body interaction and therefore optimise the performance of wearable devices, research efforts are focused on wearable antenna design and on-body channel modelling. As it is presented in the literature review (Section 1.4), there is still room for improvement in both aspects in order to achieve an optimised wearable system performance.

In the direction of wearable antenna design, it is necessary to design antennas with low profile in order to be part of user's clothing, less sensitive to body coupling and achieve an improved on-body efficiency. The trend for future wearable antennas is moving to fully integrated antennas in garments in the form of textile antennas with no rigid metallic parts, but there is not still enough evidence that textile antennas efficiency is high enough to provide an efficient communication performance. Advances have to be made in novel design concepts and fabrication with textile materials.

In the majority of wearable antenna investigations, EM simulation is mostly employed as an inexpensive and fast way to characterise the complete (3D) wearable antenna performance. Only in a few cases is combined with measurements on a realistic body phantom that is used to simulate the human body dielectric properties. Apart from the fact that the physical phantoms are very expensive and difficult to be fabricated in-house, they are cumbersome to be controlled (rotated in elevation) with the conventional roll-over-azimuth far-field measurement system. As a result, alternative measurement methods need to be proposed and developed to capture the full spherical radiation pattern with enough accuracy and practicality.

The communication of wearable devices is linked together with many significant challenges, particularly, the increasing propagation losses on the body surface, human body movement and activity that create fading and shadowing effects on the transmitted signal due to variations in body posture. These effects are especially severe when antennas are mounted on the upper limbs (arms and hands), and become extreme while the user is playing sports or doing highly dynamic activities. Due to the body motion, a wearable antenna is constantly changing its direction of maximum radiation that can lead to dynamic changes in the radio channel performance. A detailed knowledge of the on-body channel (taking into account antenna/body interactions) is required to analyse and properly design systems that will be functional on human body and communicate with other off-body links.

Hence, to ensure the efficient communication between wearable devices, the chan-

nel model needs to be characterised and modelled with respect to the communication environment and the antenna type. This on-body random channel behaviour suggests a statistical approach to the problem, which has not been considered by many studies.

The current thesis motivated from the recent proliferation of wearable devices in our everyday life, contributes to the evolution of body-centric wireless communications in the aspects of wearable antennas design and characterisation, textile antennas fabrication as well as to empirical channel modelling for on-body and off-body links.

1.3 Research Objective & Novelty

The scope of this thesis is focused on the investigation of how wearable devices perform and communicate on the surface of the human body. It is examined how the radiation characteristics of wearable antennas are affected from the close proximity interaction with human body. Wearable antennas are developed with the intention of achieving an optimised antenna system performance.

In order to achieve the complete wearable antenna performance assessment, the development of a measurement methodology based on the cylindrical near-field measurement technique using a full-body anthropomorphic phantom is demonstrated. The design and fabrication of on-body and off-body textile wearable antennas is presented and tested using the proposed measurement method. In addition, modelling of the propagation channel between wearable devices is undertaken through channel measurements, concerning several on-body setups and different antenna types. This research work is based mostly in experimental measurement results. However, an extended number of EM simulations is performed for comparison and evaluation purposes.

The novel contribution of this thesis in the field of body-centric wireless communications is summarised as follows:

- *Development of a cylindrical near-field (CNF) measurement method for wearable antennas performance characterisation on a full body anthropomorphic phantom*, which is otherwise impractical with the conventional roll-over-azimuth far-field system. The 3D far-field on-body antenna gain and on-body radiation efficiency are readily produced, which are important parameters for wearable antenna and system optimisation. The accuracy of the proposed method is validated by

comparing the on-body performance of a printed dipole with EM simulations using a homogenous anthropomorphic numerical phantom. The feasibility of characterising on-body and off-body wearable antennas is also demonstrated, using two textile wearable patch antennas (MPA & HMMPA).

- *A diagnostic tool for wearable antenna performance assessment on the surface of human body is demonstrated*, by plotting the measured near-field pattern of the antenna on the human body outline. This gives an insight of the antenna-body interaction, wave propagation around and along the body surface and can be a valuable tool for predicting the optimal antenna on-body location for a wearable multi-sensor system.

- *Design and fabrication of low profile "fully-textile" wearable antennas using a computerised embroidery machine.* The design and fabrication of a "fully-textile" higher-mode microstrip patch antenna (HMMPA) at 2.4 GHz is presented, which is suitable for on-body communications as it supports surface wave propagation. An omni-directional radiation pattern parallel to the human body surface is obtained with nearly 50% on-body radiation efficiency, by employing the CNF measurement method. In addition, a fully-embroidered circularly polarised spiral antenna is presented, which is suitable for off-body communications. This antenna design can be comfortably worn and embedded in clothing while achieving a broadband performance from 0.9-3 GHz. It has been initially designed and fabricated during a master's thesis and its performance is improved herein by adding an impedance transformer. A useful broadband characterisation of antenna-body interaction is achieved in this work by employing this well-known spiral antenna design.

- *Statistical modelling of static and dynamic on-body channels is investigated*: The feasibility of on-body channel modelling using EM simulation tools is demonstrated. A series of EM simulations is employed to study the dynamic waist-foot on-body channel when the user performs walking and running activities. Each activity (one pace) is reproduced by 30 consecutive body postures (frames) of a numerical body phantom using a 3D animation software. Channel measurements are also performed to characterise four commonly used on-body channels, with the one part fixed on the waist of the human body while the other part located on the chest, back, wrist and foot. Three wearable antennas with differ-

ent polarisation and radiation characteristics are used to examine the effect of the antenna type on the derived channel model. Channel path gain is derived, while large-scale and small-scale fading of the received signal are characterised by best-fit statistical distribution models.

1.4 Literature Review

A literature review is presented in this section concerning recent advances in textile wearable antennas, channel modelling for on-body communications and antenna measurements for on-body communications. For the sake of clarity and consistency, this literature review presents the state-of-the-art only at the ISM band with the upper limit set at 5.8 GHz.

1.4.1 Wearable Antennas

In order to design a product for a wearable application and being accepted by the majority of consumers, the radio components need to be hidden, conformal to the body, small in size and light weight. In this direction, a possible integration of the radio system within everyone's daily clothes is not far from reality. Therefore, the antennas integrated in such a device need to preserve the above characteristics and consume as far as low power possible to maximise battery life. To achieve this, the antennas need to be insensitive to the effect of the human body. Thus, a low coupling between antennas and body is required in order to obtain high radiation efficiency and low specific absorption rate (SAR) [11].

The wearable antenna performance is significantly affected by the close proximity to the human body; for example, in terms of reduced gain and efficiency due to power absorption, radiation pattern deformation (varying propagation conditions), resonance frequency detuning and variations in impedance matching level and bandwidth due to antenna-body capacitive coupling. These effects vary between different antenna designs and separation distances [12].

This antenna/ body interaction is also dependent on the frequency range of operation of wearable antennas, for which the energy does not penetrate deeply in the body (typically above 1 GHz) and appears significantly different between narrowband and ultra-wideband cases. For both, the near field coupling with the body modifies the antenna currents, hence the input impedance matching, and induces energy absorp-

tion. However, in the narrowband case, the dominant effect, and major drawback, is the shift of the resonance frequency causing mismatch, in addition to the losses inside the body, resulting in severe reduction of the total efficiency. This review is focused on the investigation of the performance of narrowband wearable antennas.

There have been many works that try to characterise the degradation of antenna performance in proximity to the body. It is shown that antennas with full ground plane such as microstrip patches have minimum susceptibility to the body presence, as a shield is formed between them. In [12], a parametric study to evaluate how the antenna-body spacing affects the antenna performance has been presented. It is proved that the further the antenna moves away from the body surface, the lower is the absorption in the human body.

Rigid & Textile Wearable Antenna Designs

Wearable antennas have evolved through the years starting from rigid antenna prototypes made solely from solid dielectrics and copper sheets, to textile antennas with a flexible dielectric substrate and conductive textiles, and recently to fully-textile antennas that are directly woven on fabrics with specialised conductive fibres. Rigid wearable antennas cover the majority of the available literature with many different antenna designs and radiation properties [11, 13, 13–21].

Hall et al. have done extensive studies in narrowband antennas to find the most suitable for on-body applications, especially at 2.4 GHz ISM band [13] (Fig.1.4 [13]). Antennas for on-body communications need to have a radiation pattern shape that minimises the link loss [11]. Because attenuation inside the human tissue is very high, propagation around the human body into shadow regions is mostly obtained via surface/ creeping waves. It has been found that an antenna with polarisation perpendicular to the surface of the body induces strong surface waves and is best-suited for on-body communications [11]. Among the five antennas tested in Fig.1.4, the top loaded monopole antenna with ground plane shows the best performance with respect to path loss, due to the omnidirectional radiation pattern in the direction tangential to the body surface, in contrast to a loop antenna that exhibits high propagation losses and fading.

In [21], a dual-band (2.4 GHz, 5.2 GHz) “button” antenna for WLAN applications was presented. The antenna has the size of a standard metal button used in denim jeans, and can be easily integrated in clothes. The antenna has monopole-

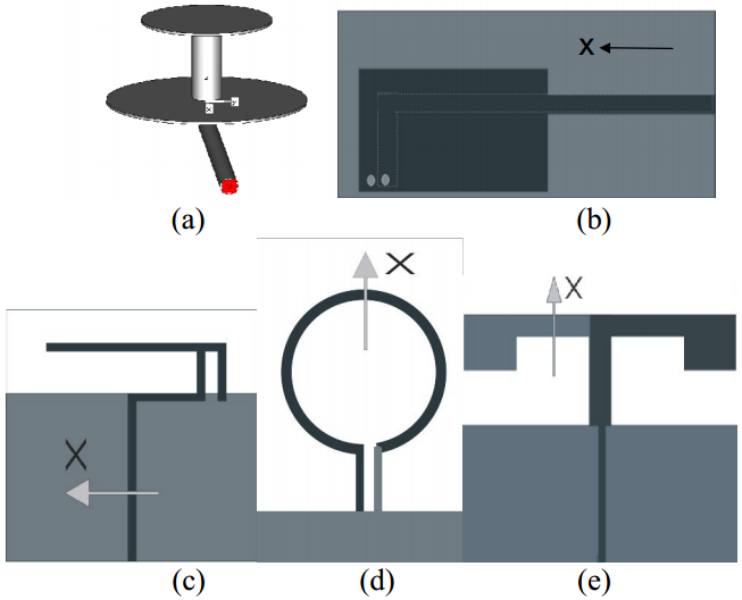

Figure 1.4 (a) Top loaded monopole, (b) planar inverted F antenna (PIFA), (c) printed inverted F antenna (IFA), (d) loop, (e) dipole [13].

like radiation performance in both frequency bands of operation. While a monopole antenna offers low propagation losses, although it has the drawback of a high profile. Subsequently, a planar inverted-F antenna (PIFA) or higher-mode microstrip patch antenna (HMMPA) offer a reasonable compromise between practicality and performance.

In [16], Scanlon et al. presented a higher-mode microstrip patch antenna operating at 2.45 GHz (Fig.1.5a) that outperforms other commonly used designs (Fig.1.5b) for on-body communication. The HMMPA antenna has the advantage of a vertical monopole-like radiation pattern with a low-profile. Two grounding posts offset from the feed are used to force nulls in the electric field between the groundplane and patch element. In this way, despite a total antenna height of only $\lambda/20$, the on-body coupling performance is comparable to that with a quarter wavelength monopole with ground plane and significantly higher than that measured with a fundamental mode (TM_{01}) microstrip patch antenna. A stacked-patch antenna with switchable (on-body/ off-body) propagation mode was also developed at 2.45 GHz in [20], using RF switches to control the grounding post for the on-body mode.

As an alternative, a planar inverted F antenna (PIFA) created from a folded $\lambda/4$ monopole that is stretched to form a plate was proposed in [22] by Salonen. Due to its small size and high gain, it can be used in a WBAN system (Fig.1.6).

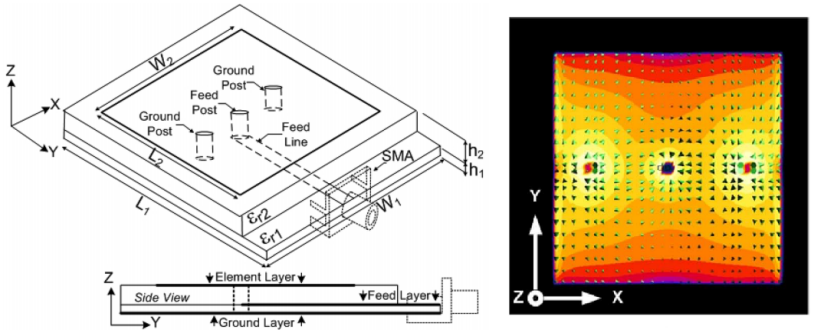

(a)

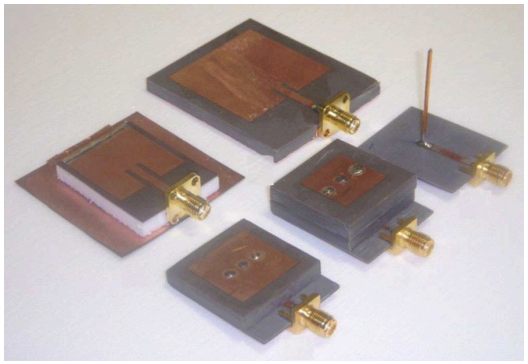

(b)

Figure 1.5 (a) Geometry of higher mode microstrip patch antenna (HMMPA) and normalized current magnitude distribution, (b) fabricated wearable antennas on rigid dielectric (Taconic TLY-3) substrate [16].

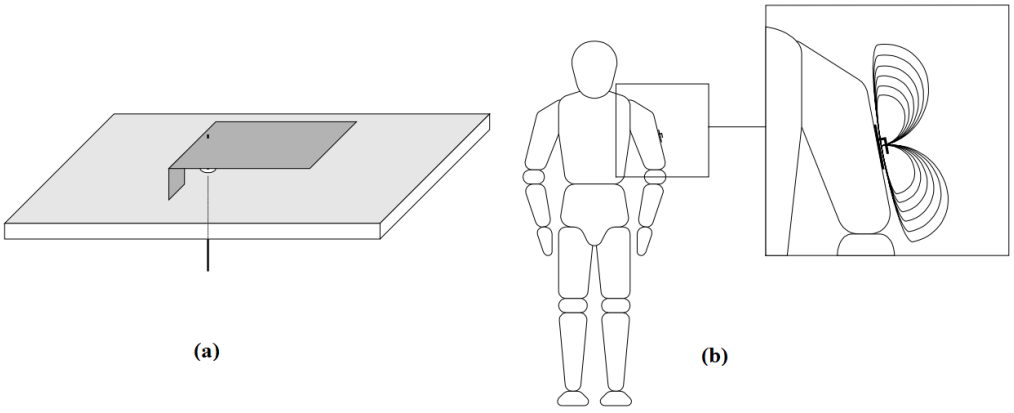

Figure 1.6 (a) Basic geometry of Planar Inverted F antenna (PIFA), and (b) a possible placement on human body [22].

In the recent years, the trend of "smart" clothing requires textile based antennas that offer flexibility and integration to user's clothing without compromising the performance. The main difference between conventional copper based and textile based antennas is that the conductive surface of the conventional copper antenna is continuous, which easily achieves high conductivity and uniform electromagnetic fields, yielding high efficiency antennas. Creating a highly efficient textile based antenna is a challenge due to the discontinuous and anisotropic surface of the conductive textile. A systematic study of characterising different types of conductive textiles is undertaken in [23]. It is demonstrated that a patch antenna fabricated with conductive textiles achieves a gain of 6.6 dB and radiation efficiency of 79% in comparison to a reference copper patch antenna that obtains a gain of 7.4 dB and radiation efficiency of 95%. Hence, the conductive textile materials can replace the solid metal sheets in wearable applications with minimal performance degradation while adding functionality through wearability. Embroidery using conductive thread can achieve both high conductivity and flexibility.

Several antennas made out of textile materials have been proposed to enable the integration of wireless devices in garments and smart clothes [22, 24–32]. In [25], a circularly polarised patch antenna (Fig.1.7) integrated into protective clothing for fire-fighters was introduced. The antenna was printed on a flexible pad of foam, which is commonly used in protective clothing.

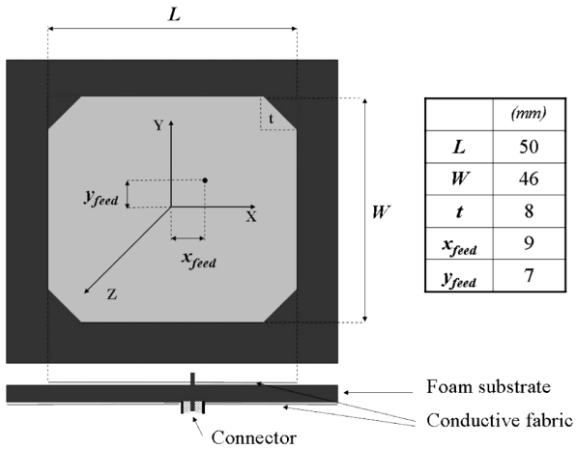

Figure 1.7 Truncated corner circularly polarised microstrip patch antenna on a flexible pad foam [25].

The effect of bending and crumbling of textile antennas has been studied thoroughly by Langley et al. [27, 28]. In this study, a Printed IFA (Fig.1.8a) [27] design

is investigated at 2.4 GHz. It made of felt and conductive Zelt materials. It was concluded that antennas efficiency and radiated power were significantly degraded from crumpling in both free space and on-body cases.

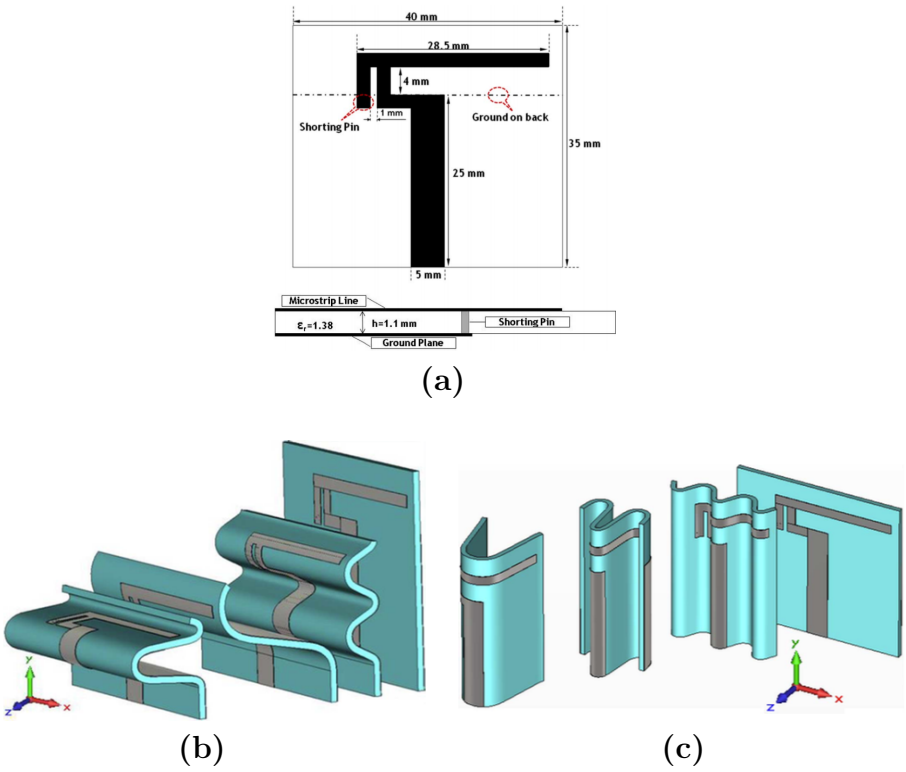

Figure 1.8 (a) Printed IFA design, and EM modelling of (b) bending and (c) crumpling effects [27].

In [26], a flexible dual-band patch antenna (at 2.45 and 5.5 GHz) printed on an EM band gap (EBG) textile substrate made of felt (Fig.1.9) was proposed. Results

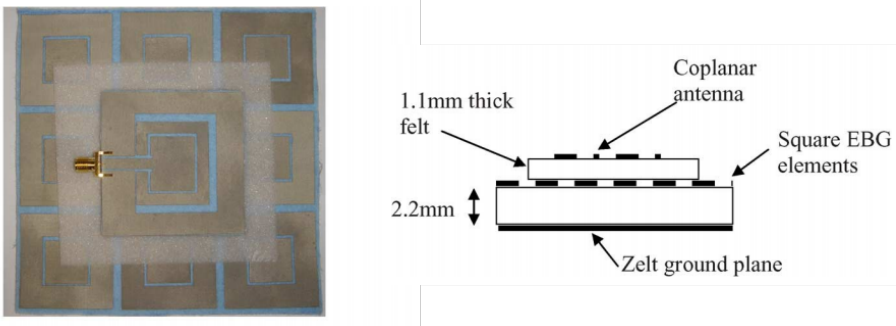

Figure 1.9 Dual-band coplanar antenna on EBG plane [26].

demonstrated that by introducing the EBG, the radiation into the body is reduced by over 10 dB, and the antenna gain is improved by 3 dB. However, the antenna is big in size (120 x 120 mm).

Some remarkable low-profile, flexible and conformal textile antenna designs have been proposed in the literature [2, 23, 33–42] for on-body and off-body wireless communications systems. These textile antennas can be part of any type of clothing or garment such as scarf, purse or suitcase. As such, the antennas no longer needs to be kept in the cell phone or smartwatch and thus significantly enhancing their radiation performance for reliable connectivity. The ultimate purpose of textile-based wearable antennas is to replace antennas on conventional portable wireless devices and operate on the surface of human body.

Different fabrication technologies have been used to realise the conductive part of textile wearable antennas, as they are presented in [43] (Fig. 1.10). A wearable patch antenna can be made from (a) conductive textile materials ("e-textiles"), (b) etched copper, (c) screen printed and (d) copper foil on textile substrate. The simplest approach is to integrate, knit, or embroider conducting wires or conductive yarns for the realisation of dipole-like antennas, and copper tape for planar antennas into a piece of clothing. Although conducting wires and copper tape are flexible, they are not breathable, and they may affect the comfort of the person wearing the jacket. Therefore, they do not provide fully integrated textile antenna solutions.

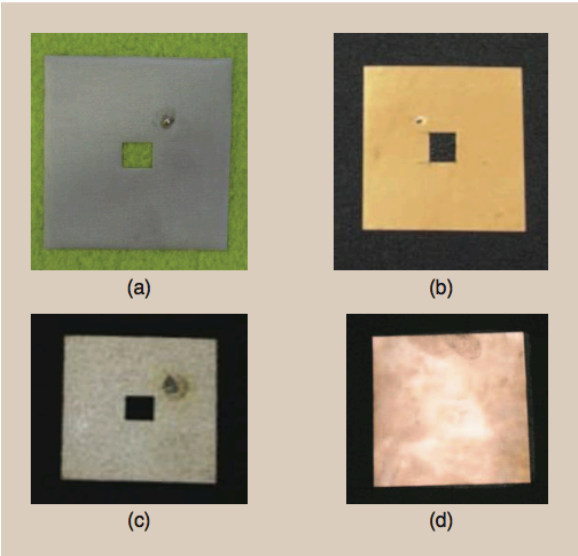

Figure 1.10 Wearable patch antennas realised with different conductive parts [43].

A more appropriate technique to realize full-fabric antennas consists of attaching e-textiles, which are typically copper- or copper-nickel-plated nonwoven fabrics, to the textile substrate. Ouyang et al. [44] wove electrotextile microstrip antenna patches by combining conductive and nonconductive yarns.

Additive techniques may be applied, such as screen or inkjet printing, to define antenna, reflector, and ground-plane patterns on the garment [45, 46] it was demonstrated that textile antennas may be inkjet printed, provided that a screen-printed interface layer is first applied to reduce the surface roughness of the textile substrate.

Embroidered patch antennas [47] have recently gained in popularity thanks to the availability of low-cost automatic embroidery machines that operate with conductive yarns. These machines enable the study of different embroidery patterns for the antenna and ground plane.

A successful attempt to realise fully textile body-worn antennas by weaving or embroidering conductive fibres in normal fabrics has been made in Loughborough University [30, 31] and in Ohio State University [32]. In [32], Ag-Zylon conductive fibres were embroidered on polyester (PDMS) fabric that offers high flexibility, light weight performance and low surface resistivity accomplishing several remarkable antenna designs (Fig.1.11 [32]).

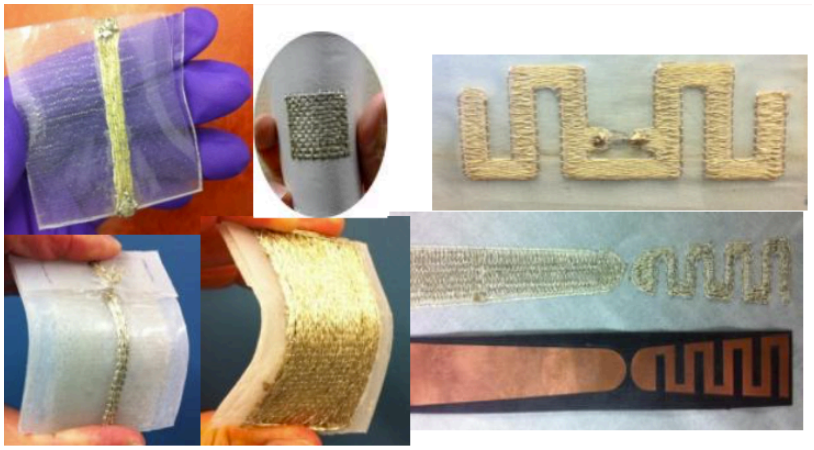

Figure 1.11 Picture of several embroidered wearable antennas [32].

In [30], the researchers obtained good repeatability and similar behaviour to printed patch antennas with embroidered patch antennas (Fig.1.12 [30]) using Amberstrand (2 Ohms/feet) as a conductive thread in respect to copper tape counterparts by varying stitch spacing, direction and density.

Finally, in [40], an interesting parametric study on the effect of thread thickness

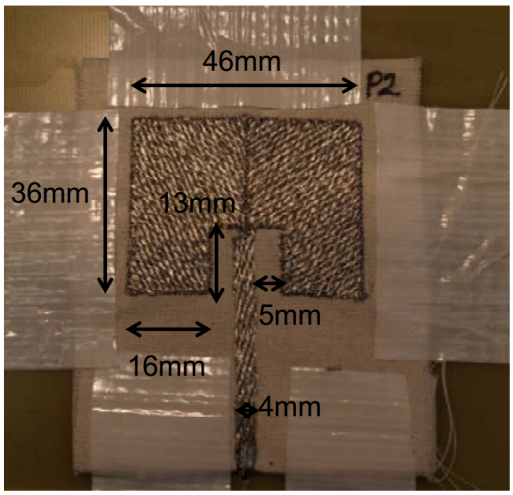

Figure 1.12 Embroidered patch antenna with diagonal stitching [30].

and stitching interval on the radiation efficiency of embroidered patch antennas is presented. The fabricated patch antennas on felt substrate employing silver-coated threads (Liberator) are shown in Fig.1.13 [40]. With the t = 0.8 mm antenna, the radiation efficiency improves slightly from 78.5% to 80.8% as d is increased from 0.25 to 3 mm. On the other hand, for the t = 0.2 mm antenna, the radiation efficiency drops from 88.2% to 62.4% with the same d increment. It is then concluded that a high antenna radiation efficiency (80.8%) can be achieved with a wide interval between the threads, when a thicker conductive thread is used.

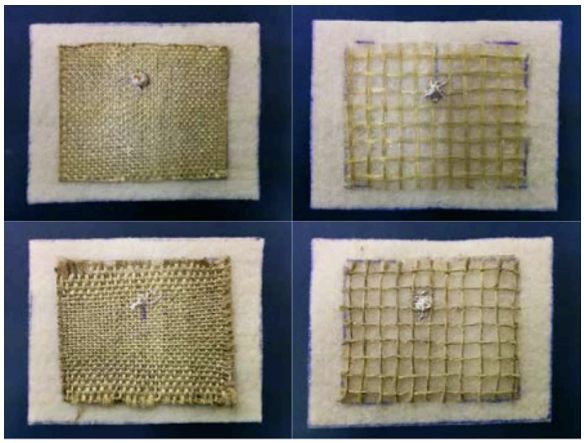

Figure 1.13 Picture of embroidered patch antennas with different thread thickness t and stitching interval d: upper-left t= 0.2 mm and d = 0.25 mm, upper-right is t = 0.2 mm and d = 3.0 mm, bottom- left is t = 0.8 mm and d = 0.25 mm, and bottom-right is t = 0.8 mm and d = 3.0 mm. [40].

1.4.2 On-Body Antenna Measurements

While there have been many attempts to characterise numerically wearable antenna performance on the human body, there is a lack of enough experimental studies due to the need for advanced measurement facilities and human body phantoms.

With conventional far-field measurement techniques, it is cumbersome (both due to mechanical and time constraints) to capture a sufficient number of radiation pattern cuts that can accurately determine antenna performance parameters, such as the radiation efficiency. This is due to the majority of the roll-axis positioners, which are essential for the rotation of the antenna in the elevation plane, cannot handle the heavy weight ($\approx$ 90 Kg) and the size of a full-body phantom. In [48], the far-field measurement of a wearable antenna was demonstrated by replacing the metallic coaxial cable with an optical fibre. With this setup, only the azimuth plane of the far-field pattern was feasible to be measured using a head and torso anthropomorphic phantom (Fig. 1.14).

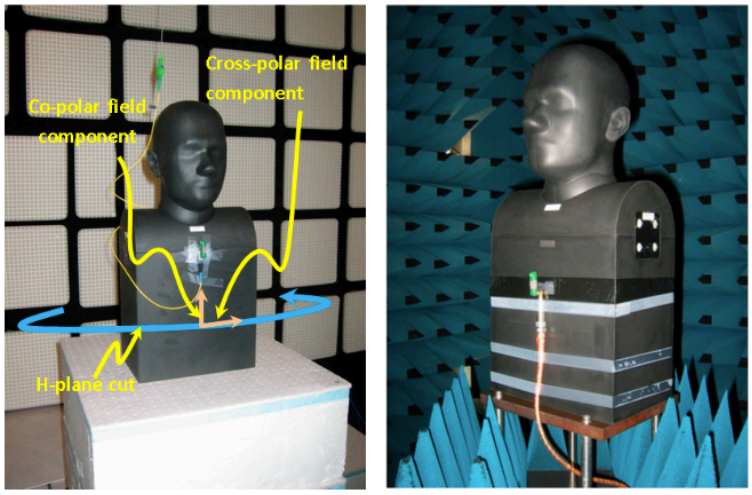

Figure 1.14 Radiation pattern measurement using a head and torso anthropomorphic phantom in a conventional far-field anechoic chamber [48].

In [49], the radiation efficiency of textile wearable antennas was derived from far-field measurements by employing the 3D far-field pattern integration method. To enable the rotation in the elevation, a small (25 x 30 x 6 cm) rectangular phantom with homogeneous dielectric material to simulate the human torso was created. Moreover, a modified Wheeler cap method including a small cylindrical body phantom below the antenna was also employed in [50] to measure the efficiency of on-body antennas.

However, in both studies, different interactions take place compared to using a full-body phantom that lead to inaccuracy in the antenna efficiency estimation.

Through recent studies [51–54], the reverberation chamber method has been introduced as a useful tool for determining wearable antenna efficiency on a live human subject without the need for radiation pattern measurements. While this measurement technique has been proven accurate and repeatable over a lot of cases, it lacks the electromagnetic insight of the on-body antenna performance which can be gained from the measured radiation patterns.

Figure 1.15 Reverberation chamber measurement of textile antenna efficiency on a real human body [51].

In the last two decades, the near-field measurement technique, found in spherical [55] (STARGATE SG-62) (Fig. 1.16a), [56] (RAMS) (Fig. 1.16b) and cylindrical configurations [57–59], has been successfully implemented as an alternative method for assessing the far-field radiation performance of antennas, both in free space and in close proximity to the user (handset antennas).

Recently, there is a growing interest to investigate wearable antennas performance with spherical [60] and cylindrical [38, 61] near-field measurements. So far, a limited amount of test cases and antenna types has been investigated. In [60], a spherical near-field facility was used to characterise wearable antennas on a custom made oval torso phantom (Fig. 1.17). In [38, 61], the potential of characterising fabric antennas on the torso of a human body phantom was demonstrated in the BAE Systems cylindrical near-field test facility (CNFT). The radiation patterns for azimuth and elevation planes were derived. The results showed a good agreement with simulations. However, the capability of using the near-field measurement technique has not

yet been demonstrated in full-size body phantoms with anthropomorphic shape and different types of wearable antennas and frequencies of operation.

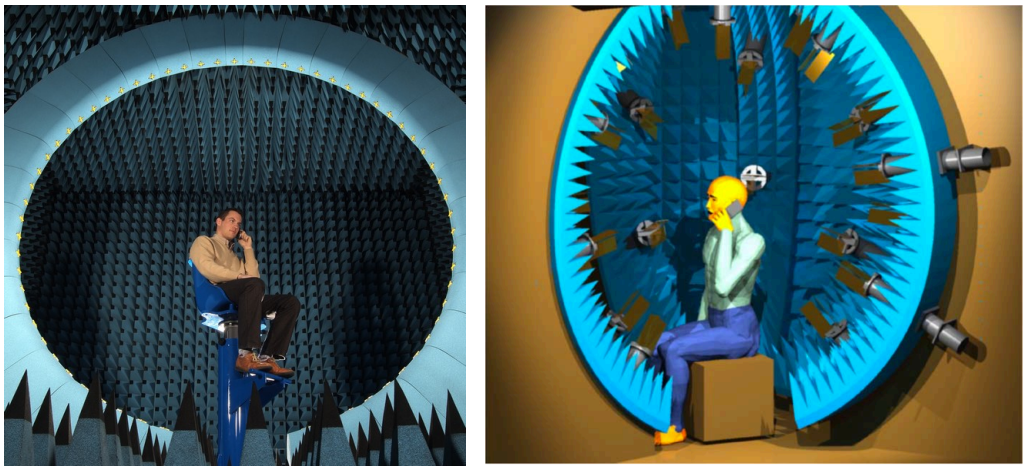

(a) **(b)**

Figure 1.16 Commercial (a) STARGATE SG-62 and (b) RAMS spherical near-field measurement systems [55, 56].

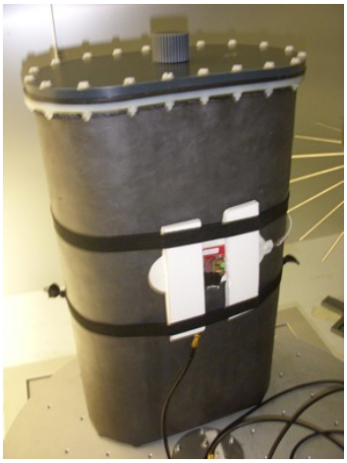

Figure 1.17 Wearable antennas characterisation on a custom made oval torso phantom [60].

1.4.3 On-Body Channel Modelling

An overview of the most common approaches on the propagation and channel modelling for on-body communications is presented here in detail. Together, some theoretical background is provided for a better understanding. The big variability of the

antenna/body interaction and the different on-body propagation mechanisms let us consider the human body as an extremely complex environment for the operation of wireless devices. Hence, the communication channel modelling becomes an interesting but challenging task that has been examined with several approaches. The first effort to standardise the BANs, both for narrowband and ultra-wideband systems has been attempted by the IEEE 802.15.6 working group through extensive measurement campaigns [62]. Guidelines are developed for wireless technologies that incorporate the effect of human body in a range of user scenarios. Recently, some review papers that cover the majority of the research efforts to model the on-body and off-body propagation channels have been found in the open literature [63], [5].

In all cases, two types of channel models may be created:

- A theoretical (or deterministic) model
- An empirical (or stochastic) model

A theoretical model is created using the fundamental principles of electromagnetic wave theory (Maxwell's equations) or ray-tracing techniques and permits a precise modelling of a specific situation at link level. It is intended for detailed exploration of the influence of human body on antenna structures. Although, it requires a detailed description of the propagation environment and is therefore not suitable for modelling of complex environments.

An empirical model is derived from a set of propagation measurements and is intended to provide a convenient basis for statistical modelling of the channel. Compared to the theoretical model, the empirical model uses a simplified description of the environment. Appropriate efforts could be made to ensure that the two sets of models are consistent with each other. Most of the studies reported in the literature take the empirical approach, which is less complex than the theoretical and will be covered in the following sections. Some of the analysis is made in various environments with specific user actions (e.g. sitting down, standing still, walking indoors, running outdoors, e.t.c.) considered separately (scenario-based channel model) or aggregated to create a more universal channel model [64]. Studies focused in path loss and first order statistics will be discussed.

Path Loss

Unlike traditional wireless communications, the path loss for body-centric communications is dependent on the geometry of the human body and the different signal path

trajectories that can be formed. Moreover, propagation mechanisms on the human body are very diverse, mainly combining free space propagation, diffraction (surface or creeping waves) and scattering on the body surface, and off-body reflections (from the surrounding environment). Hence, different on-body signal paths with the same length can be subject to very different propagation mechanisms and thus large differences in path loss. As a result, it is quite difficult to use a general distance dependent path loss model to accurately describe the various channels formed on the surface of human body.

The classical approach, which could be quoted as physical, considers modelling the path loss as a function of inter-antennas distance for a specific part of the human body (such as around or in front of the torso, or along arm or leg, etc.) [13, 65–68].

- **Log-distance model:**

  The path loss model (in dB) between the transmitting and the receiving antennas as a function of the distance d based on the Friis formula in free space is described by [69, 70]:

$$PL(d) = PL_0 + 10nlog_{10}(\frac{d}{d_0}) \tag{1.1}$$

  where PL_0 is the path loss at a reference distance d_0, and n is the path loss exponent.

For the body-centric channel, the PL_0 term depends not only on the reference distance, showing an increasing trend especially for links around the torso, but also on the antenna near-field interaction with body, that results to energy absorption in the body that affects the total efficiency of each antenna. Consequently it depends on the used antenna type, e.g. narrowband or broadband, with ground plane or not, well-balanced or not, etc., and, on the separation distance between the antenna and the body. As a result, an optimised wearable antenna design could improve system performance. This strong antenna/body interaction makes the antenna an "intrinsic" part of the channel that cannot be easily de-embedded. Hall et al. have provided a method [71] that the antenna gain can be de-embedded from the propagation channel gain by performing several channel measurements with different antenna polarisations in respect to body surface, although some approximations are considered.

Alternatively to the above conventional approach that is still widely used for modelling path loss in body-centric scenarios, there are some other path loss models developed by the IEEE 802.15.6 [4]:

- **Power law model:**

$$PL(d_{[mm]})[dB] = a \cdot log_{10}(d_{[mm]}) + b + N \tag{1.2}$$

where a and b are parameters of the model, N is a normally distributed variable, centered with standard deviation σ_N and d is the distance between the transmitter and the receiver.

The model parameters for body surface communication (CM3) at 2.4 GHz ISM band as derived from measurements in anechoic environment and in hospital room are given in Table 1.1 [72].

Table 1.1 Power Law Model Parameters [72]

Parameter	Hospital Room	Anechoic Chamber
a	6.6	29.3
b	36.1	-16.8
σ_N	3.8	6.89

- **Exponential model:**

$$PL(d)[dB] = P_0 + \gamma \cdot (d - d_0) \tag{1.3}$$

where γ denotes the path loss exponent and P_0 denotes the path loss at a reference distance d_0.

This model is proposed essentially for UWB channels; it is used e.g. in [73] for the propagation along or around torso in an anechoic chamber environment.

- **Hybrid (Exponential-"Saturation") model [74]:**

This kind of model is "hybrid" in the sense that it merges a local propagation model (on-body to on-body) and the influence of the environment (typically multi-path components (MPCs) reflecting off the floor and the walls) resulting in an exponential part for "short distances" (on-body mechanism) and a "saturation" behaviour of the PL for larger distances, accounting for MPCs that become dominant in an indoor environment. It can be used for narrow-band channels at 915 MHz and 2.4 GHz bands. The hybrid path loss model is written as:

$$PL(d_{[cm]})[dB] = -10 \cdot log_{10}(P_0 e^{-m_0 d_{[cm]}} + P_1) + \sigma_p n_p) \tag{1.4}$$

where P_0, P_1 and m_0 are parameters of the model.

In this model, $PL[dB]$ represents the path loss at a distance d measured around the body surface. The P_0 parameter corresponds to the average losses that occur close to the transmitter depending on the antenna type. The P_1 parameter is the average attenuation of the MPCs in an indoor environment. The parameter m_0 represents the average exponential decay rate (in dB/cm) of the creeping wave component travelling around the body surface, n_p is a zero mean and unit variance Gaussian random variable, and σ_p is the lognormal variance in dB around the mean, which represents the variations measured at different body curvatures, tissue properties, and antenna radiation properties in different body and room locations.

The model parameters for an on-body surface to on-body surface scenario (CM3) based on measurements conducted at 2.45 GHz are shown in Table 1.2 [74]. It is observed that the path loss follows an exponential decay around the perimeter of the body and it flattens out for large distances due to the contribution of MPCs from the indoor environment.

Table 1.2 Saturation Model Parameters [74]

Parameter	**Value**
P_0[dB]	-25.8
m_0[dB/cm]	2
P_1[dB]	-71.3
σ_p[dB]	3.6

- **Scenario-Based model [75, 76]:**
  In this scenario-based approach, application-based radio links ("scenarios") are modelled, e.g. belt to chest for ECGs or foot to belt for Nike+ app, and the PL is derived from measurements, including various sources of variability (human body shadowing, "local positioning", posture, intentional and unintentional movements, antennas, etc.). The PL is dependent only on the propagation scenario and not on the distance [75–79]. It can be used for both narrowband and UWB channels.

$$PL[dB] = P_{T_X} - P_{R_X} + G_{amp} - L_{cable} \tag{1.5}$$

  where P_{T_X} represents the input power in the transmitted antenna port, P_{R_X} the received power, G_{amp} the amplifier gain and L_{cable} the cable losses that occur during the measurements.

Table 1.3 presents the average path loss $P[dB]$ derived from fitting the experimental data [75] in equation 1.5.

Table 1.3 Scenario-based Model Parameters [75]

	Receiver at Right Hip						Receiver at Chest		
Action	Chest	R Wrist	L Wrist	R Ankle	L Ankle	Back	Back	R Wrist	R Ankle
Standing	65.3	44.5	74.7	60.9	70.7	75.3	73	70.5	66.3
Walking	59.1	47.3	59.8	53.9	58.5	67.4	72	64.9	62.4
Running	55.9	36.3	52.5	55.0	59.0	68.5	71.7	57.4	63.3

The scenario-based approach has the advantage of not merging very different radio link situations which could be near field (NF) or far field (FF), quasi-LOS, pseudo-periodic (from LOS to NLOS), or completely NLOS (such as hip to chest,or hip to wrist or front to back). Indeed, depending on the configuration, the distance effect can be negligible in contrary to other dominant effects such as strong shadowing or fading due to movements.

A detailed state-of-the-art has been published in [63]. A very large dispersion of the results, regarding PL models is observed, both in anechoic chamber and in indoor premises. This is explained due to the lack of standard protocols regarding measurement procedures, analyses and modelling. In addition, the large variability of the BAN channel is underlined with regard to human subjects, postures and movements, used antennas types, positioning on the body and surrounding environment. Moreover, applicability of the proposed models is not established generally, as it is not clear whether they are specific or nonspecific, as well the collected statistical sets often seem either too small or too specific.

Overall, exponential models present a typical attenuation coefficient γ ranging from 1 to 2 dB/cm at 2.4 GHz, and power law models with PL exponents ranging from 1.5 to 5 depending on the frequency range, LOS/NLOS configurations, and environment that have been resulted from path loss modelling [80]. Typical PL ranges from 30 to 110 dB have been found, depending on the frequency [4], the radio link configuration (LOS/NLOS) including body postures or motion [81], the environment type, the antenna type [82] and its distance to the body for most of them.

Some general trends of the PL are listed:

- The higher the frequency, the stronger the PL value.

- The shadowing effect of the body is strong, e.g. typically ranging between 5 and 15 dB in the 3- 5 GHz band.
- Because of the rich MPCs from the surrounding environment, PL values are higher in anechoic environment.
- Antenna types, and even more, antenna distance to the body, may cause PL variations as high as 15 dB.

An alternative approach to gain knowledge about the path loss variations has been given in [83] via extensive numerical simulations. In this approach, antennas are attached on a walking avatar at 2.45 GHz. A pseudo-moving action is obtained using an animation software that created 30 frames of motion. In respect to simulations, the same procedure is performed in an anechoic chamber to examine the consistency between simulations and measurements. The results show a quite promising matching between simulation and measurement results that born hopes for future development in numerical techniques including human body motion factor.

Channel Fading

In body-centric communications, propagation paths can experience fading due to many different reasons. It could be due to the changing distance between the antennas, changing orientations of the antennas relative to each other and the body, due to shadowing by body parts, or it could be caused by the scattering of several multi-path components from the body itself or the local environment. It is quite clear that the human body mobility should be taken into account in order to accurately describe the channel characteristics in realistic BAN applications. Fading can be categorised in: small-scale and large-scale fading. An example of large-scale and small-scale fading components on a received signal power is presented in Fig.1.18.

The time-dependent power transfer function $P(t_n)$ of the received signal can be expressed as [84]:

$$P(t_n) = G_0 \cdot S(t_n) \cdot F(t_n) \tag{1.6}$$

where G_0 represents the mean channel gain, $S(t_n)$ and $F(t_n)$ the large-scale and small-scale fading components.

Due to the variation of human body posture caused by the movement of body parts, path loss given from equation (1.1) will deviate from the mean value for a

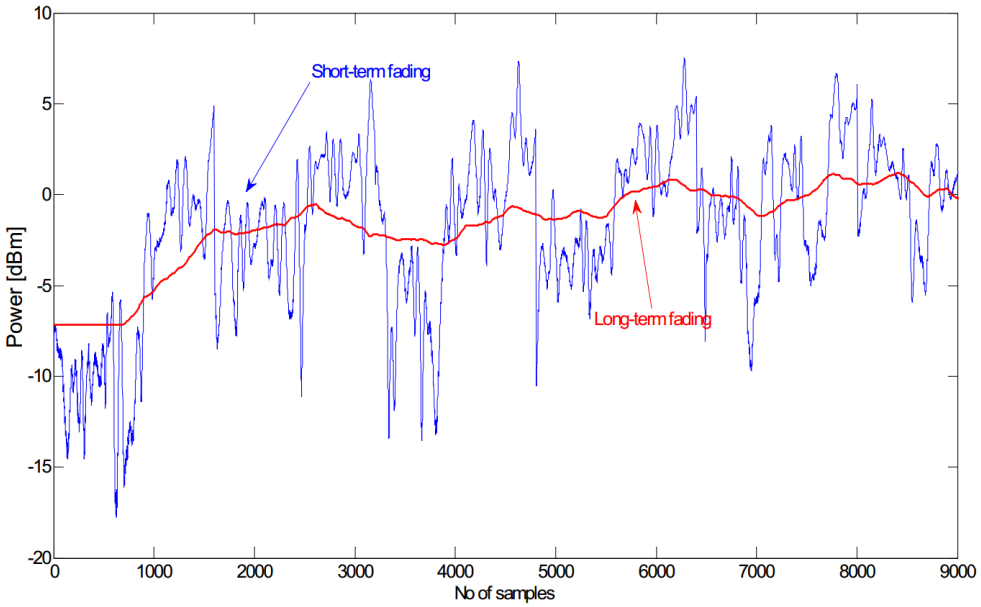

Figure 1.18 Received signal power comprising of large-scale and small-scale fading components.

given distance. This phenomenon is called *shadowing*, and it reflects to the path loss variation around its mean value. Shadowing should be considered for stationary and non-stationary position of body.

When shadowing is considered, the total path loss PL can be expressed as:

$$PL = PL(d) + S, \tag{1.7}$$

where $PL(d)$ is expressed by the equation (1.1) and S represents the shadowing component. Body shadowing, is generally expressed as a zero mean random variable with standard deviation σ that follows the lognormal distribution (or normal distribution in dB):

$$S(t_n)[dB] \sim N(0, \sigma_{S_S}) \tag{1.8}$$

It is worth to mention that in some cases [4] it has been found that the standard deviation is higher in an anechoic environment rather than in indoor premises due to the presence of human body.

To extract the large-scale fading signal component (due to body shadowing), the received signal is often filtered using an appropriate window size [77, 84–86]. The size of the window (in time) is often directly related to the BAN link and the user's actions. For example, in [84], an on-body measurement campaign at 2.45 GHz is presented with antennas attached on torso and limbs. By applying a sliding temporal

window of 10 channel samples (or 200 ms), a correlated lognormally-distributed large-scale fading is separated from the small-scale fading component. Shadowing strictly depends on the movement type and the human body. In this study, it is shown that when the subject is not moving the impact of body shadowing is moderate; however, when the subject is moving, the degree of shadowing increases and becomes dependent on the way each human subject moves and the different path trajectories formed.

Small-scale fading refers to the rapid changes of the amplitude and phase of the received signal due to changes in local environment and rapid body movement that give rise to multipath reflections, in a short period of time.

Many contributions on channel modelling using first order statistics have been done by many research groups. Extensive measurement campaigns using either VNA or remote wireless nodes have been undertaken. Significant contribution has been made by the University of Birmingham and Queen Mary University of London [14, 82,87], Queen's University of Belfast [77,88,89], CEA-Leti (France) [79,84,85,90] and NCSR "Demokritos" (Greece) [91–96]. Worldwide, contributions have come from NICT in Japan and, NICTA in Australia [97]. More specifically, it has been found that small-scale fading follows Rician [77, 98] for a mobile user, while large-scale fading is best described by Lognormal [82, 98] or Weibull [99] distributions. At a given frequency, the best fit statistical model and its parameters are dependent on the specific channel, subject, antenna and its orientation.

Popular on-body fading models have been fitted by lognormal distribution [100, 101], Rayleigh distribution [102], Rice [77, 84–86, 103], Nakagami-m [99, 100], and Weibull [97, 99].

In Rayleigh fading, the received signal is comprised of a large number of scattered signal components, each with random amplitude and uniform phase. Rayleigh fading has been reported for on-body links where communications occur around the human torso at both 915 MHz and 2.45 GHz [102]. It is believed that diffracting components around the back of the body in distance greater than 35 cm, become significantly attenuated. Then, the received signal is made up of reflected components, which follow a Rayleigh distribution. It is expressed by:

$$f_{rayleigh}(r) = \frac{r}{\sigma^2} exp(-\frac{r^2}{2\sigma^2}), r \geq 0 \tag{1.9}$$

In on-body channels where there is line of sight (LOS), strong on-body reflection, or dominant creeping wave component, it may be more appropriate to model the distribution of received signal by using the Rice PDF. The PDF of Rice fading signal

envelope is given by:

$$f_{rice}(r) = \frac{r}{s^2} exp(-\frac{r^2 + c^2}{2s^2}) I_0(\frac{cr}{s^2}), r \geq 0 \tag{1.10}$$

where: c denotes the peak amplitude of the dominant component. In the absence of a dominant component (c = 0), the Rice PDF becomes equivalent to the Rayleigh PDF.

In [77, 84–86, 102], the Rice K factor has been used. The Rice K factor is defined as the ratio of the dominant power component (c^2) to the scattered power component ($2s^2$), i.e., $K = c^2/2s^2$. When $K \to 0$, the dominant component c decreases, the fading becomes closer to Rayleigh fading, and when $K \to \infty$, the channel no longer exhibits fading. In [77], [84] it was observed that when the human subject was stationary, the estimated K factors for on-body communications channels are large, e.g., K = 316 for the right chest to left back at 868 MHz while human subject was stationary in anechoic chamber [88], as there was very little small-scale fading. In contrast, when the human subject becomes mobile, K factors are observed to decrease especially within indoor environments, were signal components returned toward the body from the local surroundings act to increase the scattered power in on-body channels (K = 1.82 for the same channel in [77] while the human subject was mobile in an open office environment). It has also been reported that the magnitude of the K factor also changes with time [103] while the test subject performed various everyday activities such as driving a car, walking outdoors and indoors, and sitting. Ricean fading has been reported in [102] for on-body link distances less than 25 cm; it was observed that as the separation distance of the on-body link increases, the K factor decreases due to greater attenuation of the creeping wave component.

Lognormal fading that describes mostly large-scale fading, can describe small-scale fading for stationary cases where the user is standing still and channels experience negligible movement, such as on the torso [14, 102, 104]. The lognormal probability density function (PDF) for a signal envelope r, with mean μ and standard deviation σ, used to describe the scattering of a single ray, may be expressed as:

$$f_{lognormal}(r) = \frac{1}{r\sigma\sqrt{2\pi}} exp(-\frac{(ln(r) - \mu)^2}{2\sigma^2}), r > 0 \tag{1.11}$$

where μ is the mean and σ standard deviation of the signal envelope r.

Nakagami-m fading has been reported in a number of studies characterising BAN channels. In [89], channel measurements made at 2.45 GHz with wireless nodes

distributed across the body, covering the head, upper front and back torso, and the limbs. It was observed that when the test subject was stationary, Nakagami-m parameters were always much larger than 1, irrespective of the operating environment. In an anechoic environment, when the user was moving, the measured Nakagami-m parameters were observed to decrease due to an increase in the diffuse contributions from the body and interruption of the on-body creeping wave component. Similarly to Rice K factor reported in [102], the Nakagami-m parameter was typically observed to decrease with increasing separation distance between on-body antennas. Fading in on-body channels was also observed to increase when the user moved into a multipath environment, showing that the local surroundings are an important consideration for on-body systems. For on-body links operating at 4.5 GHz [99], Nakagami-m fading has also been found to occur for scenarios when the test subject performed walking movements in an anechoic chamber.

The PDF of Nakagami fading signal envelope is given by:

$$f_{nakagami-m}(r) = \frac{2m^m r^{2m-1}}{\Gamma(m)\Omega^m} exp(-\frac{mr^2}{\Omega}), r \geq 0 \tag{1.12}$$

where $m = E^2(R^2)/var(R^2)$ and $\Omega = E(R^2)$.

Nakagami-m random variables may be generated as the sum of m independent Rayleigh components with equal mean power Ω/m. Rayleigh PDF appears as a special case of the Nakagami-m PDF when $m = 1$. The Nakagami-m distribution has the advantage over the Rayleigh and Rice PDFs in that it can model fading which is worse than Rayleigh, i.e., m < 1.

Weibull fading has been reported for on-body measurements made at 2.36 GHz while the test subject was walking and running [97] and at 4.5 GHz for walking and standing up/sitting down motions [99]. It is suggested that the Weibull model should be used for on-body links that experience severe fading such as the shoulder and ankle while the user was walking.

The PDF of a Weibull distributed envelope may be written as:

$$f_{weibull}(r) = \frac{b}{a}(\frac{r}{a})^{b-1} exp(-\frac{r}{a})^b, r \geq 0 \tag{1.13}$$

where a is the scale parameter that is related to the average fading power and b is the shape parameter of the distribution that represents the severity of fading. Again, the Rayleigh distribution may be obtained from the Weibull distribution by setting a = 2.

1.5 Thesis Outline

In Chapter 2, channel modelling of four common on-body channels that experience static or dynamic body movement is achieved by the best fit statistical distributions. The on-body channels are formed with the one part fixed on the waist of the human body while the other part located on the chest, back, wrist and foot. Numerical methods and measurements are used to study the effect of human body shadowing and multi-path fading and the antenna type on the transmitted signal between wearable antennas.

In Chapter 3, two textile wearable patch antenna types are developed and fabricated. The first type, a higher-order mode patch antenna (HMMPA) is suitable for on-body communications since it radiates omni-directionally on the body surface. The second type, a conventional patch antenna (MPA) is appropriate for off-body communications since it radiates away from the body surface. Both are tested via EM simulations on a homogenous specific anthropomorphic mannequin (SAM) phantom and compared with a detailed voxel (HUGO) model.

In Chapter 4, the proposed cylindrical near-field (CNF) measurement method is described in detail together with the measurement setup that guarantees the measurement accuracy. A reference printed dipole is measured in vertical and horizontal polarisation on the full-body SAM phantom to demonstrate the validity of the proposed measurement method. EM simulation results are employed for comparison. Three on-body locations are considered, namely on chest, head and shoulder. Afterwards, the MPA and HMMPA wearable antennas are investigated on chest at 2.4 and 5.8 GHz ISM band in terms of their near-field and far-field performance on the body surface. The mean effective gain of wearable antennas is also determined that characterises them in realistic off-body propagation scenarios.

In Chapter 5, the potential of antenna integration in “smart” clothing is demonstrated. The design, fabrication and characterisation of fully-textile wearable antennas is presented. A novel fabrication method using a state-of-the-art digital embroidery machine is used, which provides the potential of automating the fabrication process while achieving an optimised performance on the human body. A fully-textile HMMPA antenna is realised with textile embroidered vias, which provide an enhanced on-body wave propagation. Following this, an embroidered broadband spiral antenna exhibiting a circular polarisation is presented, which makes it suitable for off-body communications.

In Chapter 6, conclusions are drawn and the future extension of this thesis research is presented.

In Appendix A, the theoretical background of the dielectric properties of human body is presented, together with the most popular physical and numerical phantoms used in wearable antenna investigations.

In Appendix B, the statistical distribution models that are used for the modelling of on-body channels are listed in Chapter 2, while in Appendix C the CDFs of the small-scale fading for the four on-body channels are plotted, including all the theoretical distribution models. In Appendix D the goodness-of-fit tests that have been employed to decide the best-fit models are explained, together with the derived statistics for all the theoretical distribution models of small-scale fading.

Finally, in Appendix E, the Matlab code developed for the creation of the 2D near-field patterns presented in Chapter 4 is provided.

References

[1] A. Tariq and H.Ghafouri-Shiraz, "On-Body Antenna for Vital Signs and Heart Rate Variability Monitoring," In *2011 Loughborough Antennas and Propagation Conference, LAPC 2011*, (2011).

[2] T. Haagenson, S. Noghanian, P. de Leon, and Y. Chang, "Textile Antennas for Spacesuit Applications: Design, simulation, manufacturing, and testing of textile patch antennas for spacesuit applications.," IEEE Antennas and Propagation Magazine **57(4),** 64–73 (2015).

[3] *Gartner, "Worldwide Wearable Devices Sales to Grow 18.4 Percent in 2016"*, Available online: http://www.gartner.com/newsroom/id/3198018.

[4] K. Y. Yazdandoost and K. Sayrafian, "Channel model for body area network (BAN)," IEEE 802.15 Working Group Document (2010).

[5] S. Cotton, R. D'Errico, and C. Oestges, "A review of radio channel models for body centric communications," Radio Sci. **49,** 371–388 (2014).

[6] Federal Communications Commission (FCC), "Rules and Regulations. MICS Band Plan," (1999).

[7] European Telecommunications Standards Institute (ETSI), "Electromagnetic compatibility and radio spectrum matters (ERM); Radio equipment in the frequency range 402 MHz to 405 MHz for ultra low power active medical implants and accessories; Part 1: Technical characteristics, including electromagnetic compatibility requirements, and test methods: European Standard," (2002).

[8] Federal Communications Commission (FCC), "Evaluating Compliance with FCC Guidelines for Human Exposure to Radiofrequency Electromagnetic Fields," (1997).

[9] ETSI EN 300 440-2, "Electromagnetic compatibility and Radio spectrum Matters (ERM); Short range devices; Radio equipment to be used in the 1 GHz to 40 GHz frequency range; Part 2: Harmonized EN covering essential requirements of article 3.2 of the R&TTE Directive," (2008).

[10] "Commission Implementing Decision of 11 December 2013 amending Decision 2006/771/EC on harmonisation of the radio spectrum for use by short-range devices and repealing Decision 2005/928/EC, Available online: http://eur-lex.europa.eu/l," .

[11] P. S. Hall and Y. Hao, *Antennas and Propagation for Body-Centric Wireless Communications. Second Edition*, 2nd ed. (Artech House, Inc., 2012).

[12] A. Alomainy, Y. Hao, and D. M. Davenport, "Parametric study of wearable antennas with varying distances from the body and different on-body positions," In *IET Seminar Digest*, **2007,** 84–89 (2007).

[13] P. S. Hall, "Antenna Challenges for Body Centric Communications," IEEE Antennas and Propagation Magazine **49(3),** 41–58 (2007).

[14] A. Alomainy, Y. Hao, A. Owadally, C. G. Parini, Y. Nechayev, C. C. Constantinou, and P. S. Hall, "Statistical Analysis and Performance Evaluation for On-Body Radio Propagation With Microstrip Patch Antennas," IEEE Transactions on Antennas and Propagation **55(1),** 245–248 (2007).

[15] A. Sani, A. Alomainy, G. Palikaras, Y. Nechayev, Y. Hao, C. Parini, and P. S. Hall, "Experimental Characterization of UWB On-Body Radio Channel in Indoor Environment Considering Different Antennas," IEEE Transactions on Antennas and Propagation **58(1),** 238–241 (2010).

[16] G. Conway and W. Scanlon, "Antennas for Over-Body-Surface Communication at 2.45 GHz," IEEE Transactions on Antennas and Propagation **57(4),** 844–855 (2009).

[17] A. A. Serra, P. Nepa, G. Manara, and P. S. Hall, "Experimental investigation of diversity techniques for on-body communication systems," IET Seminar on Antennas and Propagation for Body-Centric Wireless Communications pp. 63–66 (2007).

[18] G. A. Conway, W. G. Scanlon, and S. L. Cotton, "The performance of on-body wearable antennas in a repeatable multipath environment," In *2008 IEEE International Symposium on Antennas and Propagation and USNC/URSI National Radio Science Meeting, APSURSI*, (2008).

[19] A. R. Chandran, G. A. Conway, and W. G. Scanlon, "Pattern switching compact patch antenna for on-body and off-body communications at 2.45 ghz," In *European Conference on Antennas and Propagation, EuCAP 2009, Proceedings*, pp. 2055–2057 (2009).

[20] W. G. Scanlon and A. R. Chandran, "Stacked-patch antenna with switchable propagating mode for UHF body-centric communications," In *2009 IEEE International Workshop on Antenna Technology, iWAT 2009*, (2009).

[21] B. Sanz-Izquierdo, F. Huang, and J. C. Batchelor, "Small size wearable button antenna," In *European Space Agency, (Special Publication) ESA SP*, 626 SP (2006).

[22] P. Salonen, L. Sydanheimo, M. Keskilammi, and M. Kivikoski, "Small planar inverted-F antenna for wearable applications," In *International Symposium on Wearable Computers, Digest of Papers*, pp. 95–100 (1999).

[23] Y. Ouyang and W. J. Chappell, "High frequency properties of electro-textiles for wearable antenna applications," IEEE Transactions on Antennas and Propagation **56(2),** 381–389 (2008).

[24] P. J. Soh, G. Vandenbosch, S. L. Ooi, and N. Rais, "Design of a broadband all-textile slotted PIFA," IEEE Transactions on Antennas and Propagation **60(1),** 379–384 (2012).

[25] C. Hertleer, H. Rogier, L. Vallozzi, and L. V. Langenhove, "A textile antenna for off-body communication integrated into protective clothing for firefighters," IEEE Transactions on Antennas and Propagation **57(4),** 919–925 (2009).

[26] S. Zhu and R. Langley, "Dual-Band Wearable Textile Antenna on an EBG Substrate," IEEE Transactions on Antennas and Propagation **57(4),** 926–935 (2009).

[27] Q. Bai and R. Langley, "Bending of a small coplanar textile antenna," In *2010 Loughborough Antennas and Propagation Conference, LAPC 2010*, pp. 329–332 (2010).

[28] Q. Bai and R. Langley, "Crumpling of PIFA textile antenna," IEEE Transactions on Antennas and Propagation **60(1),** 63–70 (2012).

[29] T. Kellomaki and W. G. Whittow, "Bendable plaster antenna for 2.45 GHz applications," In *Antennas and Propagation Conference, 2009. LAPC 2009. Loughborough*, pp. 453–456 (2009), iD: 1.

[30] S. Zhang, A. Chauraya, W. Whittow, R. Seager, T. Acti, T. Dias, and Y. Vardaxoglou, "Embroidered wearable antennas using conductive threads with different stitch spacings," In *Antennas and Propagation Conference (LAPC), 2012 Loughborough*, pp. 1–4 (2012).

[31] A. Chauraya, S. Zhang, W. Whittow, T. Acti, R. Seager, T. Dias, and Y. C. Vardaxoglou, "Addressing the challenges of fabricating microwave antennas using conductive threads," In *Antennas and Propagation (EUCAP), 2012 6th European Conference on*, pp. 1365–1367 (2012).

[32] L. Zhang, Z. Wang, and J. L. Volakis, "Textile Antennas and Sensors for Body-Worn Applications," Antennas and Wireless Propagation Letters, IEEE **11,** 1690–1693 (2012).

[33] P. Massey, "GSM fabric antenna for mobile phones integrated within clothing," In *Antennas and Propagation Society International Symposium, 2001. IEEE*, **3,** 452–455 vol.3 (2001).

[34] T. F. Kennedy, P. W. Fink, A. W. Chu, N. J. Champagne, G. Y. Lin, and M. A. Khayat, "Body-Worn E-Textile Antennas : The Good , the Low-Mass , and the Conformal," **57(4),** 910–918 (2009).

[35] P. J. Soh, G. A. E. Vandenbosch, S. L. Ooi, and N. H. M. Rais, "Design of a broadband all-textile slotted PIFA," IEEE Transactions on Antennas and Propagation **60(1),** 379–384 (2012).

[36] T. Kaufmann and C. Fumeaux, "Wearable Textile Half-Mode Substrate-Integrated Cavity Antenna Using Embroidered Vias," IEEE Antennas and Wireless Propagation Letters **12,** 805–808 (2013).

[37] C. Hertleer, H. Rogier, L. Vallozzi, and L. V. Langenhove, "A textile antenna for off-body communication integrated into protective clothing for firefighters," IEEE Transactions on Antennas and Propagation **57(4),** 919–925 (2009).

[38] J. Matthews and G. Pettitt, "Development of flexible, wearable antennas," In *Antennas and Propagation, 2009. EuCAP 2009. 3rd European Conference on*, pp. 273–277 (2009).

[39] R. Seager, S. Zhang, A. Chauraya, W. Whittow, Y. Vardaxoglou, T. Acti, and T. Dias, "Effect of the fabrication parameters on the performance of embroidered antennas," IET Microwaves, Antennas Propagation **7(14),** 1174–1181 (2013).

[40] T. M. Nguyen, J.-T. Chung, and B. Lee, "Radiation Characteristics of Woven Patch Antennas," IEEE Transactions on Antennas and Propagation **63(6),** 663–666 (2015).

[41] D. L. Paul, H. Giddens, M. G. Paterson, G. S. Hilton, and J. P. McGeehan, "Impact of Body and Clothing on a Wearable Textile Dual Band Antenna at Digital Television and Wireless Communications Bands," IEEE Transactions on Antennas and Propagation **61(4),** 2188–2194 (2013).

[42] L. Zhang, Z. Wang, and J. L. Volakis, "Textile Antennas and Sensors for Body-Worn Applications," IEEE Antennas and Wireless Propagation Letters **11,** 1690–1693 (2012).

[43] P. Nepa and H. Rogier, "Wearable Antennas for Off-Body Radio Links at VHF and UHF Bands: Challenges, the state of the art, and future trends below 1 GHz.," IEEE Antennas and Propagation Magazine **57(5),** 30–52 (2015).

[44] Y. Ouyang, E. Karayianni, and W. J. Chappell, "Effect of fabric patterns on electrotextile patch antennas," In *IEEE Antennas and Propagation Society, AP-S International Symposium (Digest)*, **2,** 246–249 (2005).

[45] A. Chauraya, W. G. Whittow, J. C. Vardaxoglou, Y. Li, R. Torah, K. Yang, S. Beeby, and J. Tudor, "Inkjet printed dipole antennas on textiles for wearable communications," IET Microwaves, Antennas Propagation **7(9),** 760–767 (2013).

[46] W. G. Whittow, A. Chauraya, J. C. Vardaxoglou, Y. Li, R. Torah, K. Yang, S. Beeby, and J. Tudor, "Inkjet-Printed Microstrip Patch Antennas Realized on Textile for Wearable Applications," IEEE Antennas and Wireless Propagation Letters **13,** 71–74 (2014).

[47] A. Tsolis, W. Whittow, A. Alexandridis, and J. Vardaxoglou, "Embroidery and Related Manufacturing Techniques for Wearable Antennas: Challenges and Opportunities," Electronics **3(2),** 314–338 (2014).

[48] T. Loh, D. Cheadle, and L. Rosenfeld, "Radiation Pattern Measurement of a Low-Profile Wearable Antenna Using an Optical Fibre and a Solid Anthropomorphic Phantom," Electronics **3(3),** 462–473 (2014).

[49] D. L. Paul, H. Giddens, M. G. Paterson, G. S. Hilton, and J. P. McGeehan, "Impact of Body and Clothing on a Wearable Textile Dual Band Antenna at Digital Television and Wireless Communications Bands," Antennas and Propagation, IEEE Transactions on **61(4),** 2188–2194 (2013).

[50] P. S. Hall, "Antennas Challenges for Body Centric Communications," In *Antenna Technology: Small and Smart Antennas Metamaterials and Applications, 2007. IWAT '07. International Workshop on*, pp. 41–44 (2007).

[51] S. J. Boyes, P. J. Soh, Y. Huang, G. A. E. Vandenbosch, and N. Khiabani, "Measurement and performance of textile antenna efficiency on a human body in a reverberation chamber," IEEE Transactions on Antennas and Propagation **61(2),** 871–881 (2013).

[52] G. Conway, W. Scanlon, C. Orlenius, and C. Walker, "In Situ measurement of UHF wearable antenna radiation efficiency using a reverberation chamber," IEEE Antennas Wirel. Propag. Lett. **7,** 271–274 (2008).

[53] G. Conway, W. Scanlon, C. Nunn, and A. Burdett, "Layered RF phantom characterization for wireless medical vital sign monitors," In *Antennas and Propagation Society International Symposium (APSURSI), 2013 IEEE*, pp. 2201–2202 (2013).

[54] A. Alomainy and T. H. Loh, "Experimental Evaluation of Wearable Antenna Efficiency for Applications in Body-Centric Wireless Networks," RF and Wireless Technologies for Biomedical and Healthcare Applications (IMWS-Bio) pp. 1–2 (2014).

[55] P. O. Iversen, P. Garreau, and D. Burrell, "Real-time spherical near-field handset antenna measurements," IEEE Antennas and Propagation Magazine **43(3),** 90–94 (2001).

[56] J. Krogerus, J. Toivanen, C. Icheln, and P. Vainikainen, "Effect of the Human Body on Total Radiated Power and the 3-D Radiation Pattern of Mobile Handsets," IEEE Transactions on Instrumentation and Measurement **56(6),** 2375–2385 (2007).

[57] W. Leach and D. Paris, "Probe compensated near-field measurements on a cylinder," IEEE Transactions on Antennas and Propagation **21(4),** 435–445 (1973).

[58] J. Brown and E. Jull, "The prediction of aerial radiation patterns from near-field measurements," Proceedings of the IEE - Part B: Electronic and Communication Engineering **108(42),** 635–644 (1961).

[59] A. D. Yaghjian, "Near-field antenna measurements on a cylindrical surface: A source scattering-Matrix formulation," Technical report, Boulder, Colorado : Dept. of Commerce, National Bureau of Standards, Institute for Basic Standards, Electromagnetics Division (1977) .

[60] G. Conway and W. Scanlon, "Antennas for Over-Body-Surface Communication at 2.45 GHz," IEEE Transactions on Antennas and Propagation **57(4),** 844–855 (2009).

[61] J. Matthews, B. Pirollo, A. Tyler, and G. Pettitt, "Body wearable antennas for UHF/VHF," In *Loughborough Antennas and Propagation Conference, LAPC 2008, Loughborough*, pp. 357–360 (2008).

[62] "IEEE Standard for Local and metropolitan area networks - Part 15.6: Wireless Body Area Networks," IEEE Std 802.15.6-2012 pp. 1–271 (2012).

[63] C. Roblin, R. D'Errico, J. M. Gorce, J. M. Laheurte, and L. Ouvry, "Propagation channel models for BANs: an overview," In COST 2100 (2009).

[64] D. B. Smith, L. W. Hanlen, and T. A. Lamahewa, "A new look at the body area network channel model," In *Proceedings of the 5th European Conference on Antennas and Propagation, EUCAP 2011*, pp. 2987–2991 (2011).

[65] J. Ryckaert, P. D. Doncker, R. Meys, A. D. L. Hoye, and S. Donnay, "Channel model for wireless communication around human body," Electronics Letters **40(9),** 543–544 (2004).

[66] A. Fort, C. Desset, J. Ryckaert, P. D. Doncker, L. V. Biesen, and P. Wambacq, "Characterization of the ultra wideband body area propagation channel," In *Ultra-Wideband, 2005. ICU 2005. 2005 IEEE International Conference on*, p. 6 pp. (2005).

[67] A. Fort, C. Desset, P. D. Doncker, P. Wambacq, and L. V. Biesen, "An ultra-wideband body area propagation channel model - From statistics to implementation," IEEE Transactions on Microwave Theory and Techniques **54(4),** 1820–1826 (2006).

[68] W. Joseph, E. Reusens, G. Vermeeren, and L. Martens, "Experimental determination of on-body channel for two humans in multipath environment," In COST 2100 (2009).

[69] E. Reusens and W. J. et al., "On-body measurements and characterization of wireless communication channel fro arm and torso of human," International Workshop on Wearable and Implantabel Body Sensor Networks pp. 26–28 (2007).

[70] A. Fort and J. R. et al., "Ultra-wideband channel model for communication around the human body," IEEE Journal on Selected Areas in Communications **24,** 927–933 (2006).

[71] L. Akhoondzadeh-Asl, Ph.D. thesis, University of Birmingham,UK, 2011.

[72] B. Zhen, T. Aoyagi, and R. Kohno, "Reasons for Time-Varying Fading of Dynamic On-Body Channels," In *Wireless Communications and Networking Conference (WCNC), IEEE*, pp. 1 – 5 (2010).

[73] IEEE, "802.15 WPAN Task Group 6 (TG6) Body Area Networks,".

[74] A. Fort, "Channel Model for WBAN," IEEE P802.15 Report (2008).

[75] D. Miniutti, L. Hanlen, D. Smith, A. Zhang, D. Lewis, D. Rodda, and B. Gilbert, "Narrowband channel characterization for body area networks," IEEE 802.15 Working Group Document (2008).

[76] N. Kang, C. Cho, S. Park, , and E. T. Won, "Channel models for WBANs-Samsung Electronics," IEEE 802.15 Working Group Document (2008).

[77] S. L. Cotton and W. G. Scanlon, "A statistical analysis of indoor multipath fading for a narrowband wireless body area network," In *IEEE International Symposium on Personal, Indoor and Mobile Radio Communications, PIMRC*, (2006).

[78] S. L. Cotton and W. G. Scanlon, "Characterization and modeling of on-body spatial diversity within indoor environments at 868 MHz," IEEE Transactions on Wireless Communications **8(1),** 176–185 (2009).

[79] R. D'Errico and L. Ouvry, "Time-variant BAN channel characterization," In *IEEE International Symposium on Personal, Indoor and Mobile Radio Communications, PIMRC*, (2009).

[80] R. Verdone and A. Zanella, *Pervasive Mobile & Ambient Wireless Communications* (Springer, London, 2012), pp. 1–695.

[81] C. Oliveira, C. Lopez, M. Machowiack, and L. M. Correia, "Characterization of on-body communications at 2.45 GHz," In *Proceedings of the 6th International Conference on Body Area Networks*, BodyNets '11 (2011).

[82] Y. I. Nechayev, P. S. Hall, and Z. H. Hu, "Characterisation of narrowband communication channels on the human body at 2.45 GHz," IET Microwaves, Antennas & Propagation **4(6),** 722–722 (2010).

[83] M. Gallo, P. S. Hall, Q. Bai, Y. I. Nechayev, C. C. Constantinou, and M. Bozzetti, "Simulation and Measurement of Dynamic On-Body Communication Channels," IEEE Transactions on Antennas and Propagation **59(2),** 623–630 (2011).

[84] R. D'Errico and L. Ouvry, "A Statistical Model for On-Body Dynamic Channels," International Journal of Wireless Information Networks **17(3-4),** 92–104 (2010).

[85] L. Lingfeng, D. Raffaele, O. Laurent, D. D. Philippe, and O. Claude, "Dynamic Channel Modeling at 2.4 GHz for On-Body Area Networks," Advances in Electronics and Telecommunications **2(4),** 18–27 (2011).

[86] R. Rosini and R. D'Errico, "Comparing On-Body dynamic channels for two antenna designs," In *LAPC 2012 - 2012 Loughborough Antennas and Propagation Conference*, (2012).

[87] P. S. Hall *et al.*, "Antennas and propagation for on-body communication systems," IEEE Antennas and Propagation Magazine **49(3),** 41–58 (2007).

[88] S. L. Cotton and W. G. Scanlon, "Characterization and modeling of the indoor radio channel at 868 MHz for a mobile bodyworn wireless personal area network," IEEE Antennas and Wireless Propagation Letters **6,** 51–55 (2007).

[89] S. L. Cotton, G. A. Conway, and W. G. Scanlon, "A time-domain approach to the analysis and modeling of on-body propagation characteristics using synchronized measurements at 2.45 GHz," IEEE Transactions on Antennas and Propagation **57(4),** 943–955 (2009).

[90] R. D'Errico, R. Rosini, and M. Maman, "A performance evaluation of cooperative schemes for on-body area networks based on measured time-variant channels," In *IEEE International Conference on Communications*, (2011).

[91] A. Michalopoulou, T. Zervos, K. Peppas, F. Lazarakis, A. A. Alexandridis, K. Dangakis, and D. I. Kaklamani, "The influence of the wearable antenna type on the on-body channel modeling at 2.45 GHz," In *2013 7th European Conference on Antennas and Propagation, EuCAP 2013*, pp. 3044–3047 (2013).

[92] A. Michalopoulou, A. A. Alexandridis, K. Peppas, T. Zervos, F. Lazarakis, K. Dangakis, and D. I. Kaklamani, "Statistical analysis for on-body spatial diversity communications at 2.45 GHz," IEEE Transactions on Antennas and Propagation **60(8),** 4014–4019 (2012).

[93] A. Michalopoulou, T. Zervos, K. Peppas, F. Lazarakis, A. A. Alexandridis, K. Dangakis, and D. I. Kaklamani, "Impact of channel modeling on accurate estimation of on-body channel capacity," In *Proceedings of 6th European Conference on Antennas and Propagation, EuCAP 2012*, pp. 3125–3129 (2012).

[94] A. Michalopoulou, A. A. Alexandridis, K. Peppas, T. Zervos, F. Lazarakis, K. Dangakis, and D. I. Kaklamani, "On-body channel statistical analysis based on measurements in an indoor environment at 2.45 GHz," IET Microwaves, Antennas and Propagation **6(6),** 636–645 (2012).

[95] A. Michalopoulou, T. Zervos, K. Peppas, F. Lazarakis, A. A. Alexandridis, K. Dangakis, and D. I. Kaklamani, "On-body diversity channels at 2.45 GHz: Measurements and statistical analysis," In *Proceedings of the 5th European Conference on Antennas and Propagation, EUCAP 2011*, pp. 2982–2986 (2011).

[96] A. Michalopoulou, A. A. Alexandridis, K. Peppas, T. Zervos, F. Lazarakis, K. Dangakis, and D. I. Kaklamani, "On-body channel modelling: Measurements and statistical analysis," In *2010 Loughborough Antennas and Propagation Conference, LAPC 2010*, pp. 201–204 (2010).

[97] D. Smith, L. Hanlen, D. Miniutti, J. A. Zhang, D. Rodda, and B. Gilbert, "Statistical characterization of the dynamic narrowband body area channel," In *2008 1st International Symposium on Applied Sciences in Biomedical and Communication Technologies, ISABEL 2008*, (2008).

[98] Y. I. Nechayev, Z. H. Hu, and P. S. Hall, "Short-Term and Long-Term Fading of On-Body Transmission Channels at 2 .45 GHz," In *2008 Loughborough Antennas and Propagation Conference, LAPC*, pp. 657–660 (2009).

[99] M. Kim and J. I. Takada, "Statistical model for 4.5-GHz narrowband on-body propagation channel with specific actions," IEEE Antennas and Wireless Propagation Letters **8,** 1250–1254 (2009).

[100] S. L. Cotton and W. G. Scanlon, "An experimental investigation into the influence of user state and environment on fading characteristics in wireless body area networks at 2.45 GHz," IEEE Transactions on Wireless Communications **8(1),** 6–12 (2009).

[101] V. G. Chaganti, D. B. Smith, and L. W. Hanlen, "Second-order statistics for many-link body area networks," IEEE Antennas and Wireless Propagation Letters **9,** 322–325 (2010).

[102] A. Fort, P. W. C. Desset, and L. van Biesen, "Indoor body-area channel model for narrowband communications," IET Microwaves, Antennas & Propagation **1,** 1197–1203 (2007).

[103] Y. Nechayev, P. Hall, and Z. Hu, "Characterisation of narrowband communication channels on the human body at 2.45 GHz," IET Microwaves, Antennas & Propagation **4(6),** 722 (2010).

[104] S. L. Cotton and W. G. Scanlon, "Characterization of the on-body channel in an outdoor environment at 2.45 GHz," In *European Conference on Antennas and Propagation, EuCAP 2009, Proceedings*, pp. 722–725 (2009).

Chapter 2

Statistical Channel Modelling for On-Body Communications

2.1 Introduction

The human body is considered as an extremely complex environment for the communication of wireless devices. The on-body communication channel suffers from the complex antenna-body electromagnetic interaction, the increased propagation losses and fading due to human body movement.

Hence, the importance of statistical channel modelling in this area of wireless communications is extremely high, due to the big variability of the interaction effects with human body. As a result of channel modelling, a reliable and efficient communication between wearable devices can be guaranteed, with the lowest transmitted power and highest data rate possible.

The main focus of this chapter is to study the effect of the antenna type, the location on the human body and the type of user movement in the derived channel model. Three wearable antenna types with different polarisation and radiation characteristics are considered to examine the different antenna-body interaction effects. An understanding of the on-body performance of each antenna type is achieved. Static and dynamic on-body channels are considered with the wearable antennas located in either static or moving body parts.

In order to characterise channel fading effects owing to changes in body posture and rapid body movement, user's walking and running activities are considered. The receiving node is fixed on the waist while the transmitting part is located on the chest,

back, wrist or foot. Channel measurements and EM simulations are employed in order to characterise the path gain, large-scale and small-scale fading effects applied to the received signal. Best fit statistical distribution models are derived to characterise fading in these commonly used on-body channels.

The outline of the chapter is structured as follows: in Section 2.2, the waist-foot dynamic communication channel between two wearable antenna types is examined via EM simulations, including the user's dynamic movement. Path gain and large-scale fading effect are statistically modelled. In Section 2.3, on-body channel measurements are demonstrated, with the user walking in an anechoic environment and wearable antennas placed on different on-body locations. Four on-body channels are selected and modelled, i.e two dynamic channels: foot-waist (FW) and wrist-waist (WW), and two static channels: chest-waist (CW) and back-waist (BW), which are representative of the majority of the on-body communication links. Finally, in Section 2.4, conclusions are drawn on the modelled on-body communication channels.

2.2 Channel Modelling via EM Simulations

This study has been focused on modelling the dynamic waist-foot communication channel via extensive EM simulations using an adequate number of different body postures. The influence of body posture and movement on the channel path gain (PG) is investigated. The effect of the antenna type is also taken into account by using two different printed antennas, an inverted-F antenna (IFA) and a higher mode microstrip patch antenna (HMMPA), both operating at 2.45 GHz ISM band.

Therefore, the waist-foot channel path gain is modelled with a simple distance-dependent model and the large-scale fading, which is evident due to body movement and polarisation mismatch of antennas, is statistically modelled. The path gain and large-scale fading models can be found useful for optimising a specific wearable application and link budget prediction. For each antenna type, two different cases are investigated through simulations: a human body phantom (a) walking and (b) running. In every case, the receiving antenna is attached on the waist and the transmitting antenna on the foot of the animated numerical phantom. A realistic (open space) environment is modelled by including "open" boundaries except the conductive floor that is modelled as an "electric" boundary. This creates a multipath environment where a significant propagation mode appears through ground floor reflections. This will have an effect on the derived path gain and large-scale fading estimation.

2.2.1 Antenna Design

Two planar printed (PCB) antennas are designed with monopole-like radiation characteristics and different polarisations: a printed inverted-F antenna (IFA) [1] that excites an E-field tangential to the body surface, and a higher mode microstrip patch antenna (HMMPA) [2] that excites a linearly polarised E-field normal to the body surface. Both antennas radiate omni-directionally and fulfil the requirements for wearable antennas, as they are compact, low-profile and can be easily placed conformally on the body surface. In Fig. 2.1, the two antenna designs are presented, which are optimised in CST Microwave Studio with antenna dimensions listed in Table 2.1.

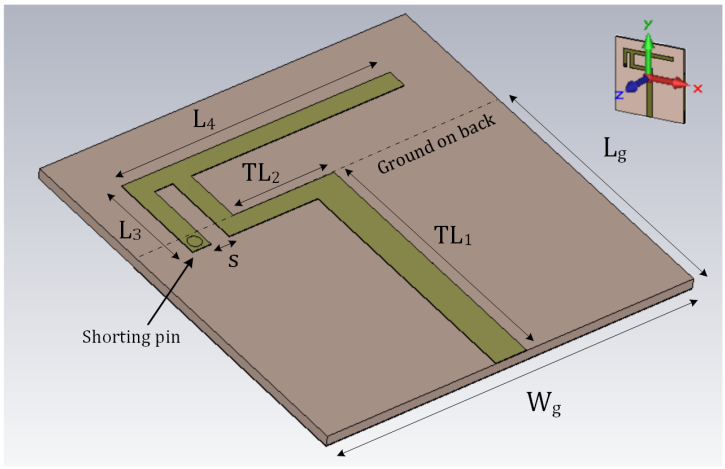

(a)

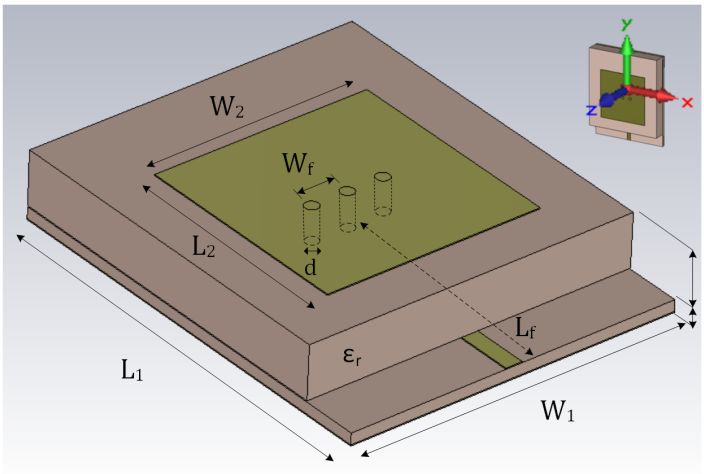

(b)

Figure 2.1 Design of (a) inverted-F antenna (IFA) and (b) higher mode microstrip patch antenna (HMMPA) in CST Microwave Studio.

Table 2.1 Antenna dimensions in mm for 2.45 GHz ISM band.

Antenna	***Dimensions (mm)***								
IFA	$\mathbf{TL_1}$	$\mathbf{TL_2}$	$\mathbf{L_3}$	$\mathbf{L_4}$	$\mathbf{L_g}$	$\mathbf{W_g}$	**s**		
	20	8.25	7.42	22	20	30	1.5		
HMMPA	$\mathbf{W_1}$	$\mathbf{L_1}$	$\mathbf{W_2}$	$\mathbf{L_2}$	$\mathbf{h_1}$	$\mathbf{h_2}$	$\mathbf{W_f}$	**d**	$\mathbf{L_f}$
	30	37	19.7	19.7	4.75	1	3.3	1.2	20

IFA antenna (Fig. 2.1a) is designed on 30 x 30 mm FR4 substrate ($\epsilon_r = 4.3$,$tan\delta$= 0.025) with thickness of 0.8 mm, while HMMPA antenna (Fig. 2.1b) consists of a multilayer Taconic TLY-3 substrate ($\epsilon_r = 2.33$, $tan\delta = 0.0009$). All the metallic parts are assumed as Perfect Electric Conductor (PEC) thin sheet for simulation acceleration.

The coupling performance of the HMMPA antenna type is expected to be greater than the IFA type as it supports surface wave propagation together with the existence of ground plane that has been proven useful to reduce the amount of absorbed energy to the body. Both antennas have the advantage of being side-fed rather than bottom (probe-) fed, allowing a close body fitting that is essential for wearable applications. In order to reduce the sensitivity of antenna characteristics to body proximity a separation of 20 mm is maintained.

2.2.2 Simulation Setup

A significant number of publications dealing with dynamic on-body channel modelling using EM simulation tools emerges in [1, 3–6]. The EM simulation body model used in this work is presented in Fig. 2.2. The channel propagation coefficient $|S_{21}|$ on the human model is calculated while performing walking and running. The transmitting antenna is attached on right or left ankle, with the receiving antenna mounted on left waist position.

The procedure of creating the animated human model can be accomplished with a variety of available animation software. At first, a human body phantom is chosen from a library containing models of various gender, size and shape. Following, the animation of movement is performed in the form of 30 successive frames. For each movement, the 30 frames cover the time period of one pace with a speed of 7 Km/h for walking and 14 Km/h for running. The sample frames of different body postures

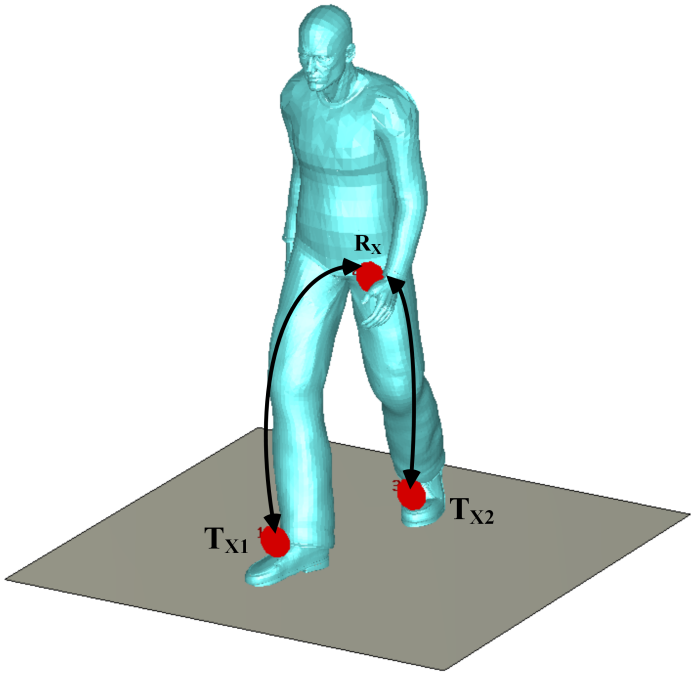

Figure 2.2 Waist-foot on-body links investigated on a detailed human body phantom, in CST Microwave Studio.

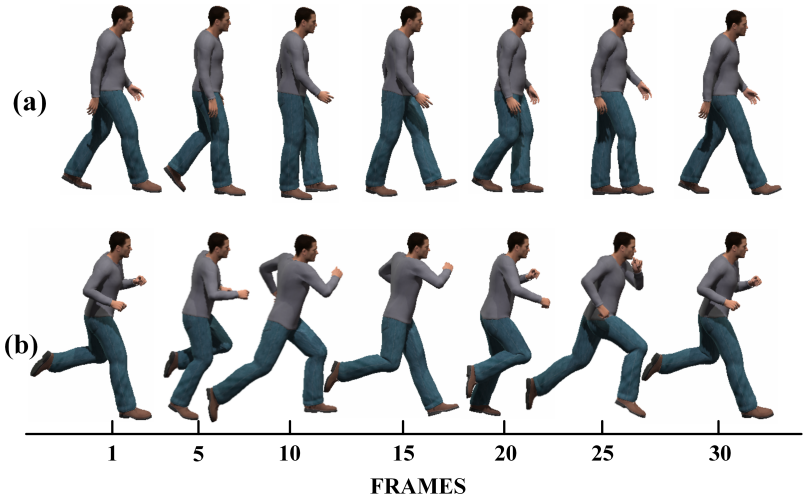

Figure 2.3 Consecutive human body postures (frames) for: (a) Walking and, (b) Running activities.

for walking and running are shown in Fig. 2.3. Moreover, a realistic propagation environment is recreated by including an infinite ground floor. A 3D solid model in .obj format for every frame is exported to be used in the EM solver.

After importing the human model with different postures in the EM simulation

software, CST Microwave Studio™, the next step is to define the dielectric material properties of human tissue, using a homogeneous dielectric material dataset, defined by standards in [7]. The relative permittivity and conductivity are defined for 2-3 GHz frequency range by using the 4th order Cole-Cole dispersion model as explained in Appendix A. Specifically, for 2.45 GHz, $\epsilon_r = 39.2$ and $\sigma = 1.79$ S/m respectively.

Attention is paid to the simulation process on how to attach the antennas properly in order to maintain a constant spacing from human body surface in every frame. This is a very demanding process bearing in mind the continuous body movement and the change in orientation for every body posture. Hence, an initial simulation is performed by varying antenna spacing from body between 10 to 25 mm in order to decide which is the proper distance to avoid body distractive effects in the antenna performance. Results show that when spacing is more than 20 mm, antenna frequency detuning is minor (4 and 15 MHz shift for HMMPA and IFA respectively). As the spacing from body becomes smaller reaching 10 mm, significant detuning occurs to IFA (44 MHz shift for IFA and 6 MHz for HMMPA), while significant distortion in the radiation pattern is observed for IFA antenna ($\Delta G_{max} = 0.12$ dB for HMMPA and $\Delta G_{max} = 4.29$ dB for IFA). In addition, it is essential to choose an appropriate mesh in order to obtain a good simulation accuracy. Antennas need a dense mesh, in contrast to human body that is approximately $90\lambda_g$ in length and needs a more coarse one. Specifically, for HMMPA antenna a 0.57 mm mesh grid is selected, whereas for IFA a 0.35 mm is chosen. Finally, having completed the simulation setup, the channel path gain (PG) is calculated for every body posture and activity.

2.2.3 EM Simulation Results

In Figs. 2.4a, 2.4b, the radiation patterns of the PCB antennas are plotted in free space and on-body (waist) cases. Apparently, the on-body radiation patterns are distorted compared to the free space patterns due to the increased absorption in the human body tissue. It can be observed that in the IFA case (Fig. 2.4b), back radiation to human body is evident due to the lack of ground plane that results to a larger distortion of the on-body radiation pattern ($\theta = 180^o$ at XZ-plane). It is also shown that the quasi-omnidirectional radiation pattern of the IFA antenna becomes directional in the vicinity of the human body. In contrary, the HMMPA antenna (Fig. 2.4a) is less affected from the proximity of human body, as it is shown in the XZ-plane.

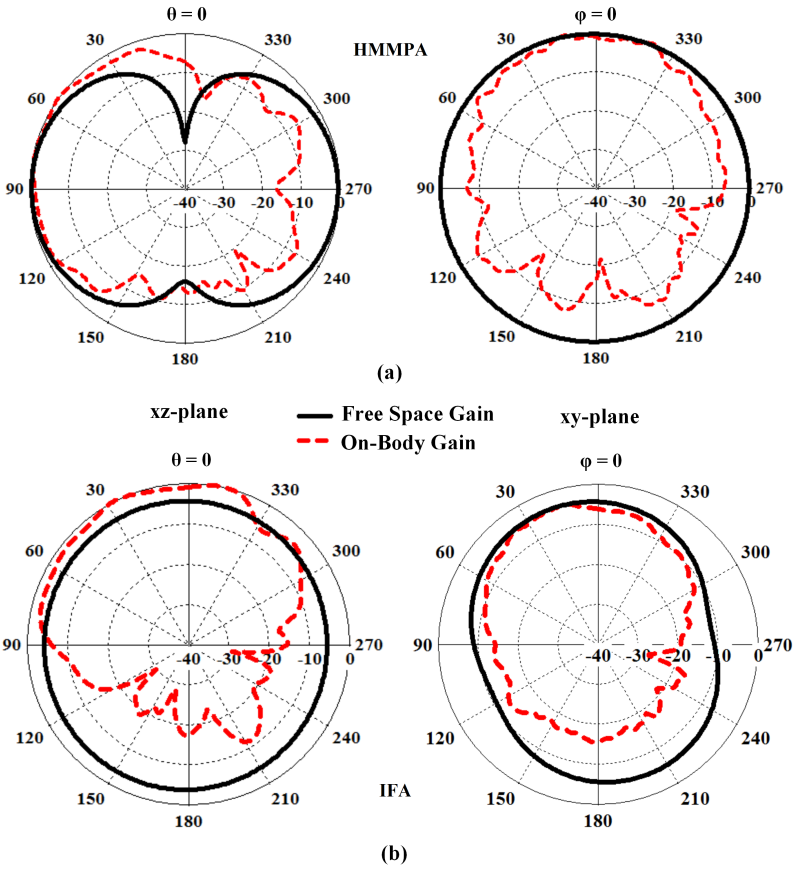

Figure 2.4 Normalised radiation patterns to the maximum on-body gain of (a) HMMPA, and (b) IFA.

IFA and HMMPA present ≈ 91% and 93% efficiency in free space, whereas on-body it is reduced to 15% and 31% respectively. The large reduction in the case of IFA is owing to the lack of ground plane under the radiating element. Their maximum gain in free space is 1.41 and 1.6, while mounted on-body is 5.68 and 2.72 respectively.

In order to gain a better understanding of the antennas coupling performance at the specific waist-foot channel, the PG between dipoles parallel and normal to the body is compared with the PG of the two PCB antennas. The corresponding results are listed in Table 2.2. As it is observed, the PG between HMMPA antennas, which is equal to −53.4 dB, approaches the PG of the normal to body dipoles, which is −47.4 dB. The PG between IFA antennas is equal to −64 dB, which is closer to that of parallel dipoles with PG of −58.7 dB. This can be explained from the fact that the polarisation of the PCB antennas resembles to the dipoles' polarisation. The main difference of the PCB antennas is that due to their low profile, a higher shadowing

and lower radiation efficiency in proximity to the body is obtained.

Table 2.2 PG comparison between dipoles and printed antennas in standing still position.

	Path Gain [dB]	
Antenna Type	$\mathbf{Tx_1 - Rx}$	$\mathbf{Tx_2 - Rx}$
Dipole //	−61.4	−56.0
IFA	−65.5	−62.5
Dipole ⊥	−44.0	−50.8
HMMPA	−50.2	−56.6

Afterwards, a series of EM simulations is performed aiming to model the exact waist-foot channel. An open space environment is modelled, where the surrounding space is modelled with absorbing ("open-space") boundaries and only the ground floor is modelled as a perfect electric conductor. Hence, the main modes of propagation are through space waves for the line of sight (LOS) propagation and through surface waves on the human body and ground floor reflections for the non line of sight (NLOS) propagation that contribute to the level of channel path gain. The channel path gain (PG) in respect to every body posture for both on-body links (waist-R foot & waist-L foot) is derived and presented in Fig. 2.5 and Fig. 2.6 for walking and running scenarios respectively.

As it is seen in walking scenario (Fig. 2.5), the HMMPA antenna achieves a higher PG up to 20 dB compared to the IFA. Moreover, PG seems more stable when using HMMPA antennas than using IFAs on both links. This can be explained from the fact that the main propagation mechanism of the HMMPA is via surface waves, where the normal E-field propagates on the body surface, as well as, it is less affected from the variation of human body posture due to the ground plane presence. In addition, the on-body radiation pattern of the HMMPA that remains omni-directional when is mounted on human body is beneficial for the PG, which is less affected by the orientation mismatch between Tx and Rx antennas. In contrary, using IFA antennas space waves are launched as the dominant mode of propagation and PG seems more dependent to LOS or NLOS conditions. More specifically, for IFA antennas larger variations of PG occur when the transmitter is attached on the right foot, since the position of the receiver is at the left side of waist, apparently due to shadowing effect of human body that leads to NLOS condition.

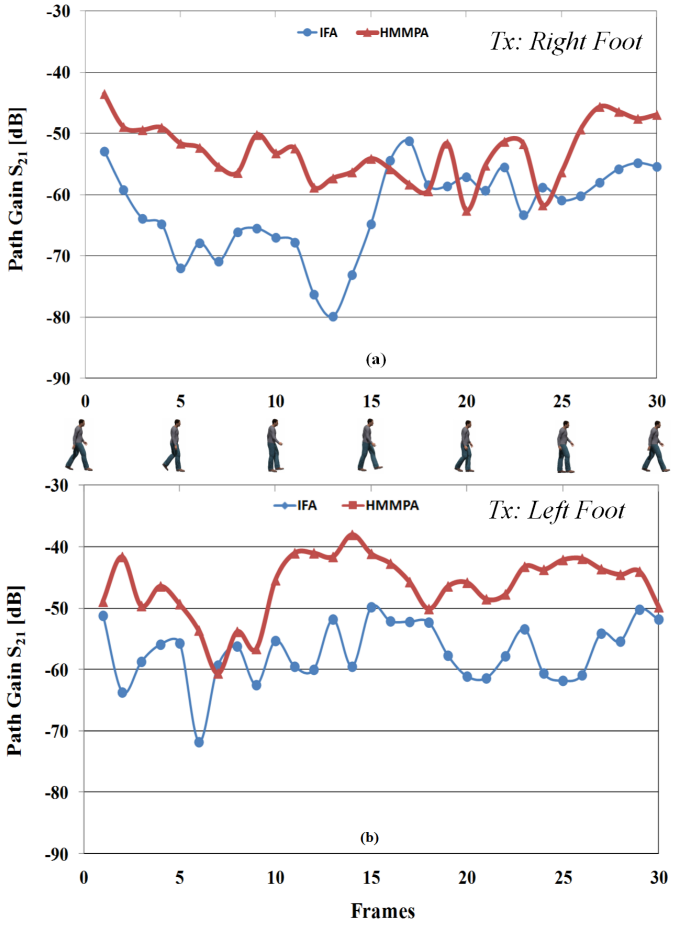

Figure 2.5 Path gain (PG) for: (a) waist-R foot and, (b) waist-L foot links in walking activity, derived from EM simulations.

On the other hand, when the phantom is running (Fig. 2.6), human body posture changes rapidly and larger distance variations between Tx and Rx antennas appear. In addition, antennas polarisation mismatch is also increased due to the highly dynamic action. A larger variation of the PG is observed with the HMMPA antennas since in many cases the main propagation is via ground floor reflections. Thus, it is clear that the path gain when using IFAs is improved, owing to the space wave propagation.

Mean (μ) and standard deviation (σ) values of PG for every link (waist-R foot & waist-L foot) are listed in Table 2.3. These values denote that in walking activity channel performance remains more stable when HMMPA antennas are used, whereas IFA antennas seem more suitable for running activity. Comparing the antennas performance between the R- and L-foot on-body links, for walking, it is observed that in waist-L foot link an improved PG is recorded with mean PG difference of 5.5 dB

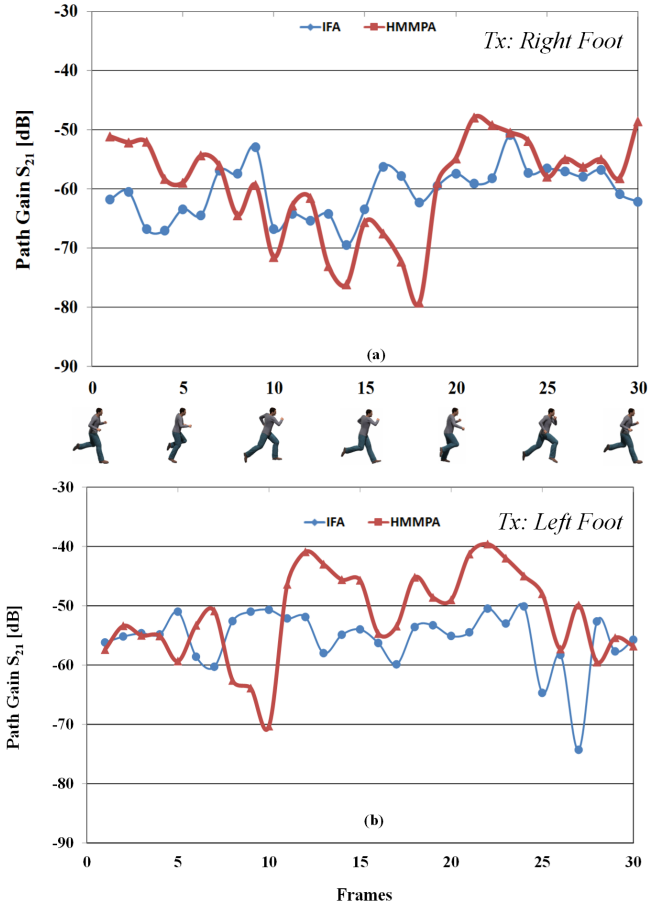

Figure 2.6 Path gain (PG) for: (a) waist-R foot and, (b) waist-L foot links in running activity, derived from EM simulations.

for IFA and 7 dB for HMMPA. The corresponding maximum PG difference derived from simulation data is 28.1 dB for IFA and 18.3 dB for HMMPA respectively. In respect to running activity, a mean PG difference of 5 dB and 7.8 dB is observed between the two links for IFA and HMMPA antennas respectively while maximum PG difference is 16.3 dB and 34.1 dB for each antenna type. Therefore, the waist-L foot on-body link, where Tx and Rx antennas lie at the same side of the body, is more suitable for this kind of dynamic activities and more stable. It is also worth mentioning that the same behaviour is expected when the antenna is mounted on the right waist position. In that case the characteristics for the waist-R foot and waist-L foot links would swap around. Finally, owing to body symmetry, the two links would present the same behaviour in the case where the receiver is placed at the central position of the waist.

Table 2.3 Mean and standard deviation of PG for the two on-body links.

	IFA		***HMMPA***	
	Waist-R foot	***Waist-L foot***	***Waist-R foot***	***Waist-L foot***
μ_{PG} *[dB]*				
Walking	−62.5	−57.0	−53.0	−46.0
Running	−60.5	−55.5	−59.4	−51.6
σ_{PG} *[dB]*				
Walking	7.2	4.9	4.8	5.1
Running	4.4	4.9	8.5	7.5

In respect to the large-scale fading effect, which its severity is described from the standard deviation σ value, it is observed that strong fading takes place in both dynamic activities. More specifically, it is seen that in walking activity when using IFA antennas channel experiences stronger fading while in running activity severe fading occurs when using HMMPA antennas.

In addition to the results above, a generalised PG model is created, based on the IEEE CM3 (Body Surface to Body Surface) standard [8]:

$$PG(d)[dB] = a \cdot \log_{10}(d) + b + N \tag{2.1}$$

where d is the distance in mm between Tx and Rx antennas, a and b are the coefficients of linear fitting and N is a Gaussian distributed variable with standard deviation σ_N that describes body shadowing effect. The corresponding model coefficients a and b are estimated by least squares fitting of the simulation results, listed in Table 2.4. The values of σ_N are not derived due to the small (30 frames) sample size. In Fig. 2.7, a comparison of the simulation results with the theoretical fitting from the above model is presented.

Table 2.4 Fitting coefficients of the on-body PG models according to (2.1).

PG Model		***a***	***b***
Walking	*HMMPA*	−215.7	589.3
	IFA	−117.4	288
Running	*HMMPA*	−23.4	13.5
	IFA	−35.6	46.9

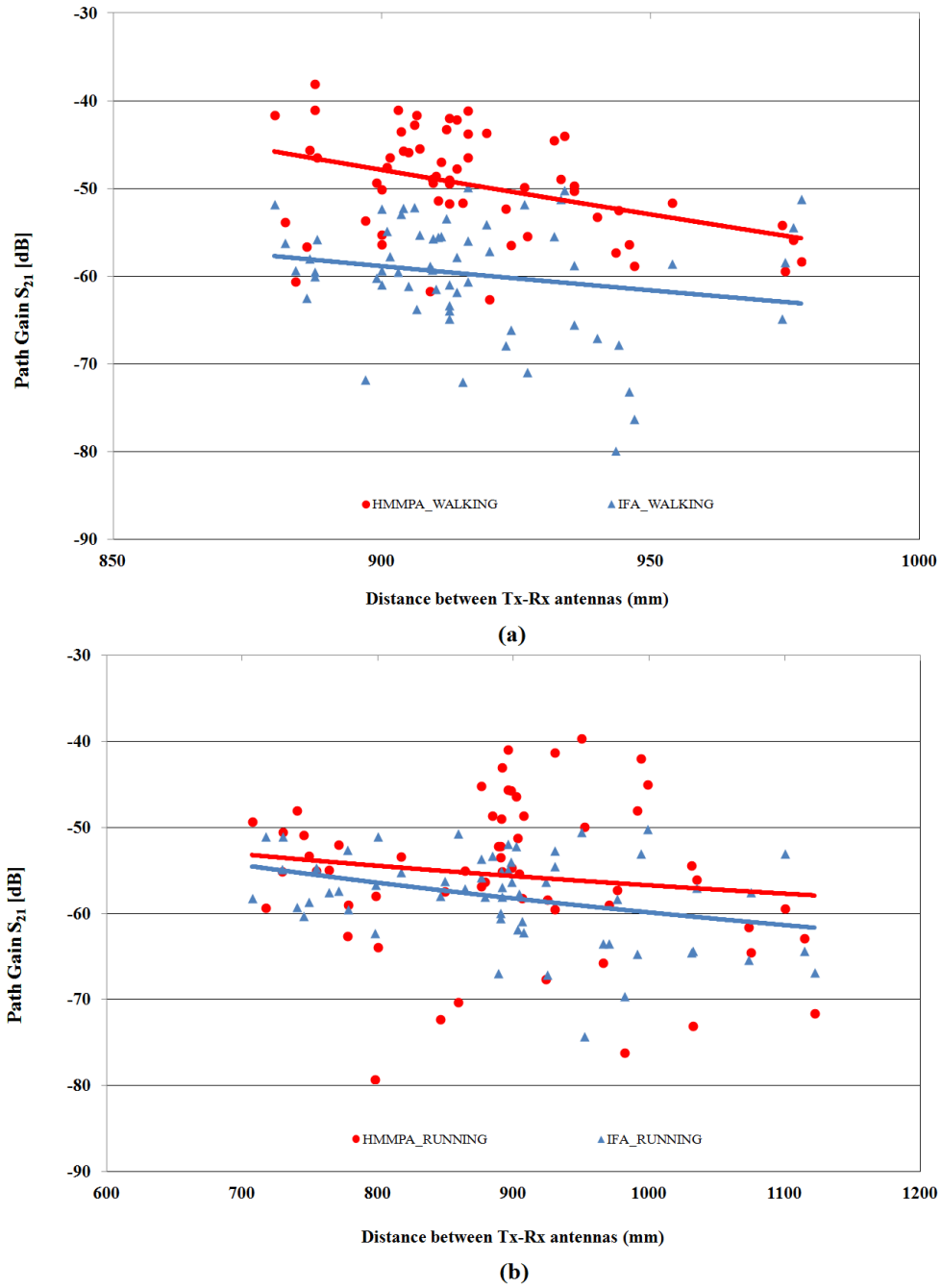

Figure 2.7 Comparison between PG models for the two antenna types in (a) Walking and (b) Running activities.

It is apparent that the distance between the transmitting and receiving antennas is not the main factor for the BAN channel fading due to the large scattering of the PG results. The close disturbance of antenna radiation pattern from human body and

change in orientation due to the body motion contribute to the channel fading. Also, the ground floor reflections contribute to the channel path gain variability, altering the far-field performance of wearable antennas.

In order to characterise the large-scale fading (shadowing) effect due to human body movement, the full 2.4 GHz ISM bandwidth (2.4-2.485 GHz) is used and both channels are merged to increase the sample size to 5100 (30 frames x 85 freq. x 2 channels) samples. The best fit cumulative distribution function (CDF) of path gain (PG) is plotted in Fig. 2.8a and in Fig. 2.8b for HMMPA and IFA antennas respectively.

The best-fit for the case of HMMPA antennas is obtained with Lognormal distribution, whereas Weibull is found more suitable to characterise shadowing between IFA antennas, using the Kolmogorov-Smirnov goodness-of-fit-test (KS-test) [9]. In Fig. 2.8a it is shown that in the HMMPA case higher body shadowing occurs for running activity, while in the IFA case (Fig. 2.8b) higher shadowing can be found for walking activity. This conclusion is obtained by comparing the empirical and theoretical CDFs as well as comparing the σ parameter for Lognormal and b for Weibull. A stronger fading occurs for higher σ values and lower b values respectively. It can be noted that Weibull distribution, describes Rice distribution when $b > 2$, approximates Rayleigh distribution when $b = 2$ and can describe worst than Rayleigh fading when $b < 2$, reaching at $b = 1$ the exponential distribution.

In order to characterise the small-scale fading effect applied to the on-body channel due to body movement and multi-path reflections, a higher number of frames should be captured from simulations in a shorter time step. However, this small time resolution could not be obtained from simulations due to the increasing number of simulation models (frames) and simulation time needed. Hence, the small-scale fading effect of the on-body channel is characterised in the following section where channel measurements are undertaken in a short time step.

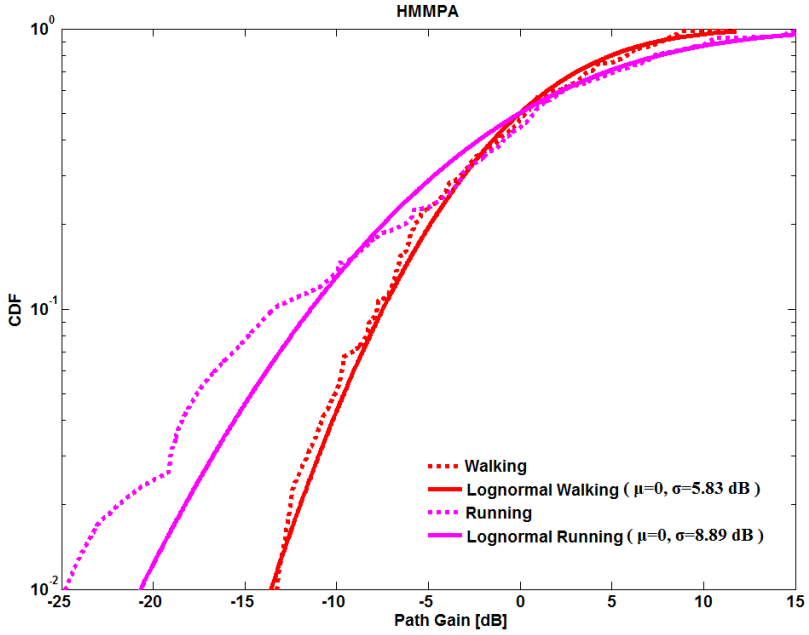

(a)

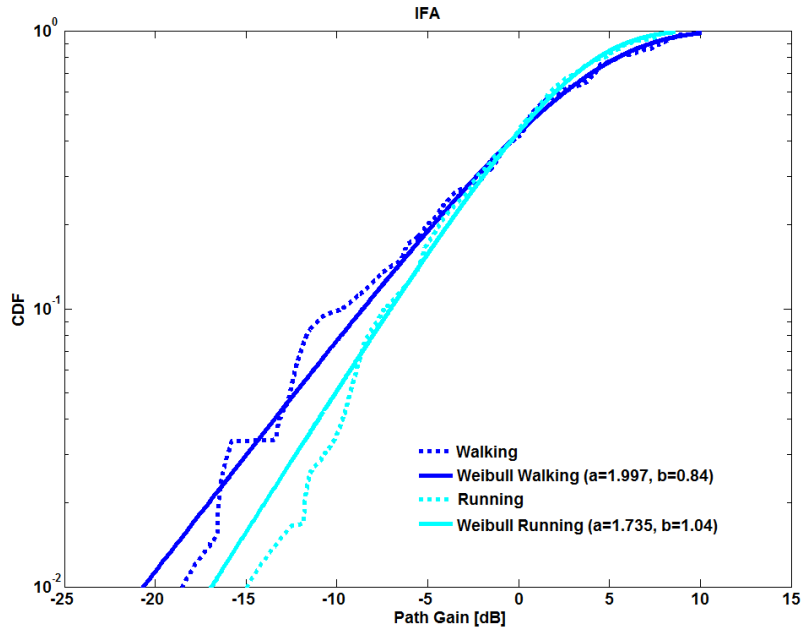

(b)

Figure 2.8 Large-scale fading model for (a) HMMPA and (b) IFA.

2.3 Channel Modelling via Measurements

Wearable devices, depending on the application, can be used in several locations on the human body, forming different communication channels with specific geometrical profiles. The on-body channels can be categorised into two distinctive groups in respect to the effects of human body motion:

The first group regards to *static* channels that remain unaffected (or negligibly affected) from body motion where wearable antennas are located around or in front of human torso. The main factors that contribute to the derived channel model are: the distance between Tx and Rx antennas, antenna-body separation distance, antenna type and frequency dependent tissue dielectric properties. On the other hand, the second group regards to *dynamic* channels where wireless devices are placed on moving parts of the body such as limbs or head. In addition to the aforementioned effects, the dominant effects that contribute to the dynamic channel models are: change in antennas orientation that causes polarisation mismatch, strong shadowing and fading from moving body parts.

Four on-body channels are selected as representative to study the majority of the on-body communication links. More specifically, foot-waist (FW) and wrist-waist (WW) channels describe antennas performance on dynamic scenarios where strong fading takes place due to highly dynamic action of limbs. In contrast, chest-waist (CW) and back-waist (BW) links define static channels that are not affected by body movement and are characterised by strong LOS and NLOS propagation respectively. The propagation mechanism of different antenna types is also investigated for both static and dynamic on-body channels. The placement of wearable antennas on the human body key locations and respective channels are illustrated in Fig. 2.9.

2.3.1 Wearable Antenna Prototypes

Three different antenna prototypes are designed and fabricated to be used for on-body channel measurements, as shown in Fig. 2.10. The geometrical characteristics of the wearable antennas are also noted. The reason of using three antenna types is to investigate the effect on the resulted on-body channel model. Each antenna exhibits different propagation characteristics on the surface of human body. Subsequently, the dominant mode of propagation due to body shadowing and movement will be determined for each antenna type. The antenna radiation performance will be also compared, in terms of pattern deformation due to the body presence.

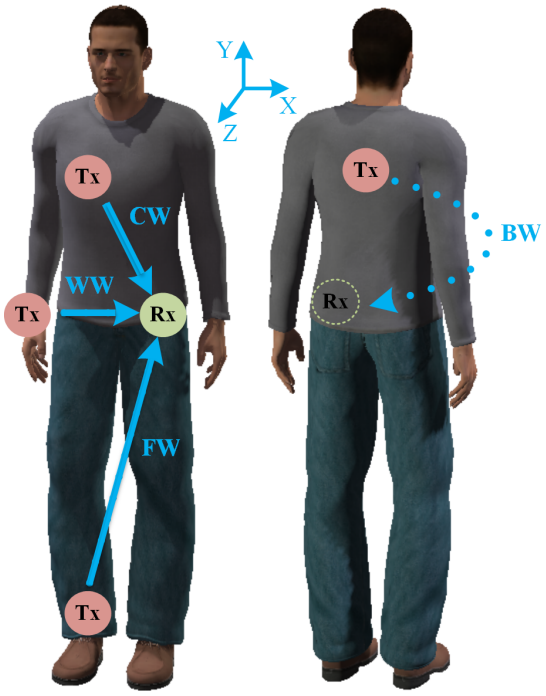

Figure 2.9 Configuration of wearable antennas forming four specific on-body channels.

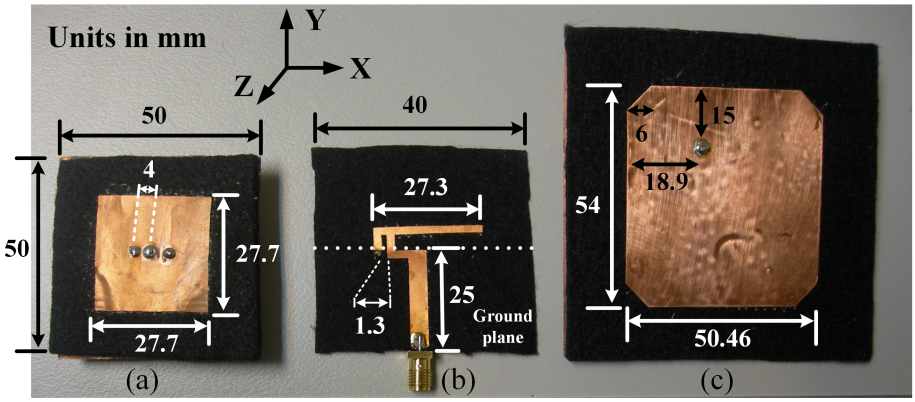

Figure 2.10 Prototypes of (a) T1, (b) T2 and (c) T3 wearable antennas.

Antenna T1, illustrated in Fig. 2.10a, is a vertically polarized higher mode rectangular patch antenna (HMMPA) with omnidirectional radiation pattern across the body surface. Antenna T2 (Fig. 2.10b) is an inverted-F (IFA) antenna horizontally polarized presenting nulls across the body surface and with lack of ground plane shielding. Antenna T3 (Fig. 2.10c) is comprised of a microstrip antenna that excites a circularly polarized wave (CPMPA) that can be advantageous when there are on-

body communication nodes that are used in a highly dynamic movement. All the antennas are fabricated using copper sheet for the conducting parts (top and bottom layer), attached on a 4.2 mm felt substrate. These wearable antennas offer flexibility, bendability, and they can be comfortably incorporated in user's clothing.

As far as T1 antenna is concerned, it exhibits a measured resonance frequency f_r = 2.435 GHz with S_{11} = -25.6 dB and bandwidth BW = 70 MHz. T2 antenna presents f_r = 2.454 GHz with $S_{11} = -30dB$ and BW = 240 MHz. T3 antenna resonates at f_r = 2.466 GHz with $S_{11} = -38dB$ and BW = 200 MHz. Also, the total efficiency (including mismatch losses) of the antennas placed at a distance of 20 mm from body surface ($\epsilon_r = 39.2$) is estimated through simulations: $e_{T1} = 57\%$, $e_{T2} = 61.5\%$ and $e_{T3} = 91.7\%$. In Fig. 2.11 the simulated radiation patterns are given for each antenna respectively in terms of the co- and cross-polarised gain component in azimuth (XZ plane) for (a) free space and (b) on-body cases.

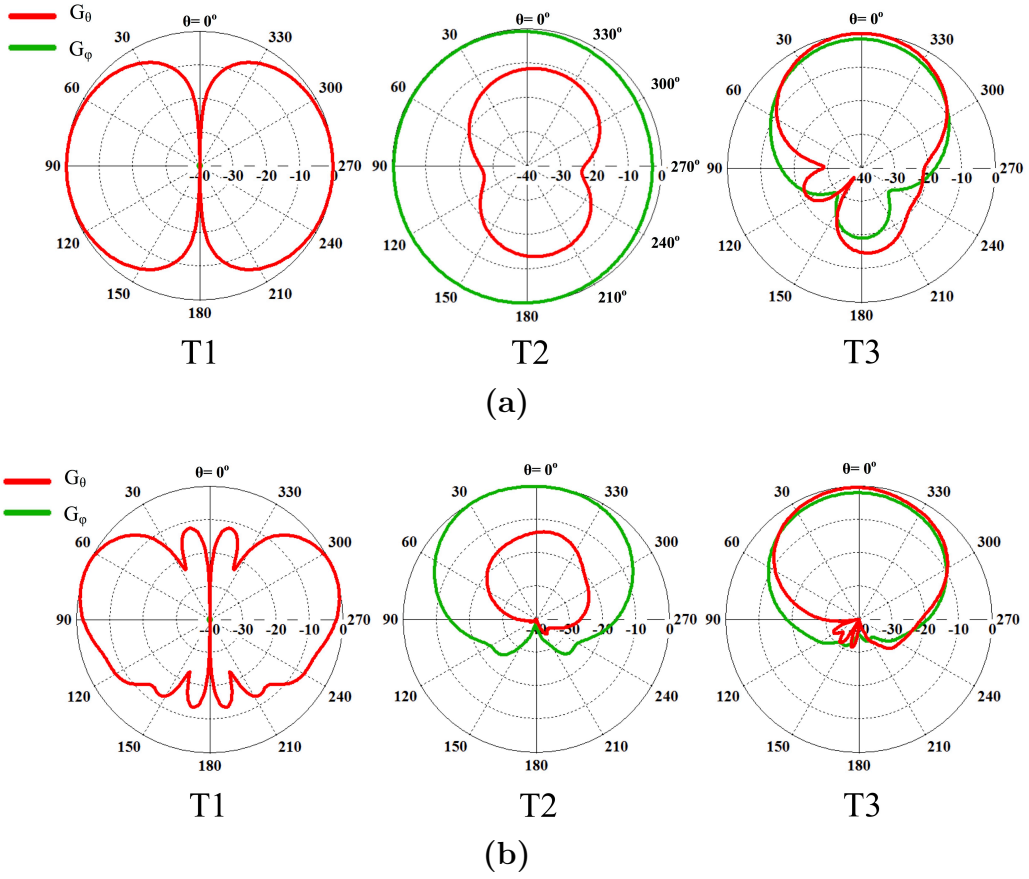

Figure 2.11 Simulated radiation patterns (G_θ and G_ϕ components) for T1, T2, and T3 antennas (a) in free space and (b) on-body.

From the derived radiation patterns the polarisation behaviour of the antennas is determined, which gives different channel characteristics. As it is seen, in Fig. 2.11a, T1 antenna has only a normal to body surface gain component (G_θ), while T2 (Fig. 2.11b) exhibits a strong parallel to body surface component (G_ϕ) and T3 (Fig. 2.11c) has both components equal, justifying the circular polarisation ($G_\theta \approx G_\phi$).

2.3.2 Channel Measurements Setup

A measurement test-bed inside an anechoic chamber is developed in order to characterise some application based channels and antennas performance in these on-body channels. In the anechoic chamber, multi-path effects from the surrounding environment are eliminated and the human body effects are solely examined. The Tx and Rx antennas are connected to the two ports of a vector network analyser (VNA). In order to measure the received signal in time domain, the VNA has been set to operate in single frequency (zero-span mode) by generating a CW signal at 2.45 GHz. The input power applied to the Tx antenna in port 1 is set at 0 dBm, while the noise floor was evaluated at -90 dBm. During the measurements the test subject is walking along a 4 m path inside the anechoic chamber, as shown in Fig. 2.12.

(a) (b)

Figure 2.12 On-body channel measurements with the test subject walking inside the anechoic chamber.

Each measurement sweep lasts 3s with 1601 samples and is repeated 10 times in order to assure the repeatability of the results. Between antennas and body, a separation of 10-20 mm is maintained to mitigate antenna detuning effect. The measured received signal power is plotted in Fig. 2.13 for the three different antennas in FW channel for standing still and walking scenarios. As it seen, the dynamic body movement causes a rapid variation in the received signal, which creates the need for statistical modelling of the on-body channel.

2.3.3 Channel Modelling Results

The power transfer function for each specific scenario can be described as the product of PG, large-scale fading component, $S(t_n)$ and small-scale fading component, $F(t_n)$ in time domain [10], [11]:

$$P(t_n) = PG \cdot S(t_n) \cdot F(t_n) \tag{2.2}$$

Large-scale fading component $S(t_n)$ can be derived by normalising the received signal envelope r to its local RMS value:

$$S(t_n) = \sqrt{\frac{1}{W} \sum_{n-W/2}^{n+w/2} r^2(t)} \tag{2.3}$$

The local RMS value of the received signal envelope is computed for each individual received envelope sample in a sliding temporal window (W). The adequacy of the normalisation depends on the selection of the appropriate W. A study of the effect of the sliding window size is attempted later on, since it is not totally clear what is the ideal number of sampling points needed. According to Hall [12], a large-scale fading decorrelation time interval of 0.5 s can be considered for all on-body scenarios. This time interval corresponds to 10 consecutive measured channel impulse responses and to an average spatial decorrelation distance (along the user movement track) of approximately 0.25 m. Within this time/distance interval, the small-scale signal fading can be considered a stationary process. In this thesis, a window size of W= 0.5 s that contains 250 samples is selected to represent a size of 4-5λ (0.5 m) in respect to 300λ (10x4 m) of the total movement in walking scenario.

In order to extract the small-scale fading component, one has to remove the effects of path gain and large-scale fading,

$$F(t_n) = P(t_n)/(PG \cdot S(t_n)) \tag{2.4}$$

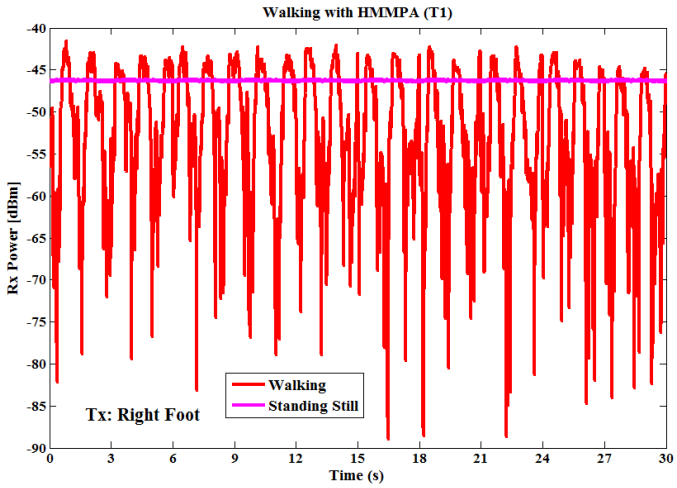

(a)

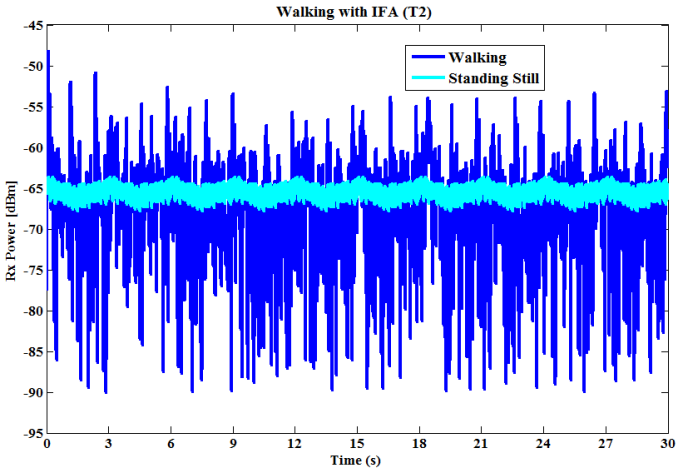

(b)

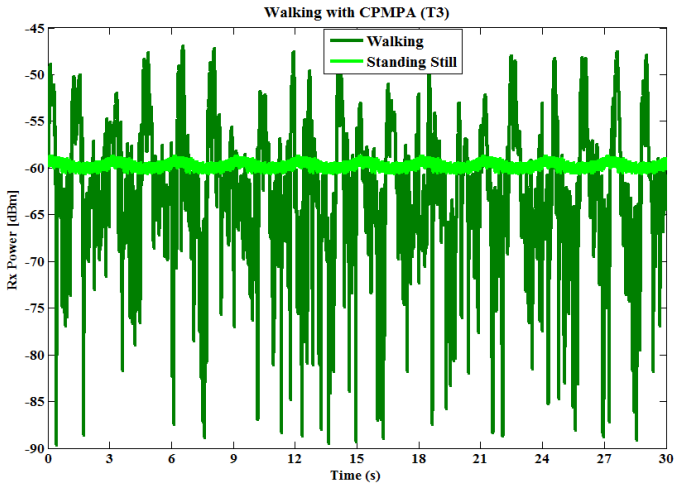

(c)

Figure 2.13 Measured received power for FW channel with (a) T1, (b) T2 and (c) T3 antennas.

A comparison of antennas performance is provided in Fig. 2.14 by plotting the channel shadowing (large-scale fading) effect on the mean path gain level ($PG \cdot \ S(t)$) in the four channel categories. The level of large-scale fading effect is described from the standard deviation σ value, listed in Table 2.6.

As it is shown in Fig. 2.14a regarding T1 antennas, chest-waist (red line) and back-waist (green line) static channels exhibit low standard deviation from the mean PG value instead of the dynamic channels that deviate more. Furthermore, relative PG levels are high enough owing to surface wave propagation, giving rise to the possibility of a low power communication between on-body devices. T2 antennas (Fig. 2.14b) present a mean PG at least 20 dB lower than T1 antennas, as well as, a higher standard deviation at the majority of the on-body channels. Only in the case of the foot-waist channel among the three antenna types, it seems that by using T2 antennas, a lower standard deviation is recorded. Presumably, this type of propagation (with tangential to body E-field component) does not seem to be beneficial for on-body scenarios. As far as T3 antennas are concerned (Fig. 2.14c), all the on-body links are not benefited by the circular polarisation. As has been presented in the literature [13] this type of antenna can be more suitable for environments that enable strong multi-path propagation, such as an indoor environment. However, it is shown that a slightly better path gain performance in FW and CW channels is achieved with T3 antennas rather than T2 antennas, owing to ground plane shielding that maintains a high antenna efficiency.

The empirical CDFs of the received signal envelope for large-scale and small-scale fading are plotted using Matlab in Figs.2.15, 2.16 and Figs.2.18, 2.19 respectively, for the four on-body channels. The best fit statistical distributions are derived using the Kolmogorov-Smirnov goodness-of-fit-test (KS test) [9], providing a statistical model that fits closely to the empirical data. The maximum likelihood method is used to estimate channel model parameters. The best fit statistical model parameters are provided in Table 2.6 for T1, T2 and T3 antennas in static (CW, BW) and dynamic (FW, WW) channels respectively. The statistical analysis method has been mostly developed in previous research studies at the same research laboratoty [14, 15].

Large-scale fading represents the slow variations of the received signal due to the dynamic human body shadowing effect, depending on the change in body posture during movement. In Figs.2.15, 2.16, except for the large-scale fading information, the relative channel path gain is observed in the RMS (mean) signal values at $CDF = 0.5$.

As it is shown in Fig. 2.15 for CW and BW channels, the best fit is achieved by

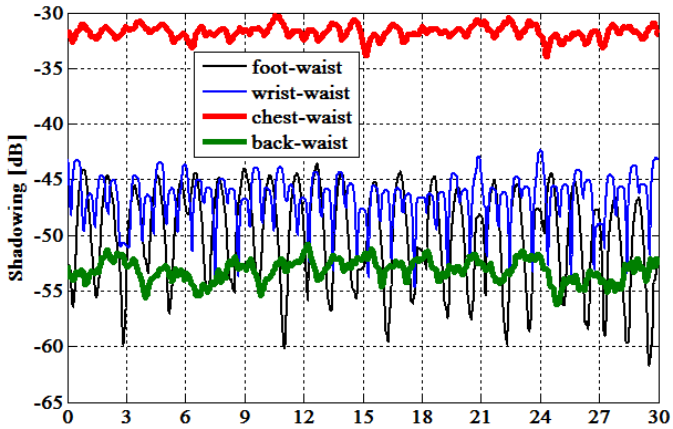

(a)

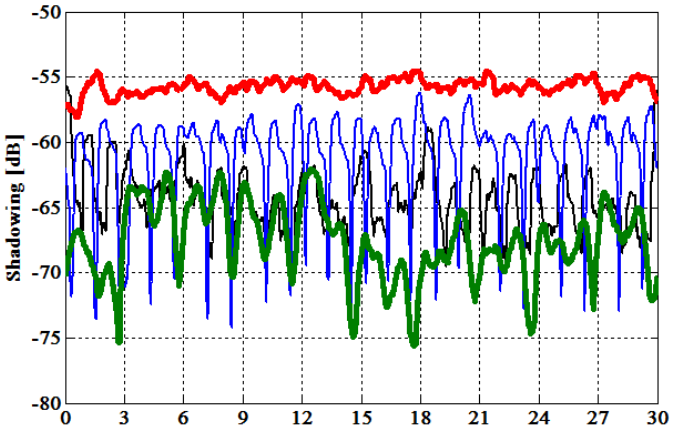

(b)

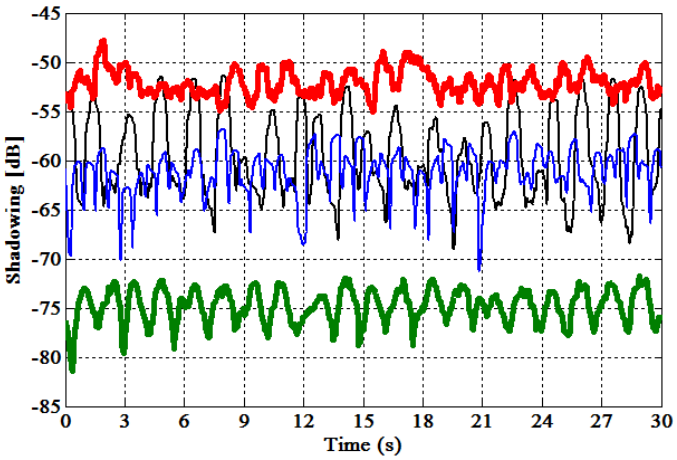

(c)

Figure 2.14 Shadowing effect during walking with (a) T1, (b) T2 and (c) T3 wearable antennas forming four different on-body channels.

Lognormal distribution for both cases as the body posture has minor effect in these two static channels. The intensity of large-scale fading is denoted by the standard deviation (σ) of Lognormal distribution. It is seen that the strongest shadowing effect in the received signal is observed in BW channel as the body arms tend to block the channel path during user's walking.

From the antennas perspective, it is shown again (Fig. 2.15) that T1 antennas provide higher channel gain up to 20 dB rather than T2 and T3. Also using T1 antennas, signal experiences minor shadowing effect in both channels owing to strong surface wave propagation. This can be seen from the small spread of the empirical CDF as well from the low σ value. In BW channel (Fig. 2.15b), the surface wave excitation is highlighted, since neither LOS nor space wave propagation are dominant.

In Fig. 2.16, large-scale fading follows Lognormal distribution in FW channel while WW channel is best fitted by Weibull distribution. Weibull distribution is used to describe vast dynamic actions, such as arm swinging when body shadowing effect is changing rapidly. However, it can be observed that the spread of the CDF of the RMS signal envelope in FW case (Fig. 2.16a) is larger than in the WW case (Fig. 2.16b).

In terms of the antennas performance, T3 antenna presents larger shadowing (σ=4.68 dB) than T1 (σ=3.54 dB) and T2 (σ=3.1 dB) antennas. In WW case, it is found that T2 antennas (b=4.07) followed by T3 antennas (b=4.92) experience stronger shadowing from body (lower b value) rather than T1 antennas (b=5.76). As a result, IFA and CPMPA antennas that radiate with maximum gain away from body are more susceptible to change of body posture when placed on dynamically moving positions.

An investigation of the effect of the temporal sliding window size to the resulting fitting model and KS-stat of the derived large-scale fading CDF is undertaken from W=10 to 250 samples (10,50,100,200,250). Both dynamic and static movement scenarios are investigated but only the dynamic scenarios are plotted in Fig. 2.17 (FW and WW), which show a larger deviation. The effect of the window in static scenarios is also demonstrated in channel for comparison that shows a minor impact. Only one antenna is used, specifically IFA antenna since it experiences the most problematic fitting.

The resulting model parameters and KS-stats for the four on-body channels in respect to the selected window size are summarised in Table 2.5. For the four channels, it is seen that the KS-stat reaches its minimum value (best fit) when 10 or 50

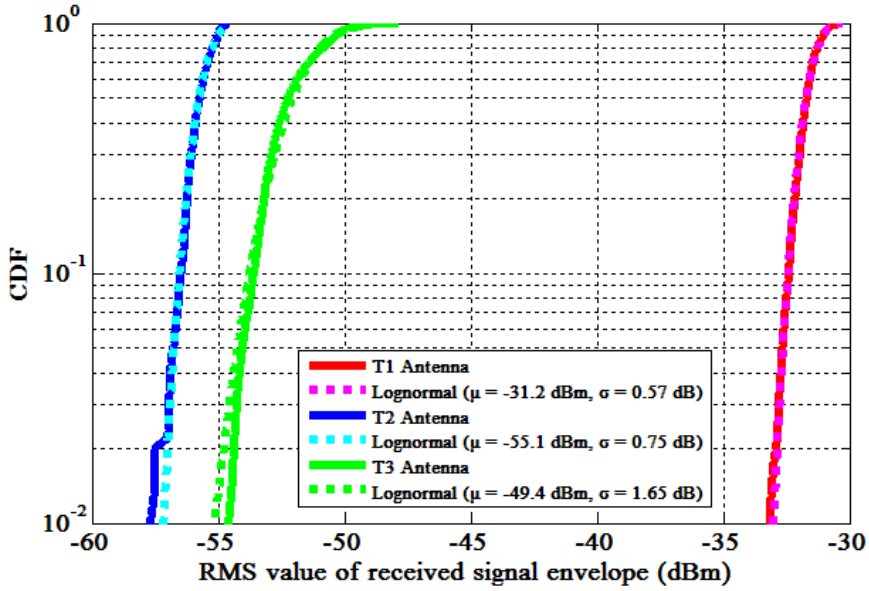

(a)

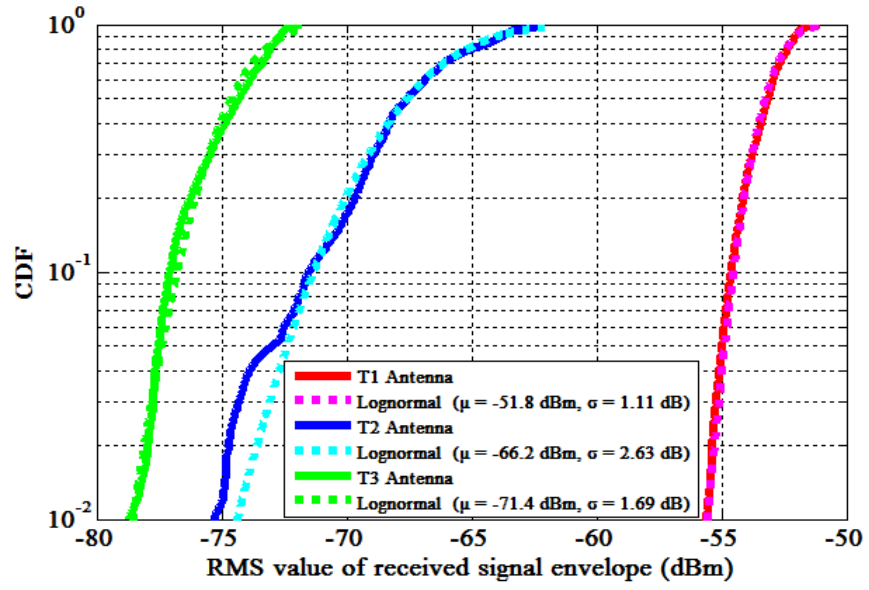

(b)

Figure 2.15 Empirical and theoretical cumulative distribution functions (CDF) of large-scale fading for (a) CW and (b) BW channels.

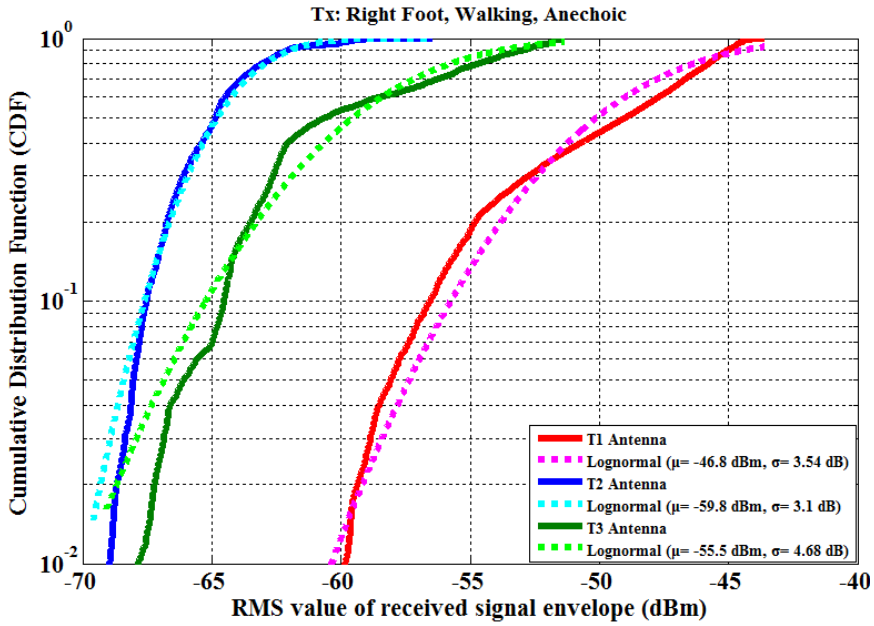

(a)

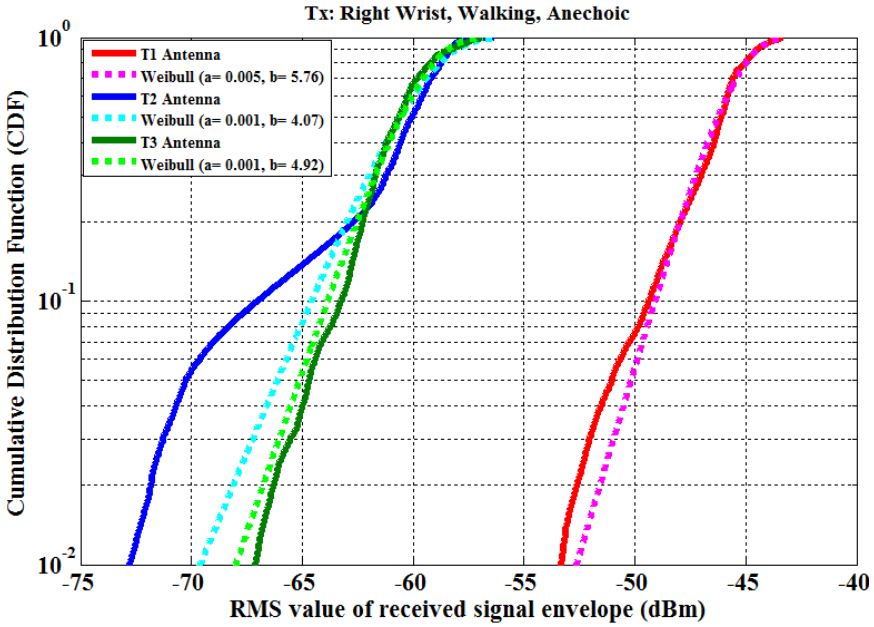

(b)

Figure 2.16 Empirical and theoretical cumulative distribution functions (CDF) of large-scale fading for (a) FW and (b) WW channels.

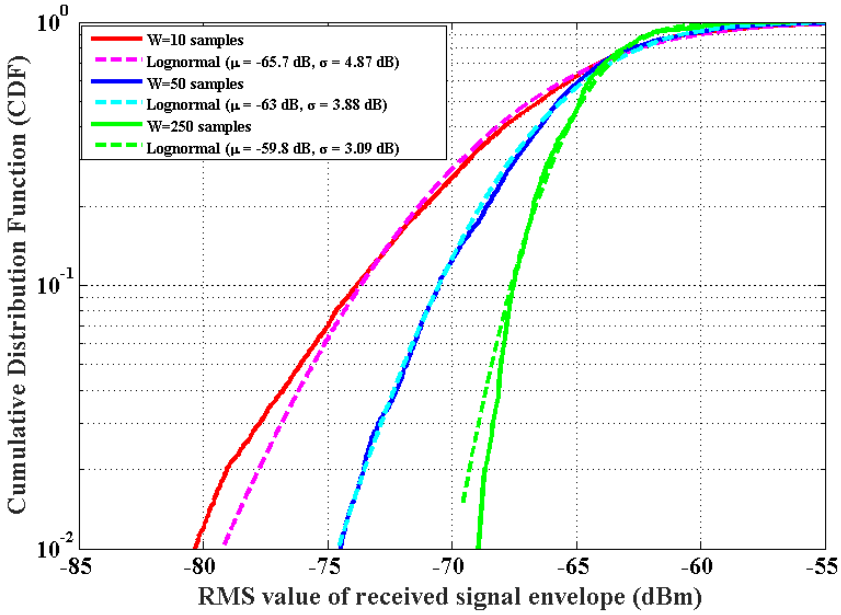

(a)

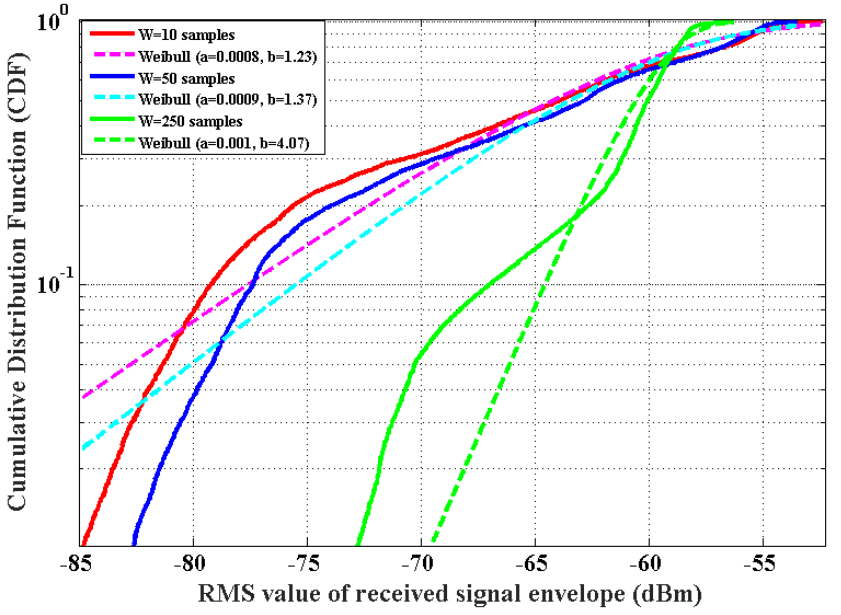

(b)

Figure 2.17 Effect of selected window size in the derived large-scale fading model for (a) FW and (b) WW channels.

Table 2.5 Impact of window size on fitted model for IFA antenna.

(a) FW

Window Size	**Lognormal**		
No. of samples	μ (dB)	σ (dB)	KS-STAT
10	-65.7	4.87	0.023
50	-63.0	3.88	0.062
100	-61.7	3.44	0.105
200	-60.3	3.21	0.124
250	-59.8	3.09	0.121

(b) WW

Window Size	**Weibull**		
No. of samples	a	b	KS-STAT
10	0.0008	1.23	0.077
50	0.0009	1.37	0.075
100	0.0009	1.61	0.102
200	0.001	2.83	0.147
250	0.001	4.07	0.109

(c) CW

Window Size	**Lognormal**		
No. of samples	μ (dB)	σ (dB)	KS-STAT
10	-55.8	1.01	0.039
50	-55.6	0.95	0.036
100	-55.5	0.90	0.041
200	-55.2	0.80	0.050
250	-55.1	0.75	0.057

(d) BW

Window Size	**Lognormal**		
No. of samples	μ(dB)	σ(dB)	KS-STAT
10	-67.7	3.34	0.034
20	-67.3	3.22	0.039
100	-67.0	3.10	0.048
200	-66.4	2.79	0.055
250	-66.2	2.63	0.055

samples are selected for the length of window size. The effect of the window size on the derived channel model parameters is significant in the case of dynamic (FW and WW) channels for both scaling μ and shaping σ parameters. In the case of static (CW and BW) channels, the effect is minor and is only evident in the shaping σ parameter. It is then concluded that different window size affects significantly the derived channel model and should be investigated and selected in every channel measurement campaign since every formed on-body channel has different characteristics.

Small-scale fading is attributed to multi-path reflections and scattering due to body motion that causes fast signal variations in a small time scale. To enable the direct comparison of the fading characteristics for each of the on-body links, all the received signal envelope samples are normalised to their respective root mean square (rms) value $\hat{r} = \sqrt{E(r^2)}$. Thus, small-scale fading is best modelled by Lognormal, Rice, Weibull and generalised $\alpha - \mu$ distributions amongst the CW and BW channels formed from the three different antennas, as shown in Fig. 2.18.

In the CW channel (Fig. 2.18a), the signal distribution using T1 and T2 antennas is quite identical with small spread/deviation from 0 dB RMS value, while using T3 antennas severe fading is applied which is noticed from the big spread from 0 dB.

In the BW channel (Fig. 2.18b), higher fading effect is applied instead of CW channel, with T1 antennas less affected from fading due to creeping waves propagation. By using T2 and T3 antennas stronger fading is observed.

Additionally, the small-scale fading component is plotted in Fig. 2.19 for FW and WW on-body channels. In these channels, small-scale fading occurs due to the multi-path reflections and scattering on the dynamically moving body parts (especially on limbs).

More specifically, in the FW case (Fig. 2.19a), Gamma distribution describes best T1 and T2 antennas' links while T3 antennas link follows Lognormal distribution, as it is proven from the minimum value of KS statistic. From the derived Gamma distribution, the estimated statistical parameter a denotes fading severity. Comparing the three empirical CDFs, it is observed that for a given probability of 10% the received signal envelope using T2 antennas is stronger by 4 dB than for T1 antennas and 2 dB than for T3 antennas, hence experiencing less fading.

In the WW case (Fig. 2.19b), T1 and T2 are fitted by Lognormal and T3 fitted by Gamma. It is found that T3 antennas seem to experience the minimum fading effect followed by T1 antennas while T2 have the worst performance. The same conclusion can be derived from the comparison of the gamma parameters for the two antennas

tested so far. It is known that the higher the a parameter is, less fading exists.

Eventually, comparing the small-scale fading of the two channels, it is seen that a small difference is presented when T1 and T3 antennas are employed, while using T2 antennas severe fading happens in WW case. This fading effect when using T2 antennas can be attributed to the large polarisation mismatch during arm movement, as well as the lack of ground plane shielding from body. These two channels are considered as highly dynamic channels that periodically change between quasi-LOS and NLOS conditions. However, they are differentiated in terms of antenna-body interaction, relative Tx-Rx distance and the amount of body shadowing applied in each case.

The best-fit statistical distribution models for the small-scale fading have been chosen from the lowest KS-statistic among all the tested distributions. However, since the KS-test tends to be more sensitive around the median value, where CDF = 0.5, and less sensitive at the extreme ends of the distribution, where CDF is near 0 or 1, in some cases it is selected by visual inspection of the fitting (especially in the tail). In Appendix D, a table with all the KS-statistic values is provided for the 6 distribution models tested at the total of 12 cases (4 channels with 3 different antenna types). As a comparison, the Kullback-Leibler (KL) test [16] is also employed that agrees with the KS results, based on channel entropy. In Appendix C the CDFs including all the distribution models are provided for each channel.

If we give a closer look at the table that includes the fitting statistics (KS-stat) in Appendix D, the generalised $\alpha - \mu$ distribution model [17] (encompasses as special cases the weibull, nakagami-m, rice and gamma) provides a close fitting to the majority of the measured channels. By visually checking the fitting of the empirical with theoretical CDFs, this conclusion is validated in 6 out of 12 times with the exception of cases T1-FW, T1-WW, T2-FW, T2-CW, T3-FW, T3-CW that fails to follow the empirical CDF in the tail.

If modelling close to mean value is primarily important, the $\alpha - \mu$ provides best fit in 9 out of 12 cases apart from T2-CW, T3-FW, T3-CW. In the rest 3 cases, lognormal provides best fit since it can easily describe low fading effects with small spread around the RMS value (nearly straight lines). Hence, the generalised $\alpha - \mu$ distribution can be exclusively used to describe the small-scale fading in on-body communication channels.

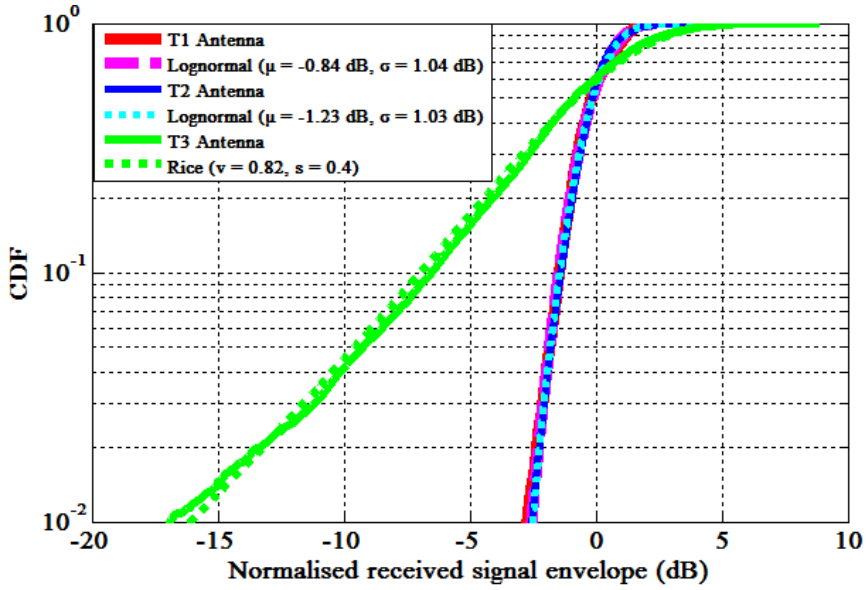

(a)

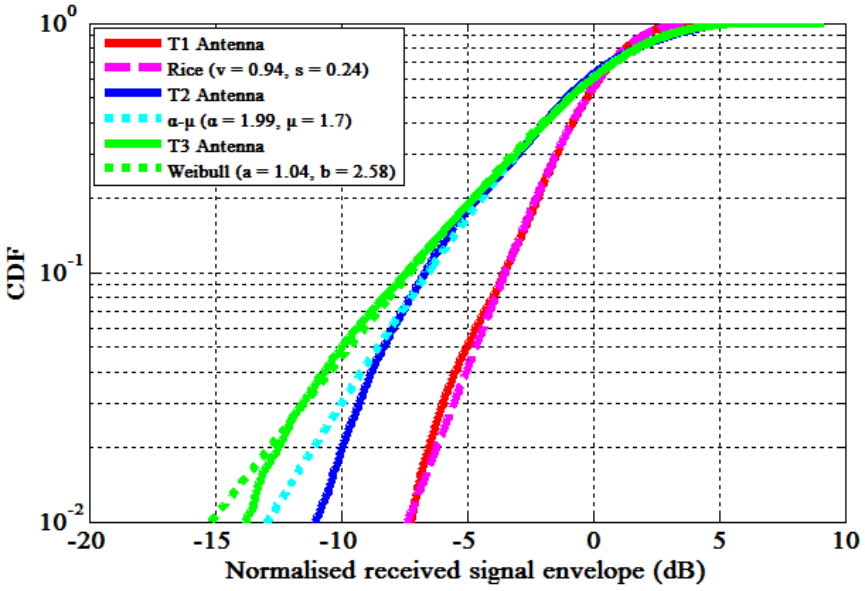

(b)

Figure 2.18 Empirical and theoretical Cumulative Distribution Functions (CDF) of small-scale fading for (a) CW and (b) BW channels.

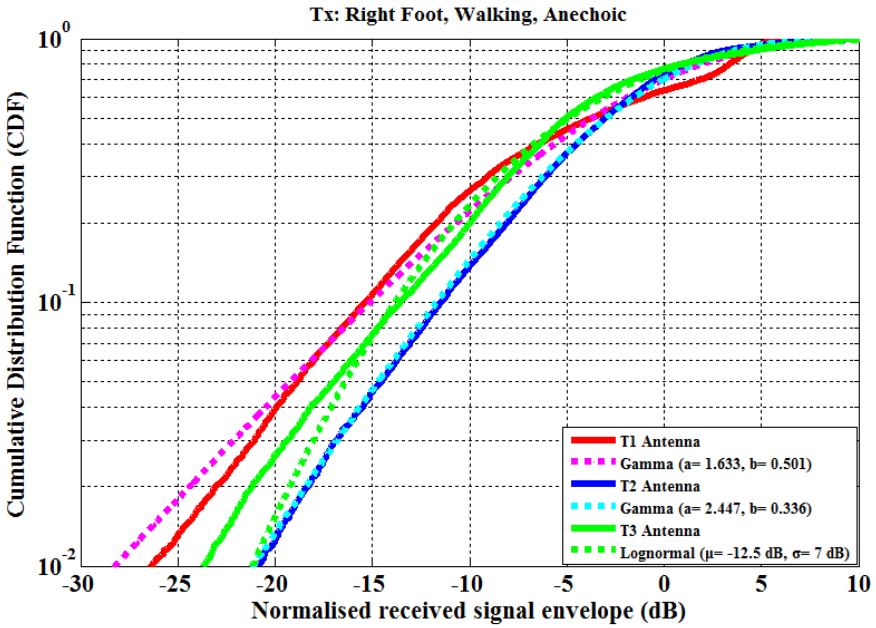

(a)

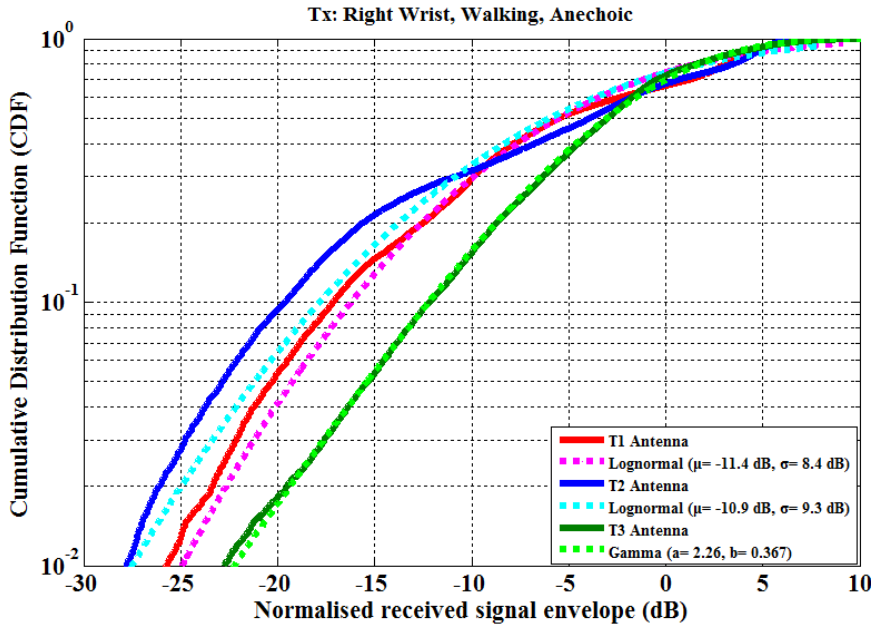

(b)

Figure 2.19 Empirical and theoretical Cumulative Distribution Functions (CDF) of small-scale fading for (a) FW and (b) WW channels.

Table 2.6 Best fit statistical model parameters.

(a) T1 Antennas (HMMPA)

Channel	Best Fit Model	
	Large-scale Fading	**Small-scale Fading**
FW	**Lognormal**	**Gamma**
	μ= -46.8 dBm, σ = 3.54 dB	α= 1.633, β= 0.501
WW	**Weibull**	**Lognormal**
	a= 0.005, b= 5.76	μ= -11.4dB, σ = 8.4dB
CW	**Lognormal**	**Lognormal**
	μ= -31.2 dBm, σ = 0.57 dB	μ= -0.84 dB, σ = 1.04 dB
BW	**Lognormal**	**Rice**
	μ= -51.8 dBm, σ = 1.11 dB	ν= 0.94, s= 0.24

(b) T2 Antennas (IFA)

Channel	Best Fit Model	
	Large-scale Fading	**Small-scale Fading**
FW	**Lognormal**	**Gamma**
	μ= -59.8 dBm, σ = 3.1 dB	α= 2.447, β= 0.336
WW	**Weibull**	**Lognormal**
	a= 0.001, b= 4.07	μ= -10.9 dB, σ = 9.3 dB
CW	**Lognormal**	**Lognormal**
	μ= -55.1 dBm,σ = 0.75 dB	μ= -1.23 dB, σ = 1.03 dB
BW	**Lognormal**	α-μ
	μ= -66.2 dBm, σ =2.63 dB	α= 1.99, μ= 1.7

(c) T3 Antennas (CPMPA)

Channel	Best Fit Model	
	Large-scale Fading	**Small-scale Fading**
FW	**Lognormal**	**Lognormal**
	μ= -55.5 dBm, σ = 4.68 dB	μ= -12.5 dB, σ = 7 dB
WW	**Weibull**	**Gamma**
	a= 0.001, b= 4.92	a= 2.26, b= 0.367
CW	**Lognormal**	**Rice**
	μ= -49.4 dBm, σ = 1.65 dB	ν= 0.82, s= 0.4
BW	**Lognormal**	**Weibull**
	μ= -71.4 dBm, σ = 1.69 dB	a= 1.04, b= 2.58

2.4 Conclusions

In this chapter, a statistical characterisation of common on-body channels is achieved through EM simulations and measurements in an anechoic environment.

In the beginning, the feasibility of on-body channel modelling through EM simulations is demonstrated for the waist-foot dynamic channel. A quasi-continuous dynamic user's movement is achieved using a human body phantom created in an animation software with different body postures. The path gain and large-scale fading (body shadowing) are examined between two types of wearable antennas; HMMPAs or IFAs, and two types of movement; walking or running. A higher path gain (up to 20 dB) is achieved in walking when employing omni-directional patch antennas (HMMPA) that support surface wave propagation and have a maximum gain across the body surface instead of IFA antennas that are based on space wave propagation. However, when the phantom is running, a comparable path gain between the two antenna types is observed. In terms of large-scale fading effect due to changes in body posture, a higher shadowing effect happens in the running activity with HMMPA antennas, while with IFA antennas a higher shadowing can be found in walking activity.

Afterwards, a statistical analysis of commonly used on-body channels (chest-waist, foot-waist, wrist-waist and back-waist channels) through channel measurements is performed. Subsequently, four application-based on-body channel models are derived by choosing the best fit statistical distributions. Wearable antennas performance is evaluated amongst the four on-body channels. The on-body channels performance is tested using three different antenna types with different radiation characteristics.

Comparing the response of the on-body channels, both in terms of path gain and fading, it is seen that the channel response is strongly dependent on the specific antenna characteristics. It is found that when using HMMPAs less body shadowing and higher mean received power of up to 20 dB are observed at both LOS (CW) and NLOS (BW) channels owing to strong surface wave propagation. Large-scale fading is best described by Lognormal distribution in the majority of the on-body channels, which is explained by the low body shadowing effect at CW, BW and FW channels. Only in the WW channel, large-scale fading is best modelled by Weibull distribution that is due to the highly dynamic wrist action.

Small-scale fading is more dependent on the user movement rather than the specific antenna type. Small-scale fading is found stronger in the dynamic on-body channels (FW and WW) rather than in the static on-body channels (CW and BW),

which are less affected from the body movement. Especially, in the WW case, high small-scale fading occurs due to the highly dynamic wrist action that oscillates between LOS and NLOS paths. Four different statistical distributions (Lognormal, Rice, Weibull and the generalised $\alpha - \mu$) provided the best fit small-scale fading models that reveals the large variability of the contributing effects.

It is then concluded from this analysis that the wearable antennas placed in static body parts experience less body shadowing and fading effects due to body movement rather than in dynamic moving parts. Subsequently, wearable systems that communicate on the body torso can achieve an unobstructed communication with low power and high data rates. Respectively, wearable systems with antennas on moving body parts would be strongly affected from body movement. Hence, the derived channel models are important for system designers to be able to optimise the wearable system performance on the human body. Moreover, in the total of four on-body channels, HMMPAs outperform IFAs and CPMPAs presenting higher path gain and less fading due to the omnidirectional radiation across the body surface as well as the surface wave propagation. In the following chapters, the HMMPA antenna will be thoroughly investigated as a promising candidate antenna for on-body communications and a novel textile prototype will be developed.

References

[1] M. Gallo, P. S. Hall, Q. Bai, Y. I. Nechayev, C. C. Constantinou, and M. Bozzetti, "Simulation and Measurement of Dynamic On-Body Communication Channels," IEEE Transactions on Antennas and Propagation **59(2),** 623–630 (2011).

[2] G. Conway and W. Scanlon, "Antennas for Over-Body-Surface Communication at 2.45 GHz," IEEE Transactions on Antennas and Propagation **57(4),** 844–855 (2009).

[3] M. Gallo, P. S. Hall, and Y. I. Nechayev, "Use of Animation Software in Simulation of On-Body Communications Channels at 2.45 GHz," IEEE Transactions on Antennas and Propagation Letters **7,** 321–324 (2008).

[4] T. Aoyagi, M. Kim, J. Takada, K. Hamaguchi, and R. Kohno, "Body Motion and Channel Response of Dynamic Body Area Channel," In *European Conf. on Antennas and Propagation (EuCAP 2011)*, pp. 3293–3297 (2011).

[5] S. Swaisaenyakron, P. R. Young, and J. C. Batchelor, "Animated Human Walking Movement for Body Worn Antenna Study," In *Loughborough Antennas & Propagation Conference*, pp. 1–4 (2011).

[6] B. Zhen, T. Aoyagi, and R. Kohno, "Reasons for Time-Varying Fading of Dynamic On-Body Channels," In *Wireless Communications and Networking Conference (WCNC), IEEE*, pp. 1 – 5 (2010).

[7] *IEC, Human exposure to radio frequency fields from hand-held and body. Part 2: Procedure to determine the specific absorption rate (SAR) in the head and body for 30 MHz to 6 GHz handheld and body-mounted devices used in close proximity to the body*, Available online: https://webstore.iec.ch/publication/6590.

[8] K. Y. Yazdandoost and K. Sayrafian, "Channel model for body area network (BAN)," IEEE 802.15 Working Group Document (2010).

[9] W. H. Press, S. A. Teukolsky, W. T. Vetterling, and B. P. Flannery, "Numerical Recipes in C," Cambridge Univ. Press (1992).

[10] R. Steele and L. Hanzo, *Mobile Radio Communications* (IEEE, 1999).

[11] R. D'Errico and L. Ouvry, "A Statistical Model for On-Body Dynamic Channels," International Journal of Wireless Information Networks 17 (2010).

[12] P. S. Hall and Y. Hao, *Antennas and Propagation for Body-Centric Wireless Communications. Second Edition*, 2nd ed. (Artech House, Inc., 2012).

[13] C. Hertleer, H. Rogier, L. Vallozzi, and L. Van Langenhove, "A textile antenna for off-body communication integrated into protective clothing for firefighters," IEEE Transactions on Antennas and Propagation **57(4),** 919–925 (2009).

[14] A. Michalopoulou, A. A. Alexandridis, K. Peppas, T. Zervos, F. Lazarakis, K. Dangakis, and D. I. Kaklamani, "Statistical analysis for on-body spatial diversity communications at 2.45 GHz," IEEE Transactions on Antennas and Propagation **60(8),** 4014–4019 (2012).

[15] A. Michalopoulou, A. A. Alexandridis, K. Peppas, T. Zervos, F. Lazarakis, K. Dangakis, and D. I. Kaklamani, "On-body channel statistical analysis based on measurements in an indoor environment at 2.45 GHz," IET Microwaves, Antennas and Propagation **6(6),** 636–645 (2012).

[16] K. P. Burnham and D. R. ANDERSON, "Kullback-Leibler Information as a Basis for Strong Inference in Echological Studies," Wildlife Research **28,** 111–119 (2001).

[17] M. D. Yacoub, "The $\alpha - \mu$ distribution: a general fading distribution," In *The 13th IEEE International Symposium on Personal, Indoor and Mobile Radio Communications*, **2,** 629–633 (2002).

Chapter 3

Wearable Textile Antennas: Design and Fabrication

The antenna is an essential part of today's wireless body area networks. Its complexity depends on the radio transceiver requirements and on the profile of the surrounding environment. In order to successfully design a wearable antenna, knowledge of the nature and the magnitude of interactions between the antenna and the human body is required over a broad range of frequencies. The variability of the different body profiles in combination to antennas with different radiation characteristics creates a driving force in the direction of a systematic characterisation. A properly designed wearable antenna not only enables reliable connectivity but also helps preventing excessive battery energy consumption due to an improvement in radiation efficiency [1].

A prospective wearable antenna for body-centric applications needs to be compact, light weight, small in size, flexible and conformal to the body surface. In addition, it should be insensitive to detuning in close proximity to human body while maintaining high radiation efficiency and low specific absorption rate (SAR) levels. For off-body communications, a radiation pattern with maximum gain in the direction off the body surface is desired, whereas for on-body communications, antennas should radiate the energy around the body surface. The off-body propagation is mostly comprised of space waves with a part scattered at the body surface, while on-body propagation can consist of surface waves, diffracted waves, scattered waves and space waves [2].

3.1 Introduction

Three different wearable antennas, one printed and two textile antennas, are designed, fabricated and tested on the human body for operation at 2.4 and 5.8 GHz ISM band. The idea of selecting the specific antenna types arises from the need to examine the antenna/ body interaction in respect to different radiation characteristics and frequency of operation. Moreover, the selected wearable antennas will be used in Chapter 4 in order to demonstrate the universal applicability of the proposed near-field measurement method for wearable antenna characterisation on an anthropomorphic body phantom.

The first antenna presented herein, a printed dipole antenna [3], is used as the worst case wearable antenna that distinctively shows a strong interaction effect with human body due to the high power absorption, which alters the omni-directional radiation pattern in free space to directional on the surface of human body. As far as the two textile wearable antennas are concerned, a microstrip patch antenna (MPA) and a higher-order mode microstrip patch antenna (HMMPA) are selected. The patch antennas are good candidates for operation in body-centric wireless communications due to their low profile and insensitivity to human body presence. The MPA antenna [1, 2] with vertical polarisation is favourable for off-body communications. It excites a broadside radiation pattern off the body surface and, due to its ground plane, the antenna remains almost unaffected from the body presence. The HMMPA antenna [2, 4] has a normal-to-body polarisation and radiates omni-directionally across the body surface that makes it useful for on-body communications.

The selected patch antenna designs are adapted to be comfortably used for wearable applications, by employing textile materials either only at the substrate or also at the conductive parts. Felt fabric is used in both cases as the antenna substrate while copper sheet and copper posts are used for the conductive parts. In Chapter 5, fully-textile designs will be presented, replacing the rigid metallic parts with metallised nylon fabric (Nora-Dell) or embroidered with conductive thread . To obtain the desired antenna performance, an optimisation in CST Microwave Studio is employed by adjusting the dimensions of the conductive and dielectric parts.

The wearable antennas are simulated and tested in terms of impedance matching $|S_{11}|$, far-field radiation performance in free space and on the human body. Two different full body anthropomorphic numerical models are used, one homogeneous and one layered with realistic tissue properties in order to investigate the effect of the body

tissue type to the installed antenna performance. More specifically, simulation results are derived using a homogenous SAM phantom while a comparison is undertaken with the voxel HUGO model as a reference. No effect of the ground or surrounding objects is modelled since this study is focused only on the effect of the user's body.

An antenna design workflow is illustrated in Fig. 3.1 that shows all the intermediate steps that are taken to realise an efficient wearable antenna. It starts from the materials selection and their dielectric characterisation, and is completed with the derivation of antenna performance via measurements. These steps are presented in the following sections of this chapter apart from the last step of the antenna measurement that is presented thoroughly in the next chapter.

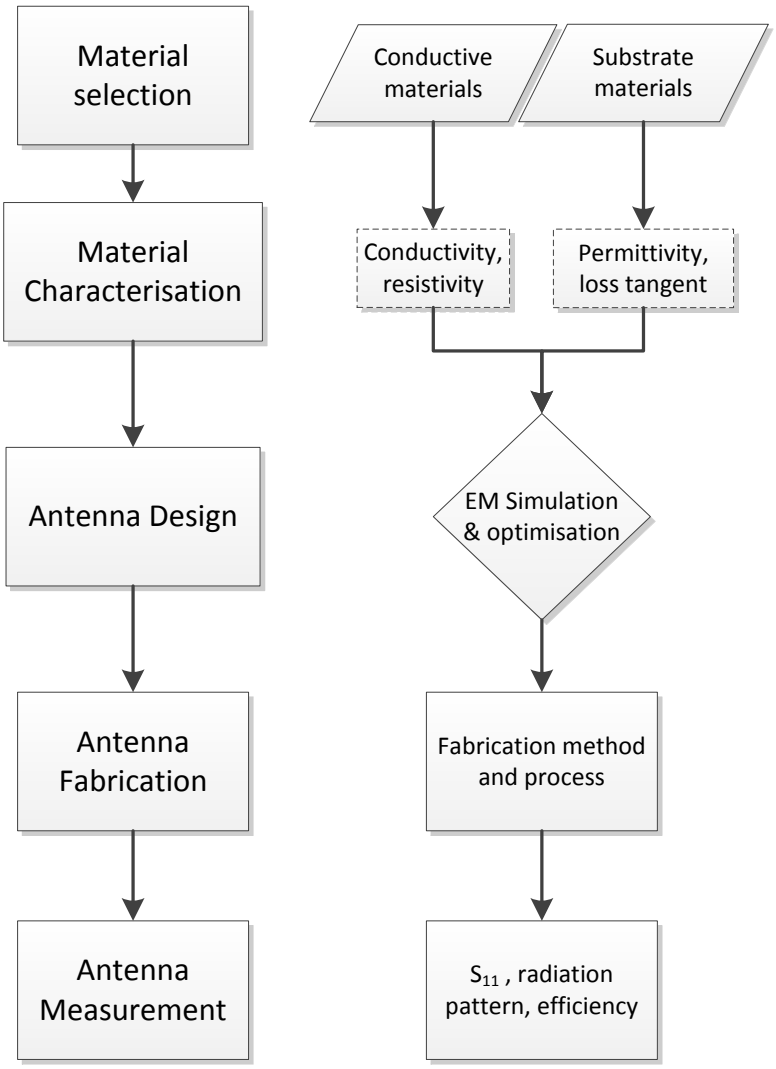

Figure 3.1 Antenna design workflow to realise a wearable antenna [5].

3.2 Materials Selection

A flexible textile antenna, similarly to conventional rigid PCB antennas, consists of two basic parts: the conductive material which is used for the radiating elements and the ground plane, and the dielectric material which is used as a substrate.

As far as the conductive materials are concerned, pure metallic and metal-plated textile materials are used in this study. For the first type, copper sheet is used which exhibits high conductivity, shaping and assembling simplicity and low cost. In order to be attached on the substrate, a melted adhesive web or a sprayed adhesive foam is used that does not alter the substrate permittivity. For the second type of metal-plated textile materials ("e-textiles"), they reach an effective conductivity up to 10^6 S/m [6]. To achieve this, soft textile materials such as nylon, are coated with metals, by weaving or knitting the non conductive fabric using conductive threads. "E-textiles" can be sewn directly into clothing offering more flexibility and comfort to the wearer. In the current study, Nora-Dell fabric (produced by Shieldex) has been used as a conductive textile [7]. More details about this material, are given in the Chapter 5 where the presented antennas are fabricated using this conductive cloth. The electrical properties of copper sheet and Nora-Dell are listed in Table 3.1.

Table 3.1 Electrical properties of the conductive materials.

Conductive Material	***Sheet Resistance*** (Ω/sq)	***Conductivity*** (S/m)
Copper (t= 0.07 mm)	0.0005	$2.86 \cdot 10^7$
Copper (t= 0.1 mm)	0.0005	$2 \cdot 10^7$
Nora-Dell (t= 0.13 mm)	0.005	$1.54 \cdot 10^6$

As for the dielectric materials, felt of different thickness and density is used. The relative permittivity and loss tangent is dependent on the production process and is essential to be measured before the antenna design stage. In the next section, two dielectric properties characterisation techniques are presented that are used for felt characterisation.

3.3 Dielectric Properties Characterisation of Fabric Materials

In order to be able to characterise the dielectric properties (relative permittivity ϵ_r and loss tangent $tan\delta$) of fabric materials, which will then be used for the fabrication of textile antennas, two different techniques are employed. These are the "printed stub resonator" [8, 9] and the "split-post dielectric resonator" [10] techniques.

As far as the first method is concerned, the microstrip line T-resonator method is only valid for a single frequency characterisation (2.45 GHz in this study), which is determined by the printed resonator length. The T-branch stub resonator has a length of a quarter-guided wavelength $\lambda_g/4$. The effective permittivity and loss tangent can then be extracted using the formula in [8]. The steps to perform a dielectric characterisation of the fabric using this method are as follows: the $|S_{21}|$ parameter for the $\lambda_g/4$ stub (Fig. 3.2) is measured using a vector network analyser (VNA). After this step, simulation of the $|S_{21}|$ parameter for the $\lambda_g/4$ stub is carried out using CST Microwave Studio [11]. The value of the relative permittivity is then adjusted in simulations so that the simulated and the measured $|S_{21}|$ vs frequency curves coincide in the resonance frequency. Since the curves are matching in the resonance frequency, the value of the relative permittivity (ϵ_r) has been derived. For the derivation of loss tangent (tanδ), this value is adjusted until the two curves match also at the level of the $|S_{21}|$ magnitude.

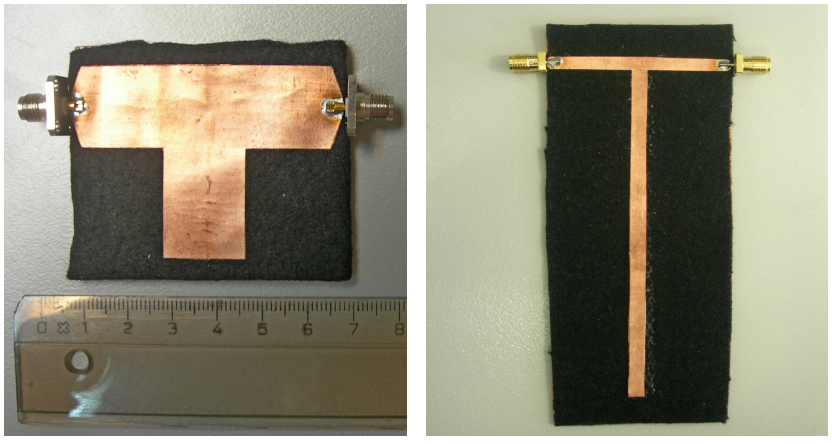

(a) **(b)**

Figure 3.2 Fabric characterisation using the printed (open) stub resonator for (a) 4.2 mm felt and (b) 1.1 mm felt

This method of dielectric characterisation is applied here for a felt fabric of 4.2 mm thick (Fig. 3.2a) and 1.1 mm thick (Fig. 3.2b). Copper sheet of 0.1 mm is used for the metallic parts of the ground plane and the microstrip line. The line width and stub length are designed for stub resonance close to 2.4 GHz. For the 4.2 mm felt, the best match is obtained using $\epsilon_r = 1.13$ (Fig. 3.3a), while for the 1.1 mm felt is $\epsilon_r = 1.39$ (Fig. 3.3b). Concerning the loss tangent ($tan\delta$), which influences the magnitude of $|S_{21}|$, it is found 0.001 and 0.011 respectively. These estimated values will be used for antenna simulations at 2.45 GHz but also at 5.8 GHz since the dispersion rate with frequency is very small at these materials.

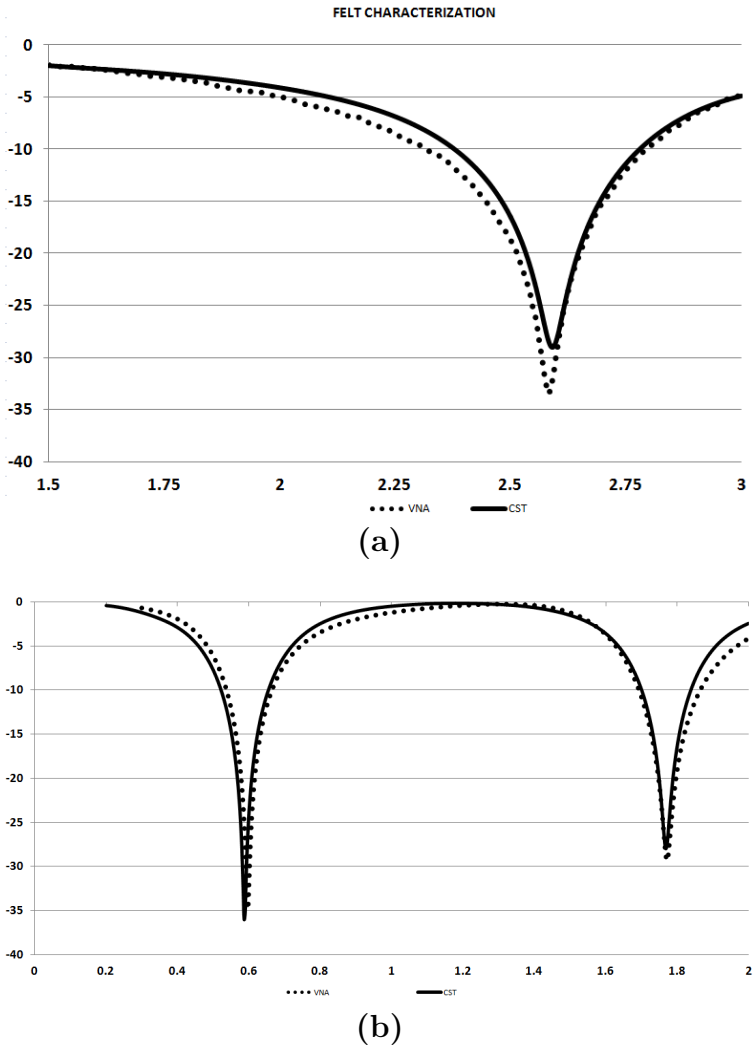

Figure 3.3 $|S_{21}|$ measurement using the printed (open) stub resonator for (a) 4.2 mm felt and (b) 1.1 mm felt.

In the second method, a microwave Q-meter (Fig. 3.4a) connected with a split post dielectric resonator (Fig. 3.4b) are used to measure the complex permittivity of fabrics. The split-post dielectric resonator technique is suitable to characterise low loss non dispersive materials in a single frequency with superior accuracy. This is achieved by comparing the resonant frequency and the quality factor (Q) of the $|S_{21}|$ between an empty resonator and a loaded with the dielectric material under test. The frequency shift determines the relative permittivity (ϵ_r) value while the Q factors, obtained by measuring the 3 dB bandwidth of the $|S_{21}|$ in the loaded and empty states determine the loss tangent ($tan\delta$). A split-post resonator consists of a metal cavity which is comprised of two dielectric resonators. The Q-meter is connected with the computer to derive the results without needing a vector network analyser. Two felt samples are measured with this method, one blue felt fabric with thickness of 2.9 mm and a green felt of 1 mm.

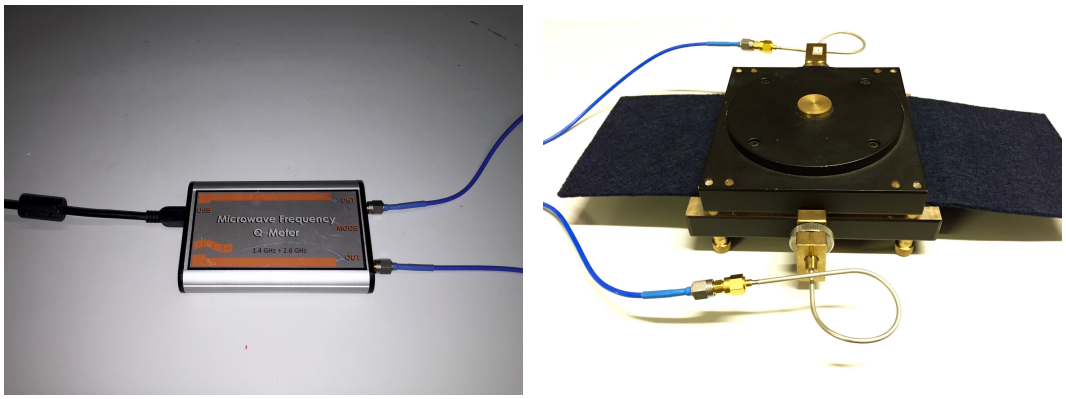

(a) **(b)**

Figure 3.4 (a) Q-meter connected with the computer, and (b) split-post dielectric resonator loaded with a piece of felt.

The results for the felt fabric characterisation gathered from both techniques are listed in Table 3.2. It should be noted that the 4.2 mm and 1.1 mm felt fabrics are two different materials with specific material density created with a different fabrication process. Compared to other characterisation methods such as the broadband method [12], the advantages of this one is the simplicity, no need for special equipment, and, finally, its applicability to all types and sizes of fabrics. This method is well suited to textiles whose dielectric characteristics are not highly variable with frequency (i.e., materials that are not dispersive). In case where the permittivity varies with frequency (dispersive textile materials), a broadband method is more preferable [12].

Table 3.2 Measured dielectric properties of felt fabric, used as substrate.

Substrate	***Method***	***Thickness (mm)***	ϵ_r	$tan\delta$
Black (thick) felt	Printed-stub	4.2	1.13	0.0010
Black (thin) felt	Printed-stub	1.1	1.39	0.0110
Blue felt	Split-post	2.9	1.185	0.0012
Green felt	Split-post	1	1.2	0.0013

3.4 EM Simulation Setup

Following the substrate characterisation of wearable textile antennas, the EM simulation setup is presented, which is an important step of the wearable antenna modelling. The EM simulation software that is used throughout this thesis is CST Microwave Studio. Among CST Microwave Studio's available solvers, Time Domain (TD) solver is selected based on the fast and memory efficient Finite Integration Technique (FIT), which outperforms in calculation time the Frequency Domain (FD) solver for electrically large problems, including the human body. The Integral Equation (I) solver based on the method of moments is also used for large structures (especially for wire antennas) but since it uses a surface mesh is not suitable for modelling in detail the RF absorption inside the body. A hexahedral volume mesh is used in the TD solver. The number of mesh cells reaches in some cases 10 million cells when a full body phantom is included, which needs approximately 1 to 3 hours of simulation time with normal hardware resources. Perfectly Matched Layer (PML) (labelled "Open" boundary) is selected in order to approximate free space conditions.

Some significant EM simulation challenges are imposed in the process of designing and evaluating a wearable antenna attached on the human body. Since the body behaves as a lossy medium with large relative permittivity ($\epsilon_r \approx 40$), the incoming wave travels slower inside the body rather than in free space ($\epsilon_r = 1$). The effective wavelength of the wave penetrating in the human body at the ISM band (at 2.4 GHz) will be shorter than in free space [13] by:

$$\lambda_g = \frac{\lambda_0}{Re\{\sqrt{\epsilon_r - j\sigma_e/\omega\epsilon_0}\}} \tag{3.1}$$

The electrical size of a 1.8 m body model is then calculated from (3.1) to be almost $90 \cdot \lambda_g$ at 2.4 GHz (Fig. 3.5a). Hence, the computational space, which is the space occupied by the full-body phantom becomes extremely large. The numerical prob-

lem needs an increased calculation time to converge and demands enough hardware resources.

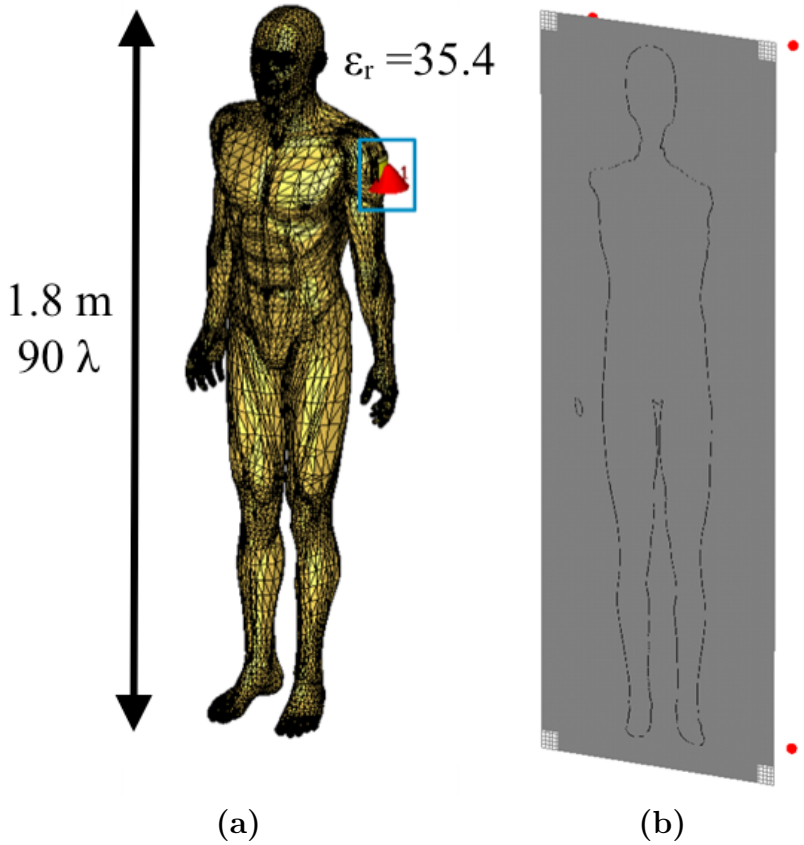

Figure 3.5 (a) Picture of the numerical full-body SAM phantom, and (b) the resulted fine mesh discretisation in CST Microwave Studio.

For the determination of the correct mesh resolution, it is important to use a maximum mesh cell size of $\lambda_g/20$ especially close to the interface between the antenna and the human body in order to accurately calculate the effect of the body coupling on the antenna's current distribution.

Another challenge in the simulation procedure occurs from the definition of the material properties of the human body. There is an inconsistency among the different material properties assigned on the simulated body phantoms in the literature. To tackle this inconsistency, two human body phantoms are used, which is the homogenous SAM phantom and the layered HUGO voxel phantom. The homogenous SAM

phantom is assigned with a dispersive relative permittivity and conductivity across the frequency band that follows the MCL-T tissue equivalent liquid based on 2/3 muscle tissue properties [14]. This target value is used since the dielectric characteristics of the body estimated from outside the body surface are equivalent to nearly 2/3 of the muscle tissue's dielectric properties. This numerical phantom is selected to match with the actual SAM phantom that is used for the near-field measurements in Chapter 4. The SAM phantom is compared with the HUGO model from the Visible Human Project. The so-called Voxel Man is a dissected male corpse sliced into several thousand layers created from anatomical data set with realistic tissue properties [11].

The dispersive relative permittivity and conductivity values of the SAM phantom up to 10 GHz are plotted in Fig. 3.6. It is observed that the relative permittivity of the equivalent tissue is being reduced while the conductivity is increased for increasing frequency. The wavelength and penetration depth into the SAM phantom, compared to the free space wavelength are calculated using [15] and shown in Fig. 3.7. Power absorption into the human body can be determined from the penetration depth, the high value of which in low frequencies results to severe antenna frequency detuning, return loss and gain degradation as well as to radiation pattern deformation.

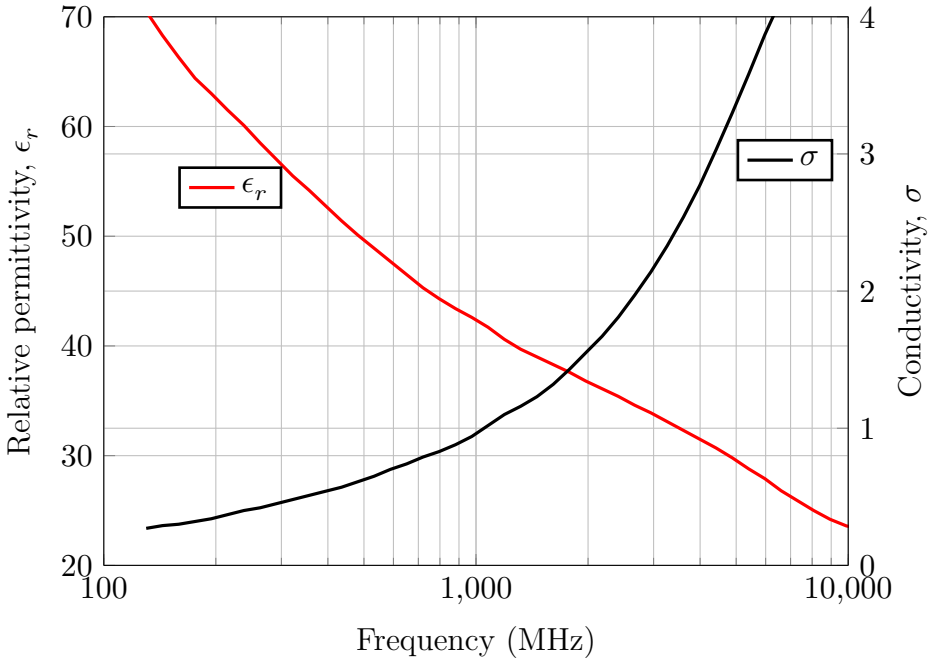

Figure 3.6 Relative permittivity, ϵ_r and effective conductivity, σ of the homogenous SAM phantom based on 2/3 muscle tissue [16].

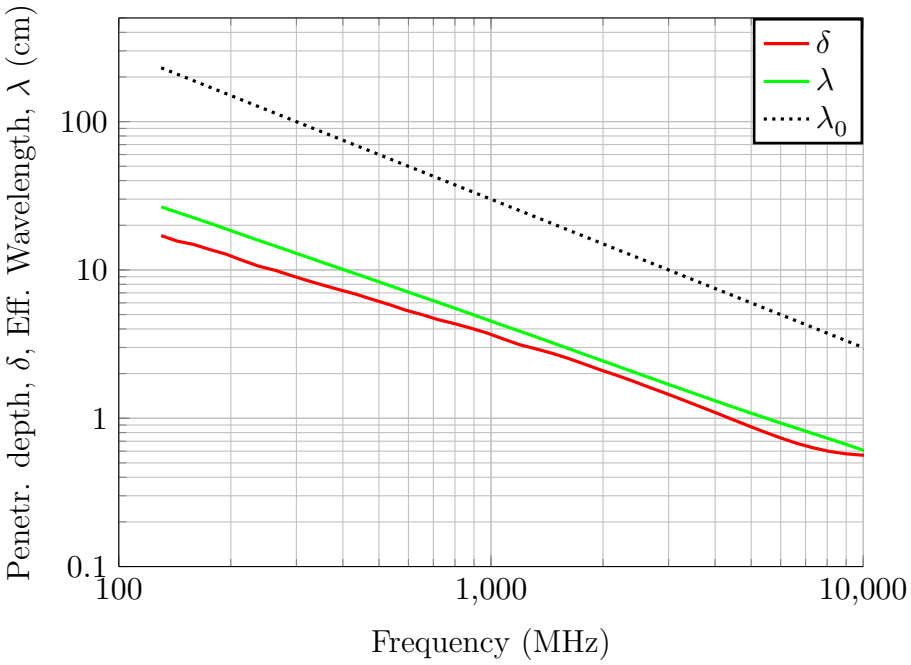

Figure 3.7 Penetration depth, δ and effective wavelength, λ (in cm) inside the homogenous SAM phantom, calculated from the equations in [15] .

Another challenge that arises from simulating the antenna in close proximity to a human body model is the non uniformity of the phantom's surface. It is important then to keep the distance of the wearable antenna from the body surface consistent among the different antenna models, body locations and even body models.

For the antenna feeding, waveguide and discrete face (lumped resistor) ports have been used. However, to achieve a more controlled antenna excitation, a standardised SMA connector model is used, which is also employed in the antenna fabrication (Fig. 3.8).

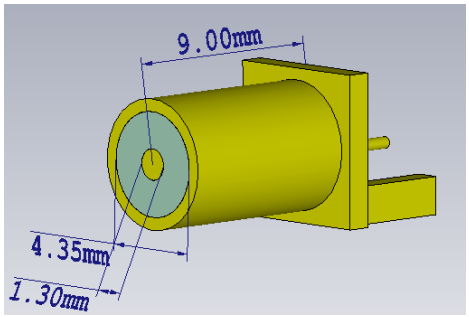

Figure 3.8 SMA connector used in EM simulations.

3.5 Printed Dipole Antenna

3.5.1 Antenna Design

The first antenna type utilised in this study is a variation of coplanar strips dipole antenna. Instead of printing the dipole on a single layer of the dielectric substrate, as it is shown in the case of the coplanar strips dipole (Fig. 3.9a), the two dipole arms are printed on the opposite surfaces of the substrate to simplify the feed arrangement (Fig. 3.9b). This antenna is used as the worst case wearable antenna, due to the lack of ground plane, which reveals the strong interaction with the human body and acts as a reference in order to present the performance improvement of the wearable antennas shown later in this chapter.

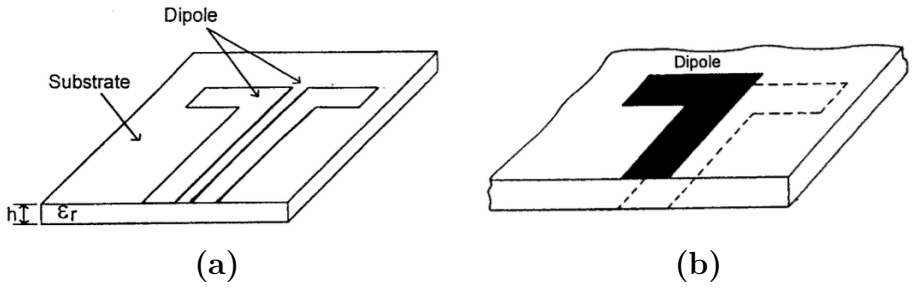

Figure 3.9 (a) Sketch of the coplanar dipole antenna and (b) opposite side dipole antenna [3].

The designed dipole antenna is comprised of two dipole folded arms printed on both sides of a Taconic PCB substrate, shown in Fig. 3.10. It is fed via a "parallel strip" line [17], printed on the opposite sides of the substrate, which is connected to the SMA connector at the side of the Taconic board. The design of the parallel strip line is simply related to the design of a microstrip line [3].

To achieve a good impedance matching for the side-fed design (instead of employing a probe-fed design), the parallel strip line was carefully designed at a length of a quarter-wavelength ($\lambda_g/4$) at the specific frequency of operation (2.45 and 5.8 GHz) to operate as an impedance transformer to match the center-fed dipole to the end-fed dipole impedance. The characteristic impedance of the quarter-wavelength transformer is found to be $Z_0 = 60.6\ \Omega$ (derived from: R_s(center-fed dipole)$\times R_p$(end-fed dipole)$= Z_0^2$) that matches the 50 Ω input impedance of the coaxial feeding line (R_p) with the folded dipole 73 Ω input impedance (R_s).

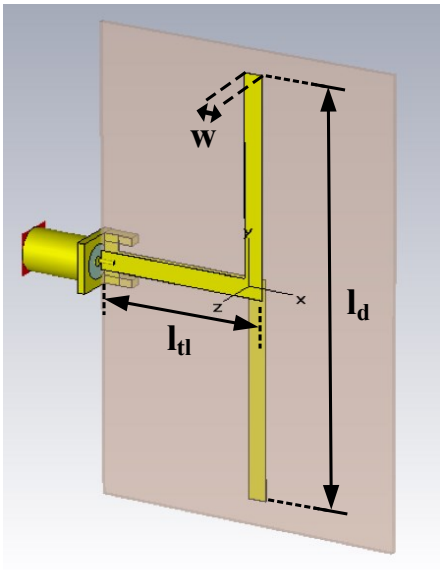

Figure 3.10 Design of printed dipole antenna in CST Microwave Studio.

However, this is a balanced feeding structure with equal and opposite currents flowing to the two parallel lines. In this case, a balanced-to-unbalanced (balun) transformer may be needed to match the unbalanced coaxial cable with the balanced parallel strips line and avoid currents to flow in the outer surface of the outer conductor of the coaxial cable and produce unwanted cable radiation.

To investigate the necessity of adding a balun structure to the printed dipole, the measured reflection coefficient (presented in Chapter 4) was investigated. Looking at the S_{11} results for 2.4 and 5.8 GHz (Fig. 3.12 and Fig. 3.13), no obvious effect on the resonance frequency and the level of S_{11} was spotted. This is explained mainly due to the presence of the quarter-wavelength parallel strip line between the coaxial cable and the dipole arms that offers a narrowband impedance matching. Hence, the use of a balun was not found necessary in this structure and was not fabricated.

The antenna dimensions have been optimised to operate in 2.4 GHz and 5.8 GHz ISM band, shown in Table 3.3.

Table 3.3 Antenna dimensions of the printed dipole antenna.

Frequency (GHz)	***Dimensions (mm)***		
	$\mathbf{l_d}$	$\mathbf{l_{tl}}$	**w**
2.4	54	22.3	2.4
5.8	23.3	10	1.8

3.5.2 EM Simulation Results

The simulation model of the printed dipole placed on the torso of two different numerical (homogeneous SAM and voxel HUGO) phantoms is shown in Fig. 3.11.

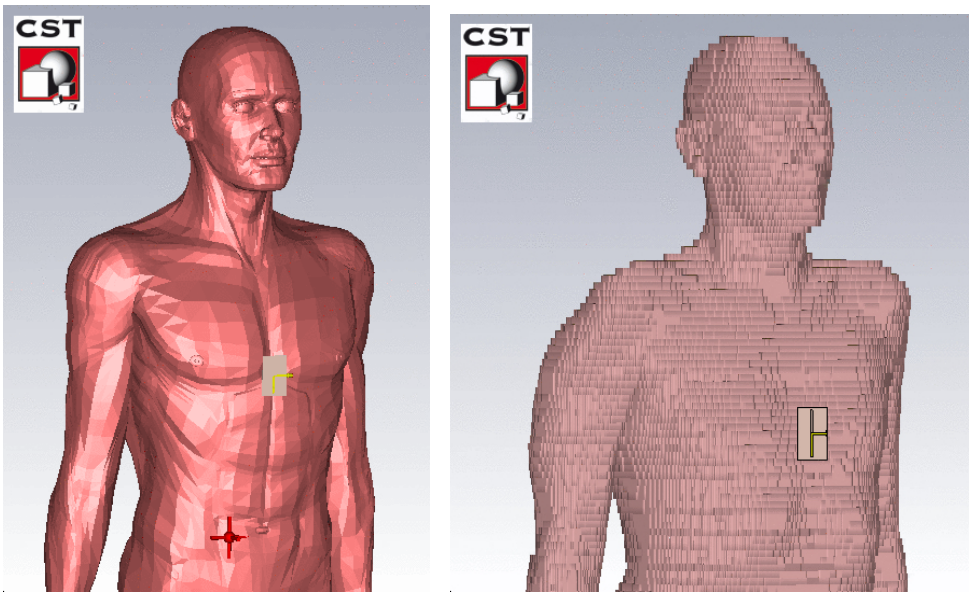

(a) (b)

Figure 3.11 Simulation model of printed dipole on (a) homogeneous SAM phantom and (b) voxel HUGO phantom in CST Microwave Studio.

A comparison of the $|S_{11}|$ performance of the printed dipole in free space and at different body phantoms is presented in Fig. 3.12 and Fig. 3.13 for 2.4 GHz and 5.8 GHz respectively. It is shown that there is a large resonance frequency detuning and $|S_{11}|$ degradation in respect to free space. This behaviour is expected since there is no ground plane in the printed dipole's design and half of the radiation pattern is facing the body surface.

More specifically, at 2.4 GHz (Fig. 3.12), frequency detuning (downshift) reaches 147 MHz when the antenna is placed at 10 mm from the surface of SAM phantom, with 15 MHz smaller detuning when the antenna is placed on voxel phantom. In terms of the level of $|S_{11}|$ of the printed dipole on the body, it is degraded but still remains lower than -20 dB. When the printed dipole is attached directly to the SAM phantom (0 mm separation distance), this effect is more significant with the level of $|S_{11}|$ reaching -11.5 dB but with a detuning of less than 65 MHz. Looking at the printed dipole's behaviour at 5.8 GHz (Fig. 3.13), the effect of resonance frequency

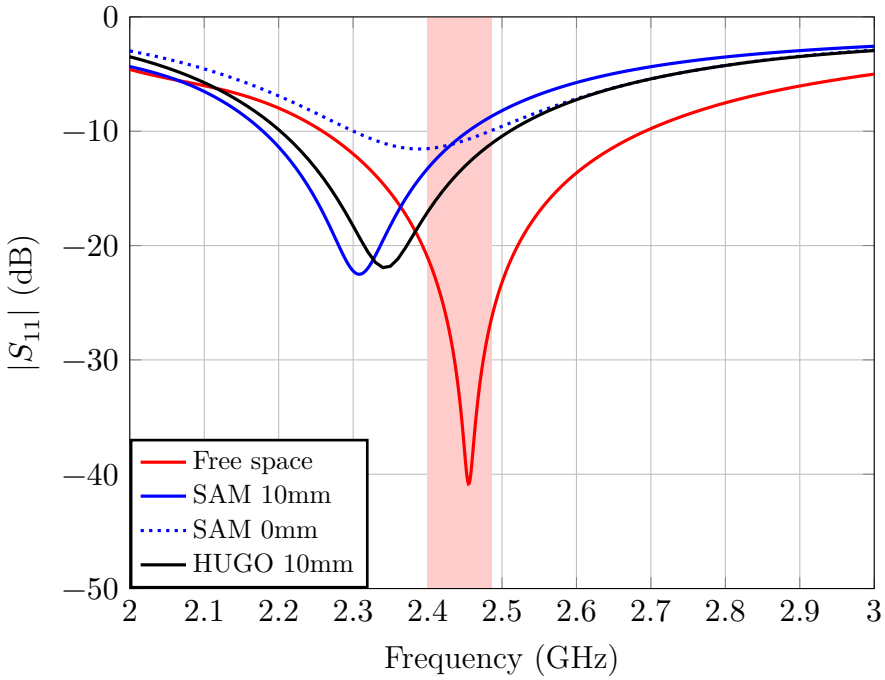

Figure 3.12 Reflection coefficient $|S_{11}|$ of printed dipole at 2.4 GHz.

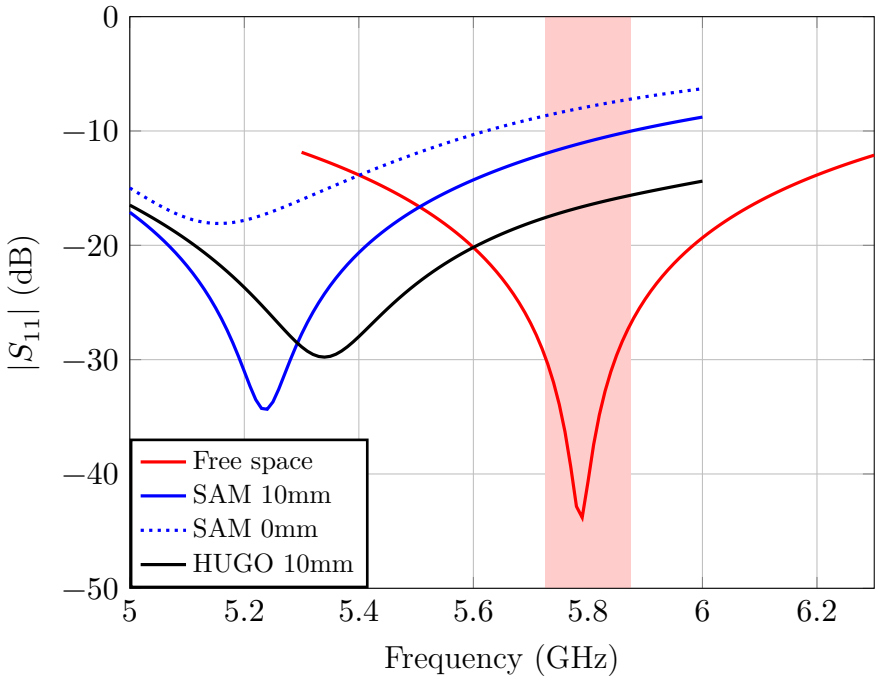

Figure 3.13 Reflection coefficient $|S_{11}|$ of printed dipole at 5.8 GHz.

detuning is more highlighted. However, at both frequency bands, the $|S_{11}|$ remains lower than the limit of -10 dB with the only exception in the case of 0 mm separation distance from human body at 5.8 GHz.

The far-field radiation patterns of the printed dipole antenna at 2.4 and 5.8 GHz are plotted in Fig. 3.15 and Fig. 3.16 respectively. To enable a better understanding of the following radiation patterns, a schematic of the azimuth (XZ-) plane including the body phantom, is plotted in Fig. 3.14. The radiation pattern of the printed dipole in terms of the radiated (IEEE) gain for co-polarised and cross-polarised components is compared among free space, on SAM phantom with two separation distances and on voxel phantom.

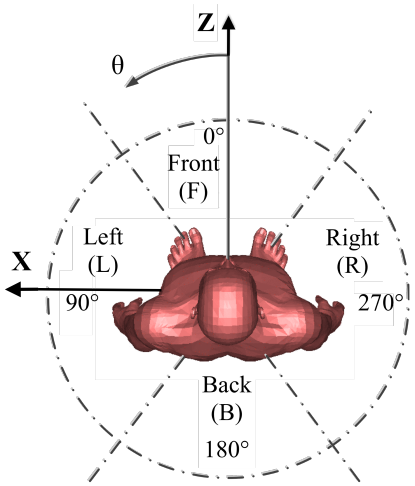

Figure 3.14 Schematic of the azimuth plane including body phantom.

More specifically, at 2.4 GHz, the effect of the antenna-body interaction is mostly denoted at the range between $\theta = 60^o$ to $\theta = 300^o$ (mostly at the backward direction) in the azimuth plane. The magnitude of degradation in the antenna gain from free space to on-body case, exceeds 20 dB due to the presence of human body. In the forward direction (F), ranging between $\theta = 300^o$ to $\theta = 60^o$, there is a close matching between free space and on-body cases. When the antenna is placed on the voxel phantom, a small gain increase is noticed while in the backward direction (B) the gain is sharply reduced at the direction of $\theta = 180^o$. When the antenna is placed flush against the SAM phantom (0 mm separation distance), the gain appears to be reduced by at least $5dB$ for every azimuth angle compared to the 10 mm separation distance.

Looking at the performance of the printed dipole at 5.8 GHz, the same interaction

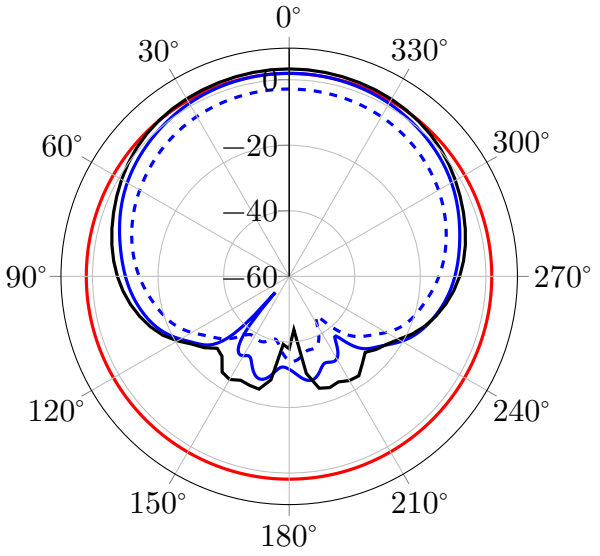

(a)

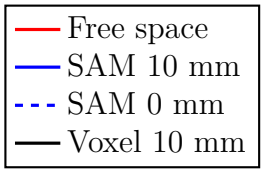

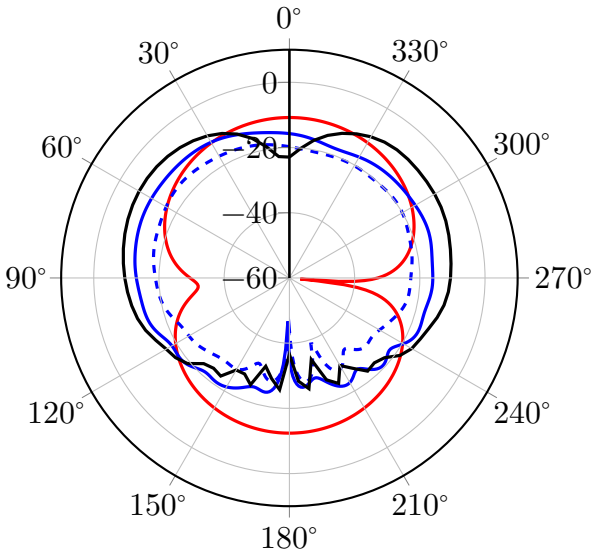

(b)

Figure 3.15 Far-field gain patterns (in dBi) of printed dipole in XZ (Azimuth plane) at 2.4 GHz. (a) Co-polarised and, (b) cross-polarised components.

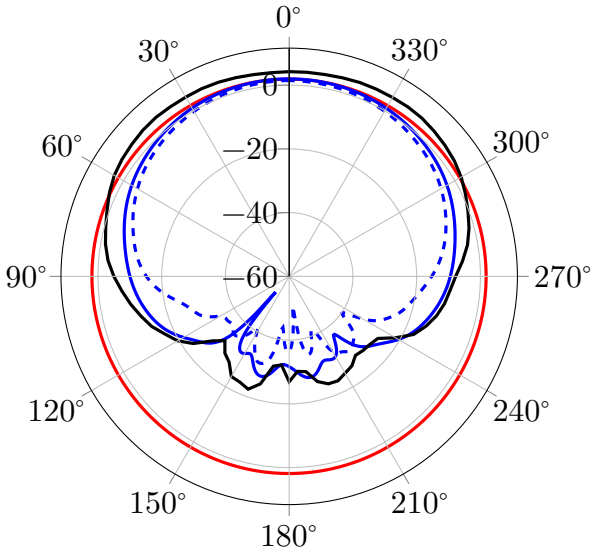

(a)

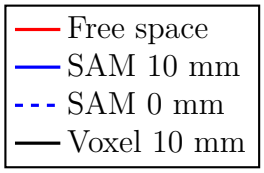

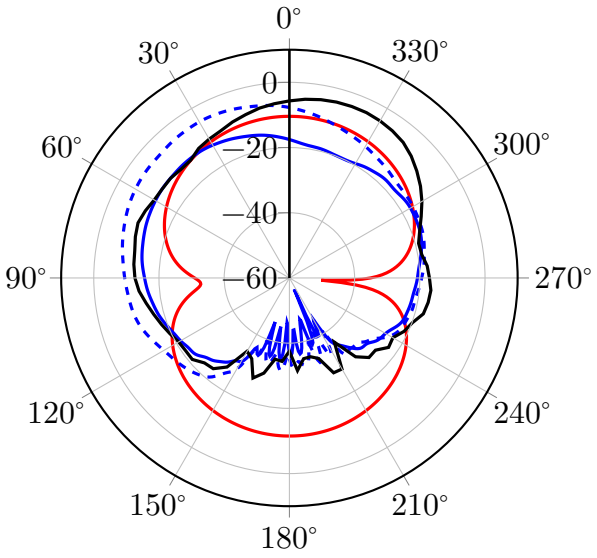

(b)

Figure 3.16 Far-field gain patterns (in dBi) of printed dipole in XZ (Azimuth plane) at 5.8 GHz. (a) Co-polarised and, (b) cross-polarised components.

is evident at the backward direction (B) between the SAM and HUGO phantoms. When the antenna is placed directly on SAM phantom (0 mm separation distance), at the forward direction (F) the gain appears almost the same with the free space, while for the rest of the pattern it is significantly degraded. When the antenna is placed on the voxel phantom, the gain appears higher than in the SAM phantom case for the whole azimuth cut and higher than the free space case only for the range between $\theta = 300^o$ to $\theta = 60^o$ (F).

3.5.3 Antenna Fabrication

The fabricated printed dipole prototypes for operation at 2.4 and 5.8 GHz are shown in Fig. 3.17. They have been fabricated from Taconic TLY-5 laminate by chemically etching the copper at both sides of the substrate. The 0.78 mm TLY-5 substrate material has an $\epsilon_r = 2.2$ and $\tan\delta = 0.0009$ with 0.035 mm copper metallisation layer in each side. A SMA jack connector is soldered at the side of the board feeding the printed dipole's parallel strips transmission line.

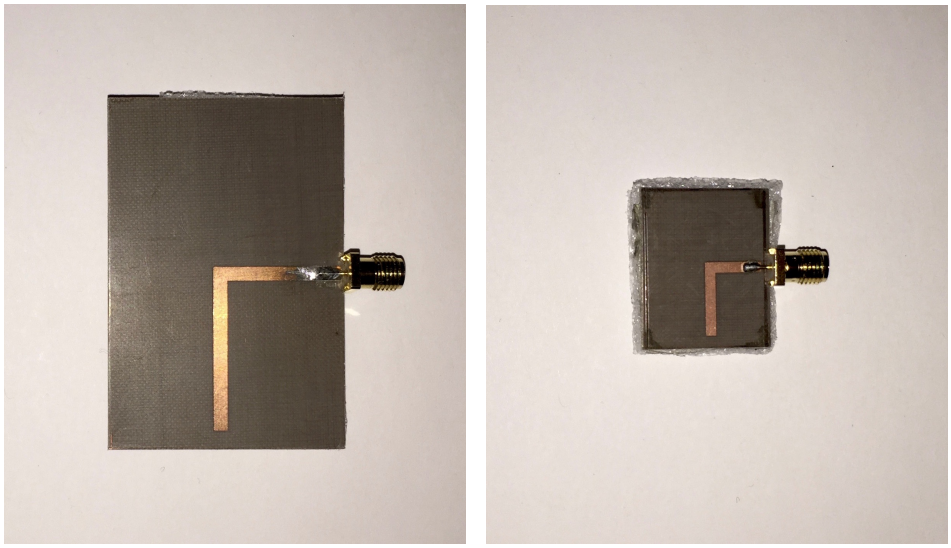

(a) **(b)**

Figure 3.17 Picture of the printed dipole antenna prototypes (a) at 2.4 and (b) 5.8 GHz ISM band.

3.6 Textile Higher Mode Patch Antenna

In this section, a textile higher mode microstrip patch antenna (HMMPA) is presented, which is an ideal candidate to be embedded in wearable devices for on-body communications. It is designed and fabricated in felt fabric material in probe-fed and side-fed realisations for operation at 2.4 and 5.8 GHz. The main purpose of employing this design is to realise a low-profile flexible wearable antenna with omnidirectional radiation characteristics on the surface of the human body.

3.6.1 Antenna Design

The higher mode microstrip patch antenna (HMMPA) had been initially proposed by Delaveaud in [18] as a "monopolar wire patch antenna" and was later adopted to on-body communications by Conway [19]. It excites an E-field perpendicular to the body surface, and radiates an omni-directional radiation pattern in the endfire direction ($\theta = 90^o$ and $\theta = 270^o$). According to the literature [2, 19], it has been shown that antennas which provide polarisation normal to human body surface can support the propagation of surface or creeping waves and are favourable for on-body communications. This polarisation can be also achieved by a wire monopole antenna above a ground plane, placed normal to the body surface, however due to its height is impractical for wearable applications. Hence, the HMMPA achieves the desired on-body performance while being compact, low-profile, lightweight and can be easily worn conformally to the body surface.

In [18, 20, 21], the HMMPA is analysed in terms of its equivalent circuit. The corresponding HMMPA geometry as designed in CST Microwave Studio, alongside with its equivalent circuit model are shown in Fig. 3.18a, b respectively. This kind of antenna is fed by a coaxial probe (feed) which is connected to the top hat through the ground plane and the dielectric substrate. Without shorting wires, the HMMPA acts as an in series RLC resonant circuit caused by the resistance ($R_{feed} \approx 50\Omega$) and inductance of the feed (L_{feed}), and the capacitance of the antenna (C_{patch}) formed by the top patch and the ground plane.

Adding a shorting wire, a short-circuit to the capacitance of the antenna is added that introduces a parallel inductance ($L_{ground,wire}$) on the capacitance . This creates a parallel resonance at a lower frequency than the classical fundamental mode of the patch ($\lambda/4$ instead of $\lambda/2$). The resonance frequency is smaller than the fundamental antenna mode by approximately a factor of 2. It is primarily set by the

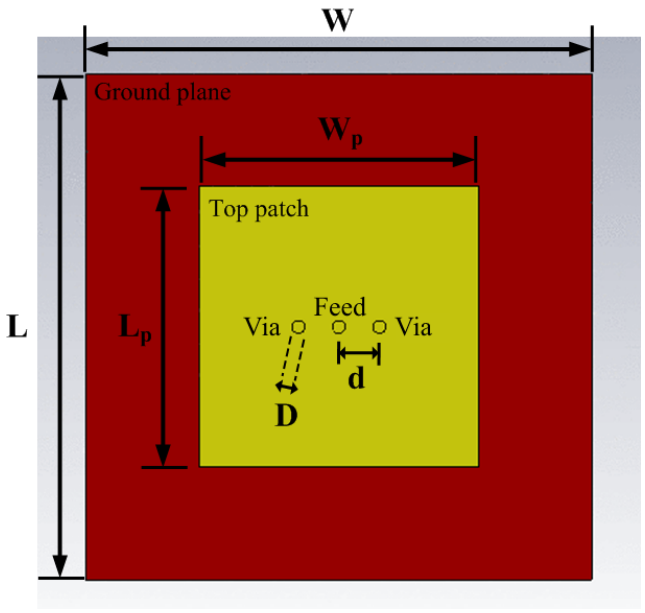

(a)

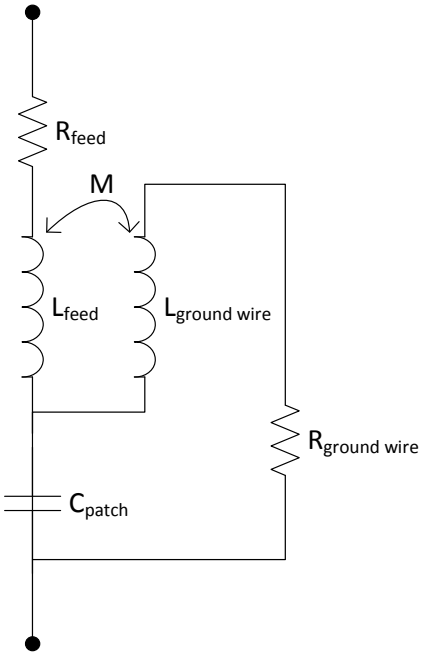

(b)

Figure 3.18 (a) Design of probe-fed HMMPA in CST Microwave Studio, and (b) its equivalent circuit model.

patch surface, the height and the permittivity of the substrate (capacitance of the antenna) and the number of ground wires (shunt inductance). However, the characteristics of the ground wires mainly have an effect on the magnitude of the parallel resonance. Therefore, the introduction of additional ground wires increases the number of physical parameters, and allows easier control of the real and imaginary part of the input impedance near the parallel resonance. This particular working mode is characterised by a high concentration of currents on the shorting wire. The resulting radiation pattern reveals a monopole-like radiation pattern.

This new kind of patch antenna reveals that a microstrip patch antenna with appropriately situated feeding and ground wire(s) can radiate an electromagnetic field omnidirectionally with very good efficiency for frequencies situated below the classical cavity resonance mode.

The main antenna parameters, and their effect on the equivalent circuit model, that influence the antenna input impedance are:

- The size of ground plane W. The larger the ground plane, the higher the radiation resistance due to the edge effects of the ground plane.
- The radius of ground wires D. The smaller the radius, the higher the real part of input impedance ($R_{ground,wire}$).
- The radius of the feeding probe. The larger the radius, the lower the imaginary part of input impedance ($X_{L,feed}$).
- The ground wire/ feeding probe separation d. The Q-factor increases when the distance between the ground wire and the feeding probe increases.
- The height and permittivity of the dielectric substrate influence the BW. The higher the substrate height and lower permittivity, the higher BW is achieved. So, by choosing felt as antenna substrate (low permittivity) a higher BW is obtained.

In the current study, the desired ("parallel resonance") mode is excited by using two shorting vias at an offset distance from the centre feed via. The centre feed via generates a maximum (peak) of the electric field amplitude while the two shorting vias force nulls (nodes) in the electric field. The theoretical electric field amplitude distribution below the radiating patch is drawn in Fig. 3.19, derived from EM simulation. It is observed that in X-axis direction, the electric field varies by one full cycle

while in the Y-axis varies by half cycle. No phase change in the electric field appears due to the $\lambda/4$ patch size.

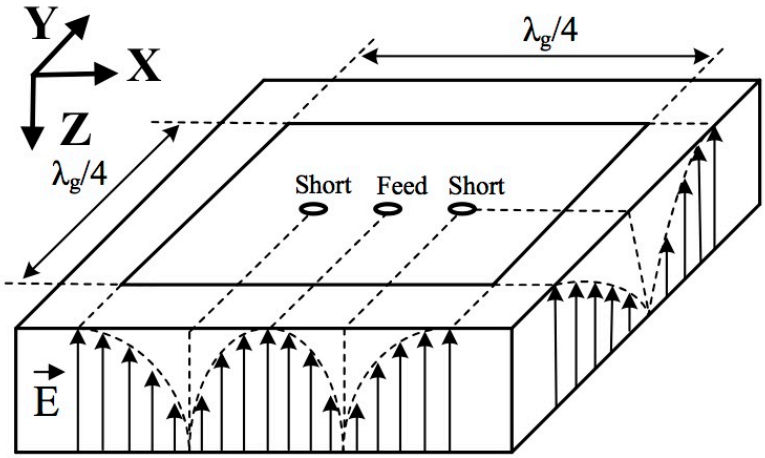

Figure 3.19 Theoretical electric field distribution of the "parallel resonance" mode of HMMPA antenna.

In order to achieve the exact resonant frequency, the patch size was properly adjusted, and impedance matching tuned by varying the distance between the shorting vias. Felt of 4.2 mm and 2.9 mm was used as the substrate for probe-fed and side-fed realisations respectively. The resulting antenna dimensions for operation at 2.4 GHz and 5.8 GHz are listed in Table 3.4.

Table 3.4 Dimensions of the probe-fed HMMPA antenna for operation at 2.4 GHz and 5.8 GHz ISM band.

Frequency	***Dimensions (mm)***					
	W	**L**	$\mathbf{W_p}$	$\mathbf{L_p}$	**D**	**d**
2.4 GHz	50	50	27.7	27.7	1.3	4
5.8 GHz	20	20	10.3	10.3	0.5/0.6	2.675

The HMMPA antenna has been initially designed as probe-fed antenna. However, the protruding SMA connector imposes some restrictions during the on-body simulation and measurement since its size ($\approx 10mm$) limits the minimum separation from the body surface. To overcome this limitation, a multilayer HMMPA antenna was designed by adding one more layer of felt (1 mm thick) for the microstrip line

feeding between the substrate and the ground plane to realise a side-fed design. The microstrip line is connected with the top patch using a pin via. The design of the side-fed HMMPA antenna at 2.4 GHz is shown in Fig. 3.20.

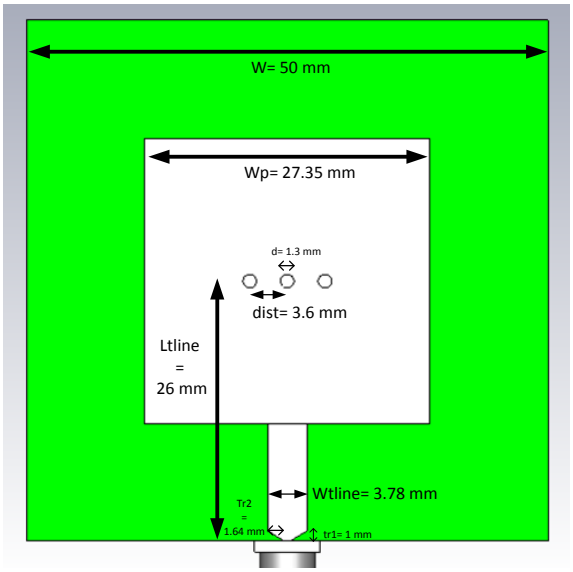

Figure 3.20 Design of side-fed HMMPA antenna in CST Microwave Studio.

3.6.2 EM Simulation Results

The side-fed HMMPA antenna is tested on SAM and HUGO numerical body models, as it is shown in Fig. 5.5.

The resulted $|S_{11}|$ of the HMMPA antenna, it is plotted for 2.4 GHz and 5.8 GHz operation in Fig. 3.22 and Fig. 3.23 respectively. Starting from 2.4 GHz frequency band, the narrowband performance of the patch antenna is noticed in free space with 70 MHz of -10dB bandwidth (BW). A negligible detuning effect is observed at the on-body cases since the ground plane minimises the interaction with the body. However, BW is slightly affected, by getting wider especially for the voxel case. At 0mm separation distance from SAM phantom, a larger detuning is noticed.

Moving to the 5.8 GHz band, the BW (400 MHz in free space) is found larger than in the 2.4 GHz frequency band for all the cases, exceeding the operational BW. The interaction with the body is stronger, which is explained by the higher body scattering effect due to the electrically larger body size in this frequency. This interaction is evident due to the large frequency detuning, which extends up to 250 MHz in the

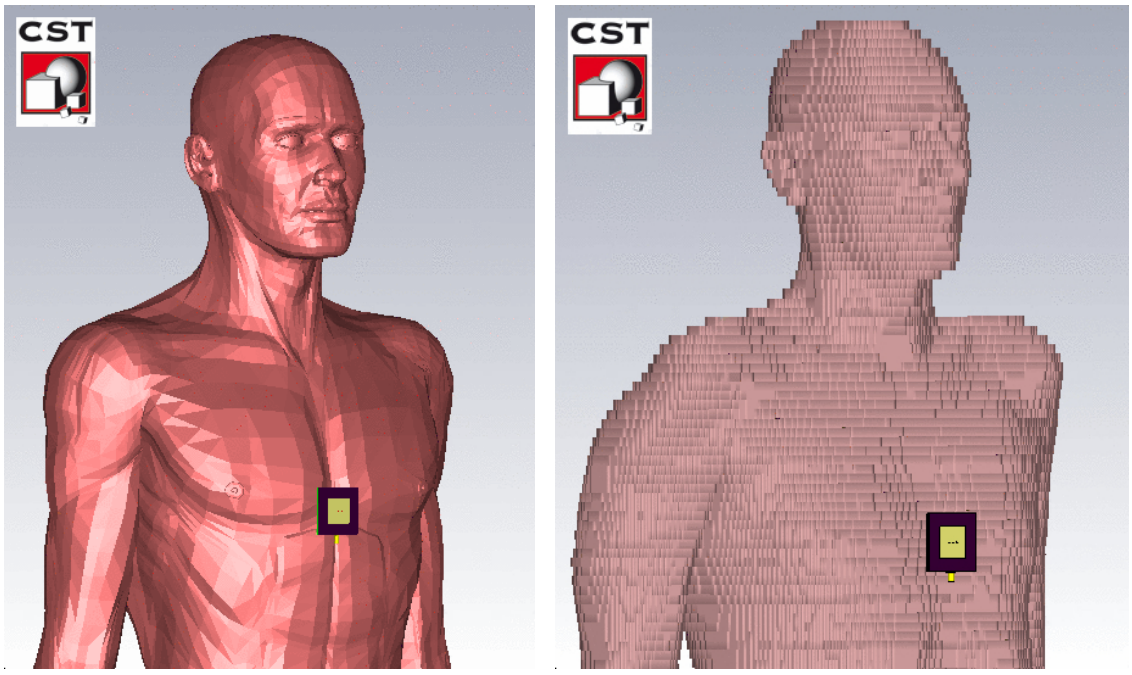

Figure 3.21 Simulation model of HMMPA antenna on (a) SAM and (b) HUGO voxel phantom in CST Microwave Studio.

case of 0mm separation distance from SAM phantom. It is then concluded that the screening property of the ground plane from the body in higher frequencies is less effective.

As far as the far-field patterns are concerned, the co-polarised and cross-polarised antenna gain is plotted in Fig. 3.24 for 2.4 GHz and in Fig. 3.25 for 5.8 GHz. Comparing the free space to on-body performance at 2.4 GHz, a minor difference can be observed in the null level at $\theta = 0^o$ (F), while a larger difference is spotted at the back lobe level (B). Due to the body absorption and body scattering to a part of the radiated field, back lobe level is reduced by at least 10 dB than in the free space case. This effect is more pronounced at the voxel phantom case. Accordingly, the cross-polarised component of the HMMPA on the voxel phantom at the forward direction (F) is found larger than the cross-polarised components at 0 mm and 10mm separation distance from SAM phantom, which remain below -20 dB. This increase of the cross-polarised component reveals the stronger interaction with the human body. The direction of maximum gain has also been affected due to the presence of the body. More specifically, it has been tilted from $\theta = 93^o$ in free space to $\theta = 70^o$

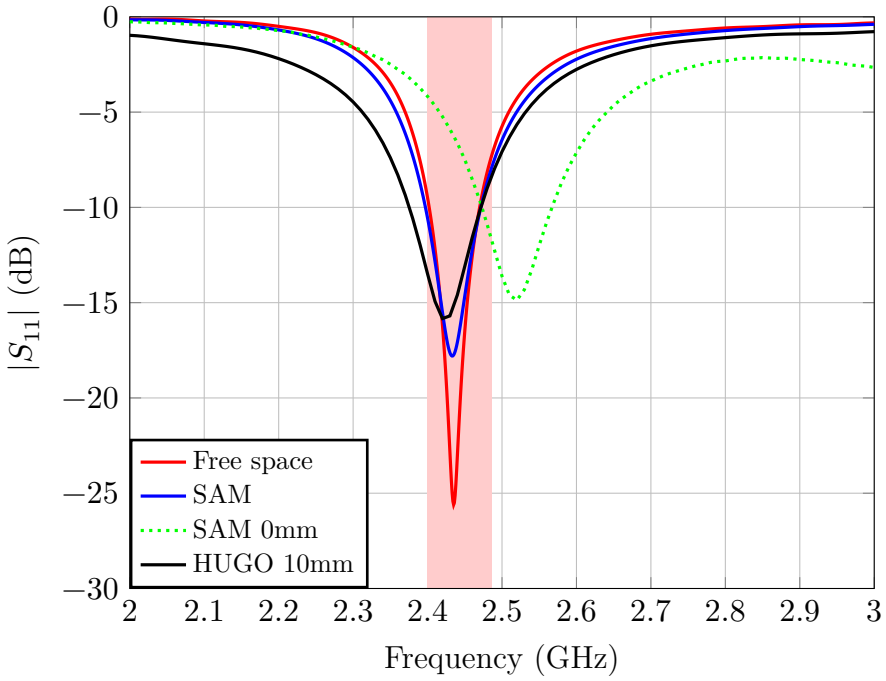

Figure 3.22 Reflection coefficient $|S_{11}|$ of HMMPA at 2.4 GHz ISM band.

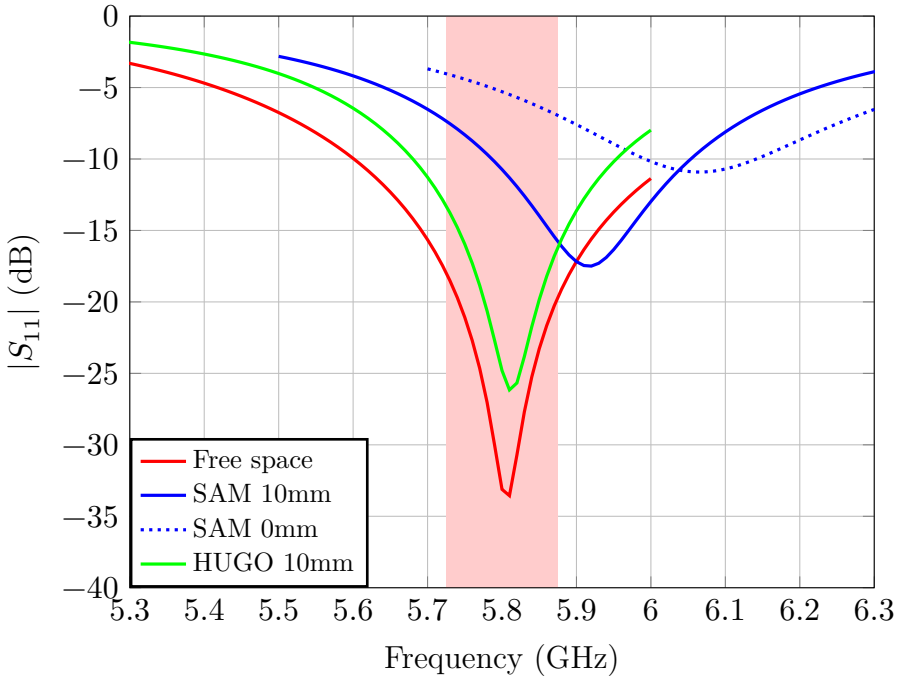

Figure 3.23 Reflection coefficient $|S_{11}|$ of HMMPA at 5.8 GHz ISM band.

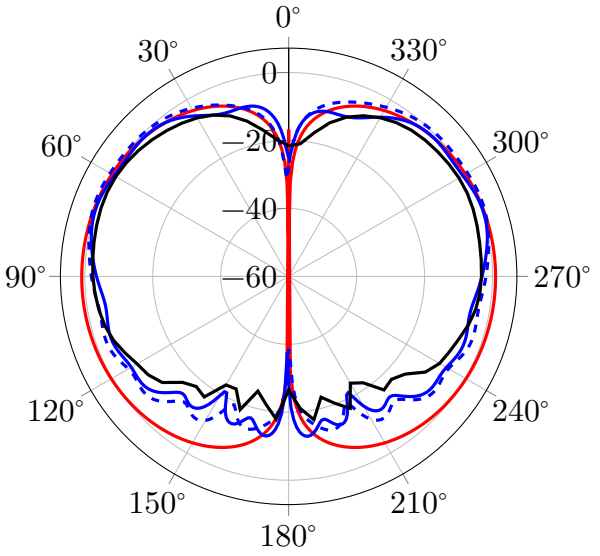

(a)

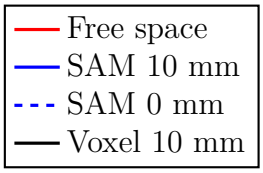

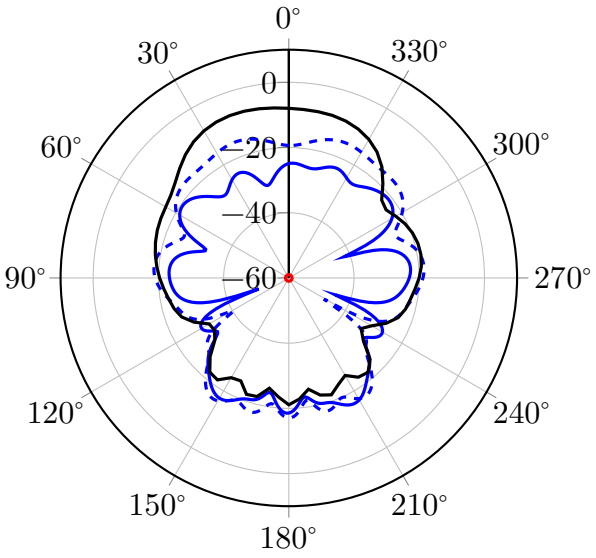

(b)

Figure 3.24 Far-field gain patterns (in dBi) of HMMPA in XZ (Azimuth plane) at 2.4 GHz. (a) Co-polarised and, (b) cross-polarised components.

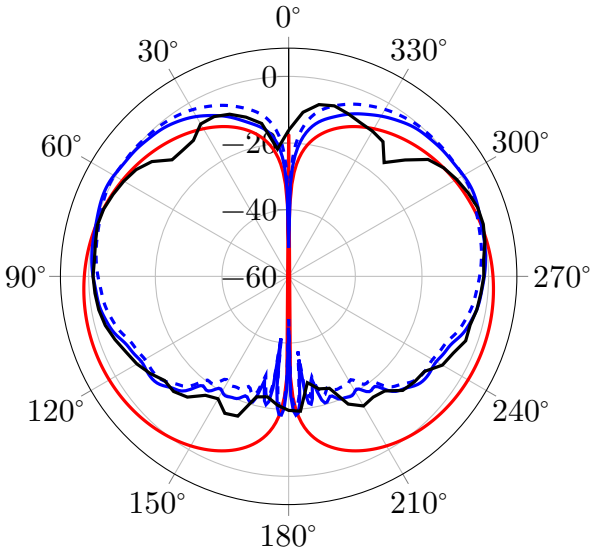

(a)

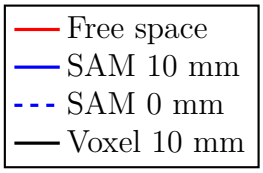

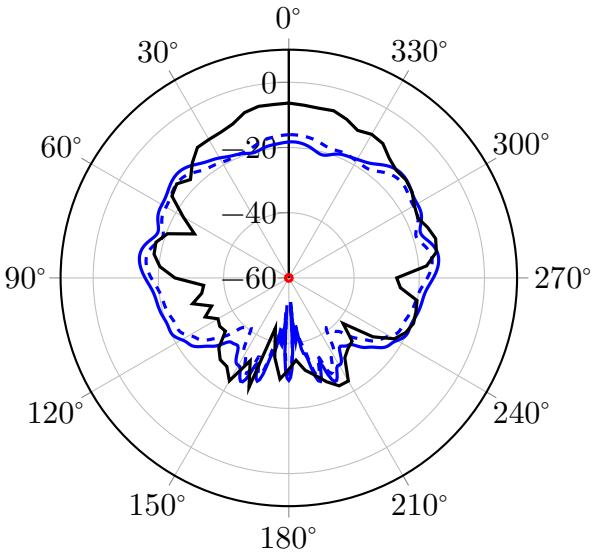

(b)

Figure 3.25 Far-field gain patterns (in dBi) of HMMPA in XZ (Azimuth plane) at 5.8 GHz. (a) Co-polarised and, (b) cross-polarised components.

on-body.

A similar radiation performance is found in the 5.8 GHz frequency band. The direction of maximum on-body gain remains at $\theta = 70^o$, although the back lobe level is even further reduced than in the 2.4 GHz case. The cross-polarised component regarding the SAM phantom is almost identical, which means than the proximity of the antenna to the body surface does not alter its radiation characteristics. A higher cross-polarised component is observed when the antenna is placed on the voxel phantom.

3.6.3 Antenna Fabrication

The fabricated HMMPA antenna prototypes are shown in Figs. 3.26a,b at 2.4 GHz and in Fig. 3.26c at 5.8 GHz. In all these three prototypes, the assembly process has been done manually. The copper sheet for the top patch and ground plane is cut with PCB milling machine (Fig. 3.26a), manually with scissors (Fig. 3.26b) and with chemical etching (Fig. 3.26c), according to the antenna dimensions listed in Table 3.4. For the antenna feeding, an SMA connector for (a,b) prototypes and a miniaturised U.FL cable for (c) prototype is used.

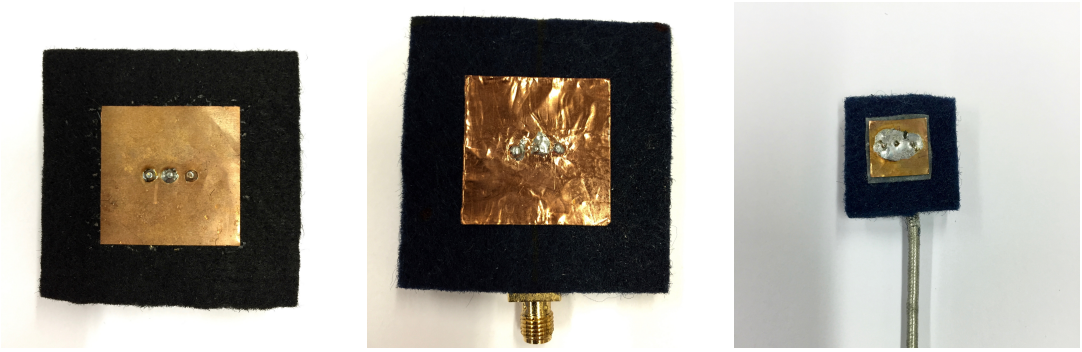

(a) **(b)** **(c)**

Figure 3.26 (a) Picture of the fabricated HMMPA antenna prototype for (a,b) at 2.4 GHz. (c) at 5.8 GHz ISM band.

The most difficult part during the antenna fabrication process is spotted at the precise placement and soldering of the feeding and shorting vias that play an important role in the antenna desired performance. This part is even more challenging for the 5.8 GHz HMMPA antenna where the antenna dimensions are extremely small and precision by hand is hardly achieved.

In Chapter 5, a multilayer fully-textile embroidered HMMPA antenna is proposed, which preserves the same radiation performance with more flexibility and integration to clothing while simplifying the manufacturing process and the vias realisation with conductive thread.

3.7 Textile Patch Antenna

The most popular patch antenna design, which is also advantageous for off-body communications, is the microstrip patch antenna (MPA) operating at the fundamental (TM_{01}) mode. It excites a broadside radiation pattern away from the body surface and, due to its large ground plane, the antenna remains almost unaffected from the body presence.

3.7.1 Antenna Design

The MPA antenna design for 2.4 GHz and 5.8 GHz operation is presented in Fig. 3.27a and Fig. 3.27b respectively together with the final dimensions, according to [1].

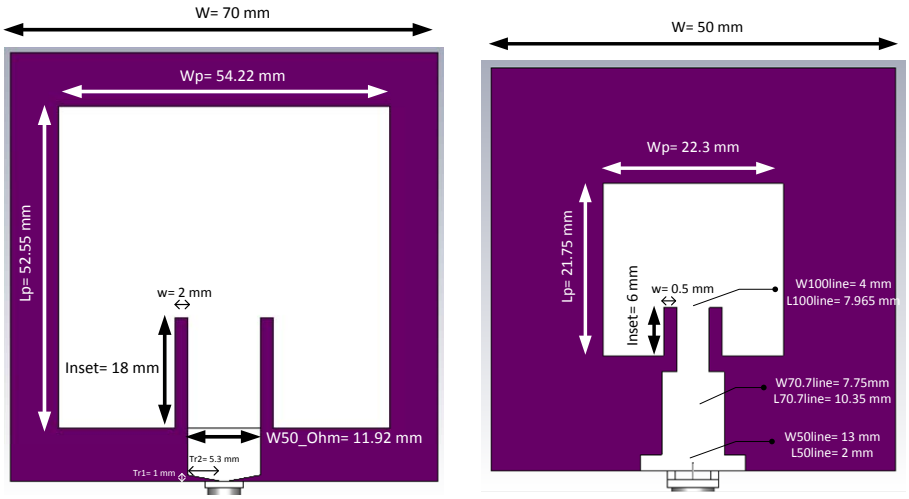

Figure 3.27 (a) Picture of the designed MPA antenna for (a) 2.4 GHz and (b) 5.8 GHz ISM band.

3.7.2 EM Simulation Results

The MPA antenna is tested on the SAM and HUGO numerical body models, as it is shown in Fig. 3.28. The $|S_{11}|$ performance is shown in Fig. 3.29 and Fig. 3.30 for 2.4 GHz and 5.8 GHz respectively. It is observed that the $|S_{11}|$ of the patch antenna remains unaffected when it is placed close to the body surface due to the large ground plane. However, this antenna characteristic is not seen at 5.8 GHz, where frequency detuning takes place. This result can be explained by the fact that the body is electrically larger at higher frequencies, as it happens with the HMMPA.

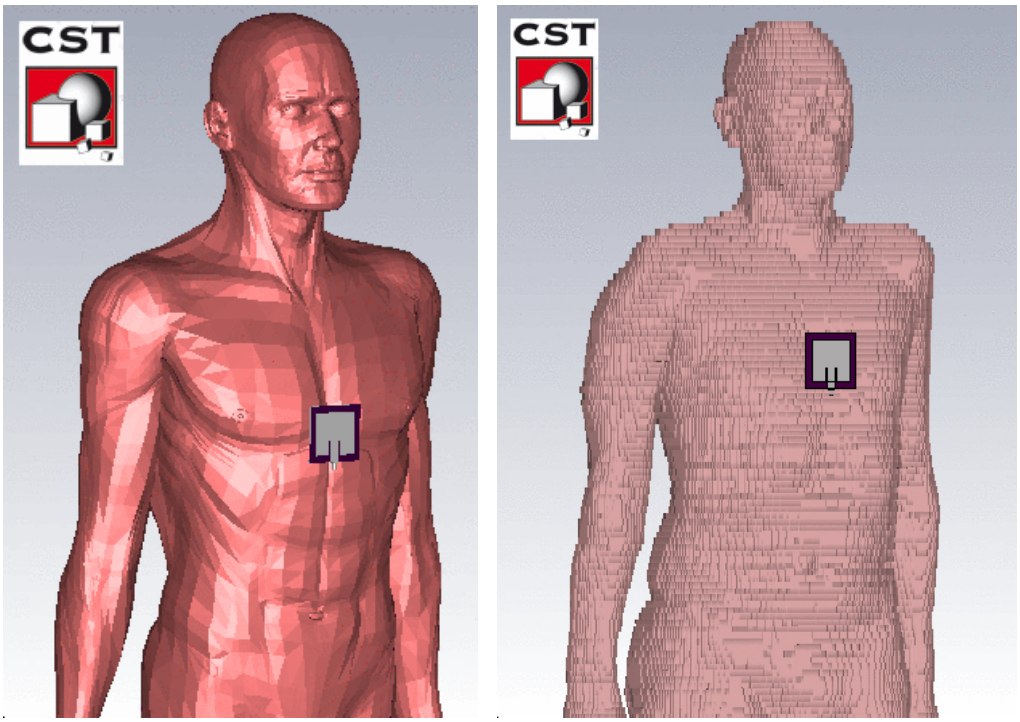

Figure 3.28 Simulation model of MPA antenna on (a) SAM and (b) HUGO voxel phantom in CST Microwave Studio

Looking at the radiation performance of the patch antenna at 2.4 GHz (Fig. 3.31a), no difference is observed at the front part (F) of the radiation pattern between the free space and on-body cases. The antenna-body interaction is mostly evident in the backward direction (B) of the radiation pattern. A small degradation of less than 15 dB is observed in contrast to printed dipole antenna (Section 3.5), where

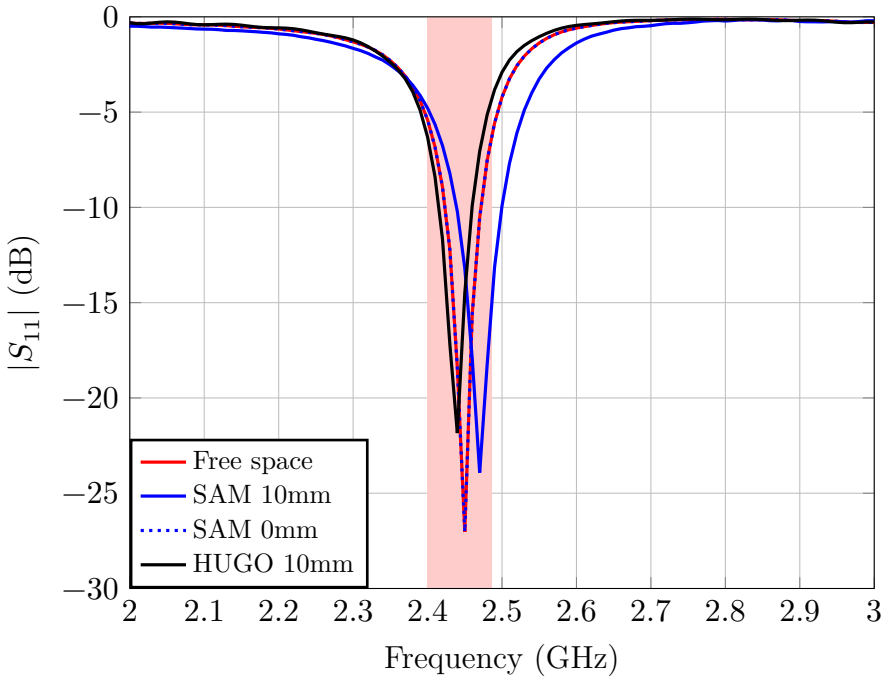

Figure 3.29 Reflection coefficient $|S_{11}|$ of MPA at 2.4 GHz ISM band.

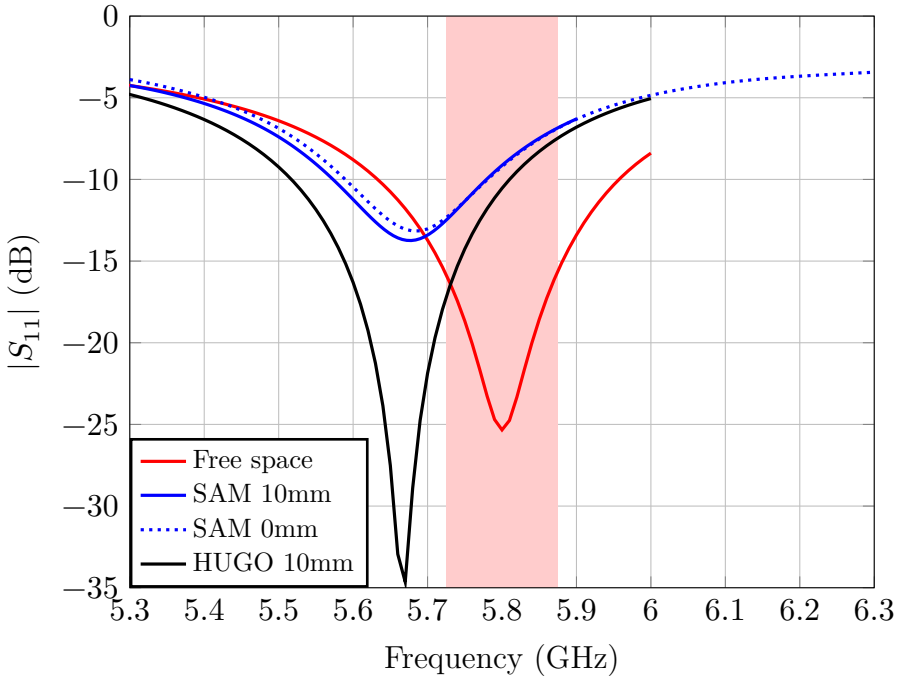

Figure 3.30 Reflection coefficient $|S_{11}|$ of MPA at 5.8 GHz ISM band.

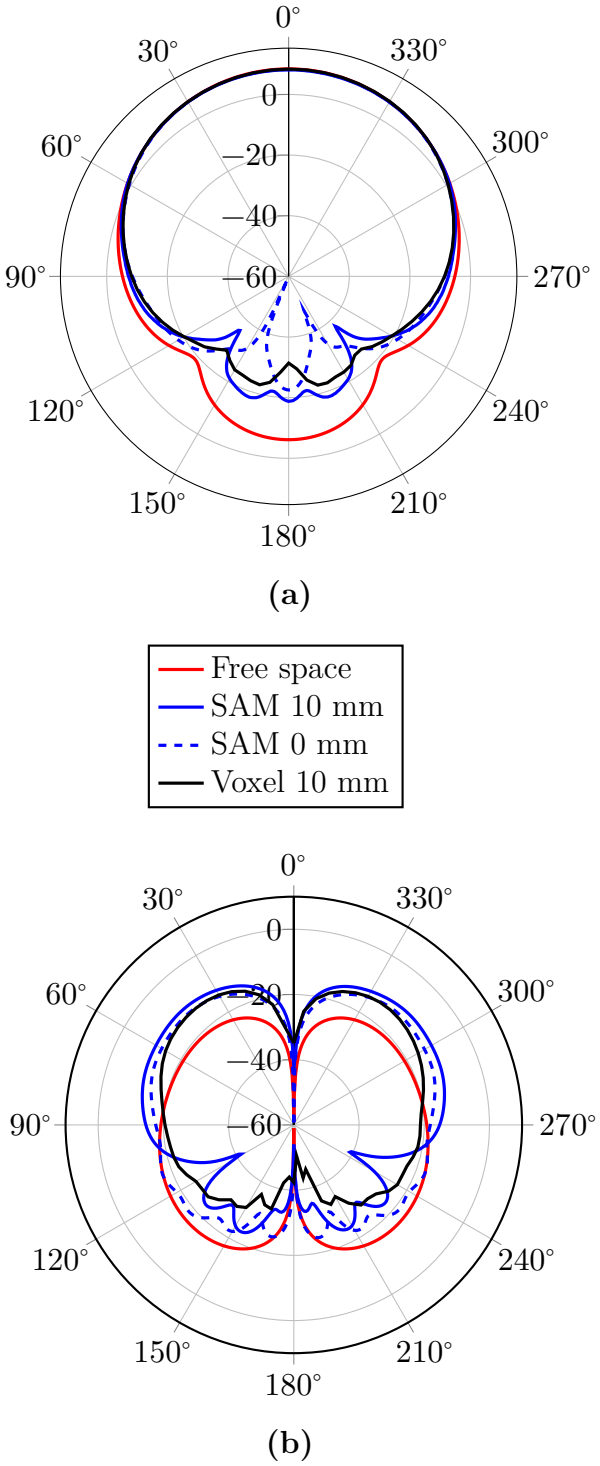

Figure 3.31 Far-field gain patterns (in dBi) of MPA in XZ (Azimuth plane) at 2.4 GHz. (a) Co-polarised and, (b) cross-polarised components.

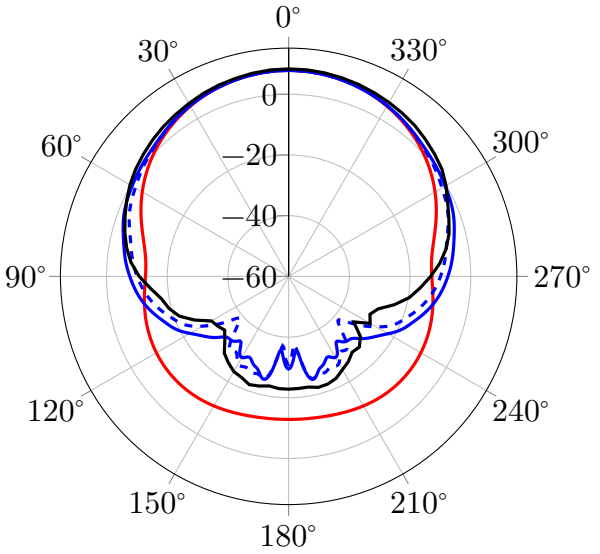

(a)

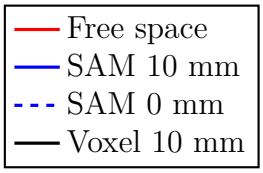

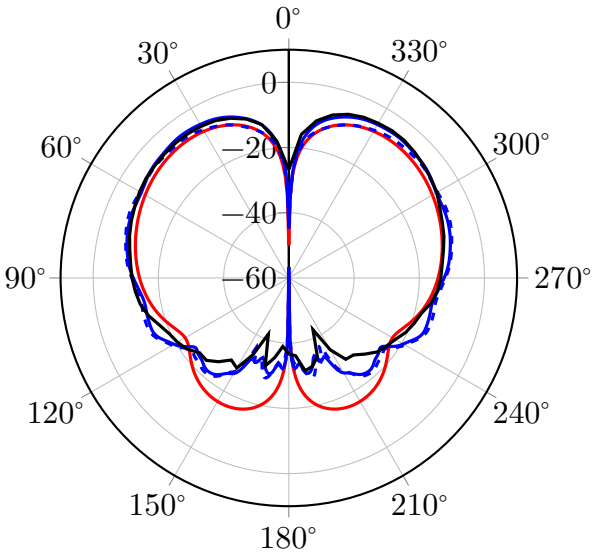

(b)

Figure 3.32 Far-field gain patterns (in dBi) of MPA in XZ (Azimuth plane) at 5.8 GHz. (a) Co-polarised and, (b) cross-polarised components.

a reduction of 30 dB was found. In terms of the cross-polarised component of the on-body cases (Fig. 3.31b), it is increased by 10 dB in respect to free space but still remains 20 dB lower than the equivalent co-polarised component. As far as the 5.8 GHz is concerned, both the co- and cross-polarised components remain unaffected at the front part (F) of the radiation pattern, for both free space and on-body cases. Although, a broadening of the main lobe can be spotted. At the back part (B) of the radiation pattern, the interaction with the body is increased in respect to 2.4 GHz. It is then concluded that the maximum MPA antenna gain is not affected, although the level of body absorption is increased from the 2.4 GHz case, where the size of ground plane is large enough in respect to body.

3.7.3 Antenna Fabrication

For the MPA antenna fabrication, copper sheet and felt are used. The fabricated prototypes are shown in Fig. 3.33a and Fig. 3.33b for 2.4 GHz and 5.8 GHz respectively. For the case of 2.4 GHz, manual cutting of the top and bottom conductive parts was employed while in the 5.8 GHz, etching was used in order to achieve a better precision.

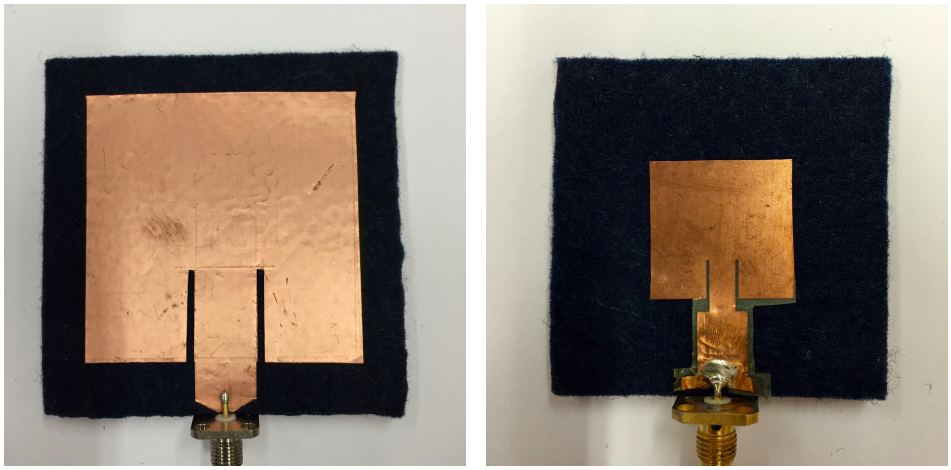

(a) **(b)**

Figure 3.33 Picture of the fabricated MPA antenna operating at (a) 2.4 GHz and (b) 5.8 GHz ISM band.

3.8 Conclusions

Two textile wearable antenna prototypes are presented in this chapter starting from the textile materials selection and dielectric characterisation, up to the fabrication. A printed dipole antenna is also fabricated and used as a reference antenna. Simulation results are provided in order to gain an understanding on the wearable antennas' interaction with the human body. To simulate the human body, a homogenous SAM phantom and a detailed voxel HUGO model are employed and compared. It is shown that by using the homogenous SAM phantom, an accurate modelling of the wearable antenna on the human body is achieved that closely matches the performance on the detailed voxel HUGO model, avoiding the increased computational complexity.

More specifically, in respect to printed dipole's performance on the human body, a large resonance frequency shift and radiation pattern degradation in the backward direction are spotted on the simulation results. This behaviour is expected due to the absence of ground plane shielding as well as the omni-directional shape of the radiation pattern that result to a significant absorption of a part of the radiated power inside the body.

In the case of the textile patch antennas, the frequency detuning effect and radiation pattern distortion are limited due to the presence of ground plane. Nevertheless, in the case when HMMPA antenna is directly attached on-body (0 mm separation), a strong frequency shift is noticed, moving the BW of operation outside of the ISM band. The far-field radiation pattern of HMMPA is reduced by at least 10 dB in the back lobe level due to the body proximity while the direction of maximum is tilted from parallel to body surface to 20^o outwards. Although, the omni-directional radiation pattern shape of HMMPA antenna, parallel to body surface, is maintained that makes it suitable for on-body communications. As for the MPA antenna performance, it remains unaffected from body presence at 2.4 GHz while a noticeable frequency detuning is found at 5.8 GHz. The far-field radiation pattern remains unaffected due to the ground plane presence. It is then concluded that patch antennas preserve their radiation characteristics when attached on the body, however the impedance matching can be affected in some cases. This can be explained from their inherent narrowband performance that can move outside of the operational bandwidth for even small resonance frequency shifts.

Some challenges in the fabrication process of textile antennas are also presented, which are mainly focused in the case of HMMPA antenna where shorting vias need to

be precisely placed for the proper excitation of the higher-order mode. In general, the assembly process becomes challenging in the 5.8 GHz due to the shorter wavelength and consequently antenna size, which makes even a small inaccuracy in the antenna dimensions, significant in the resulted antenna performance.

In the following chapter, the fabricated antennas will be tested with the proposed near-field measurement method for wearable antenna assessment on a full-body anthropomorphic phantom.

References

[1] C. A. Balanis, *Modern Antenna Handbook*, 1st ed. (John Wiley & Sons, Inc., Hoboken, NJ, USA, 2008).

[2] P. S. Hall and Y. Hao, *Antennas and Propagation for Body-Centric Wireless Communications. Second Edition*, 2nd ed. (Artech House, Inc., 2012).

[3] R. Garg, *Microstrip antenna design handbook* (Artech House Library, 2001), pp. 400–401.

[4] G. A. Conway, W. G. Scanlon, and D. Linton, "Low-Profile Microstrip Patch Antenna for Over- Body Surface Communication at 2.45 GHz," IEEE 65th Vehicular Technology Conference, 2007. VTC2007-Spring. pp. 392–396 (2007).

[5] H. R. Khaleel, *Innovation in Wearable and Flexible Antennas* (WIT Press , 2007), pp. 1–215.

[6] Y. Ouyang and W. J. Chappell, "High frequency properties of electro-textiles for wearable antenna applications," IEEE Transactions on Antennas and Propagation **56(2),** 381–389 (2008).

[7] *Nora Dell-CR Conductive Metallized Nylon Fabric*, Available online: http://www.shieldextrading.net/pdfs/NoraDell%20CR.pdf.

[8] B. S. Cook and A. Shamim, "Inkjet printing of novel wideband and high gain antennas on low-cost paper substrate," IEEE Transactions on Antennas and Propagation **60(9),** 4148–4156 (2012).

[9] D. Liu, U. Pfeiffer, J. Grzyb, and B. Gaucher, *Advanced Millimeter-Wave Technologies: Antennas, Packaging and Circuits* (Wiley, 2009), Chap. 5.

[10] J. Krupka and R.G. Geyer and J. Baker-Jarvis and J. Ceremuga, "Measurements of the Complex Permittivity of Microwave Circuit Board Substrates Using Split Dielectric Resonator and Resonant Cavity Techniques," In *7th International Conference on Dielectric Materials Measurements & Applications*, pp. 21–24 (Bath, UK, 1996).

[11] *CST Microwave Studio ™, Transient Solver*, Available online: https://www.cst.com/Products/CSTMWS/Solvers/TransientSolver.

[12] E. Salahun, P. Queffelec, M. L. Floc'h, and P. Gelin, "A broad-band permeameter for "in situ" measurements of rectangular samples," IEEE Transactions on Magnetics **37(4),** 2743–2745 (2001).

[13] Z. N. Chen, *Antennas for Portable Devices* (2015), pp. 1–290.

[14] C. Gabriel, "Tissue equivalent material for hand phantoms," Physics in Medicine and Biology **52(14),** 4205 (2007).

[15] D. Andreuccetti and R. Fossi, "Dielectric properties of human tissues: definitions, parametric model, computing codes," Technical report, N.TR/ICEMM/13.00, IFAC-CNR, Firenze (2000) .

[16] *MCL-T whole-body solid SAM phantom*, Available online: http://www.mcluk.org/solid_bodies.php.

[17] H. A. Wheeler, "Transmission-Line Properties of Parallel Strips Separated by a Dielectric Sheet," IEEE Transactions on Microwave Theory and Techniques **13(2),** 172–185 (1965).

[18] C. Delaveaud, P. Leveque, and B. Jecko, "New kind of microstrip antenna: the monopolar wire-patch antenna," Electronics Letters **30(1),** 1–2 (1994).

[19] G. Conway and W. Scanlon, "Antennas for Over-Body-Surface Communication at 2.45 GHz," IEEE Transactions on Antennas and Propagation **57(4),** 844–855 (2009).

[20] B. Jecko and C. Decroze, "The Monopolar Wire Patch Antenna concept," In *Antennas and Propagation, 2007. EuCAP 2007. The Second European Conference on*, pp. 1–5 (2007).

[21] L. Huitema and T. Monediere, *Progress in Compact Antennas* (InTech, 2014), pp. 1–212.

Chapter 4

Cylindrical Near-Field (CNF) Measurements of Wearable Antennas

In this chapter, the potential of the cylindrical near-field scanning technique to the characterisation of wearable antennas is demonstrated. A cylindrical near-field (CNF) measurement method is proposed, using the available near-field chamber facility at Loughborough University, to facilitate the complete assessment of wearable antennas on the human body. Since the use of live human subjects is limited due to practical reasons, a full-body anthropomorphic SAM phantom is employed, calibrated to simulate accurately the human body dielectric (and geometrical) properties up to 6 GHz. The novelty of the proposed measuring system is that offers the full-body characterisation of wearable antennas in contrast to conventional far-field systems that have been proved useful only for small size approximate body phantoms. The required measurement time and space of the measurement facility are also reduced. The 3D radiation pattern and the installed antenna gain and efficiency are readily produced after near-field to far-field transformation. These are important parameters for optimising wearable system design (for example optimise the communication link between an on-body sensor with an external mobile device) through accurate link budget calculations. This measurement system can be used as a repeatable test-bed for evaluating the performance of wearable antennas. The accuracy is retained for any antenna-body tissue separation distance and on-body location. Thus, wearable antenna designs can be optimised with the aim of achieving better impedance matching,

less radiation pattern distortion and absorption in the human body.

The fabricated wearable antenna prototypes, presented in the previous chapter, are measured using the proposed CNF method at 2.4 and 5.8 GHz ISM bands. These two frequency bands are commonly used in wireless networks (WLAN), such as Bluetooth and Wi-fi, in the Industrial, Scientific and Medical (ISM) band. The majority of the wearable devices in the market operate in these bands. It is investigated how the antenna gain and radiation efficiency are affected from the frequency dependent electromagnetic properties of the biological tissue and the relative electrical size of the body. The measured antenna radiation patterns and near-field patterns are presented, with the latter graphically presented in the outline of human body.

In Section 4.1, an introduction to near-field measurement techniques is presented, with emphasis on the cylindrical technique. Afterwards, in Section 4.2, the proposed CNF measurement setup is described in detail, together with the EM simulations setup that are used to indicate the measurement accuracy. Thus, near field and far field measurement results of the reference printed dipole are compared with EM simulations and discussed in Section 4.3. The effect of different antenna polarisation and on-body location is also included in this section. In Section 4.4, the MPA and HMMPA wearable antennas are investigated in terms of their near field and far field performance on the body surface. It will be shown that this measurement methodology can adequately describe the majority of the wearable antenna types. Moreover, in Section 4.5, the mean effective gain of wearable antennas is also calculated in order to characterise their performance in realistic off-body propagation conditions. Finally, in Section 4.6, conclusions are drawn.

4.1 Introduction

In order to evaluate the installed performance of low gain wearable antennas [1] in the presence of the human body, it is essential to measure the radiation pattern over a full sphere. With conventional far-field measurement techniques [2] it is cumbersome (both due to mechanical and time constraints) to capture a sufficient number of radiation pattern cuts that can accurately determine antenna performance parameters, such as the radiation efficiency. This is due to the majority of the roll-axis positioners, which are essential for the rotation of the antenna in the elevation plane, cannot handle the heavy weight ($\approx$ 90 Kg) and the size of a full-body phantom.

In the case of the cylindrical near-field measurement technique, which appears

as a cost-effective solution and easy to implement, the far-field radiation pattern is obtained after scanning on a cylindrical surface that encloses the antenna under test. No special positioning systems are required, as in the case of conventional far-field measurements, which offers the possibility of testing wearable antennas on a full-size body phantom. It can adequately capture the majority of antenna locations with the same setup without the need to change the phantom's orientation. Moreover, the measurement time and the volume of the measurement facility are reduced, rather than in the spherical near-field configuration that requires a lengthy process to acquire a sufficient amount of data over the sphere.

The similarity between the cylindrical scanning surface and the human body shape, which is considered as part of the antenna under test, seems to be reasonable. The cylindrical near-field system is ideal to study the close proximity interactions between wearable antennas and the human body by plotting the near field values in an equidistant surface close to the human body. The closer to the body surface the near-field is recorded, the higher the possibility to capture surface and scattered waves, in addition to space waves. After applying the near-field to far-field transformation, the 3D radiation pattern is obtained together with the on-body gain and radiation efficiency of the wearable antenna.

Despite these advantages, this measurement technique includes an inevitable truncation error in the resulting far-field radiation pattern that restricts the valid far-field region to elevation angles below $\phi = \pm 90^o$ [3]. This is attributed to the finite cylindrical scanning surface that after being transformed to a sphere in the far-field domain, fails to produce accurately the field at the extreme elevation angles of the sphere. Hence, an error in the calculation of directivity by using the pattern integration method may occur and consequently to the resulted radiation efficiency.

Therefore, this technique for wearable antennas performance assessment will be inappropriate in the case of:

- High gain antennas pointing the maximum radiation at the top or bottom faces of the measurement cylinder, e.g. for satellite applications.
- Low gain antennas that radiate significant amount of energy at high elevation angles. However, this behaviour of low gain antennas might be decreased in the presence of human body due to the increased body scattering effect.

In the current study, a cylindrical near-field measurement technique is employed, by using the available cylindrical near-field measurement facility at Loughborough

University. A solid full-body specific anthropomorphic mannequin (SAM) phantom is used to replicate human body and minimise the measurement uncertainty. A method of qualifying wearable antennas on the human body by assessing the near-field and far-field results is adopted and evaluated. The suitability of the measurement method would be assessed for antennas with different radiation characteristics. Its accuracy would be tested only with EM simulations in terms of the resulted directivity, gain and radiation efficiency, since no other measurement facility was available at that time. In order to investigate the antenna performance for various possible applications, several antenna locations are selected as each body part introduces different dielectric loading and interaction with the antenna [4].

The fabricated antenna prototypes (one printed dipole and two wearable antennas) exhibit different radiation properties and polarisation in respect to body surface. The printed dipole antenna is used as a reference antenna in horizontal and vertical polarisations, both parallel to body surface. As far as the wearable antennas under test are concerned, the microstrip patch antenna (MPA) and the higher-mode microstrip patch antenna (HMMPA) are used. The MPA antenna [5] is favourable for off-body communications as it excites a broadside radiation and, due to its ground plane, it remains almost unaffected from the body presence. The HMMPA antenna has a normal-to-body polarisation and radiates omni-directionally across the body surface that makes it useful for on-body communications [6].

4.2 CNF Measurement Setup

The cylindrical near-field measurement technique is based on the probe-corrected cylindrical near-field theory that was developed by Leach et al. [7] at Georgia Institute of Technology in 1973. A few years later, Yaghjian [8] developed the cylindrical transformation from near-field to far-field using a scattering-matrix approach.

The cylindrical near-field measurement is primarily used to produce the 3D far-field antenna radiation pattern. This is done by taking two orthogonal measurements of the E-field amplitude and phase on the desired cylindrical grid in the near-field range of the AUT, and after transformation, the far-field radiation of the AUT is obtained.

4.2.1 Scanner Geometry

The cylindrical near-field measurement system inside the anechoic chamber includes a linear scanning axis positioner (Y-slider) and an azimuth (θ^o) turntable. A schematic representation of the cylindrical near-field measurement system is shown in Fig. 4.1 [3] and the developed system at Loughborough University in Fig. 4.2.

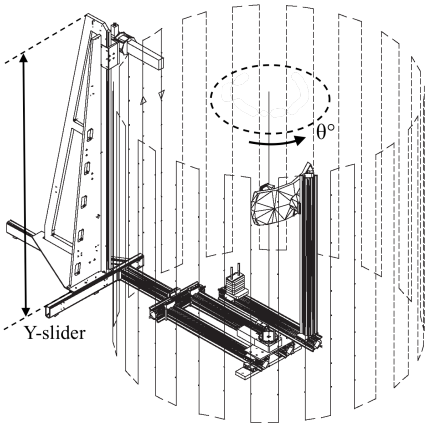

Figure 4.1 Schematic of the cylindrical near-field measurement configuration, showing the scanning probe and the antenna under test [3].

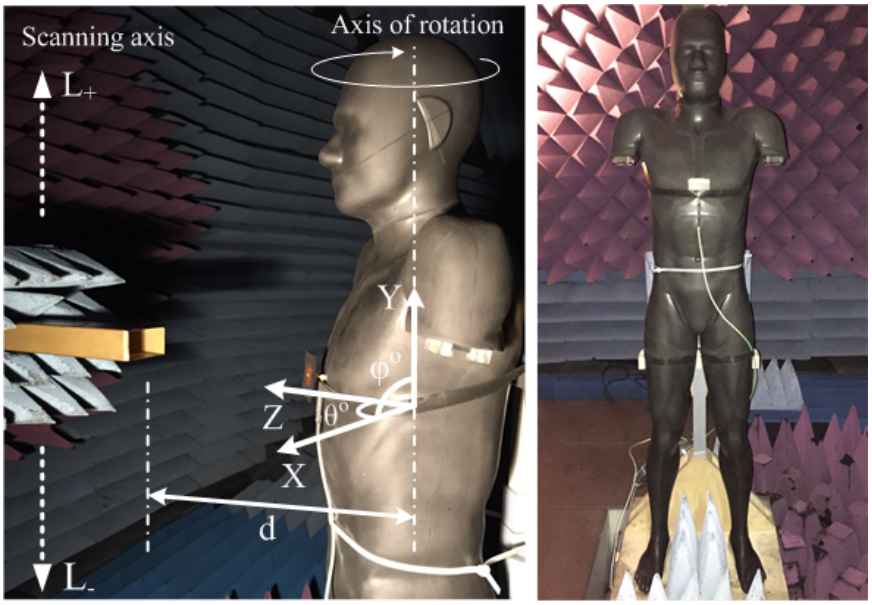

Figure 4.2 (a) Cylindrical near-field measurement setup for characterising antennas on-body at Loughborough University. (b) Full-body SAM phantom.

An open-ended rectangular waveguide probe (WR-430 for 2.4 GHz and WR-187 at 5.8 GHz) attached on the Y-slider is connected at the Tx port of a vector network analyser (VNA). The antenna under test (AUT) is placed on the surface of the SAM phantom. It is connected at the Rx port of the VNA and is rotated in azimuth using the turntable. The VNA is configured as follows: a 100 Hz IF BW and 6 dBm Tx- power are selected, while a dynamic range of more than 90 dB is provided. By rotating the waveguide probe by 90^o, two orthogonal E-field components are measured (in amplitude and phase) in the near-field range of the AUT. The full control of the VNA and the synchronisation of the linear and azimuth axis positioners is achieved by using the Orbit Midas acquisition software [9] to capture the near-field in a cylindrical surface around the AUT. After the completion of the near-field measurement, a near-field to far-field transformation is applied by using the software's transformation code. The transformation code based on a fast Fourier transform (FFT) uses the theoretical or measured probe radiation patterns to apply a correction to the acquired near-field data.

After the NF-FF transformation, the 3D far-field radiation pattern of the AUT on the SAM phantom is calculated [3]. The antenna directivity is then calculated via the pattern integration method over the full sphere using the transformed far-field results. To determine the actual gain of the AUT, the measuring probe's gain (via direct method) or a standard horn antenna's gain (via gain transfer method) is required. In this study, the measured gain is extracted from the direct method by using the probe's gain and the transformed far-field peak ratio of the received power at the AUT aperture to the input power at the probe, while subtracting the cable losses. The workflow, which is followed in every CNF measurement is shown in Fig. 4.3 [3].

4.2.2 Antennas Placement on SAM Phantom

The wearable antennas tested with the cylindrical near-field measurements are shown in Fig. 4.4. The fabricated antenna prototypes are placed in two different distances from the surface of the phantom (0 and 10 mm). The separation distance of 10 mm, using a Rohacell spacer, is selected as a commonly used distance due to the presence of clothing. The direct placement of the antenna on the body is also investigated as many wearable applications require the sensor in contact with the body surface [10].

Ideally, a physical body phantom should couple to the electromagnetic field of the

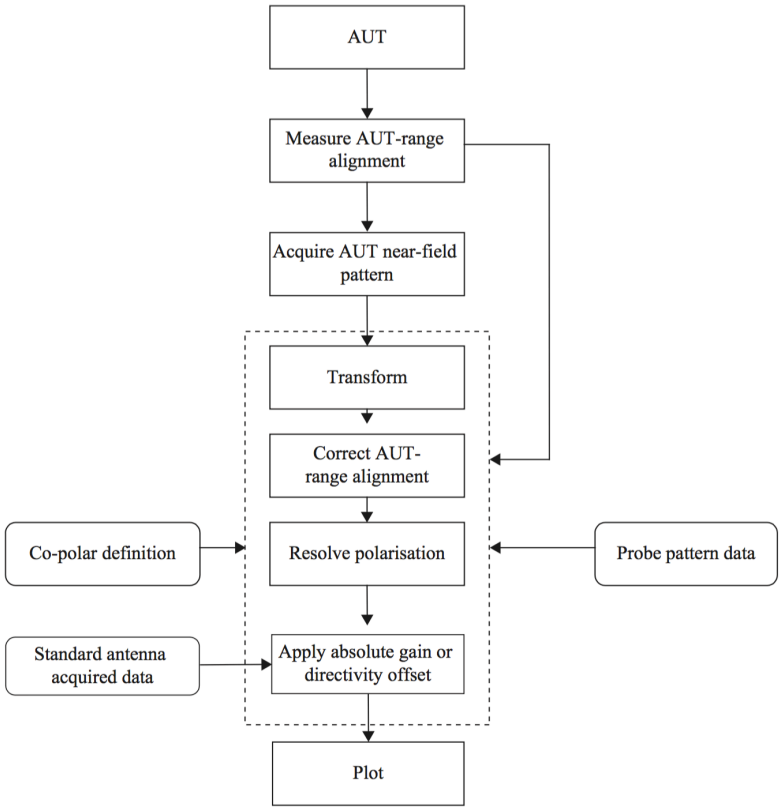

Figure 4.3 Workflow of the cylindrical near-field measurement procedure [3].

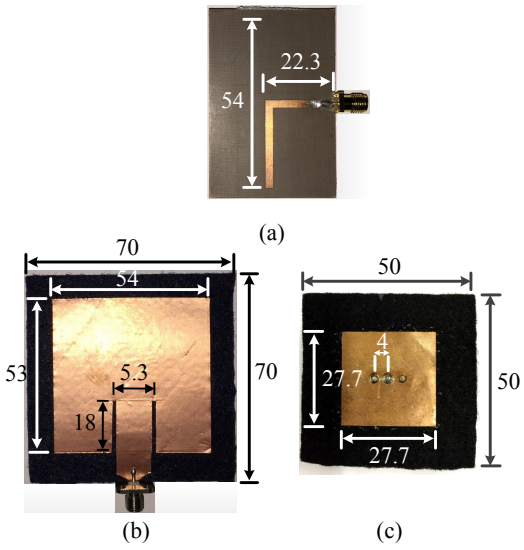

Figure 4.4 Antenna prototypes fabricated to operate at 2.4 GHz ISM band (a) printed dipole, (b) MPA and (c) HMMPA. Dimensions are shown in mm.

antenna in the same way and to the same extend as the human body. In the case of direct contact between the transceiver and the phantom's surface, the interaction is in the near field of the antenna and the coupling is mostly inductive rather than capacitive; that is, the magnetic field induces currents on the body surface. The capacitive coupling is less effective because of the high relative permittivity of the body tissue.

The solid SAM phantom is useful for applications such as radiation pattern testing, in contrary to a liquid-filled phantom that is useful for SAR testing. The advantages of a solid phantom are: its robustness, indefinite shelf life and wide frequency range (130 MHz- 6 GHz). The full-body SAM phantom is shown in Fig. 4.5a and the several body parts, which is consisted of, are shown in an exploded view in Fig. 4.5b. The phantom, which is manufactured by MCL-T [11] with geometrical characteristics

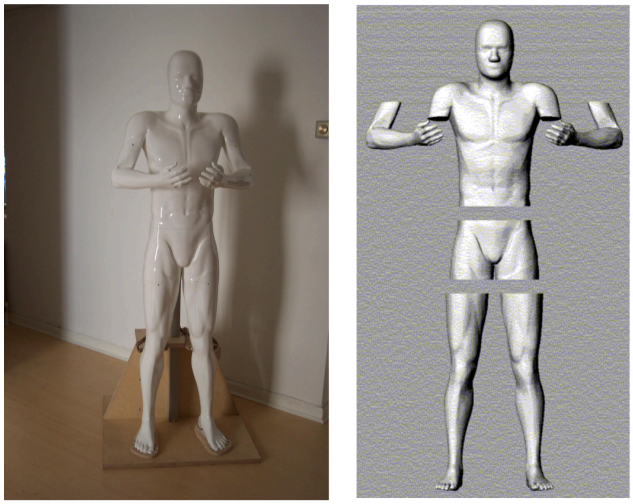

(a) **(b)**

Figure 4.5 Picture of MCL-T SAM phantom. (a) Full size view with supporting stand, (b) exploded view of connecting body parts [11].

according to the IEC62209-2 standard, is made of carbon-loaded silicone rubber with dielectric properties that match body tissue properties over a wide frequency range (30 MHz- 6 GHz). The dielectric properties of the phantom material, plotted in Fig. 4.6, follow the MCL-T broadband tissue-equivalent recipe which is based on 2/3 muscle tissue properties, found in [11].

The phantom dimensions are: 187 cm in height with waist and chest circumference 89 and 98 cm respectively. The upper torso and head is one section, the pelvic

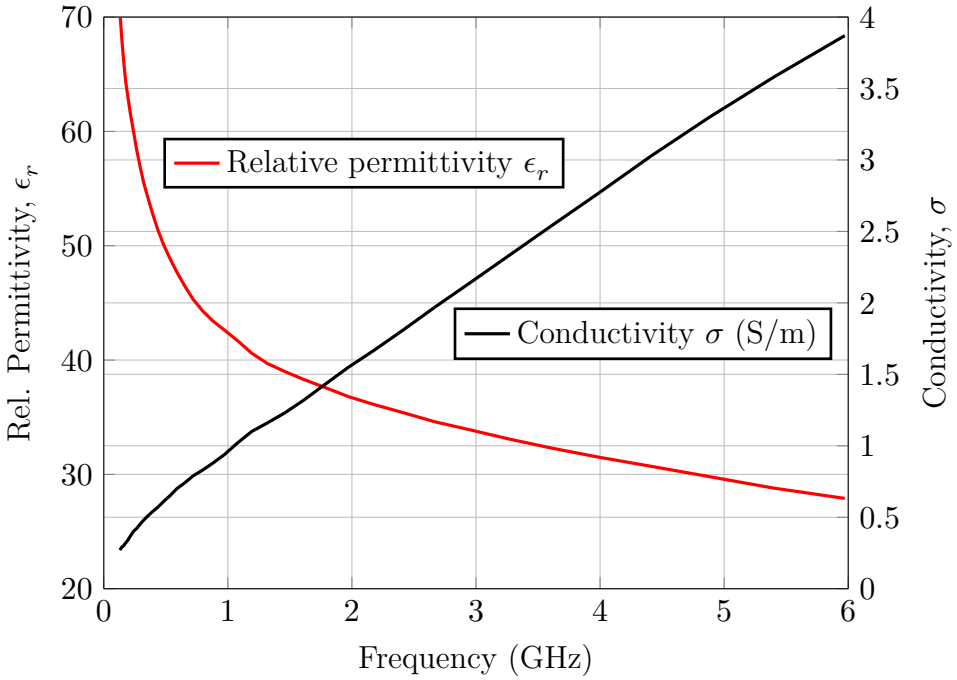

Figure 4.6 Dielectric properties of the SAM phantom up to 6 GHz [11].

region another and the arms and legs also are removable. A CAD file describing the phantom's shape is also available, and this can be imported into computational models. The whole-body phantom dimensions are listed in Table 4.1.

Arms were not available at that moment and as a result they are not included in the measurements. However, if they were included, they could be problematic for the accurate characterisation of wearable antennas placed on chest. The reason is that since the arms are bent inwards to the torso surface (as shown in Fig. 4.5), they could behave as a near-field scatterer that would lead to unpredictable results in the radiation pattern owing to multipath reflections between arms and body surface. Thus, by not including the arms in the near-field measurements, an unrealistic body posture is avoided.

By using a body phantom instead of a real volunteer no random dynamic effects such as body and/or respiratory movements take place that could introduce systematic measurement errors. Hence, the repeatability of the measurements is guaranteed.

Table 4.1 SAM phantom full-body dimensions

Dimensions	***(cm)***
Height	187 (200 on stand)
Toe-toe horizontal	23
Leg length	83
Circumference at waist	89
Circumference at chest	98
Shoulder width	53
Shoulder- top of head	27
Volume	(**Litres**)
Head & Torso	38
Torso lower	17
Leg (each)	7.5
Arm (each)	1.9
Total body	73.8

4.2.3 Alignment of Probe-AUT

Proper alignment of the AUT's aperture with the scanning probe's aperture is crucial in near-field measurements. Positioning tolerances are more strict than in far-field measurements. As a common practice, the positioning accuracy should be at the order of $\lambda/50$ to achieve $\pm 1dB$ accuracy for a side lobe level of -35 dB. To ensure the positioning accuracy, laser tracking for centering the probe's aperture (Z'-axis) with the AUT's aperture (Z-axis) is used (Fig. 4.7), at it is schematically shown in Fig. 4.8. A perfect alignment is achieved in three stages. At first, in the case of a linearly polarised probe antenna the electrical polarisation axis has to be aligned to the X' or Y' axis, respectively. This is achieved by using a spirit level at the top of the open-ended waveguide probe and rotate it until it is aligned. To align the linearly polarised printed dipole with its X or Y axis, a visual setup is done but the final inspection is completed in the final stage. In the second stage, the AUT is rotated using the turntable until the AUT aperture (Z- axis) matches with the probe's aperture (Z' axis) at $\theta = 0^o$. To achieve this, the vertical laser beam has to point at the centre of the AUT (both the phantom and the antenna), shown in Fig. 4.7a. In the final stage, the Y-slider is adjusted in order the X'Z' plane matches with the AUT's XZ plane at the 0 mm level of Y-axis (Fig. 4.7b). To do this, the horizontal laser's beam is used.

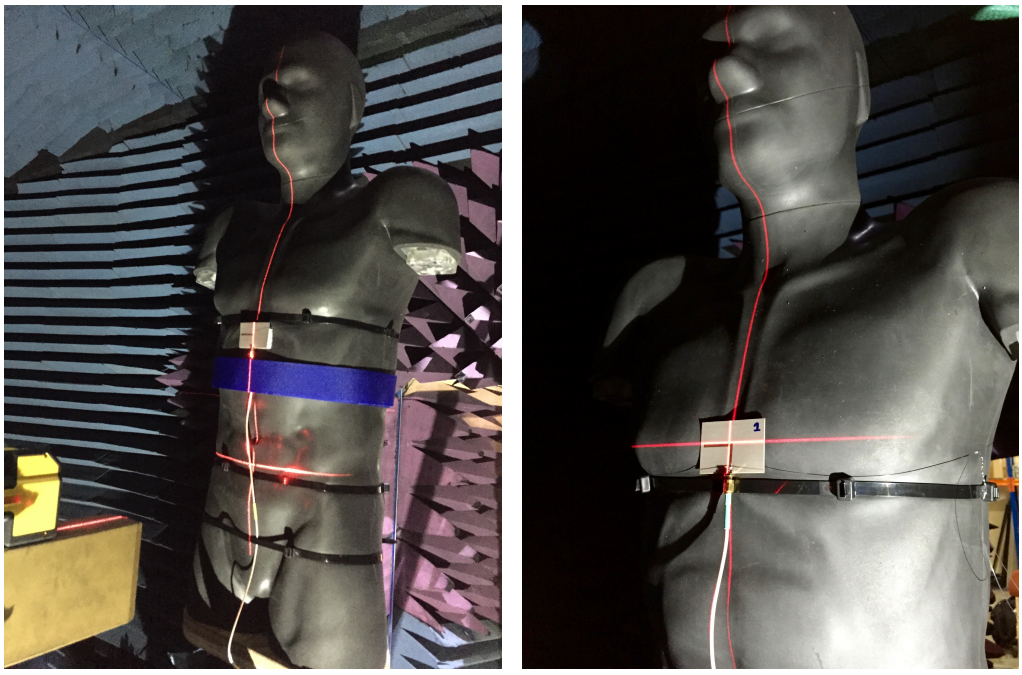

(a) (b)

Figure 4.7 Probe-AUT alignment with laser tracking (a) at the Y-axis, and (b) at XZ- plane

.

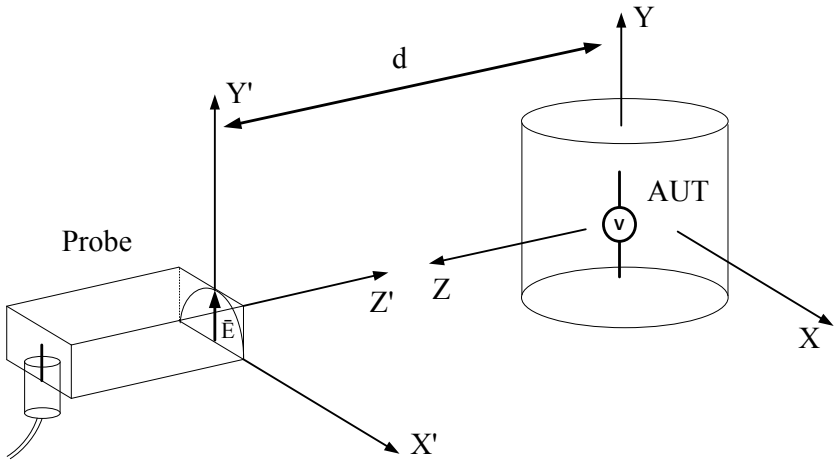

Figure 4.8 Schematic showing the desirable alignment between probe and AUT.

4.2.4 Scan Area and Sampling

To determine the sampling step of the near-field measurement, the "IEEE Recommended Practice for Near-field Antenna Measurements" [12] is followed together with [13]. Taking into account the cylindrical geometry and Nyquist criteria, the sampling step should satisfy the following: (a) in azimuth $\Delta\theta \leq \lambda/2\alpha$ ($= 22.9^o$ for 2.4 GHz and $= 9.5^o$ for 5.8 GHz), where α is the radius of the minimum cylinder that is centred on the axis of rotation and encloses AUT (the radius of body phantom in azimuth), and (b) in Y-axis $\Delta Y \leq \lambda/2$ ($= 62.5$ mm for 2.4 GHz and $= 25.85$ mm for 5.8 GHz). The final azimuth sampling is determined also from the resulted directivity value since a finer resolution in azimuth would produce a more accurate directivity measurement and, consequently radiation efficiency value. The final sampling parameters are noted in Table 4.2. The scan tab in Midas acquisition software configured for 2.4 GHz measurement, is shown in Fig. 4.9.

Table 4.2 Final near-field sampling parameters

Parameter	***f = 2.4 GHz*** (λ= 125 mm)	***f = 5.8 GHz*** (λ= 51.7 mm)
Radius of minimum cylinder enclosing AUT (α)	156 mm	
Sampling step in Azimuth ($\Delta\theta$)	5^o	
Sampling step in Y-axis (ΔY)	50 mm	25 mm

The 3D far-field radiation pattern, which is obtained from the near-field to far-field transformation, has some unavoidable truncation errors [3]. These predominantly comprise of the lack of sampling data over a portion of the propagating near- field due to the finite cylindrical measurement surface. Also, in the transformation process, Hankel functions are not defined at $\phi = \pm 90^o$. Therefore, the resulting far-field radiation pattern is restricted to a region of validity, which is qualitatively shown in Fig. 4.13.

The angle of validity ϕ_{ff} of the transformed far-field pattern is given from the following equation [5]:

$$\phi_{ff} = \tan^{-1}\left(\frac{L_y - \alpha_y}{2d}\right) \tag{4.1}$$

where: L_y is the total scanning length in the Y-axis, α_y is the AUT aperture extend in the Y- direction and, d is the separation distance between the AUT aperture and

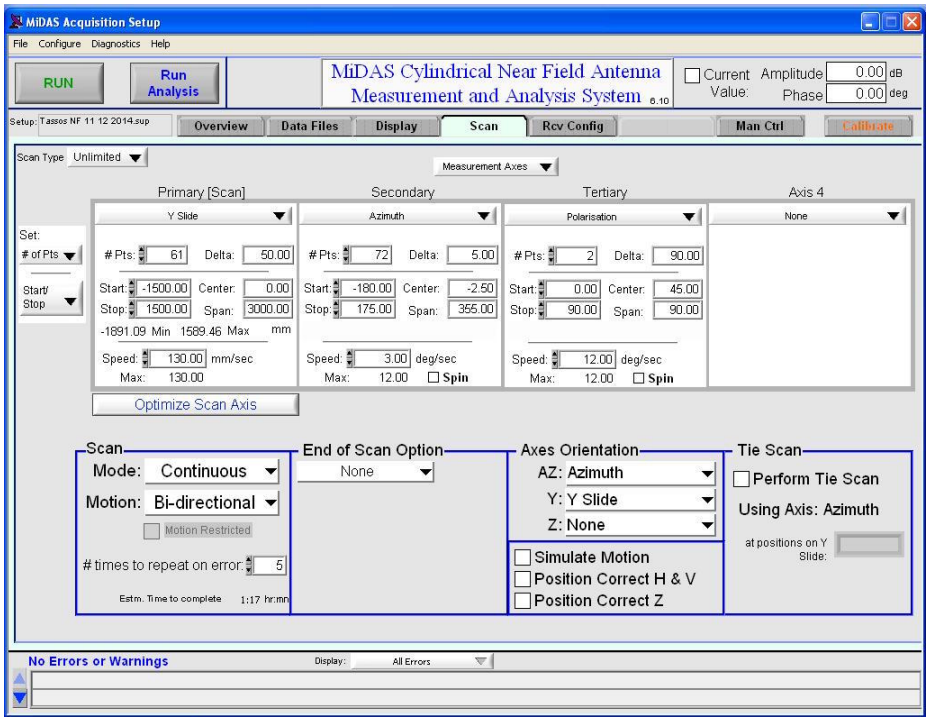

Figure 4.9 Scan configuration in Midas acquisition software, according to the sampling parameters listed in Table 4.2.

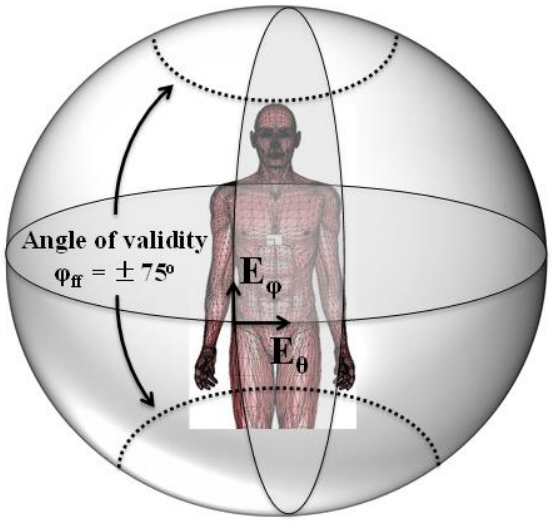

Figure 4.10 Spherical (θ-, ϕ-) far-field domain after transformation from cylindrical near-field (Vertical-, Horizontal-). Region of validity, which is specified by the angle of validity is schematically drawn, extending up to the dotted line.

the scan plane (probe aperture).

In order to minimise the scan area truncation error and, therefore achieve a larger far-field valid region, the full scanning length in the Y-axis is exploited ($\approx$ 3.5 m). Moreover, the separation distance between the probe and the AUT contributes to this effect. The closer the separation distance is selected, the higher the valid angle is expected, as it is graphically shown in Fig. 4.11. This separation distance, however, should be carefully selected in order to avoid any unwanted multiple reflections between the probe and the AUT that could create ripples in the radiation pattern. It is set at 0.375 m, which is the 3λ distance at 2.4 GHz, according to the minimum separation distance of $3\lambda - 5\lambda$ recommended in [12].

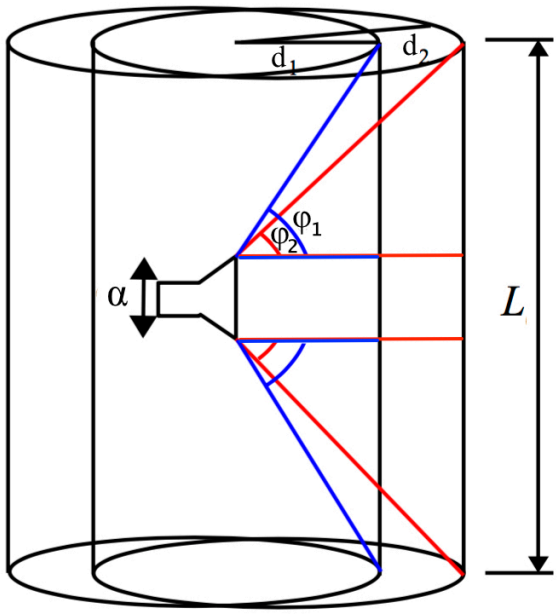

Figure 4.11 Angle of validity ϕ_{ff} for two arbitrary probe-AUT separation distances.

To calculate the angle of validity, one has to determine the AUT aperture extend in the Y- direction α_y in (4.1). In the case of wearable antenna measurements, the antenna together with the phantom comprise an effective AUT (or super antenna [14]) that contains a part of the human body in its near field region. The electrical length of the effective AUT is expected to be larger than the physical size of the wearable antenna itself, due to the scattering effects on the human body. Hence, the effective AUT aperture diameter should be considered.

In this study, since the scanning length $L_y >> \alpha_y$ and the near-field distance d is small enough, the far-field angle, calculated from (4.1), remains almost unaf-

fected from the different A_{eff} values, due to the different antenna types and different frequencies of operation under investigation.

After testing with the selected configuration, the power level at the edge of the scanning surface is found attenuated by more than 30 dB compared to the level at its centre that improves the signal-to-noise ratio (SNR) and achieves an angle of validity of more than $\phi_{ff} = \pm 75^o$.

4.2.5 Gain Calibration

Gain can be determined in several ways [12]:

1. By determining the directivity and ohmic losses in the antenna.
2. By performing a near-field scan and using the probe as the gain standard.
3. By performing two near-field scans (one with the AUT and one with a transfer standard antenna of known gain).

Gain measurement using near-field techniques is different from that in far-field measurements, since it is not dependent from the measurement distance. Direct gain near-field measurements require knowledge of the probe's gain and a measurement that represents the computed far-field peak. The maximum near field value, measured over the cylindrical surface surrounding the antenna is used from which the peak value of the far-field plane wave is computed. The computation includes also a correction for the effect of the probe's pattern. However, a normalisation is required to relate the far-field peak value of the AUT to the input power at the probe. This normalisation is done by connecting the probe's cable directly to the AUT's cable, to bypass the probe and the AUT. Thus, the computed far-field peak and bypass measurement represent a measured power ratio $(FFpeak - Bypass) = (Pr - Pt)$. The AUT gain is then calculated from the direct gain equation:

$$G_{AUT} = (P_r - P_t) - G_p + M \tag{4.2}$$

where:

- $(P_r - P_t)$ is the far-field peak ratio of the received power at the AUT aperture to the input power at the probe.
- G_p is the theoretical or measured probe gain.

- M is the mismatch losses factor of the two antennas.

As for the mismatch factor, it is derived from:

$$M = \frac{|1-\Gamma_s\Gamma_a|^2|1-\Gamma_p\Gamma_x|^2}{|1-\Gamma_s\Gamma_x|^2\left(1-|\Gamma_\alpha|^2\right)\left(1-|\Gamma_p|^2\right)} \tag{4.3}$$

where: Γ_s is the source return loss, Γ_a is the AUT return loss, Γ_p is the probe return loss and Γ_x is the receiver return loss. A 2-port calibration of the VNA is needed prior to the gain calibration, in order to derive the S_{11} of both the probe and AUT.

The sequence of gain calibration is:

1. Calculate the S_{11} mismatch factor of the AUT and the probe after performing a 2-port calibration of the VNA .

2. Perform the near-field scan to acquire the maximum near field value.

3. Connect the AUT cable to the probe cable and make a bypass (S_{21}) measurement.

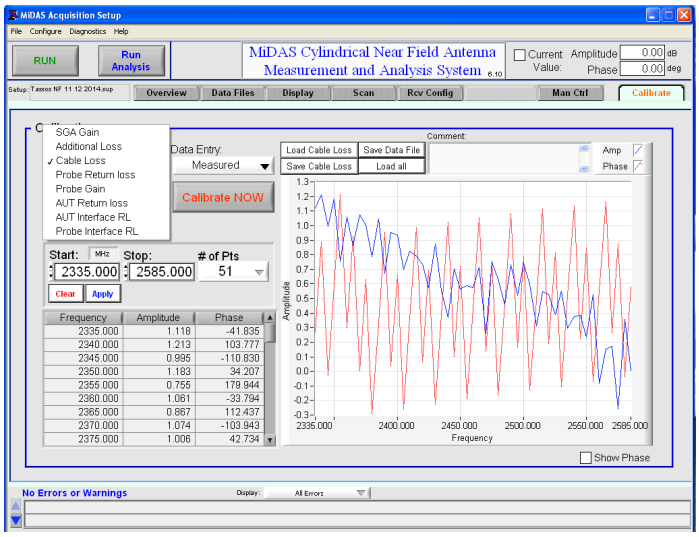

Figure 4.12 Cable loss (S_{21}) uncalibrated measurement in Midas acquisition software.

4. Compute the far-field peak value after NF-FF transformation of the measured near field peak value and adjust by the value of the bypass measurement.

5. Calculate the radiated (IEEE) gain of the AUT using (4.2).

4.3 Evaluation of CNF Measurement Method

Impedance matching, near-field and far-field measurement results of the printed dipole placed on the human body are presented in this section and compared with EM simulations in order to investigate the accuracy of the proposed measurement method. The measured near-field results are graphically presented on an outline of the human body. For the sake of briefness, only the E- and H- principal planes are presented instead of the 3D far-field pattern. The on-body locations that are used in this study are shown in Fig. 4.13.

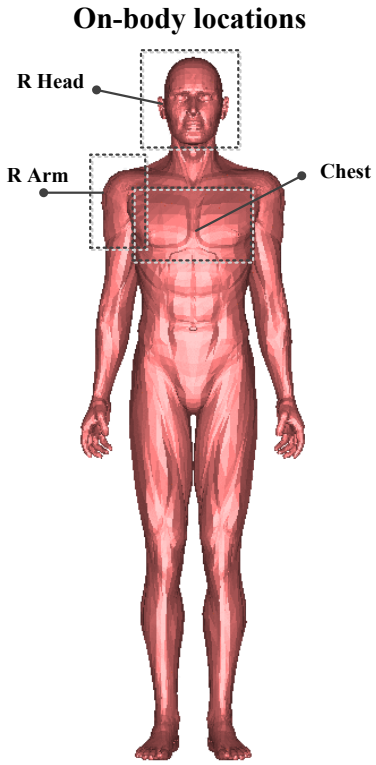

Figure 4.13 The on-body locations where the wearable antennas are tested.

4.3.1 Impedance Matching ($|S_{11}|$)

The reflection coefficient $|S_{11}|$ of the printed dipole at 2.4 GHz on different body positions derived from simulations and measurements is plotted in Fig. 4.14. It can be seen that the effect of the dielectric loading of chest, head and shoulder results in different frequency detuning and $|S_{11}|$ degradation. For the chest position, a detuning

of 147 MHz in simulations and 75 MHz in measurements occurs with respect to the free space case, while the $|S_{11}|$ magnitude degradation is 18.3 dB and 5.5 dB respectively. As for the other two positions, the effect on frequency detuning is smaller but the magnitude degradation is slightly larger than the measurement on chest. It can be concluded that the input impedance of printed dipole is dependent on the body location and as a result the total antenna efficiency would be affected. The $|S_{11}|$ degradation is expected since the lack of ground plane in the printed dipole allows a large part of the radiated energy to be absorbed in the body.

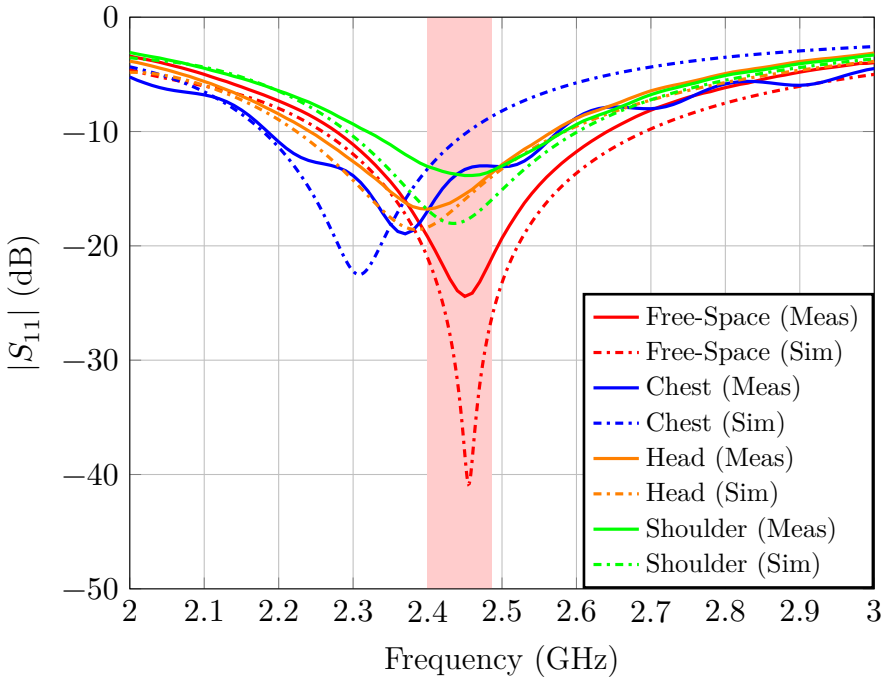

Figure 4.14 Reflection coefficient $|S_{11}|$ of printed dipole at 2.4 GHz ISM band.

The reflection coefficient $|S_{11}|$ of the printed dipole at 5.8 GHz is plotted in Fig. 4.15. It can be seen that the printed dipole on chest experiences a stronger frequency detuning rather than at 2.4 GHz, which is found to be up to 540 MHz in simulations and 230 MHz in measurements. The BW is also increased to 840 MHz rather than 275 MHz at 2.4 GHz. As a result, due to the large BW at the 5.8 GHz frequency band, the -10 dB impedance matching criterion is satisfied at all on-body locations.

Resonance frequency and -10dB bandwidth (BW) of printed dipole in free space and on chest are also listed in Table 4.3.

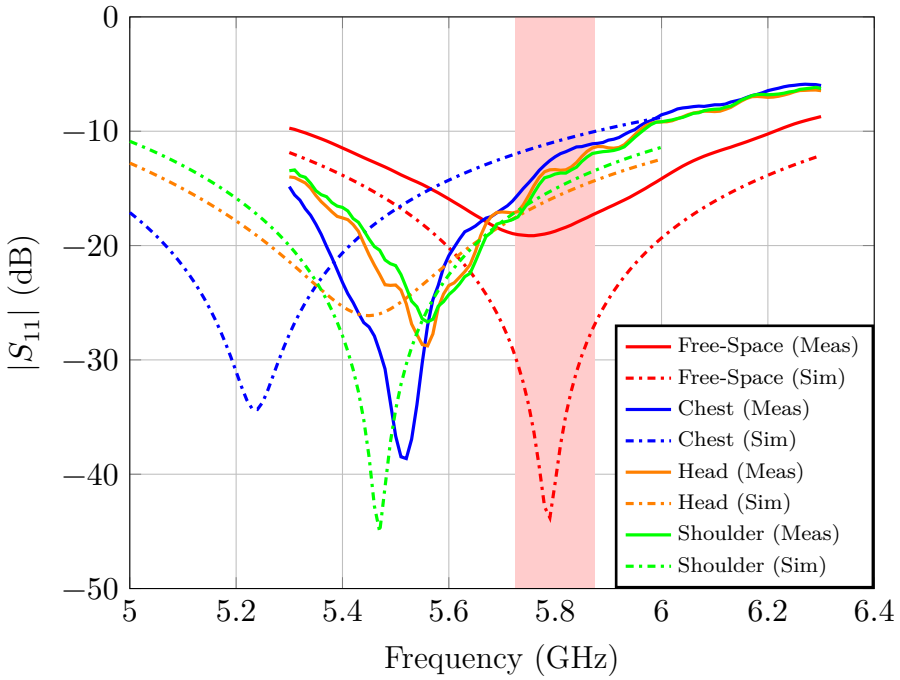

Figure 4.15 Reflection coefficient $|S_{11}|$ of printed dipole at 5.8 GHz ISM band.

4.3.2 Near-field Results

To examine the cylindrical near-field measurement accuracy for different antenna polarisations, the printed dipole is measured in horizontal and vertical orientations on the SAM phantom at 2.4 and 5.8 GHz. The near-field measurement results, compared with simulations, are presented in Fig. 4.16 and Fig. 4.17 at 2.4 and 5.8 GHz respectively.

An outline of the body at different azimuth angles (in 90^o steps) is schematically drawn to show the E-field distribution in respect to the human body. The field distribution is recorded around the body focusing in a Y-slide scanning length of ± 0.9 m. The normalised field value in respect to the maximum co-polarised value is plotted.

The results show that the measured field decay in azimuth is slower for the vertical dipole's orientation (Fig. 4.16c) rather than for the horizontal (Fig. 4.16d) at 2.4 GHz. In the horizontal dipole's orientation (Fig. 4.16d), the field is mostly propagated along the vertical axis of the body. In both cases, it is revealed that for azimuth angles $-90^o \geq \theta \geq 90^o$ (back side of the body) strong body shadowing

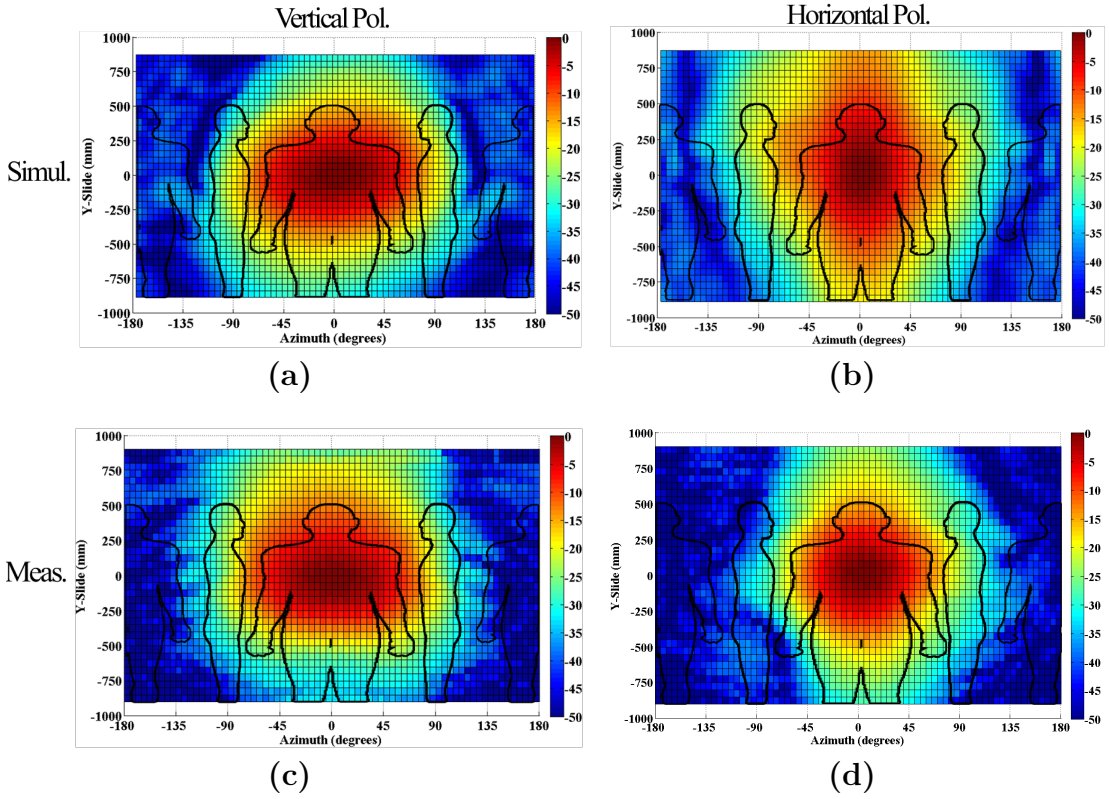

Figure 4.16 Normalised near-field patterns of printed dipole at 2.4 GHz: vertically (a), (c) and horizontally (b), (d) placed on phantom's chest.

occurs. There is a good agreement between measurements and simulations for the vertical dipole orientation. It is indicated that the measurement remains unaffected from the presence of the AUT turntable since the dipole's radiation pattern in vertical orientation exhibits a null in the direction of the turntable. However, for the horizontal orientation in which the printed dipole exhibits a maximum radiation in the Y-axis direction, a larger difference in the near field distribution between measurements and simulations is spotted. This can be possibly due to a different antenna placement, placed farther apart from the numerical phantom in respect to the physical phantom in measurements, which creates a weaker near-field interaction and more field is propagated along the maximum gain direction in the Y-axis. Therefore, the 2D near-field measurement results seem to be more reasonable rather than the simulation results, since the different dipole orientation should have a small effect on the resulted antenna interaction with human body.

In respect to the near-field results at 5.8 GHz (Fig. 4.17), the field maximum

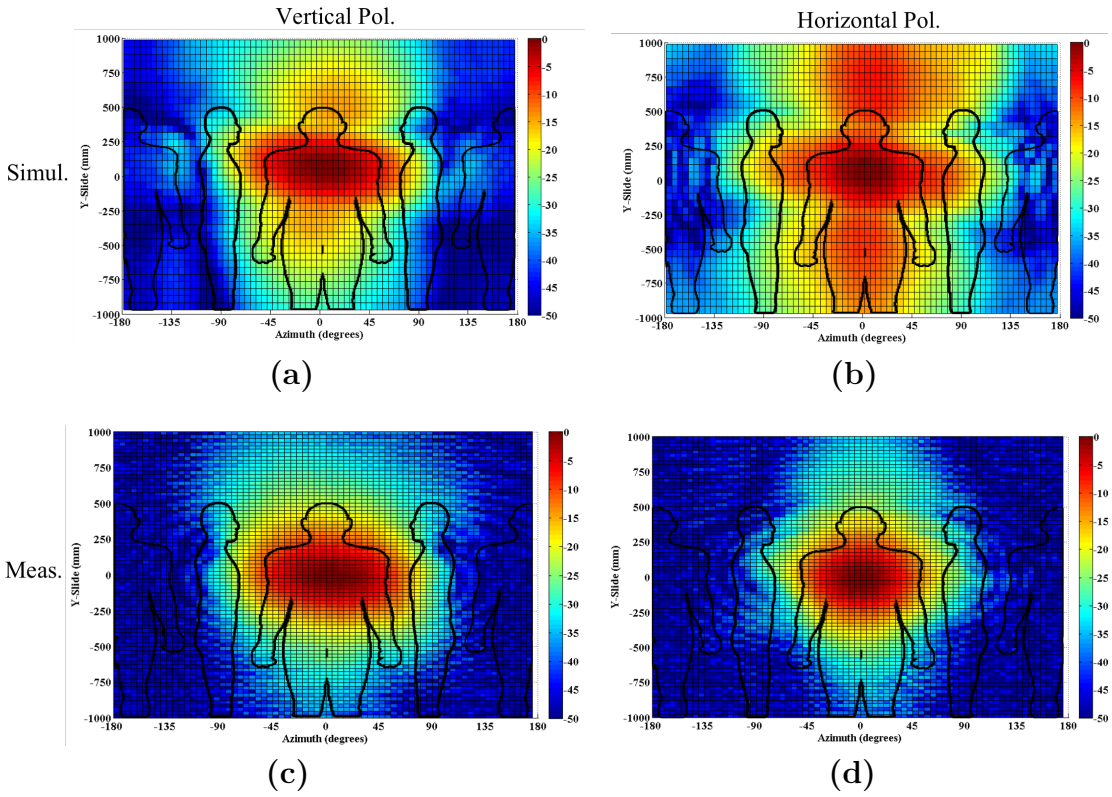

Figure 4.17 Normalised near-field patterns of printed dipole at 5.8GHz: vertically (a), (c) and horizontally (b), (d) placed on phantom's chest.

seems to be located in a smaller area in front of the chest rather than at 2.4 GHz since the field decay is faster due to the shorter wavelength at this frequency of operation. A good agreement between measurements and simulations at the vertical case is observed, where the electric field is mostly propagated around the body surface. At the horizontal case, the field is longitudinally distributed in both measurements and simulations, however the field decay is faster in measurements rather than in simulations.

Apart from the chest, two other commonly used on-body locations are investigated, i.e. head (headphones position) and shoulder (armband position), plotted in Fig. 4.18. It is clearly demonstrated that the measured electric field of the printed dipole is now concentrated close to head and shoulder locations due to the body shadowing effect. This is a validation that the CNF measurement system with the SAM phantom is properly set-up. At the 5.8 GHz case, the maximum electric field is distributed only at the close vicinity of head and shoulder whereas at 2.4 GHz the field

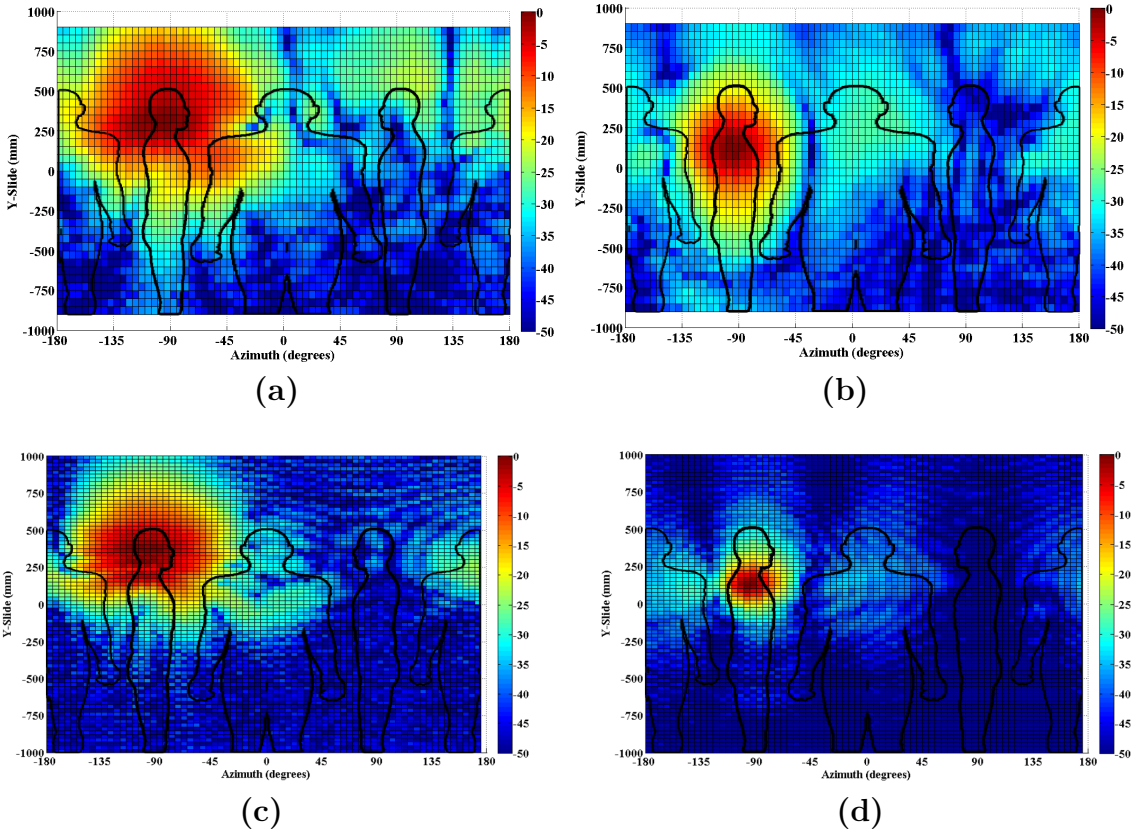

Figure 4.18 Normalised measured (E_θ) near-field patterns for printed dipole at (a,b) 2.4 GHz and (c,d) 5.8 GHz horizontally placed on head and shoulder.

is extended more around the head and shoulder respectively. The above results are a good example of the usefulness of the near-field 2D pattern as an initial assessment of the specific antenna/ body interaction when the antenna is located in different on-body positions. By graphically plotting the electric field of wearable devices on an outline of the human body, an insight of on-body propagation is gained. This can be a valuable tool for wireless network planning of wearable devices. It could enable a better communication between on-body devices of the same application as well as minimise the unwanted interference among adjacent devices of different applications. By using the information of near-field measurements, antennas can be modelled and strategically placed on the body surface in order to optimise their performance either for on-body or off-body communication systems.

The placement of the printed dipole on the SAM phantom is shown in Fig. 4.19 for the chest and in Fig. 4.20 for head and shoulder locations.

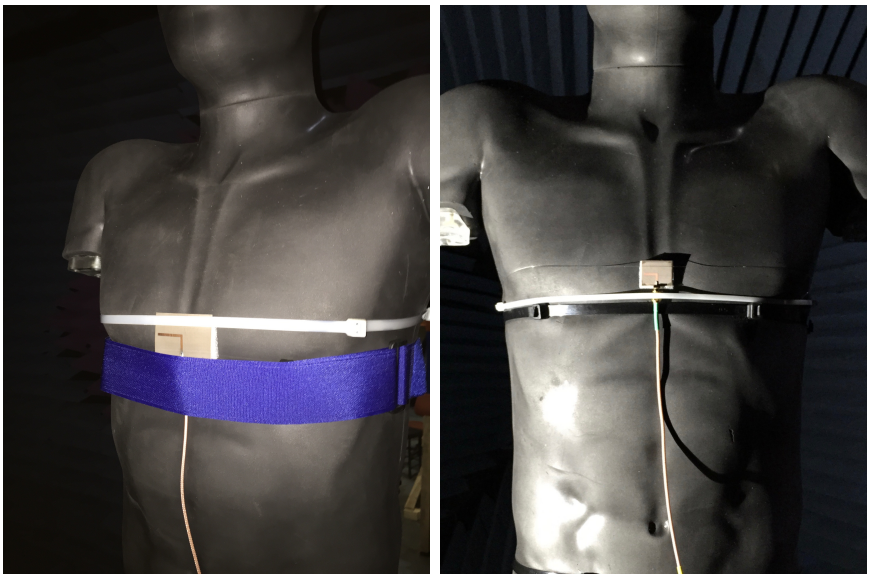

(a) (b)

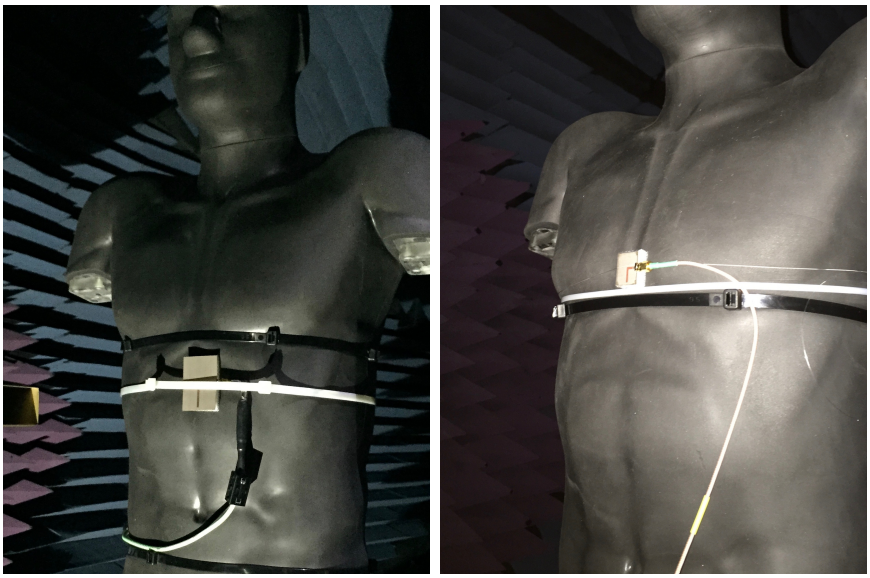

(c) (d)

Figure 4.19 Picture of the printed dipole placed in horizontal and vertical orientation on the SAM phantom's chest with 10 mm spacing for (a,c) 2.4 GHz and (b,d) 5.8 GHz.

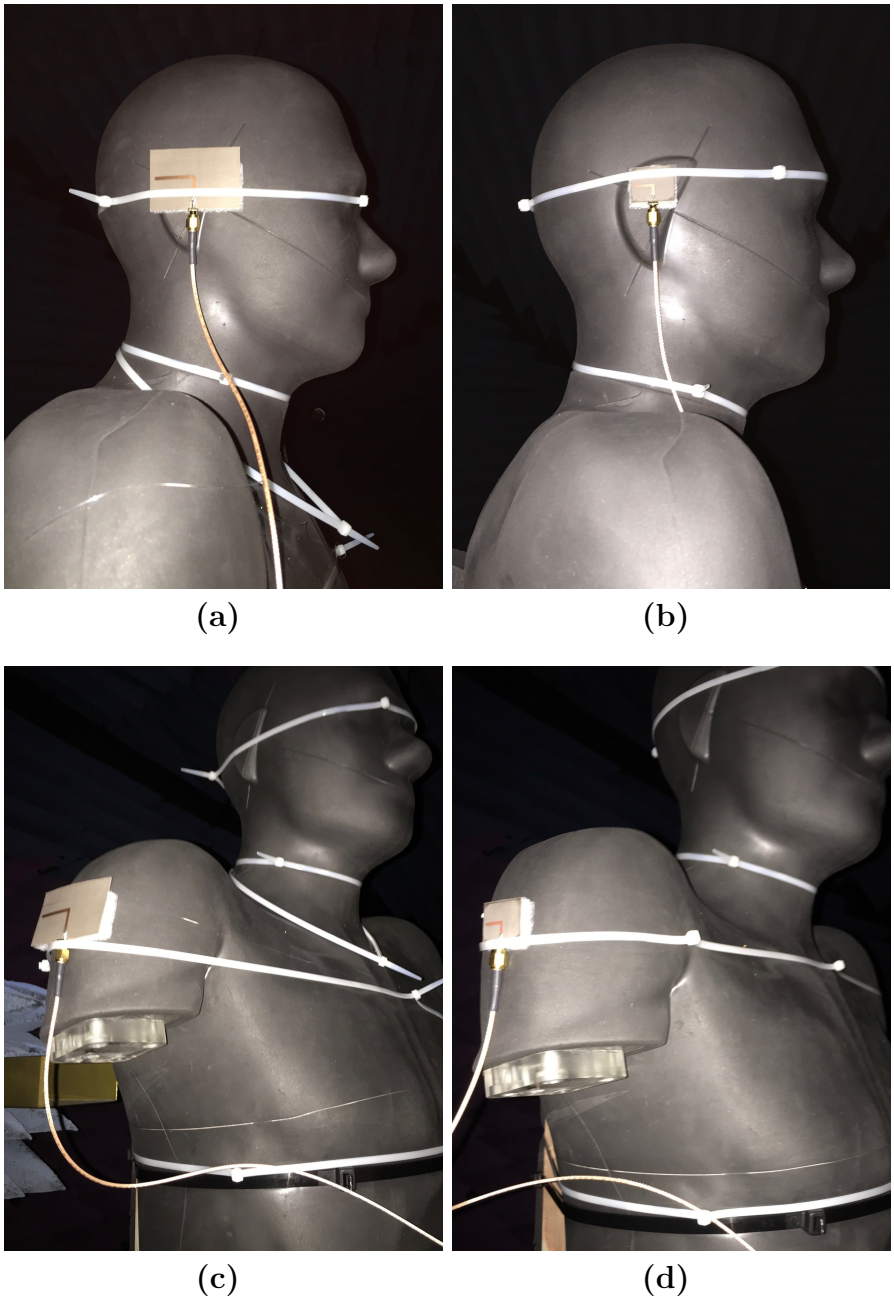

Figure 4.20 Picture of the printed dipole horizontally placed at SAM phantom's head and shoulder for (a,c) 2.4 GHz and (b,d) 5.8 GHz.

4.3.3 Far-field Results

After proving the validity of the measured near-field results in a number of cases, the validity of the transformed far-field results is examined here, compared with EM simulations. To enable the better understanding of the following radiation patterns, the azimuth and elevation planes are schematically plotted including the human body in Fig. 4.21.

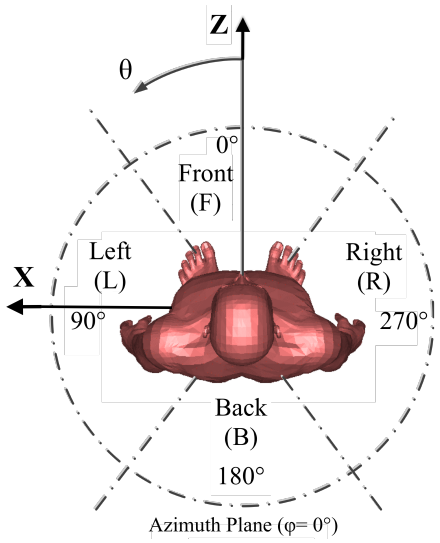

(a)

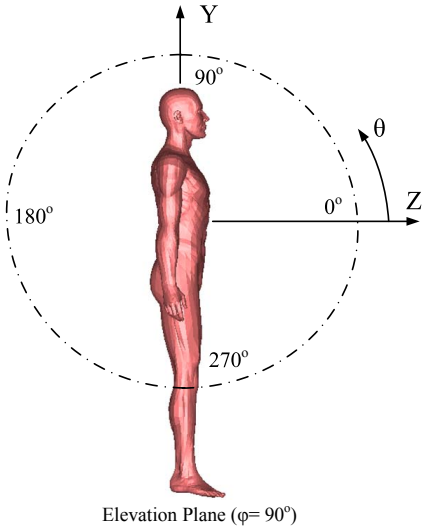

(b)

Figure 4.21 (a) Azimuth plane, and (b) elevation plane of the spherical (θ-, ϕ-) far-field coordinate system for the on-body antenna measurements.

In Fig. 4.22a and Fig. 4.22b, the XZ and YZ principal planes of the normalised far-field patterns at 2.4 GHz are plotted. Simulation results are also provided with dotted lines. It is observed that the radiation pattern is affected from the body position in which the printed dipole is placed. In general, the human body absorption and scattering mechanisms change the dipole's omnidirectional radiation pattern in azimuth plane to directional. The normalised far-field patterns at 5.8 GHz for XZ and YZ principal planes are plotted in Fig. 4.23(a) and Fig. 4.23(b). It is shown that a close matching appears in the chest position while a large discrepancy occurs in head and shoulder positions.

More specifically, the printed dipole at 10 mm separation distance from chest exhibits a gain of 2.3 dBi from measurements and 2.1 dBi from simulations at 2.4 GHz, as shown in Table 4.8. In the case of 0 mm separation distance, with the dipole directly attached to the body surface, the antenna gain is significantly degraded. A gain of -5.1 dBi is obtained from measurements and -2.7 dBi from simulations. This gain reduction in the 0 mm case can be attributed mainly to body's absorption effects that leads to antenna efficiency degradation. In the shoulder position at 10 mm separation distance, the gain is measured at 2.5 dBi and in head position scenario at 2.8 dBi. The small gain difference in shoulder and head positions in respect to chest position can be accounted to the local body geometry behind the antenna that causes different body absorption effects. Regarding the shape of the radiation patterns, there is a good agreement between the measurements and simulations in the XZ-plane. In the YZ-plane, while the measurement follows the simulation in boresight direction, however, for angles $> 75^o$ the aforementioned truncation in the radiation pattern is evident.

At 5.8 GHz, the printed dipole patterns become remarkably directive with a gain of 9.1 dBi on chest at 10 mm separation distance and decreases to 1.0 dBi at 0 mm separation distance, as shown in Table 4.9. The measured and simulated gain values are almost the same at the 0 mm separation distance, however a bigger difference is spotted at 10 mm separation distance. As for the shoulder and head positions, the gain is found 8.5 dBi and 8.9 dBi respectively at 10 mm separation distance.

The radiation efficiency of the printed dipole is calculated from the ratio of the measured gain over the measured directivity in the direction of maximum radiation ($e_{rad} = G/D$) [15]. At 2.4 GHz, when the antenna is flush with the body, the antenna radiation efficiency is resulted to 4.7% from measurements and 10.3% from simulations. The small efficiency value reveals the severe interaction with the human

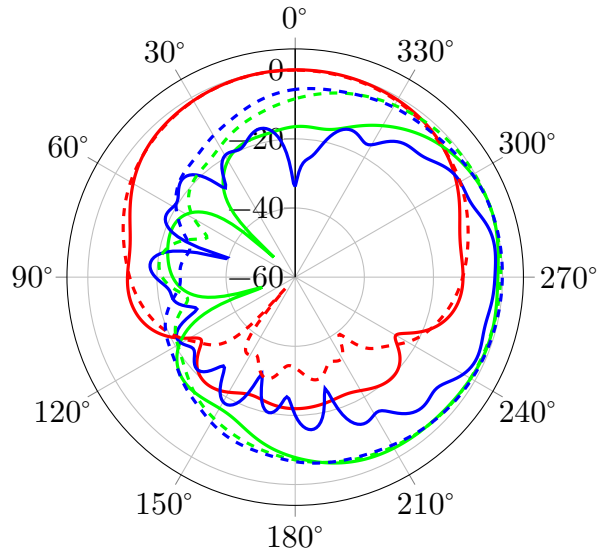

(a)

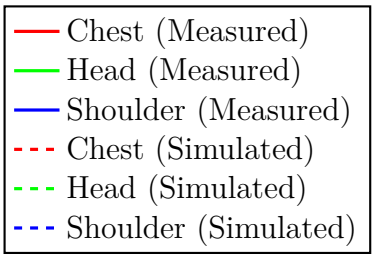

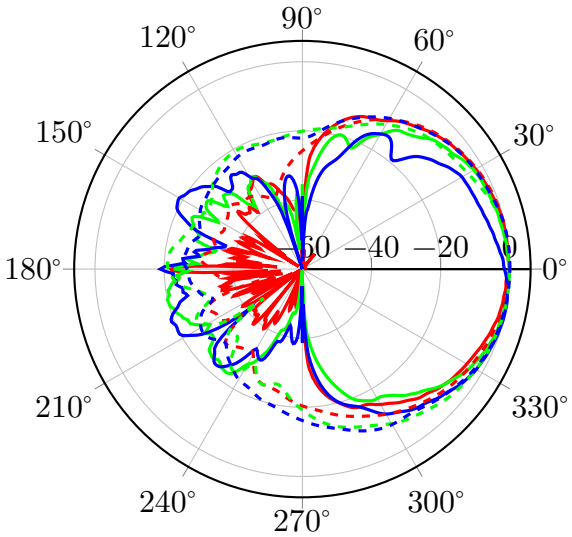

(b)

Figure 4.22 Normalised far-field pattern of printed dipole from measurements (solid line) and simulations (dotted line) at three body positions at (a) XZ-plane and (b) YZ-plane.

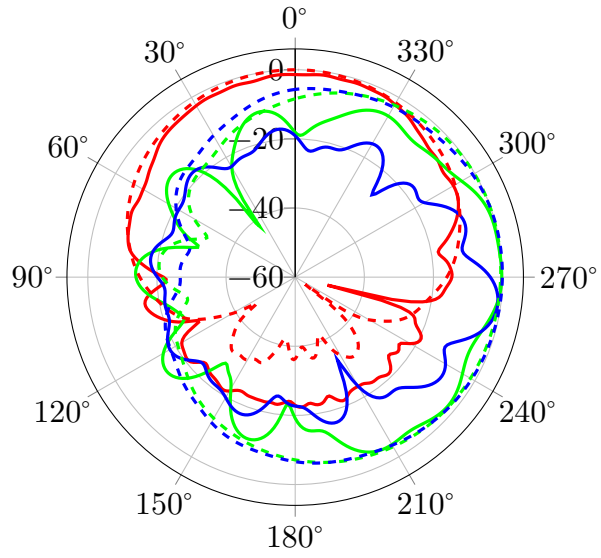

(a)

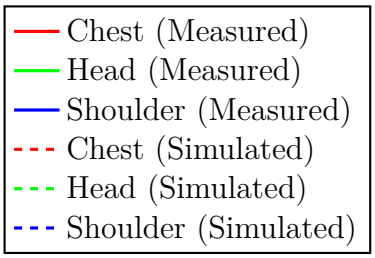

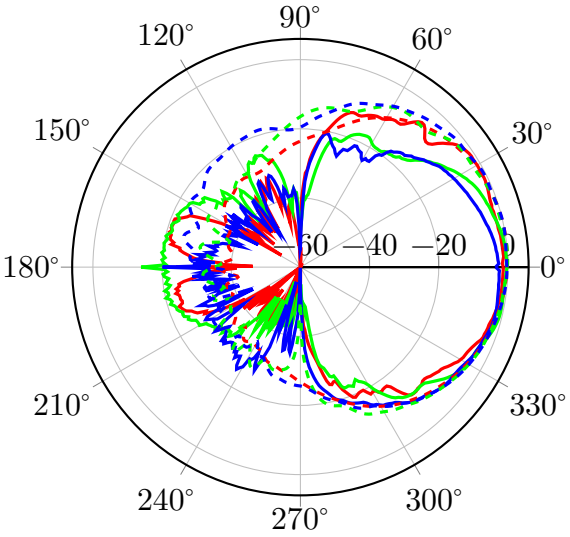

(b)

Figure 4.23 Normalised far-field pattern of printed dipole at 5.8 GHz from measurements (solid line) and simulations (dotted line) at three body positions at (a) XZ-plane (Azimuth) and (b) YZ-plane (Elevation).

body. The difference between measurements and simulations can be attributed to the non uniformity of the phantom surface in the simulation model where the antenna is in less contact with the body than in the measurements creating a slightly different interaction. In the case of 10 mm separation distance, this difference is reduced with a radiation efficiency of 22.2% from measurements and 25.5% from simulations, since the antenna is affected less from the body presence.

At 5.8 GHz, the antenna radiation efficiency is found 13.5% for 0 mm and 58.2% for 10 separation distance respectively. These values reveal that the antenna experiences a weaker interaction with the body rather than at 2.4 GHz. This is explained, since the 10 mm separation distance at 5.8 GHz is electrically longer (in terms of the wavelength) in contrast to 2.4 GHz.

For both 2.4 and 5.8 GHz, a difference between simulations and measurements of less than 12.2% (or 0.56 dB) is achieved, which provides a clear evidence of the accuracy of the proposed CNF method for the determination of wearable antennas radiation efficiency.

4.4 Wearable Textile Antennas Performance Characterisation

Wearable antennas performance is investigated, through CNF measurements, in terms of impedance matching, gain and efficiency as well as intensity of the near-field around and across the SAM phantom body surface. The two wearable textile antennas (MPA and HMMPA) have been tested in free space prior to the near-field on-body measurements to ensure that the desirable performance is obtained.

4.4.1 Textile Patch Antenna (MPA)

The placement of the MPA on the chest of SAM phantom is shown in Fig. 4.24. It can be seen from the $|S_{11}|$ response at 2.4 GHz (Fig. 4.25a) that the MPA experiences a negligible detuning effect from the interaction with the body and preserves a narrow BW, which is characteristic for patch antennas. At the 5.8 GHz, the detuning effect and the actual BW appear larger, which is an expected behaviour as the frequency increases. This effect is partly related to the electrically larger body size as well as to the higher conductivity of body tissue that couples more of the antenna radiation.

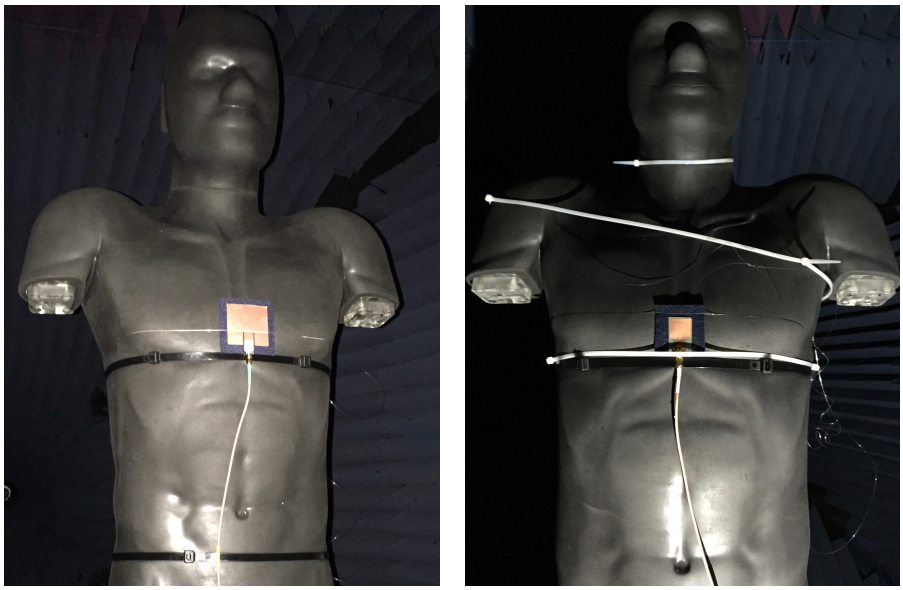

(a) **(b)**

Figure 4.24 Picture of MPA placed on the chest of SAM phantom at (a) 2.4 GHz and (b) 5.8 GHz.

However, in both frequency bands, the BW of the MPA covers the entire bandwidth of the ISM band.

The measured near-field pattern of the MPA on the SAM phantom is shown in Fig. 4.26. It can be seen that the maximum value of the vertical field component at 2.4 GHz (Fig. 4.26a) is concentrated on a small area in the front of human chest while the small value of the horizontal component (Fig. 4.26c) reveals a minor interaction with the body. This is an expected behaviour since most of the radiated field of the MPA does not interact with the body. Hence, the vertical polarisation of the MPA (for the orientation of Fig. 4.24) remains dominant between the free space and on the human body cases. At 5.8 GHz (Fig. 4.26b,d), the body scattering effect is evident since the vertical field component is distributed in a larger area of the human chest and the horizontal component appears stronger that reveals a higher interaction with the body.

Moreover, after transforming the measured vertical and horizontal near-field components to the far-field domain, the XZ ($\phi = 0^o$) and YZ ($\phi = 90^o$) radiation pattern cuts of the MPA are calculated and plotted in Fig. 4.28. A schematic of the two principal planes, including the body phantom is displayed in Fig. 4.27.

It can be seen that at 2.4 GHz (Fig. 4.28a) the main lobe's direction of the MPA

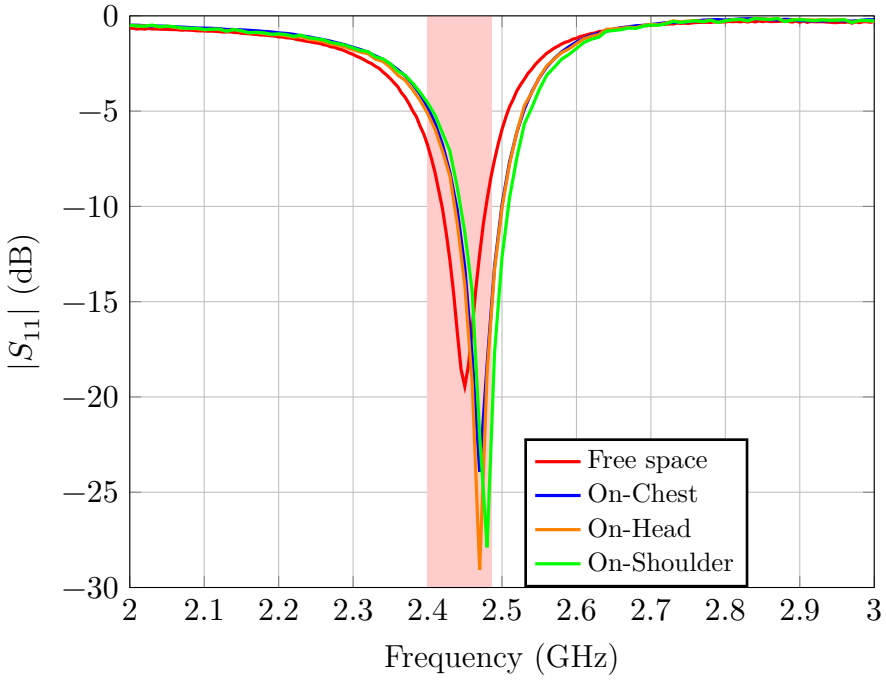

(a)

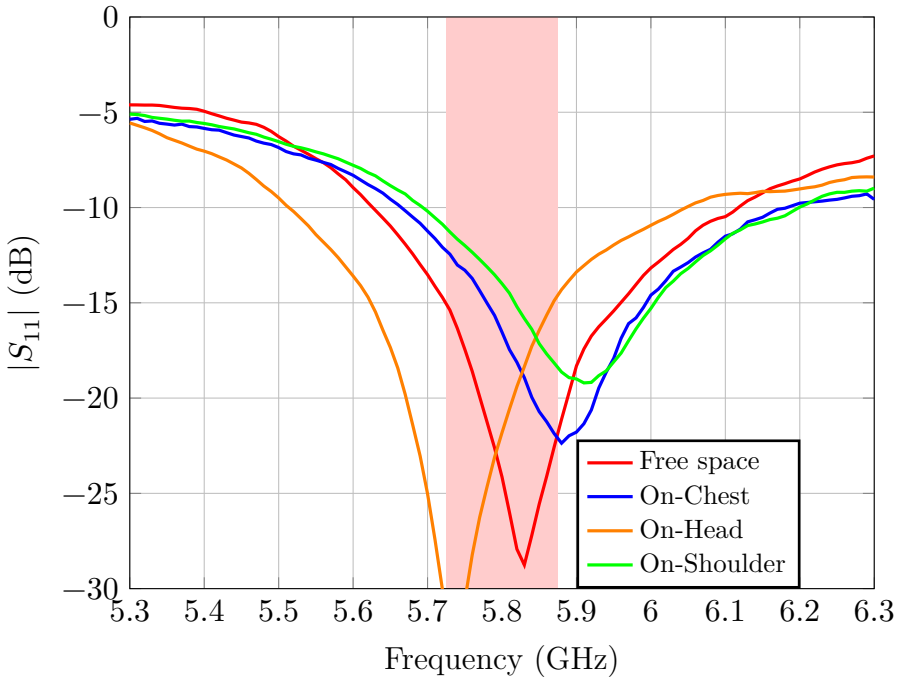

(b)

Figure 4.25 Measured reflection coefficient $|S_{11}|$ of MPA antenna at (a) 2.4 and (b) 5.8 GHz ISM band.

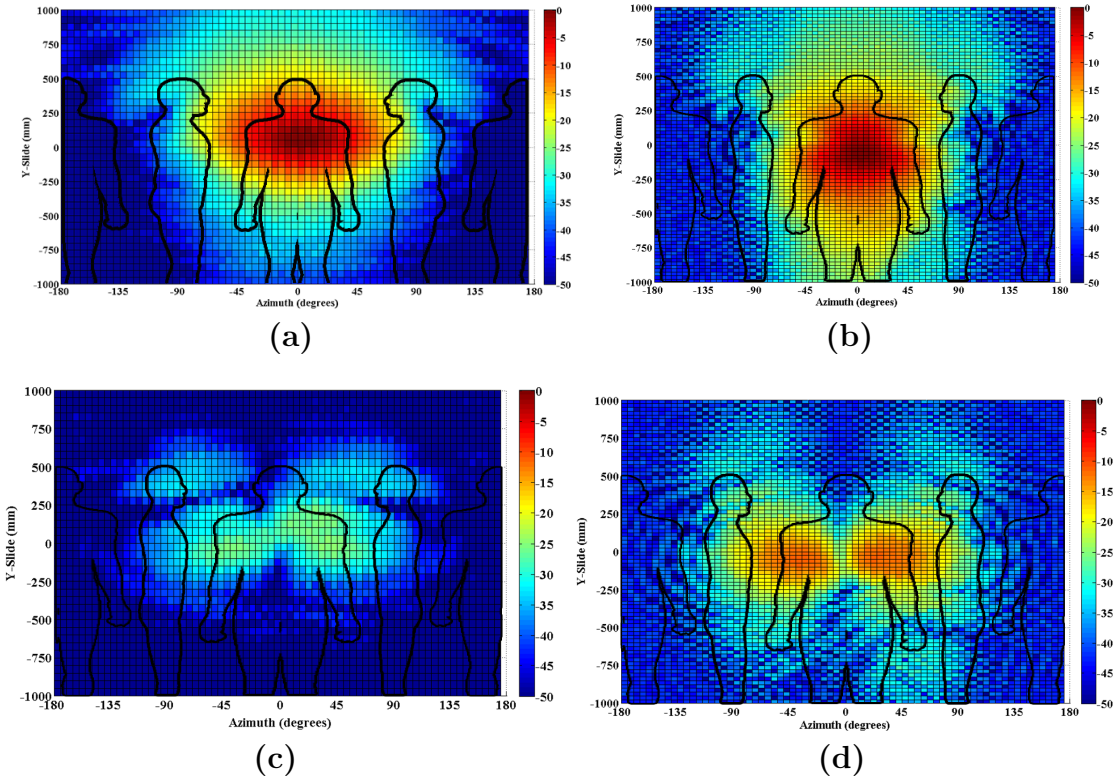

Figure 4.26 Measured near-field intensity for MPA on chest at (a,c) 2.4 and (b,d) 5.8 GHz. Vertically (E_Y) polarised (top row) and horizontally (E_θ) polarised (bottom row) components.

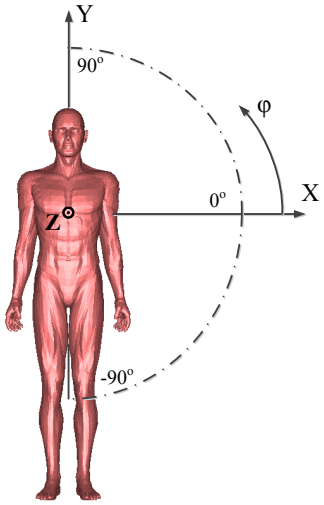

Figure 4.27 Schematic of the XZ ($\phi = 0^o$) and YZ ($\phi = 90^o$) planes for wearable antenna radiation patterns including body phantom.

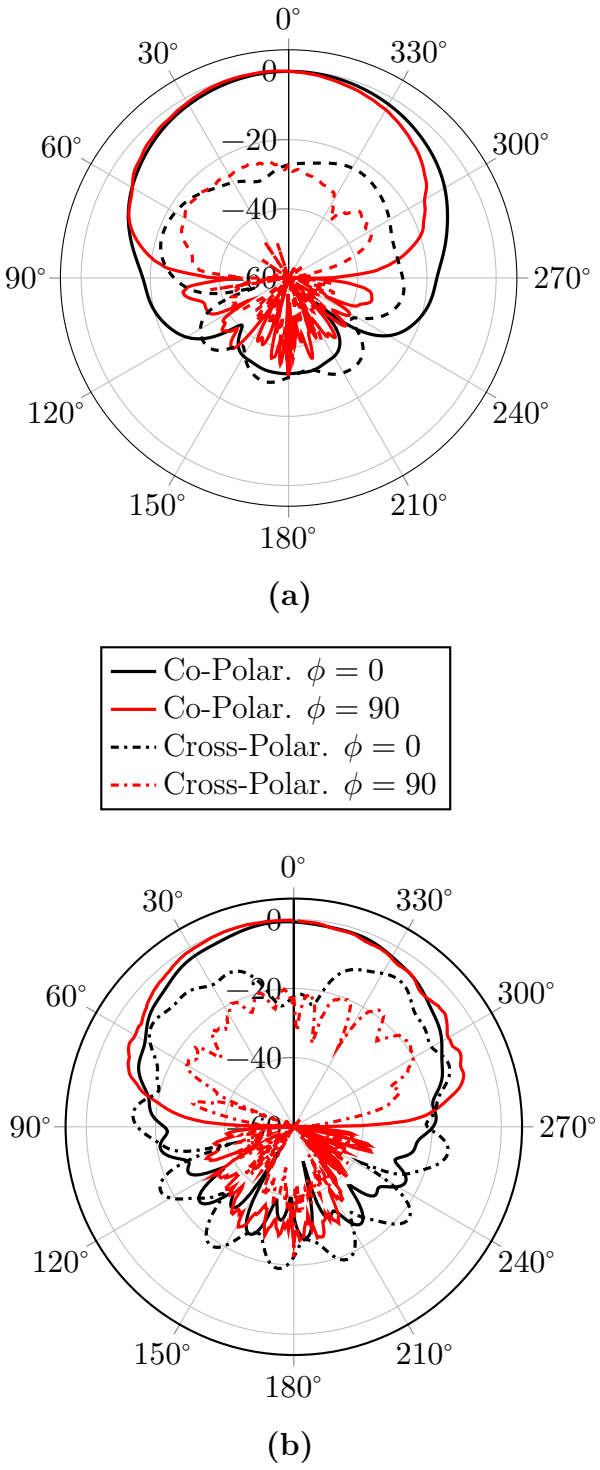

Figure 4.28 Measured normalised far-field radiation patterns in XZ-plane ($\phi = 0^o$) and YZ-plane ($\phi = 90^o$) for MPA on SAM chest. (a) 2.4 GHz and (b) 5.8 GHz.

in both planes is off-the-body surface ($\theta = 0^o$) while the cross polarised component remains at least 20 dB lower than the co-polarised component. This result reveals the minor interaction with the body due to the presence of the ground plane. At 5.8 GHz (Fig. 4.28b), it is seen that the back lobe level and the cross-polarised component in the front hemisphere are slightly increased due to the increased interaction with body, although the shape of the main lobe remains unaffected.

4.4.2 Higher Mode Textile Patch Antenna (HMMPA)

The placement of the HMMPA antenna on the chest of the phantom is presented in Fig. 4.29.

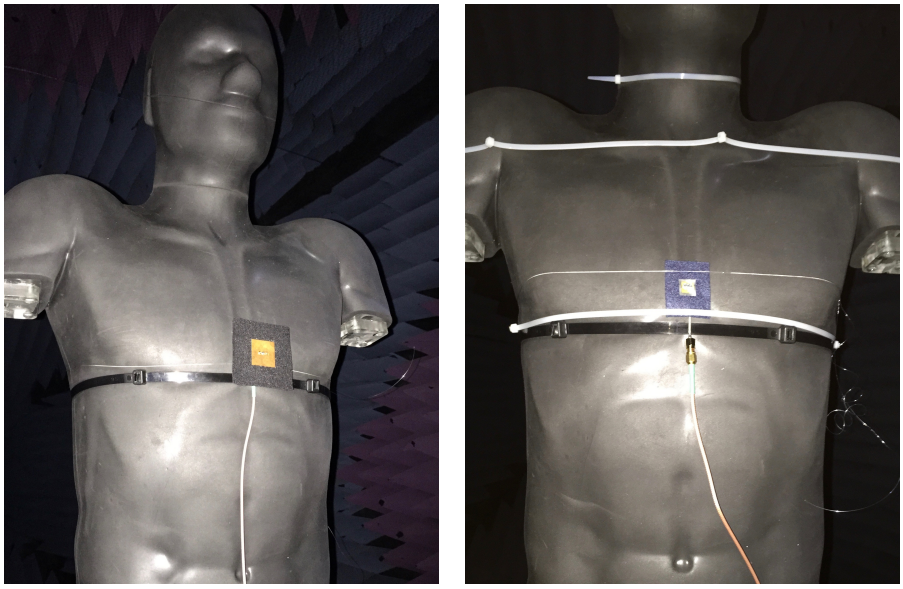

(a) **(b)**

Figure 4.29 Picture of HMMPA placed on the chest of SAM phantom at (a) 2.4 GHz and (b) 5.8 GHz.

Looking at the $|S_{11}|$ of the HMMPA placed on the chest, a negligible detuning effect is noticed at 2.4 GHz (Fig. 4.30a). The detuning effect appears stronger in the case of head and shoulder that causes part of the antenna BW not to cover the entire 2.4 GHz ISM band. In the case of 5.8 GHz (Fig. 4.30b), there is no significant detuning effect for all the body locations, however a $|S_{11}|$ magnitude degradation of 5 dB is noticed. The 5.8 GHz ISM band is fully covered from the HMMPA BW.

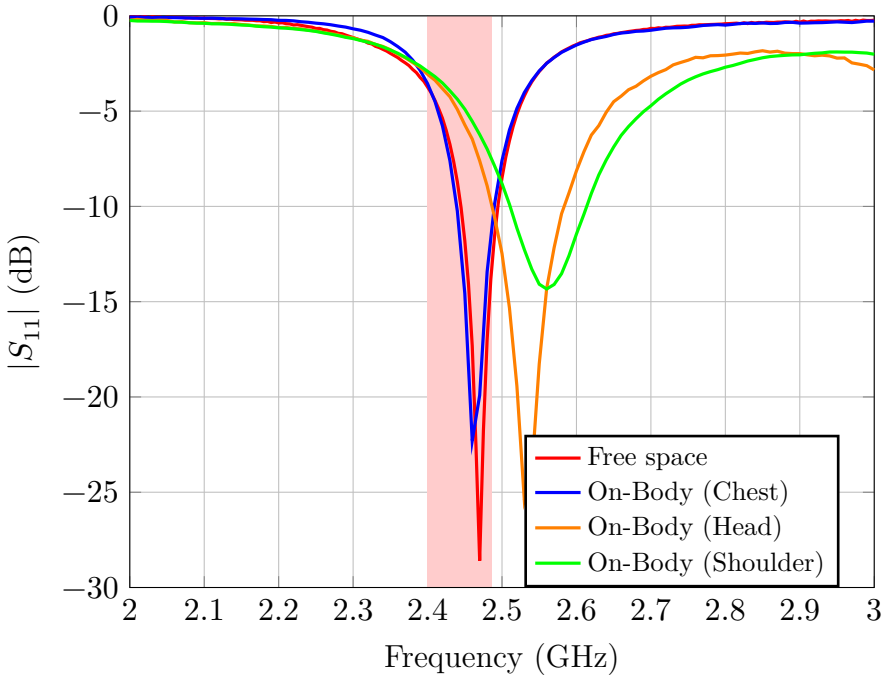

(a)

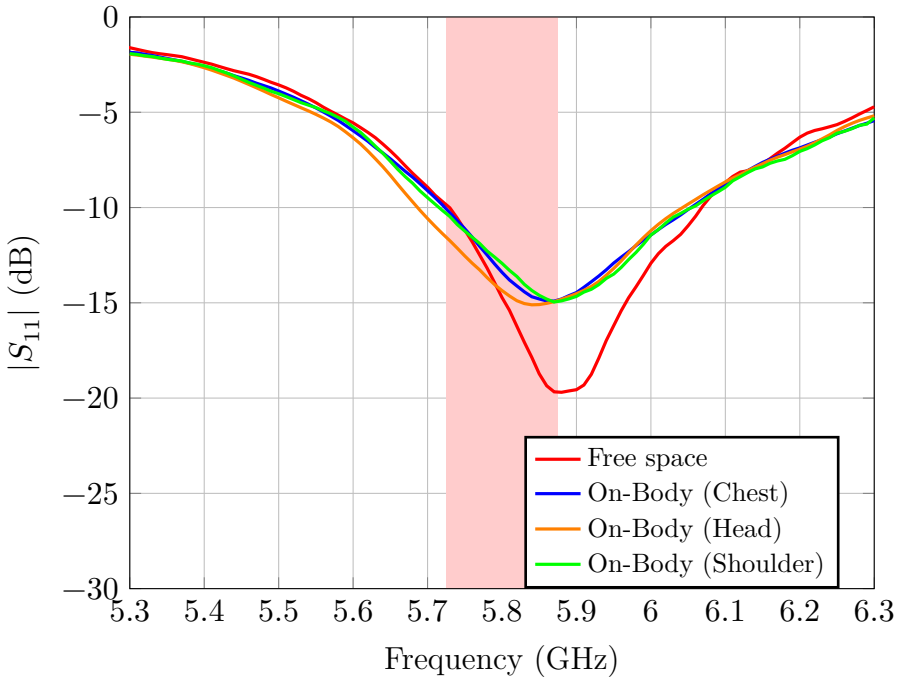

(b)

Figure 4.30 Measured reflection coefficient $|S_{11}|$ of HMMPA antenna at 2.4 and 5.8 GHz ISM band.

Looking at the vertical near-field component, in Fig. 4.31a, a coupling with the SAM phantom that extends along the vertical body axis is evident whereas in the MPA case the maximum field is concentrated close to the antenna position. At the same time, the horizontal field component in Fig. 4.31c is extended around the body surface. In comparison with the printed dipole in Fig. 4.16d, it can be observed that the field component reaches a normalised intensity value of -30 dB at the back of the body ($\theta = \pm 180^o$), while the corresponding field intensity of the printed dipole reaches the same value just at $\theta = \pm 90^o$. If the absolute near-field component had been calculated by combining both polarisations of the HMMPA, a full-body coverage would be expected around and along the body surface. It can be concluded that by using a single HMMPA antenna, an effective coverage of every sensor location on the body surface can be achieved.

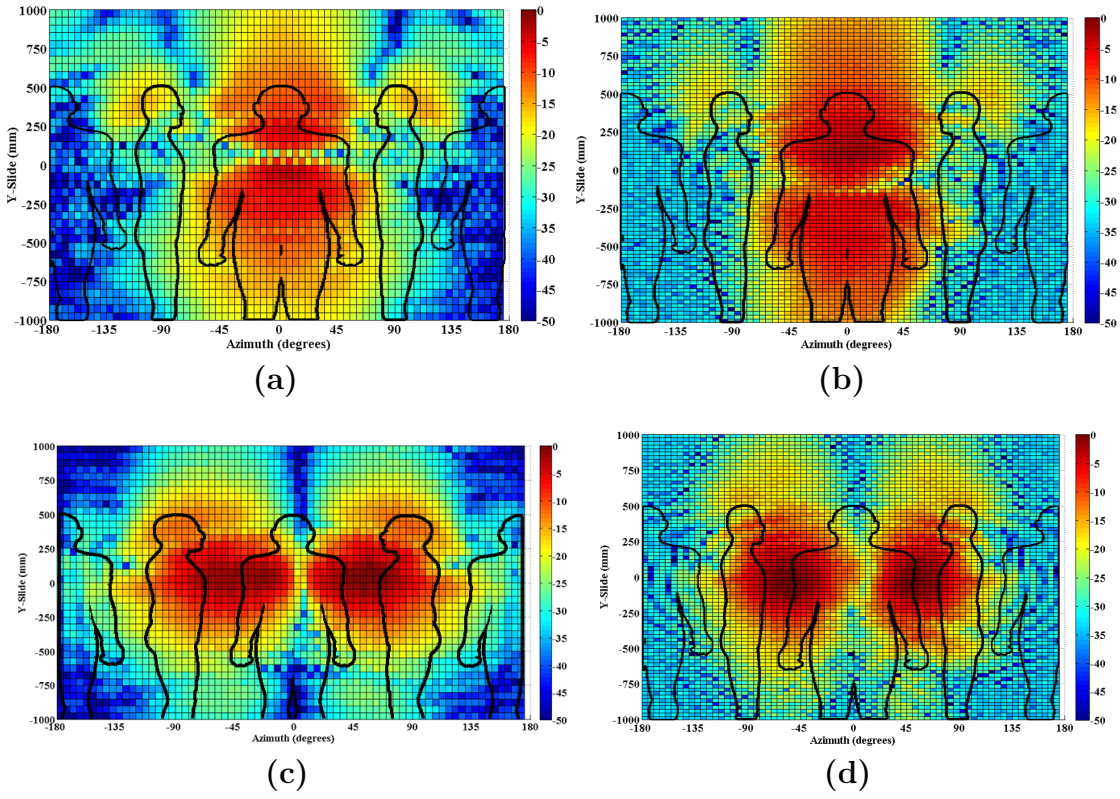

Figure 4.31 Measured near-field intensity for HMMPA on chest at (a,c) 2.4 and (b,d) 5.8 GHz. Vertically (E_Y) polarised (top row) and horizontally (E_θ) polarised (bottom row) components.

As for the dominant polarisation of HMMPA, while in free space is expected to be normal to the patch surface (captured from the horizontal polarisation component

(E_θ) of the CNF measurement system), however, in the presence of human body, the dominant polarisation cannot be distinguished. This is attributed to the coupling mechanism of the HMMPA with the human body, which enables a surface wave propagation but also leads to an increased interaction and losses. As a result, it is concluded that the body presence affects the antenna near-field distribution depending on the antenna design (e.g. with or without ground plane) as well as the excitation mode type (TM_{01} for MPA or TM_{21} for HMMPA).

Moreover, after transforming the measured vertical and horizontal near-field components to the far-field domain, the XZ and YZ radiation pattern cuts of HMMPA are calculated and plotted in Fig. 4.32. It can be seen that most of the radiation is directed around (Fig. 4.32a) and along (Fig. 4.32b) the body surface, while a null at the off-body direction ($\theta = 0^o$) is exhibited.

More specifically, in both planes the main lobe of the HMMPA is now located at $\theta = \pm 70^o$, which means that most of the radiation is forced parallel to the body surface while the radiation at the broadside direction is suppressed by almost 20 dB due to the shorting vias at either sides of the patch. The slight deviation from the main lobe direction in free space ($\theta = \pm 90^o$) is attributed to the interaction with the human body surface that causes scattering to the radiated beam.

Finally, the measured and simulated resonance frequency (f_r) and BW of the antenna prototypes in free space and on-body at 2.4 GHz and 5.8 GHz ISM band are concentrated in Table 4.3 and Table 4.4 respectively.

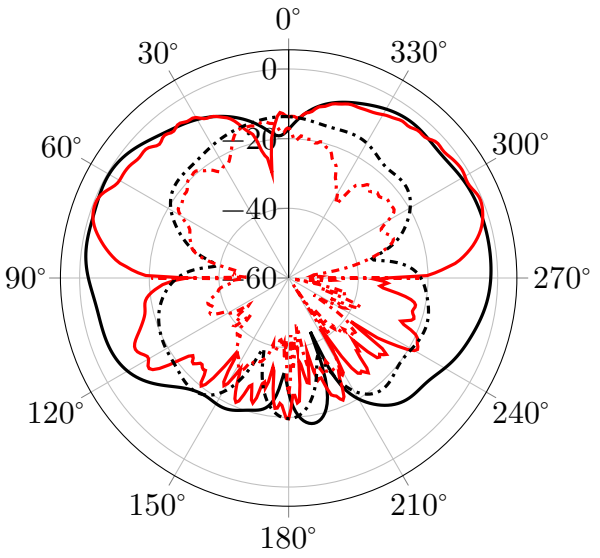

(a)

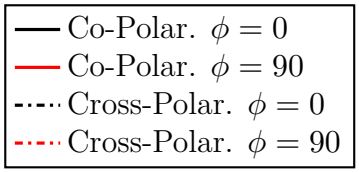

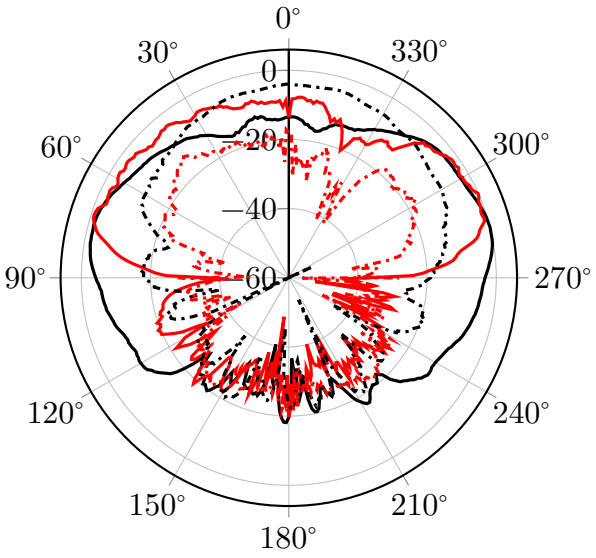

(b)

Figure 4.32 Measured normalised far-field radiation patterns in XZ-plane ($\phi = 0^o$) and YZ-plane ($\phi = 90^o$) for HMMPA on SAM chest. (a) 2.4 GHz and (b) 5.8 GHz.

Table 4.3 Resonance Frequency (f_r) and BW at 2.4 GHz ISM band

Antenna		$\mathbf{f_r}$ ***(MHz)***		**BW** ***(MHz)***	
		Meas.	***Sim.***	***Meas.***	***Sim.***
	Free Space	2450	2455	350 (14.3%)	433 (17.6%)
	On-Body	2375	2308	275 (11.6%)	275 (11.9%)
	Free Space	2450	2450	60 (2.4%)	47 (1.9%)
	On-Body	2470	2444	60 (2.4%)	42 (1.7%)
	Free Space	2470	2435	48 (1.9%)	66 (2.7%)
	On-Body	2460	2433	50 (2.0%)	73 (3.0%)

Table 4.4 Resonance Frequency (f_r) and BW at 5.8 GHz ISM band

Antenna		$\mathbf{f_r}$ ***(MHz)***		**BW** ***(MHz)***	
		Meas.	***Sim.***	***Meas.***	***Sim.***
	Free Space	5750	5790	890 (15.5%)	1100 (19%)
	On-Body	5520	5250	840 (15.2%)	1200 (22.9%)
	Free Space	5830	5800	490 (8.4%)	330 (5.7%)
	On-Body	5880	5240	500 (8.5%)	190 (3.6%)
	Free Space	5880	5810	340 (5.8%)	450 (7.7%)
	On-Body	5870	5920	340 (5.8%)	270 (4.5%)

4.4.3 Directivity, Gain and Efficiency of Wearable Antennas

The measured gain and efficiency of the MPA and HMMPA antennas are compared between free space and on-body (chest) states in Table 4.5. The effect of antenna-body coupling for different frequency bands is demonstrated. It is shown that the MPA antenna remains unaffected from the body presence at both frequency bands. The interaction with the body phantom is slightly stronger at 5.8 GHz, where the gain is increased by 1 dB from the free-space case, and efficiency drops from 89.2% to 86.5%. As for the HMMPA, it is affected more from the body presence, resulting in a gain increase of 1.6 dB at 2.4 GHz and 3 dB at 5.8 GHz and an efficiency degradation of 25% and 39.9% respectively, in respect to the free-space case. These results reveal that every antenna type has different interaction with the body, and this interaction is frequency dependent, the higher the frequency the stronger the interaction with the body.

Table 4.5 Measured Antenna Characteristics in Free Space/ On-Body (10 mm)

Antenna	***Freq.***	***Gain (dBi)***		***Rad. Efficiency (%)***	
		Free Space	***On Body***	***Free Space***	***On Body***
	2.4 GHz	8.4	8.6	93.7	93.3
	5.8 GHz	7.8	8.8	89.2	86.5
	2.4 GHz	1.9	3.5	88	63.0
	5.8 GHz	2.0	5.0	87.0	47.1

The measured directivity of the printed dipole, the MPA and the HMMPA at 0, 10 mm separation distance from the body surface is listed in Table 4.6 and Table 4.7 for 2.4 and 5.8 GHz respectively. The antenna directivity is derived from the transformed far-field results, by employing pattern integration over the full sphere.

To estimate the validity of the measured directivity, and consequently of the far-field results, it is compared with the estimated theoretical value. The theoretical directivity is based on the 3 dB (half-power) beamwidths (HPBW) of the two principal

far-field planes ($\phi = 0^o$ and $\phi = 90^o$) [5]. Supposedly that the 3 dB beamwidths are correctly tranformed from the near field measurements (the truncation affects the side lobe levels), the theoretical directivity can accurately estimate the expected wearable antenna directivity. From this comparison, the effect of the unavoidable truncation in the far-field radiation pattern (due to the finite cylindrical surface) is examined for each antenna type. In case the far-field value outside the 3 dB beamwidth is wrongly transformed, it will then produce a noticeable difference between the measured and theoretical directivity.

The theoretical directivity is calculated using the following equations [5]:

$$D_0 = \frac{4\pi(180/\pi)^2}{\Theta_{3dB,E}\Theta_{3dB,H}} \quad \text{for directional antennas} \tag{4.4}$$

and:

$$D_0 = -172.4 + 191\sqrt{0.818 + \frac{1}{\Theta_{3dB,EorH}}} \quad \text{for omni antennas} \tag{4.5}$$

where: $\Theta_{3dB,E}$ is the half-power beamwidth in the azimuth plane ($\phi = 0^o$) and $\Theta_{3dB,H}$ is the half-power beamwidth in a plane at a right angle with this ($\phi = 90^o$). For omni-directional antennas on the human body (HMMPA), each of the two beamwidths can be used for the derivation of $\Theta_{3dB,elev}$.

It is observed from Table 4.6 that the theoretical directivity value approaches the measured value for the case of the printed dipole and the MPA antenna, while for the HMMPA antenna the measured directivity is higher than the theoretical. For the HMMPA, the maximum radiation of the omni-directional pattern is spotted at the XY- plane. However, due to the truncation above $\phi = \pm 75^o$, a portion of the radiated energy is not taken into account in the calculation of the directivity and as a result appears higher than expected. Furthermore, when the measured directivity is compared with the simulated, the difference is less than 0.9 dB for the printed dipole, less than 0.4 dB for MPA and less than 2 dB for HMMPA. It is then concluded that a lower accuracy is achieved with the cylindrical near-field measurement method when assessing omni-directional antennas that their maximum radiation is not in the broadside direction facing the probe's aperture, but tangential to the body surface.

Looking at the measured directivity at 5.8 GHz (Fig. 4.7), compared with the theoretical and simulated values, in the case of the MPA antenna there is a close matching. For the printed dipole and HMMPA antennas, while there is a good agreement with the theoretical value, the simulated result is further apart. This

Table 4.6 Measured, Simulated and Theoretical Directivity at 2.4 GHz

Antenna	***Separation***	***HPBW*** (^{o})		***Directivity (dBi)***		
		$\Theta_{3dB,E}$	$\Theta_{3dB,H}$	***Theor.***	***Meas.***	***Sim.***
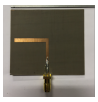	0mm	82.8	68.2	8.6	8.1	7.2
	10mm	96.4	55.8	8.8	8.8	8
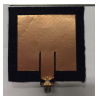	0mm	73.5	67.4	9.2	9.0	9.0
	10mm	72.9	70.1	9.1	8.9	8.5
	0mm	59.2	N/A	3.3	6.2	4.0
	10mm	47.9	N/A	4.1	5.5	4.1

Table 4.7 Measured, Simulated and Theoretical Directivity at 5.8 GHz

Antenna	***Separation***	***HPBW*** (^{o})		***Directivity (dBi)***		
		$\Theta_{3dB,E}$	$\Theta_{3dB,H}$	***Theor.***	***Meas.***	***Sim.***
	0mm	81.9	70.8	8.5	9.7	8.4
	10mm	97.2	42.5	10.0	11.4	8.9
	0mm	78.7	53.1	9.9	9.5	9.6
	10mm	91.1	46.7	9.9	9.4	9.4
	0mm	26.17	N/A	6.4	7.7	4.3
	10mm	17.86	N/A	7.9	8.2	4.3

big discrepancy is attributed mainly to the lower accuracy of the CNF measurement when assessing omnidirectional antennas and also due to the non uniformity of the chest surface of the numerical SAM phantom that creates an inconsistency in the antenna-body separation distance. In this frequency band (5.8 GHz), the results are more sensitive to small discrepancies of the separation distance with the human body between measurements and simulations. However, the measured directivity of the HMMPA antenna is closer to the theoretical value, possibly due to the bigger scattering effect of the body that allows less radiation to the high elevation angles and a larger angle of validity in respect to 2.4 GHz. Overall, in most of the cases, a good measurement accuracy is achieved, with less than 1 dB difference between the measured and simulated directivity.

The measured gain and efficiency of these antennas on the SAM phantom are listed in Table 4.8 and Table 4.9 for 2.4 and 5.8 GHz respectively. A difference of less than 5.6% at 2.4 GHz and 12.2% at 5.8 GHz is found in the antenna efficiency between measurements and simulations for all the antenna types. This result is very promising, having in mind the strong interaction in the near-field region of the wearable antennas with the full-body SAM phantom. Especially, in the printed dipole's case, which experiences the strongest interaction with body. For the two wearable MPA and HMMPA antennas, the maximum difference is even lower, 3.3% at 2.4 GHz and 4.2% at 5.8 GHz. This difference is expected to be increased with frequency since the wavelength is smaller and every error in the antenna dimensions and the placement on the body phantom becomes important.

As far as the MPA is concerned, a gain of 8.6 dBi and an efficiency of 93.3% are obtained with 10 mm separation distance. At the 0 mm separation distance, gain is slightly reduced to 8.4 dBi and efficiency drops to 87.3% owing to the stronger scattering of the radiated power on the body. The performance of HMMPA is affected more from the body presence, since the gain is found to be 3.5 dBi and 3.8 dBi for 10 mm and 0 mm separation distance respectively. The corresponding efficiency is reduced to 63.0% and 57.0% respectively.

As the antenna-body separation distance is reduced in the wearable patch antennas case, the gain is less affected from the body in contrast to the printed dipole's case. This is partly explained by the fact that in the printed dipole case, the dominant effect is the absorption of the radiated energy in the SAM phantom. While in the wearable antennas case, scattering becomes dominant, as the back radiation is shielded due to the presence of the ground plane which reduces the absorption in the

Table 4.8 Gain and Rad. Efficiency at 2.4 GHz

Antenna	***Separation***	***Gain (dBi)***		***Rad. Efficiency (%)***	
		Meas.	***Sim.***	***Meas.***	***Sim.***
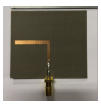	0mm	-5.1	-2.7	4.7	10.3
	10mm	2.3	2.1	22.2	25.5
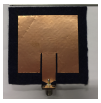	0mm	8.4	8.2	87.3	84
	10mm	8.6	8.1	93.3	91.8
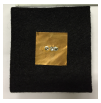	0mm	3.8	1.8	57.0	59.8
	10mm	3.5	1.9	63.0	60.0

Table 4.9 Gain and Rad. Efficiency at 5.8 GHz

Antenna	***Separation***	***Gain (dBi)***		***Rad. Efficiency (%)***	
		Meas.	***Sim.***	***Meas.***	***Sim.***
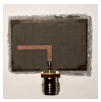	0mm	1.0	2.5	13.5	25.7
	10mm	9.1	6.2	58.2	53.6
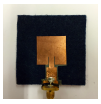	0mm	8.7	8.8	83.6	84
	10mm	8.8	9.1	86.5	91.7
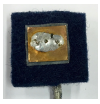	0mm	3.8	0.2	40	39.3
	10mm	5.0	1.1	47.1	47.4

body.

Several factors can impose errors in the estimation of the absolute antenna gain and consequently to efficiency, creating a deviation between measurements and simulations:

- Antenna fabrication accuracy (antenna dimensions and feeding).
- Gain calibration accuracy of the measurement system.
- Antenna placement accuracy that produces different interaction with body.
- Accuracy in assigning the material properties, dielectric and geometric body properties in the simulation.

After demonstrating the accuracy of the CNF measurement method in the characterisation of wearable antennas efficiency on chest, the effect of the different dielectric loading introduced from each on-body location is examined. For each antenna type and on-body location, the measured radiation efficiency is averaged over the full bandwidth at 2.4 and 5.8 GHz respectively.

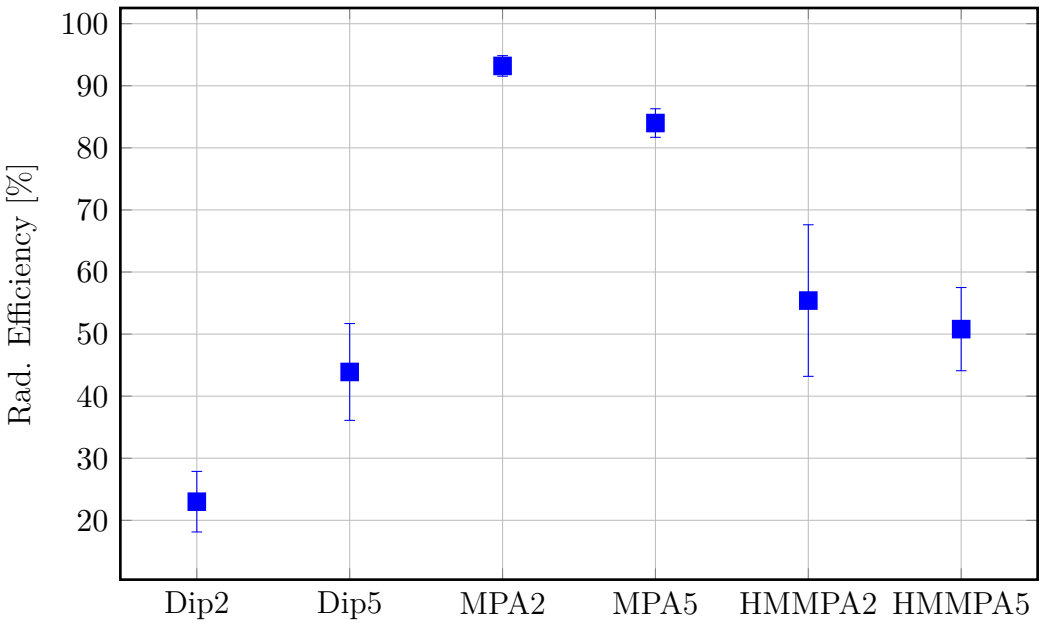

Figure 4.33 Measured radiation efficiency as a function of on-body location at 2.4 and 5.8 GHz.

The results in Fig. 4.33 show that the radiation efficiency of the patch antenna (MPA) in both frequency bands is not dependent on the body location while the

printed dipole and the higher mode patch antenna (HMMPA) are more affected. This is attributed to the different radiation characteristics and geometry of each antenna type. More specifically, the MPA shows an average radiation efficiency of 93.2% and 84% at 2.4 and 5.8 GHz with a standard deviation of 1.66% and 2.3% respectively. However, the HMMPA antenna presents a higher dependence on body location (standard deviation of 12.21% and 6.7%) while its average efficiency value is lower than the MPA (55.4% and 50.8%). The reduced efficiency in the HMMPA case is explained due to the larger body absorption, since the main part of the radiation pattern is facing the body surface. For the case of the printed dipole, the average efficiency (23% and 43.9%) is even more degraded due to the lack of ground plane that allows a strong interaction with the body tissue. The variation of its performance regarding the body location is high, with a standard deviation of 4.88% and 7.8% at 2.4 and 5.8 GHz respectively.

4.5 Mean Effective Gain of Wearable Antennas

After employing the CNF measurement technique, information about wearable antenna gain and efficiency has arisen. However, this is not enough to describe the wearable antenna performance in a realistic environment operating conditions.

The mean effective gain (MEG) is introduced as a measure of the average system gain that characterises the antenna performance in a realistic local propagation scenario. In other words, it is a simple and fast way to describe the installed antenna performance including the close disturbers (human body) and the distribution of the local propagation. With this approach, an evaluation of the off-body channel performance is achieved without the need for channel measurements. It combines the full polarimetric (3D) far-field pattern of the antenna and the power distribution of the incoming waves of a given channel angular scenario resulting into a unique gain [16]. It should become clear that MEG does not resemble or contain the actual antenna gain but uses the normalised spherical far-field antenna pattern. MEG can be also used in multiple antenna systems in order to determine the average power ratio of each individual antenna element.

The calculated mean effective gain follows the equation given in [16]:

$$MEG = \int_0^{2\pi} \int_0^{\pi} \left\{ \frac{XPR}{1+XPR} G_\phi(\theta,\phi) P_\phi(\theta,\phi) + \frac{1}{1+XPR} G_\theta(\theta,\phi) P_\theta(\theta,\phi) \right\} \sin\phi \, d\phi d\theta \tag{4.6}$$

where: $XPR = P_V/P_H$ is the mean incident power ratio between vertical ($\phi-$) and horizontal ($\theta-$) polarised incoming waves, G_ϕ and G_θ are the $\phi-$ and $\theta-$ components of the antenna power gain pattern, P_ϕ and P_θ are the angular density functions of incoming plane waves for the two components respectively.

For an ideal isotropic antenna with equal gain for each polarisation ($G_\theta = G_\phi = 0.5$), $MEG = -3dB$ independently of the propagation scenario. Respectively, for a dual-polarised isotropic propagation scenario ($P_\phi = P_\theta = 0.5$), the $MEG = -3dB$ irrespective to the antenna being used. These facts show the duality of the MEG that can be equally affected by the channel as well as antenna characteristics. The best performance is achieved when the antenna's far-field pattern and the amplitudes of the incoming waves are conjugate matched. Hence, the information of MEG can help maximise the path gain in a specific link, knowing a priori the polarisation and DoA of the incoming waves.

In this study, the mean effective gain of the printed dipole, MPA and HMMPA antennas is calculated at both 2.4 and 5.8 GHz when attached on the chest of SAM phantom. Three propagation scenarios are assumed: outdoor, outdoor-indoor and indoor propagation environment. These results can be used in some off-body propagation scenarios as well as for comparing the performance of other antennas on the human body. The optimal wearable antenna for the specific propagation scenario will be the one that maximises the MEG. Hence, it can be used to optimise wearable antennas in realistic scenarios as well as select the optimal body location. The same computational method for determining wearable antenna performance in realistic propagation conditions can be employed respectively for on-body scenarios.

Incoming (LOS) plane waves for azimuth angles are always uniformly distributed as the user's movement is considered random, while for elevation angles, plane waves follow a Gaussian angular power density function with parameters as shown in Table 4.10, after field measurements conducted in [17]. In addition, the cross-polarization ratio XPR is also provided, which is the mean power ratio between the vertically and horizontally polarised incoming waves. The higher this value the more directive is the channel behaviour.

The vertically (P_ϕ) and horizontally (P_θ) polarised incoming plane waves are described by Gaussian distribution,

$$P_\phi(\theta,\phi) = A_\phi \exp(-\frac{\{\phi-\mu_V\}^2}{2\sigma_V^2}) \quad (4.7)$$

$$P_\theta(\theta,\phi) = A_\theta \exp(-\frac{\{\phi-\mu_H\}^2}{2\sigma_H^2}) \quad (4.8)$$

where: azimuth angle varies between $0 \leq \theta \leq 2\pi$, elevation angle between $0 \leq \phi \leq \pi$, μ_V, μ_H is the mean elevation angle, and σ_V, σ_H is the elevation angle spread for vertical and horizontal polarised incoming waves. A_ϕ and A_θ are constants determined by:

$$\int_0^{2\pi}\int_0^{\pi} P_\theta(\theta,\phi)\sin\phi\, d\phi d\theta = \int_0^{2\pi}\int_0^{\pi} P_\phi(\theta,\phi)\sin\phi\, d\phi d\theta = 1 \quad (4.9)$$

Table 4.10 Statistical Parameters of the Gaussian elevation distribution for different propagation scenarios.

Scenario	***Vertical Pol.*** (E_ϕ)		***Horizontal Pol.*** (E_θ)		***XPR (dB)***
	μ_V	σ_V	μ_H	σ_H	
Outdoor	2.2^o	5.4^o	3.5^o	7.8^o	11.4
Indoor	3.8^o	8.7^o	1.9^o	10.7^o	7
Outdoor-Indoor	0.6^o	8.1^o	1.8^o	14.6^o	10.7

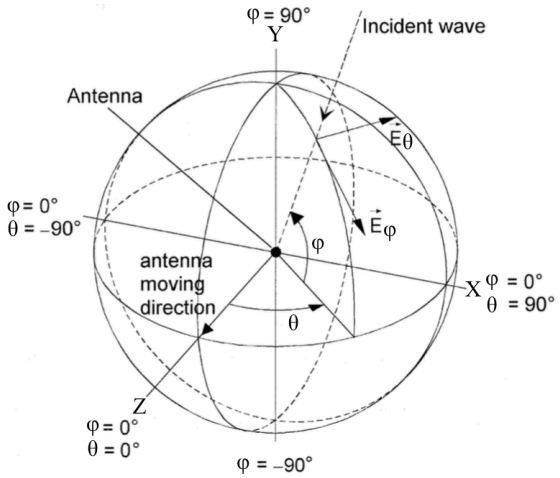

Figure 4.34 Coordinate system of the AUT and the incoming waves.

Since the wave propagation in azimuth is assumed uniform, it is expected that any antenna that shows a high MEG, achieves a high degree of pattern coverage and improves the link level. In addition, by using MEG as a single figure of merit, the quantitative difference between the measured and simulated antenna 3D far-field pattern is obtained, since the same propagation coefficients are used in both calculations.

In Fig. 4.35 and Fig. 4.36, the mean effective gain of wearable antennas is plotted, both from measurements and simulations, at 2.4 GHz and 5.8 GHz respectively, in outdoor, indoor and outdoor-indoor environment. It is shown that the measured and simulated MEG for both the MPA and dipole in vertical orientation is in perfect agreement. However, in the case of the HMMPA and dipole in horizontal orientation a noticeable discrepancy is observed, which can be attributed to the truncation error when capturing an omni-directional radiation pattern on human body with the CNF technique. Due to the dominant vertical polarisation of the incoming waves ($XPR >> 0dB$), the MPA and printed dipole in vertical orientation seem to achieve the best performance for the specific assumed scenarios. Accordingly, the worst performance is achieved from the printed dipole in horizontal orientation and the HMMPA antenna, which are more suitable for on-body links.

More specifically, the MPA antenna achieves the best off-body performance among the three different antennas, since it has the higher value of MEG over 0 dB for both frequency bands. In addition, a close matching with the simulation results is observed that proves the CNF measurement accuracy. The second best performance is achieved by the printed dipole in vertical orientation on the human body, resulting in a MEG slightly above 0 dB. Both antennas are favoured from the vertically polarised propagation profile in the selected common environments that matches with the far-field vertical E-field component.

As far as the dipole antenna in horizontal orientation is concerned, which excites a horizontal E-field component, a low MEG performance is achieved and consequently a poor matching with the propagation profile. MEG ranges from -5 dB in the indoor environment to -10 dB in outdoor. The best off-body performance, which is found in the indoor environment is due to the lower XPR or stronger horizontal component in respect to the other two propagation profiles.

At last, with HMMPA, a poor off-body performance is achieved, since it exhibits a stronger horizontal than vertical E-field component and radiates omni-directionally across the body surface while minimises the radiation around the azimuth.

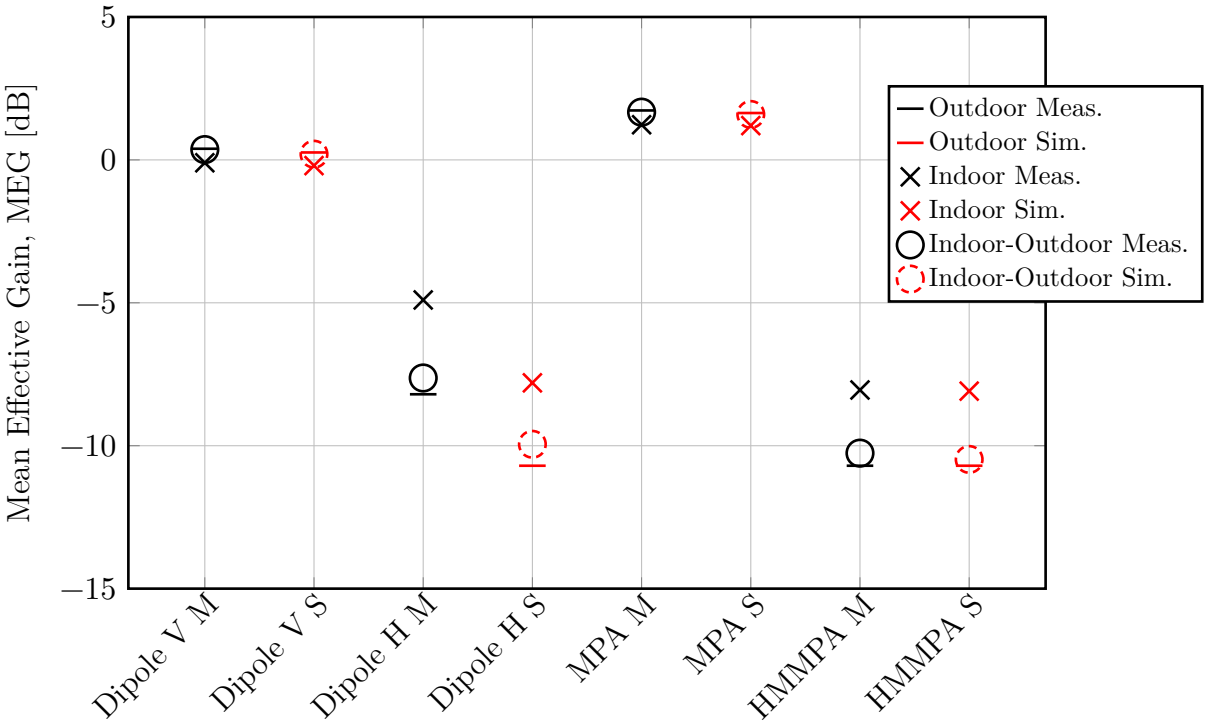

Figure 4.35 Measured and simulated MEG at 2.4 GHz.

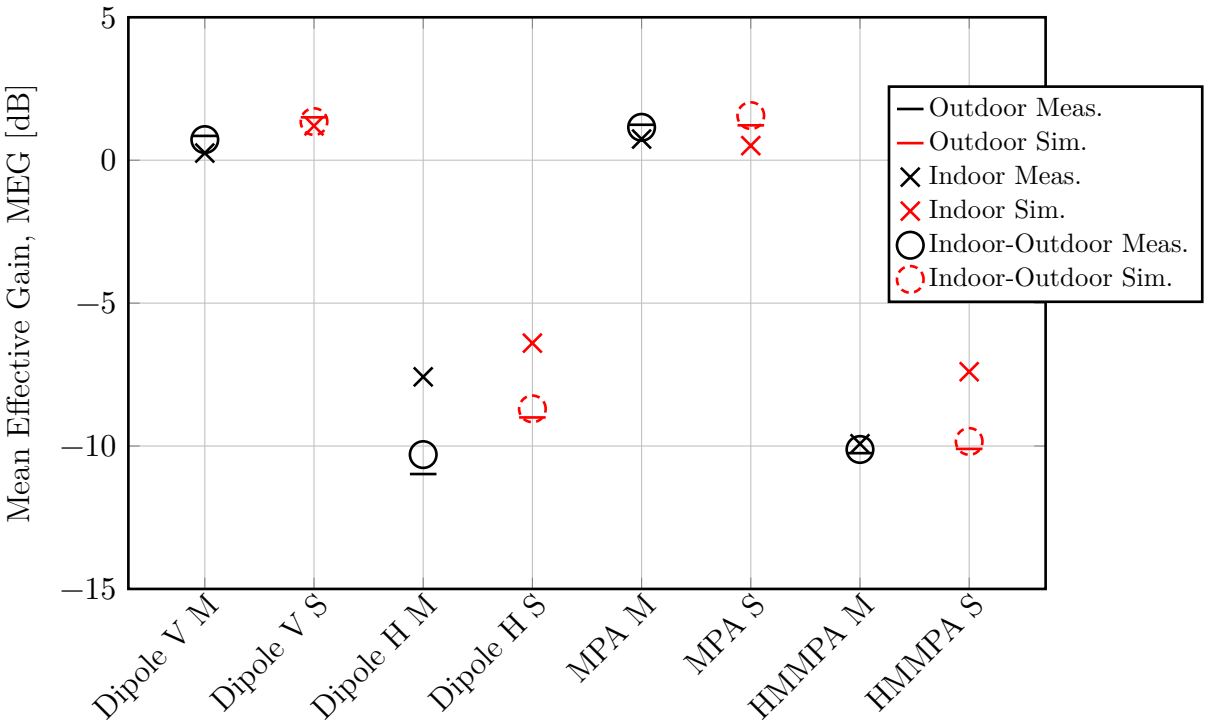

Figure 4.36 Measured and simulated MEG at 5.8 GHz.

4.6 Conclusions

In this chapter, a measurement methodology was demonstrated for analysing wearable antenna performance on the human body. A cylindrical near-field measurement is employed together with a full-body anthropomorphic phantom to simulate accurately the human body dielectric and geometrical properties. This measurement system can be used as a repeatable test-bed for evaluating the performance of wearable antennas. The accuracy is retained for any antenna-body tissue separation distance, body location and frequency of operation. Thus, wearable antenna designs can be optimised with the aim of achieving better impedance matching, less radiation pattern distortion and absorption in the human body.

To validate the proposed measurement methodology, a printed dipole is tested in two orientations and is compared with EM simulations, resulting in a good agreement. Subsequently, two wearable antennas are evaluated in terms of the near-field and far-field performance. The measured near-field pattern can be a useful tool to optimise the design of a wearable antenna system by depicting the propagation behaviour on the surface of human body. An insight is gained on how an antenna radiates in proximity to the human body and how it is influenced from the selected on-body location. Specifically, the measured electric field of the MPA is concentrated in a small area in front of the human body while the HMMPA enhances the on-body coupling mechanism since the electric field is distributed in a larger area around the human body. Furthermore, it is also demonstrated that the wearable antenna efficiency can be precisely determined from the 3D far-field pattern on the full-body SAM phantom, which is otherwise impractical with the standard far-field technique. The MPA shows a radiation efficiency of 93% and 87% at 10 and 0 mm separation distance, remaining unaffected from the body presence due to the large ground plane and the broadside off-body radiation pattern. The HMMPA presents a reduced efficiency of 57% and 63% respectively, which means that interacts more with the body due to the omni-directional radiation pattern, causing an increased energy absorption inside the body.

The off-body wearable antenna performance is also studied by calculating the mean effective gain for three different propagation environments: outdoor, indoor and outdoor-indoor. Among the three different wearable antennas tested, the MPA antenna achieves the best off-body performance, with MEG values over 0 dB, while the HMMPA antenna, exhibits a poor off-body performance with MEG values close to -10 dB.

In a future study, the CNF measurement technique can be exploited in the direction of modelling the wearable antenna performance for different body type, frequency of operation and antenna design, resulting in de-embedding the antenna characteristics from body-centric channel models.

References

[1] P. S. Hall and Y. Hao, *Antennas and Propagation for Body-Centric Wireless Communications. Second Edition*, 2nd ed. (Artech House, Inc., 2012).

[2] T. Loh, D. Cheadle, and L. Rosenfeld, Electronics .

[3] C. Parini, S. Gregson, J. McCormick, and D. J. van Rensburg, *Theory and Practice of Modern Antenna Range Measurements*, 1st ed. (IET, 2014).

[4] Y. Nechayev, P. Hall, C. Constantinou, Y. Hao, A. Alomainy, R. Dubrovka, and C. Parini, "On-body path gain variations with changing body posture and antenna position," In *Antennas and Propagation Society International Symposium, 2005 IEEE*, **1B,** 731–734 vol. 1B (2005).

[5] C. A. Balanis, *Antenna Theory: Analysis and Design*, 3rd edition ed. (Wiley-Interscience, 2005).

[6] G. Conway and W. Scanlon, "Antennas for Over-Body-Surface Communication at 2.45 GHz," IEEE Transactions on Antennas and Propagation **57(4),** 844–855 (2009).

[7] W. Leach and D. Paris, "Probe compensated near-field measurements on a cylinder," IEEE Transactions on Antennas and Propagation **21(4),** 435– 445 (1973).

[8] A. D. Yaghjian, "Near-field antenna measurements on a cylindrical surface: A source scattering-Matrix formulation," Technical report, Boulder, Colorado : Dept. of Commerce, National Bureau of Standards, Institute for Basic Standards, Electromagnetics Division (1977) .

[9] *MIDAS Measurement Software, Orbit*, Available online: http://www.orbitfr.com/content/products/midas-measurement-software.

[10] "IEEE Spectrum," IEEE **52(6),** 1–96 (2015).

[11] *MCL-T whole-body solid SAM phantom*, Available online: http://www.mcluk.org/solid_bodies.php.

[12] *IEEE Recommended Practice for Near-Field Antenna Measurements* (IEEE Antennas and Propagation Society, 2012).

[13] C. A. Balanis, *Modern Antenna Handbook*, 1st ed. (John Wiley & Sons, Inc., Hoboken, NJ, USA, 2008).

[14] F. Harrysson, J. Medbo, A. Molisch, A. Johansson, and F. Tufvesson, "Efficient experimental evaluation of a MIMO handset with user influence," Wireless Communications, IEEE Transactions on **9(2),** 853–863 (2010).

[15] "IEEE Standard Test Procedures for Antennas," ANSI/IEEE Std 149-1979 pp. 1–135 (1979).

[16] T. Taga, "Analysis for mean effective gain of mobile antennas in land mobile radio environments," Vehicular Technology, IEEE Transactions on **39(2),** 117–131 (1990).

[17] K. Kalliola, K. Sulonen, H. Laitinen, O. Kivekäs, J. Krogerus, and P. Vainikainen, "Angular power distribution and mean effective gain of mobile antenna in different propagation environments," Vehicular Technology, IEEE Transactions on **51(5),** 823–838 (2002).

Chapter 5

Novel Embroidered Wearable Antennas

Two novel wearable antennas are proposed in this chapter, which are designed and fabricated exclusively with textile materials, avoiding rigid metallic parts and dielectrics. Both designs are suitable to be fully integrated in user's clothing. A novel fabrication process using the state-of-the-art digital embroidery machine at Loughborough University is demonstrated, which can realise complex geometries with less effort and offer the potential of automating the fabrication process. The proposed textile antennas are tested with the cylindrical near-field measurement method on a full-body anthropomorphic phantom, and compared with EM simulations. A reasonable trade-off between practicality and on-body performance is achieved. It will be shown that these low profile antenna prototypes with conductive threads can operate in close contact with human body with no severe resonance frequency detuning and radiation performance reduction.

In the beginning of the chapter, a brief introduction of the e-textiles and the embroidery process for wearable antennas is presented. Following, a multilayer low-profile textile higher mode patch antenna (HMMPA) at 2.4 GHz is proposed for its ability to generate surface waves on the human body. The higher mode is achieved by utilising textile embroidered vias with conductive sewing thread in order to provide an enhanced on-body propagation. Moreover, a broadband textile spiral antenna exhibiting a circular polarisation is presented, which is suitable for off-body communications. It can be used for unobtrusive communication of military and security personnel as well as it can be implemented in safety life vests.

5.1 E-textiles

In order to realise wearable RF electronics in clothing, "e-textiles" (or "electro-textiles") are employed, which are conductive textiles that can provide high conductivity while maintaining the features of ordinary textiles such as high flexibility, durability and integration into fabrics in the manufacturing process.

The most popular techniques for the manufacturing of "e-textiles" are: by chemical deposition (electroplating) of the non-conductive fabric with a conductive layer and by knitting or weaving a non-conductive fabric with a conductive yarn. There are several commercially available conductive textiles such as the Nora-Dell [1] from Shieldex or the Pure Copper Taffeta [2] and nickel copper ripstop [3] from LessEMF.

The majority of the textile antennas found in the literature have been realised by using "e-textiles" due to the simplicity of the assembly process without needing any special equipment. Mostly planar antennas are employed, which have simple patterns that allow the conductive fabrics to be manually cut. In a recent study [4], wearable textile patch antennas have been developed to be integrated in spacesuits. Nickel copper ripstop from Less EMF Inc. was selected among several conductive materials that were tested, as the best material with low sheet resistance and high durability and was attached to the substrate with a spray adhesive. Manual cutting of the conductive layer was replaced with laser cutting to improve precision and accuracy of patch dimensions.

However, in the case of antennas with more complex patterns and shapes, a more precise control of the conductive parts is needed, which can be achieved with the embroidery process.

5.2 Embroidery Process

By employing the embroidery technique, wearable electronics can be fully integrated into clothing with enough precision while reducing the manufacturing cost [5]. It can enable the mass production of garments with integrated embroidered textile antennas. To date, a wide range of research has been carried out to investigate the performance of the conductive fabric for high frequency applications, including antennas and frequency selective surfaces [6–9]. The repeatability of flexible patch antennas, fabricated with the embroidery technique by weaving conducting patterns on fabrics has been proved in [10]. However, the embroidery technique is more useful

for dipole or spiral antennas that require a smaller length of conductive thread and may be difficult to cut out manually as opposed to patch antennas. In addition, since the currents in embroidered antennas prefer to flow along the direction of the threads rather than from thread to thread, it is more more suitable for linear antennas [11].

Two types of conductive threads or "e-fibers" are available [12] for embroidery: monofilament and multifilament. Some commonly used multifilament threads are the Liberator [13] and Amberstrand [14], shown in Fig. 5.1.

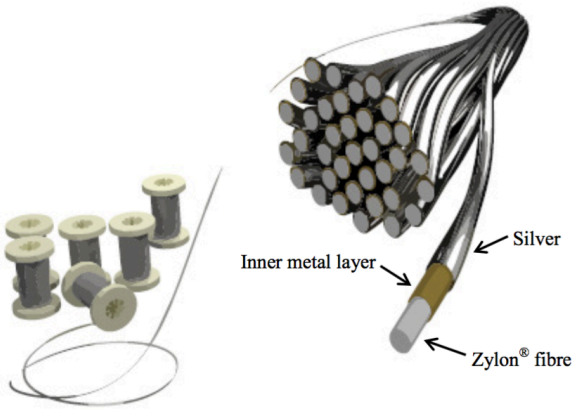

Figure 5.1 Sketch of the multi-filament commercial thread Liberator [13].

In the Liberator fiber, each filament is composed of high strength and flexible polymer core that incorporates conductive metallic coating, commonly silver, offering a high conductivity but at the expense of high cost.

Bending and compression effects to the antennas' textile substrate appear inevitably during the embroidery process. It is challenging to systematically model these effects in an EM simulator. Hence, conclusions can be drawn herein by comparing the measured (fabricated) with the simulated (flat) results. In the case of HMMPA, only compression effect is evident created between the top and ground plane in the area close to the embroidered shorting and feeding vias. The effect of bending is negligible due to the small total antenna size in body frequencies. The compression effect in the fabricated HMMPA over the simulated is not evident in both the S_{11} results and in the shape of the radiation pattern.

In the case of spiral antenna, it inevitably takes the shape of the body curvature. It is shown that the effect of bending in the impedance matching and radiation efficiency is minor, after performing a parametric simulation. Due to its comparable size to the phantom's torso, it is only measured in the realistic bended case. Compression of the

textile material due to the embroidery process is not evident by carefully selecting a stitching density that has minimum tension.

5.3 Higher Mode Embroidered Patch Antenna

This section presents an all-textile higher mode wearable patch antenna (HMMPA) that has been designed to radiate omni-directionally on the human body at 2.4 GHz ISM band. Emphasis is given to the embroidery process of the textile vias with conductive sewing thread that play an important role in generating the optimal mode for on-body operation. The embroidery technique enables the fabrication of a multilayer side-fed low-profile antenna, which could be placed flush against the body.

The proposed textile HMMPA antenna is compared with the probe-fed HMMPA antenna, presented in Section. 3.6 that was fabricated with rigid copper radiating parts, for both free space and on-body conditions. The on-body antenna performance is tested by using the CNF measurement facility with a full-body specific anthropomorphic mannequin (SAM) phantom, in the anechoic chamber. Results show that the proposed textile HMMPA antenna with vias made from conductive thread can radiate on-body with good efficiency while minimising the radiation at the broadside direction.

5.3.1 Introduction

In a number of cases, shorting vias have been used for the excitation of the monopole-like propagation mode in the form of copper vias in rigid patch antennas [15–22] or embroidered vias in fabric patch antenna realisations [23–28]. In [24], different shorting techniques have been tested through EM simulations. It was shown that by using embroidered conductive yarn instead of silver fabric or PEC, radiation gain dropped by 2.6 dB at 4.5 GHz while radiation efficiency reduced by 2.8 dB. This was attributed to high conductor losses, although the performance was improved for higher frequencies.

In a recent study, a textile circular patch antenna has been proposed with a thickness profile of 1 mm and textile embroidered shorting vias [25]. For the feeding via, the centre pin of the probe-fed coaxial connector was used instead of a conductive thread via, which introduces a non-textile part in the design. In the same work, in order to study the antenna performance, a rectangular phantom with dielectric

material properties of muscle tissue was used, which is a simplified approximation of a real human body, without considering scattering and shadowing effects from different body parts. Moreover, the probe-fed design of the proposed antenna makes it impractical to be measured directly on a real human body and the achieved relatively low on-body efficiency (14%) leaves room for further design improvement.

In the next section, the proposed multilayer HMMPA antenna design is presented together with some fabrication challenges. A normal to body polarisation that generates surface wave propagation is demonstrated through EM simulation. The measurement results are discussed in detail regarding the impedance matching and the far-field radiation characteristics.

5.3.2 Antenna Design

The optimised HMMPA antenna dimensions, as resulted from EM simulations in CST Microwave Studio, are shown in Fig. 5.2. The overall antenna size is: 5 cm x 5 cm x 0.4 cm at the 2.4 GHz ISM band. The exploded 3D view of the multilayer HMMPA antenna is shown in Fig. 5.3. It is comprised of four layers: the top patch, the felt substrate, the transmission line on top of a thin felt substrate and the ground plane.

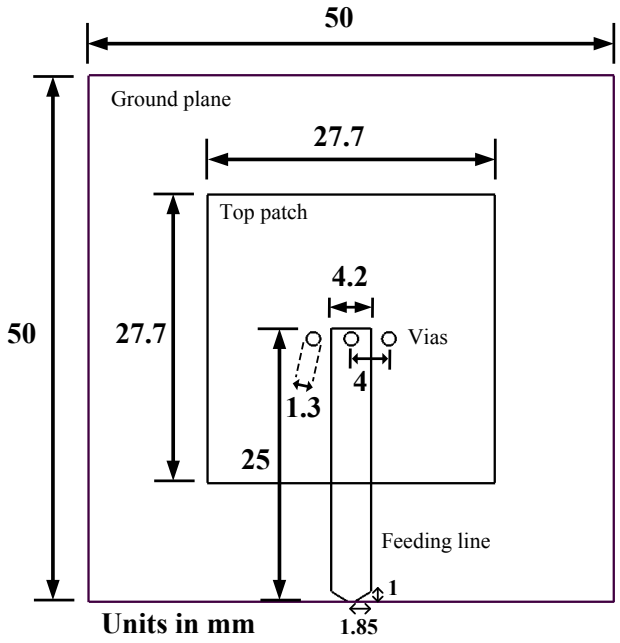

Figure 5.2 Dimensions of the textile HMMPA antenna prototype.

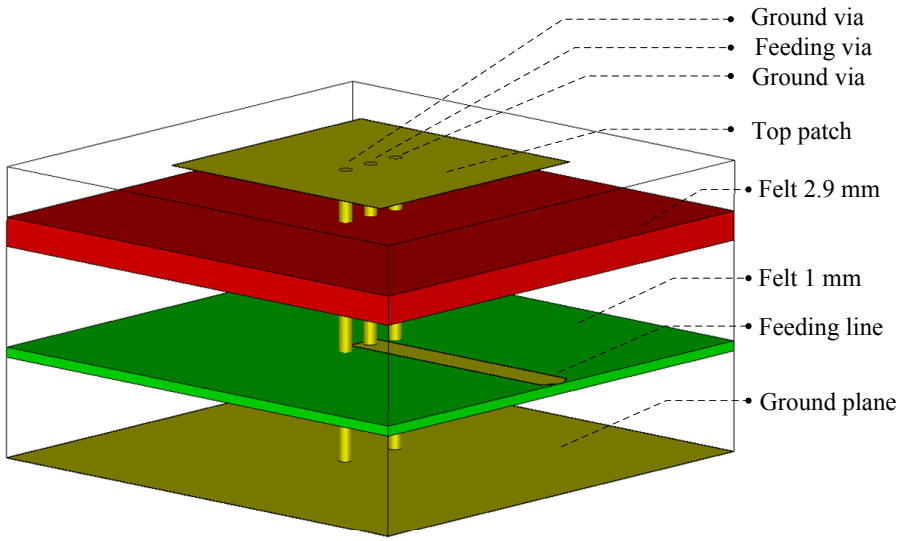

Figure 5.3 Exploded 3D view of the textile multilayer HMMPA antenna design.

The proposed HMMPA antenna is selected instead of other antenna types as the optimal choice for maximising on-body propagation. It can be comfortably worn and embedded in clothing due to its unobtrusive low-profile design. Other textile antenna types, such as PIFA or planar monopole antennas that achieve an omnidirectional radiation pattern are found in the literature [29, 30]. The textile PIFA, exhibits a comparable on-body efficiency with the HMMPA up to 40%, although it fails to generate a strong surface wave propagation. As far as a textile monopole is concerned, due to the lack of a large ground plane, the radiation pattern is distorted when placed on the body surface.

The proposed antenna can excite a strong surface or creeping wave propagation mode that results in good coverage around the body surface, reducing the path loss and minimising fading in on-body channels. Some possible applications, that are favoured from the strong on-body wave propagation of the textile HMMPA antenna, can be found in:

- *Medical and fitness applications*: where many vital signs sensor readings need to be collected from a central unit hub placed on the user's body surface.
- *Military and space applications*: where several wearable devices need to communicate with an off-body access point via an on-body central relay device.
- *Personal entertainment*, where, for example, wireless headphones or a smart

watch need to be connected with a mobile terminal placed on the surface of the human body.

5.3.3 EM Simulation of the Antenna on the Human Body

In this section, the suitability of the designed textile HMMPA antenna for on-body communications is examined via EM simulation. The electric field distribution created from the textile HMMPA antenna on the human body is presented in Fig. 5.4.

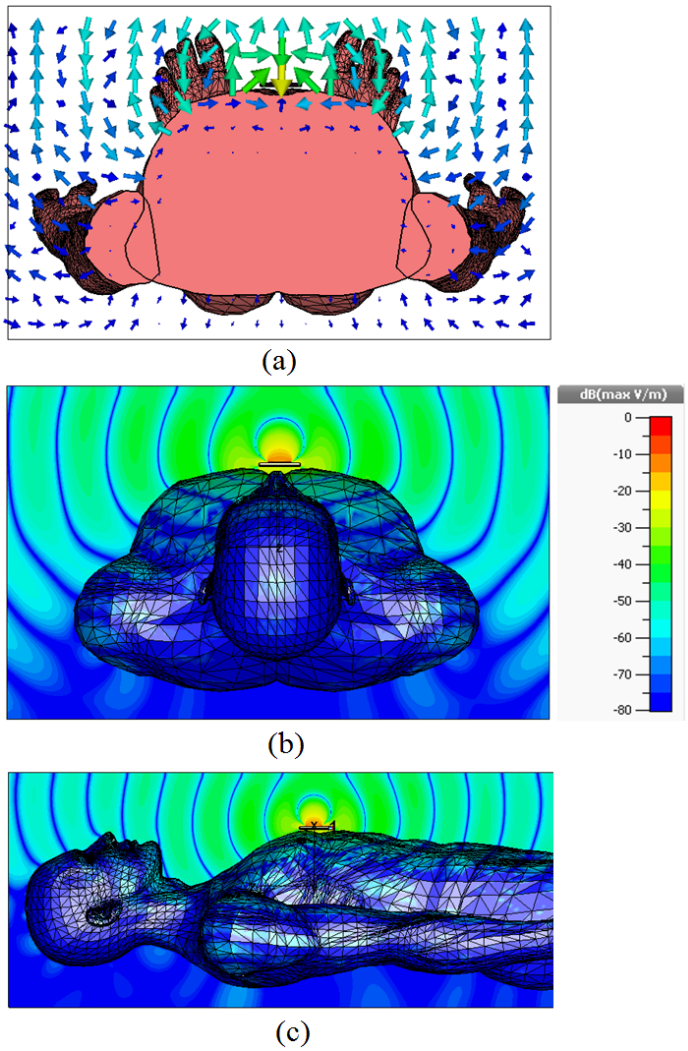

Figure 5.4 (a) Normalised electric field vector of HMMPA antenna in a cross section of SAM phantom derived from EM simulation at 2.4 GHz. Normalised electric field amplitude (b) around and (c) along SAM phantom.

The numerical model has the same geometrical and dielectric characteristics as the actual SAM phantom with homogeneous dielectric material emulating an average of human body tissues with $\epsilon_r = 35.4$ and $\sigma = 1.81$ S/m at 2.412 GHz.

In Fig. 5.4a, the normalised electric field vector in a cross section through the centre of the chest is illustrated. Moreover, the magnitude of the electric field distribution of the proposed antenna around and along the body surface is shown in Fig. 5.4b and Fig. 5.4c respectively.

A perpendicular to body electric field polarisation is achieved, which is essential for the generation of surface wave propagation [31] (Fig. 5.4a). Moreover, the penetration depth is visible which is limited in a few centimeters with a small amount of the RF energy absorbed from the body tissue. The diffraction of the propagated electric field on the body curvature is apparent (Fig. 5.4b,c). A monopole-like propagation is obtained which enables the on-body communication between low-profile wearable antennas.

The on-body coupling performance of the proposed textile HMMPA is examined via EM simulations as shown in Fig. 5.5 and compared with the printed dipole and patch antenna (MPA). The placement of the antennas at the front and back sides of the body is vertical and not conformal to the body in order to maintain the same polarisation basis since the two surfaces are not similar. The distance from the body is calculated from the centre point of each antenna to be 10 mm. The impedance matching is maintained inside the 2.4 GHz ISM band.

The $|S_{21}|$ path gain is plotted in Fig. 5.6 between two antennas placed at the front and back of a voxel phantom. It is shown that the textile HMMPA achieves a better on-body coupling performance instead of the other two antennas by 30 dB in the 2.4 GHz ISM band. This is mainly attributed to the monopole-like propagation mode that supports surface wave propagation on the surface of the human body (as shown in Fig. 5.4). The coupling performance of MPA is slightly better than the printed dipole owing to the presence of ground plane that reduces the interaction (power absorption) with human body. The high attenuation and the ripples that are evident in the MPA outside the 2.4 GHz band are due to its narrowband performance.

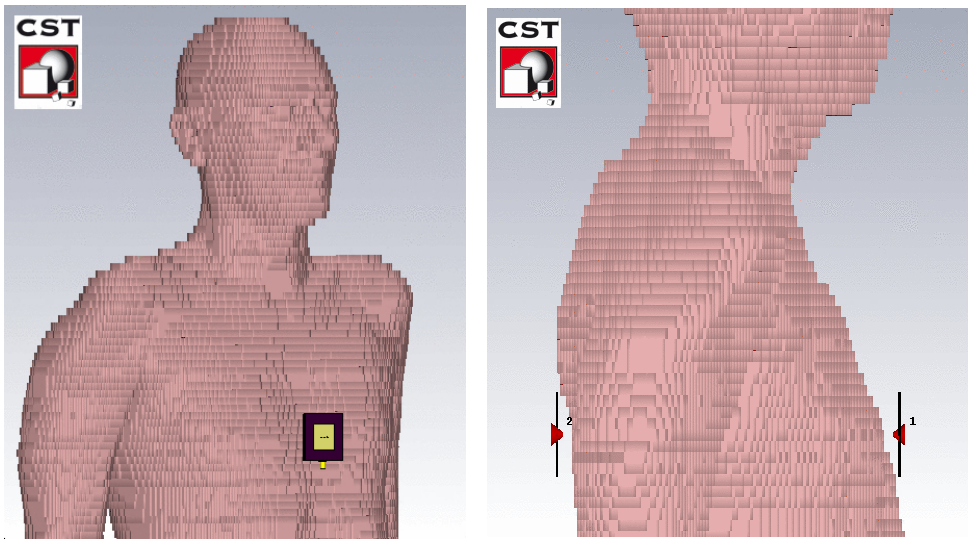

Figure 5.5 Textile HMMPA antenna attached at the front and back side of a numerical voxel phantom to simulate on-body coupling performance.

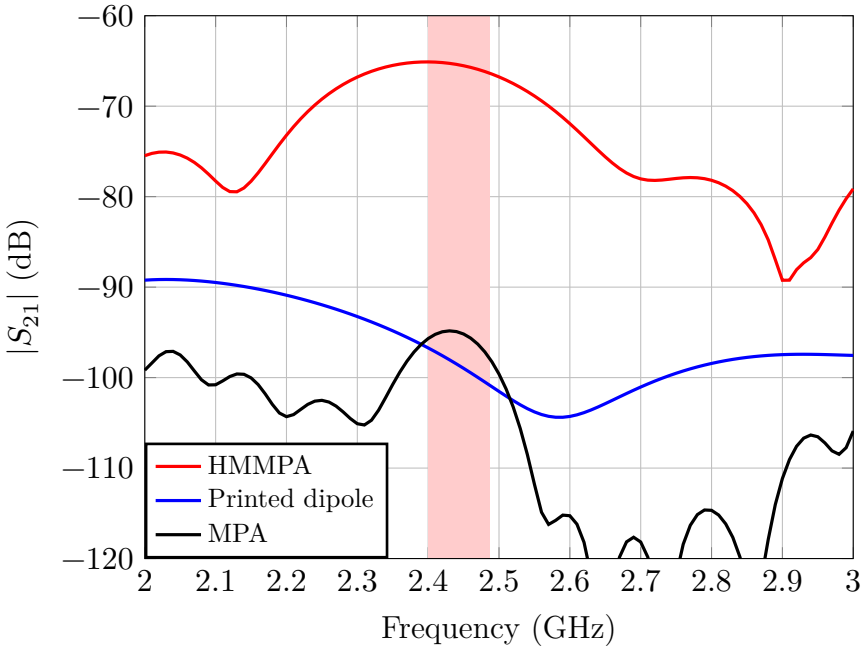

Figure 5.6 Simulated path gain $|S_{21}|$ between antennas attached at the front and back side of a numerical voxel phantom for 2.4 GHz.

5.3.4 Antenna Fabrication with the Embroidery Machine

Wearable antennas are meant to operate close to the body surface and hence they should be unobtrusive to the wearer. For antennas embedded in textile fabrics this means that the materials used should be as flexible as the fabrics.

For the creation of the antenna two conductive materials are used, Nora-Dell [1] and Liberator-20 [13]. Nora-Dell is a conductive metallized nylon fabric coated with nickel and silver that form a highly conducting flexible sheet created by Shieldex. It exhibits the same durability as fully embroidered designs, while having higher conductivity. An average surface resistance of 0.005 $\Omega/square$ according to the datasheet [1] is given (an approximate conductivity of 1.54×10^6 S/m for 0.13 mm thick Nora-Dell). It is used to create the top patch, the transmission line and the ground plane conductive parts. Liberator 20 is a 20 filament conductive thread created by Syscom Advanced Materials, Inc. Each filament has a diameter of 0.22 mm with a Vectran fiber core and is metallised with silver coating, with a DC linear resistance of around 2 Ω/ft, or an approximate conductivity of 4.5×10^7 S/m. This is used to embroider the vias that connect the top patch to the microstrip line and the ground plane.

In Fig. 5.7 the proposed textile HMMPA antenna together with the copper HMMPA antenna are displayed.

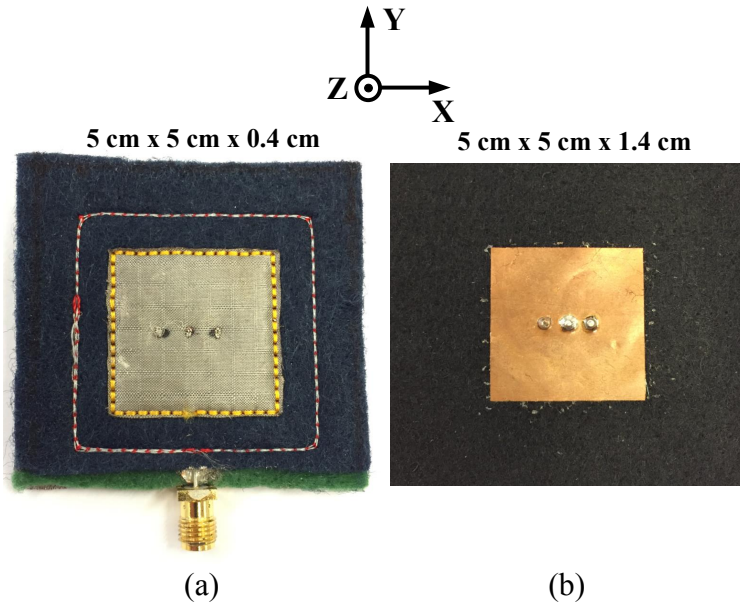

Figure 5.7 (a) Fully-textile HMMPA antenna fabricated on the embroidery machine, (b) HMMPA antenna using copper sheet and metallic vias.

The benefits of the textile HMMPA antenna over the copper HMMPA antenna are twofold. At first, the new design is made all-textile without any rigid copper parts adding more flexibility and enabling the automation of the fabrication process using the embroidery machine. Secondly, the multilayer design provides side feeding capability keeping the total thickness at 0.4 cm while the probe-fed design of the copper HMMPA antenna results in a total thickness of 1.4 cm. The multilayer side-fed design enables to be closely attached to the human body and measured directly on it.

The embroidery machine used for the fabrication of the textile HMMPA antenna at Loughborough University is shown in Fig. 5.8.

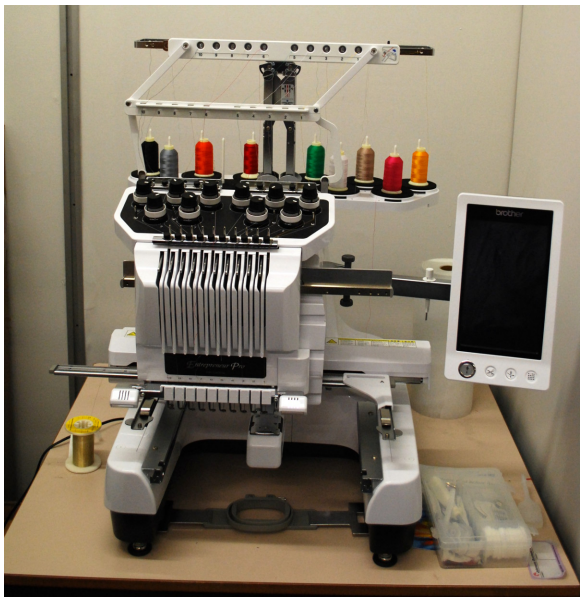

Figure 5.8 Embroidery machine at Loughborough University used for the fabrication of textile wearable antennas.

To import the design of the simulated textile antenna into the Brother Entrepreneur Pro PR1000e digital embroidery machine, PE-DESIGN NEXT software is used. This is a specialised embroidery software and not an advanced CAD software, which imposes some challenges when designing the antenna. There are three major components that need to be embroidered, the central via from the top patch to the feeding microstrip and two side vias from the top patch to the bottom ground plane.

The most important aspect in the fabrication of the embroidered vias is to keep the exact distance between the shorting vias and the centre feeding via, which is 4 mm. This distance would directly influence the antenna impedance matching as well

as the proper excitation of the desired mode and consequently its radiation pattern. Via diameter could influence the antenna performance as well. This should be 1.3 mm, as resulted from EM simulation and the previously fabricated copper HMMPA antenna. To achieve this, the embroidered vias are stitched using several conductive threads.

The different via models, which are tested in order to obtain the exact diameter and distance between the embroidered vias, are shown in Figure 5.9. For the first three models, the sewing method is set to "Satin Stitch", with the density starting at 2 lines/mm to 3 lines/mm and finally 4.5 lines/mm. For the last three models, the sewing method is set to "Concentric Circle Stitch" and the density was set to 2, 2.5 and 3 lines/mm. After testing and measuring the resulting density, it is concluded to embroider the HMMPA antenna using the 6th via model.

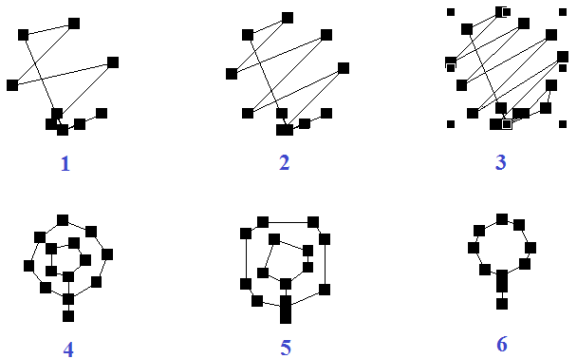

Figure 5.9 Via models with different sewing methods and stitch density.

The stages of the embroidery process are described here in detail. The first step is to stitch with conductive thread the central via to the top patch, passing through the felt dielectric to the microstrip line. This will create the feed via and hold the patch and microstrip line in place for the rest of the process. Since the via goes through the bottom side of the thin felt it could make contact with the ground plane. To prevent this, a small bit of masking tape is used to cover the bottom of the via, preventing the contact with the ground plane.

The next step is to stitch and align the top patch with the ground plane and stitch the side vias. Due to the fact that the embroidery machine is not fully prepared to handle the conductive thread, some challenges occur during the embroidery process. The main problem is that the Liberator thread unravels and is prone to break during the stitching process. To reduce these effects a small portion of oil is applied to the thread while it is being stitched. This makes the individual thread filaments

stick together and unravel less. After this, the entire design is secured in place by embroidering the perimeter of the patch to the ground plane using a non-conductive thread.

5.3.5 Free Space and On-body Antenna Measurements

The far-field performance of the textile HMMPA in free space was measured in the anechoic chamber. The positioner displayed in Fig. 5.10a yields a roll-over-azimuth far-field system with 4 $\phi-$ cuts in roll axis and 73 $\theta-$ points in azimuth. Directivity is obtained by pattern integration while gain is acquired by using the gain transfer method [32]. As far as the on-body measurement is concerned, the antenna is attached on the chest of a SAM phantom with a separation distance of 10 mm (Fig. 5.10b). This distance is obtained by using a Rohacell spacer and was chosen as the minimum reference distance for both antennas due the protruding SMA connector of the copper HMMPA antenna. To obtain the far-field on-body antenna performance, the CNF measurement technique [33] is employed with the probe scanning in the Y-axis while the antenna under test (AUT) is rotated in the azimuth plane. After transformation to far-field of the recorded near-field measurements, the on-body antenna efficiency as well far-field radiation patterns in the two principal planes (XZ- and YZ- plane) are calculated. The far-field on-body coordinate system is also shown in Fig. 5.10b.

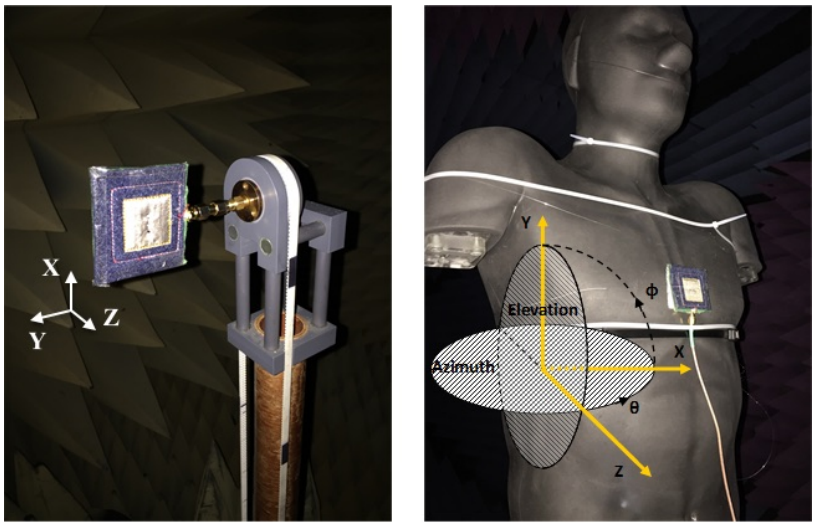

(a) (b)

Figure 5.10 Textile patch antenna in the anechoic chamber. (a) Free space, and (b) on-body measurement setup.

To begin with, the impedance mismatch performance for the textile HMMPA antenna is measured in free space and on the SAM phantom. As shown in Fig. 5.11, the $|S_{11}| = -21.3$ dB at 2.4 GHz in free space while there is a slight detuning when it is placed on-body with $|S_{11}| = -22$ dB at 2.44 GHz. In comparison, the copper HMMPA presents $|S_{11}| = -21.6$ dB at 2.45 GHz in free space while $|S_{11}| = -22.3$ dB at 2.46 GHz on-body showing negligible detuning. As far as the -10 dB bandwidth (BW) is concerned, the textile antenna presents a three times larger BW of 150 MHz ranging from 2.36 GHz to 2.51 GHz instead of 50 MHz of the copper antenna. In both free space and on-body cases, the BW is large enough to cover the entire 2.4 GHz ISM band (2.4 - 2.485 GHz).

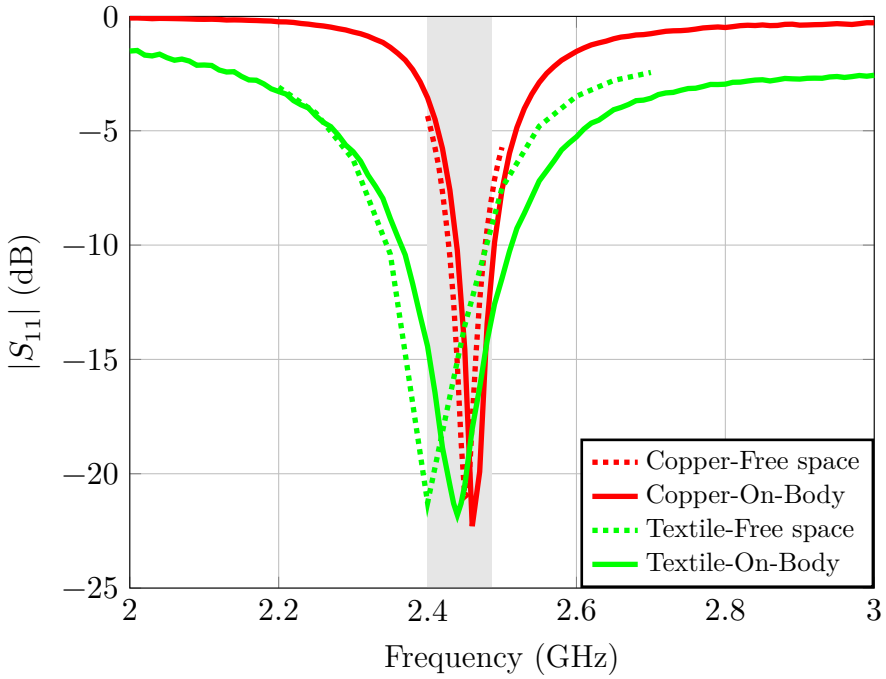

Figure 5.11 Measured reflection coefficient $|S_{11}|$ of the textile HMMPA compared to the copper HMMPA between free space (dotted line) and on-body phantom (solid line).

In order to compare the two HMMPA antennas on their ability to generate surface waves, the measured intensity of the propagated near field on the surface of the human body is plotted in Fig. 5.12a,c and Fig. 5.12b,d for the horizontal and vertical E-field components respectively. It is obvious that the prototype all-textile HMMPA antenna (Fig. 5.12a and Fig. 5.12b) generates a stronger surface wave and experiences a higher interaction with human body rather than the copper HMMPA antenna (Fig. 5.12c

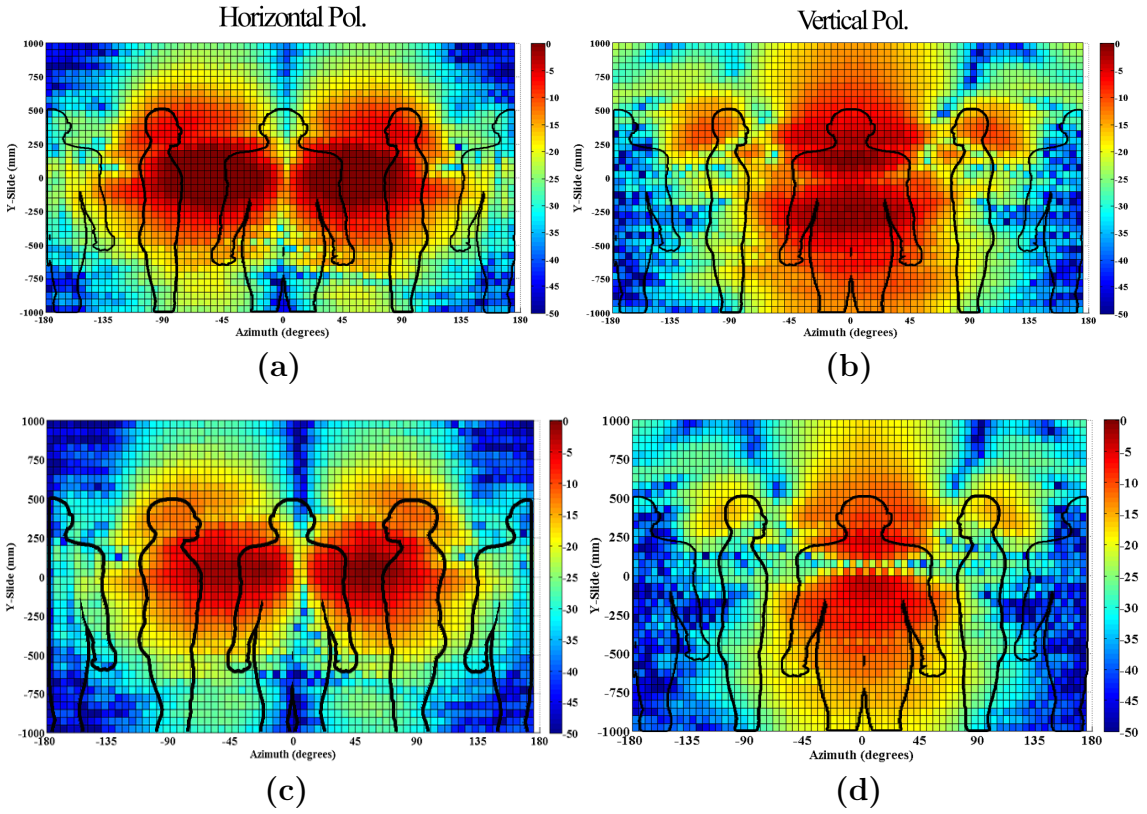

Figure 5.12 Measured near-field intensity (horizontally (E_ϕ) and vertically (E_Y) polarised components) of the textile HMMPA (a,b) and copper HMMPA (c,d) on chest.

and Fig. 5.12d). This is concluded from the higher intensity levels that are observed in the front face of the human body for vertical and horizontal field components respectively. One reason might be that the textile antenna is attached closer to the body than the copper antenna (10 mm instead of 20 mm due to the protruding SMA connector).

The far-field normalised radiation patterns in free space for XY-, XZ- and YZ-planes are plotted in Fig. 5.13 for the textile (black line) and the copper (red line) antennas. The textile antenna radiation pattern is omnidirectional in the XY-plane (Fig. 5.13a) while having nulls for $\theta = 0^o$ (boresight direction) and $\theta = 180^o$ (Fig. 5.13b, 5.13c) exhibiting a monopole-like performance. The null in the broadside direction of the radiation pattern indicates that the desired on-body mode is excited while minimising the off-body radiation, as a result of the effective performance of the embroidered shorting vias. It is also seen that the cross-polar component of the

textile antenna in both cases is quite low and similar to the copper antenna.

The on-body XZ- and YZ- far-field planes are plotted in Fig. 5.14. These two planes show the far-field radiation around and along the body. The radiation pattern shape of the textile antenna (black line) is almost identical to the copper one (red line) for both planes with the only exception of the cross polarised component, which appears slightly increased in the broadside direction. This is assigned to the stronger textile antenna interaction with the human body rather than the copper antenna, since the side-fed design enables to be conformal with the body. In respect to the free space case (Fig. 5.13b, 5.13c), it is found that a part of the radiated field in the range between $\theta = 90^o$ to $\theta = 270^o$ is suppressed, due to the shadowing and scattering from the human body. This effect is more pronounced at the YZ- plane ($\phi = 90^o$-cut) (Fig. 5.14b) where the shadowing effect is higher.

The HMMPA antenna directivity in the direction of maximum radiation ($\theta = 90^o$) in free space and on-body is given in Fig. 5.15. It can be seen that the directivity increases when the antenna is attached on the body due to the absorption of a part of the radiated power in the human body. The textile antenna directivity is similar to the copper antenna's performance in the on-body case, while the difference in the free space case appears less than 1 dB.

The HMMPA antenna gain in the direction of maximum radiation ($\theta = 90^o$) is given in Fig. 5.16 for the textile and copper patch antennas. The gain performance of the textile patch antenna is found almost $2dB$ lower than the copper antenna in both free space and on-body cases. This is attributed to the intrinsic ohmic losses of the conductive fabric and conductive thread which form a less efficient radiator. On top of this, the textile ground plane offers less shielding than the copper sheet from the near field interaction with the body.

The radiation efficiency of the textile antenna in free space is measured more than 50% (Fig. 5.17b) while the copper antenna efficiency reaches 88% at the resonance frequency (Fig. 5.17a). This difference is attributed mainly to the low conductivity of the conductive fabric and thread that are used to fabricate the textile antenna in the embroidery machine. Comparing the measured and the simulated efficiency in Fig. 5.17b, a very good matching up to 2.44 GHz is achieved. Above this frequency, the efficiency discrepancy is increased up to 10%, which is due to the accuracy of the free space measurement. By increasing the number of measurement points the difference between measurements and simulations is expected to be reduced. Moreover, an improvement on the fabrication accuracy of the textile antenna dimensions in respect

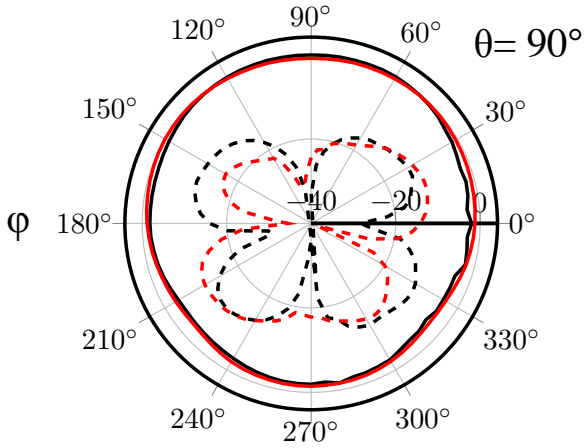

(a) $\theta = 90^o$-cut (XY- plane)

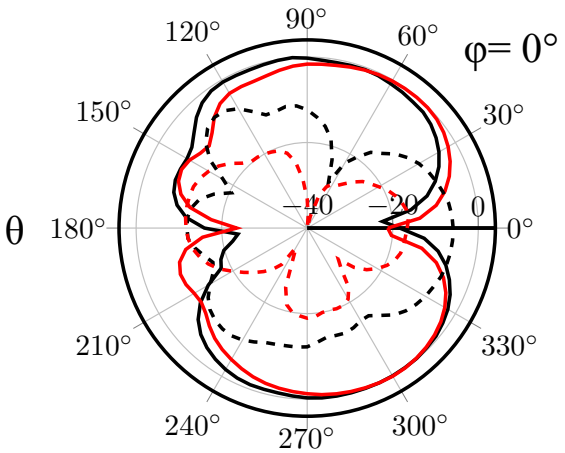

(b) $\phi = 0^o$-cut (XZ- plane)

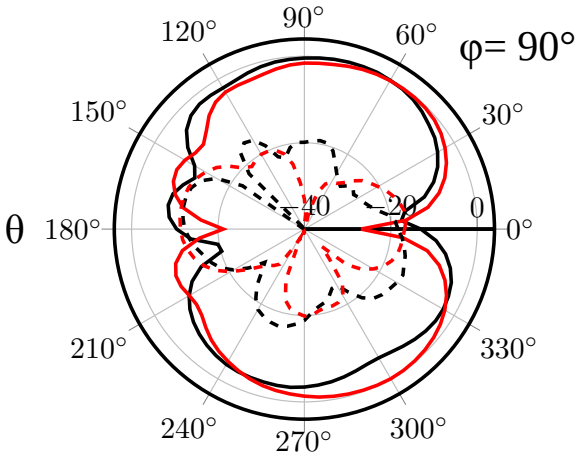

(c) $\phi = 90^o$-cut (YZ- plane)

Figure 5.13 Measured radiation pattern for textile (black) and copper (red) HMMPA antennas in free space for co-polarised (solid) and cross-polarised (dotted) components.

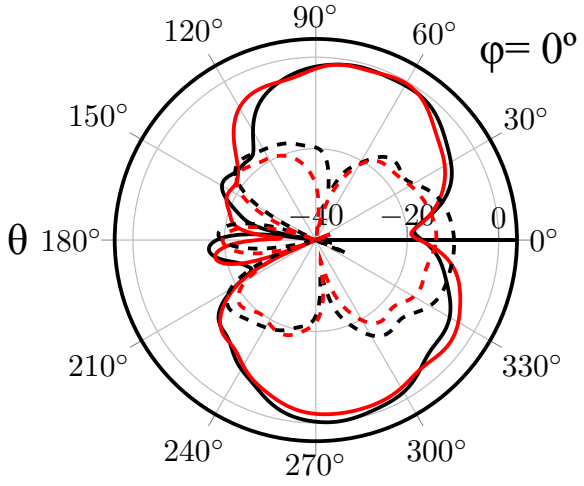

(a) $\phi = 0^o$-cut (XZ- plane)

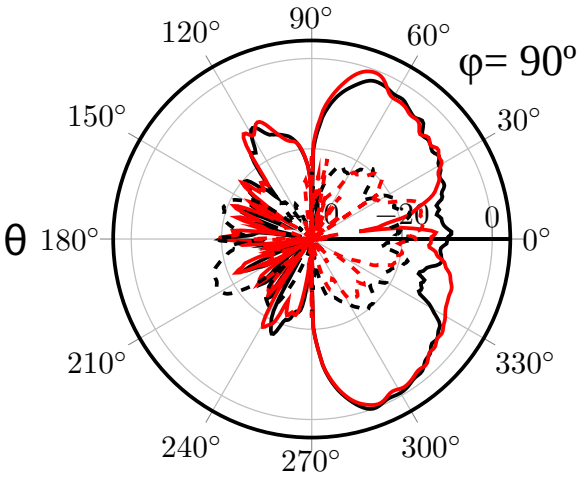

(b) $\phi = 90^o$-cut (YZ- plane)

Figure 5.14 Measured radiation pattern for textile (black) and copper (red) HMMPA antennas on torso phantom for co-polarised (solid) and cross-polarised (dotted) components. (a) XZ- and, (b) YZ-planes.

to the simulated textile antenna can contribute to eliminate this difference.

More interestingly, the on-body textile antenna efficiency deteriorates only by less than 15% on average compared to the free space efficiency, which is explained from the screening effect of the antenna's ground plane that minimise the severe interaction with the body. When it is compared with the copper antenna performance on the body, a difference of less than 20% on average is found, which is acceptable in terms of fully-textile antennas.

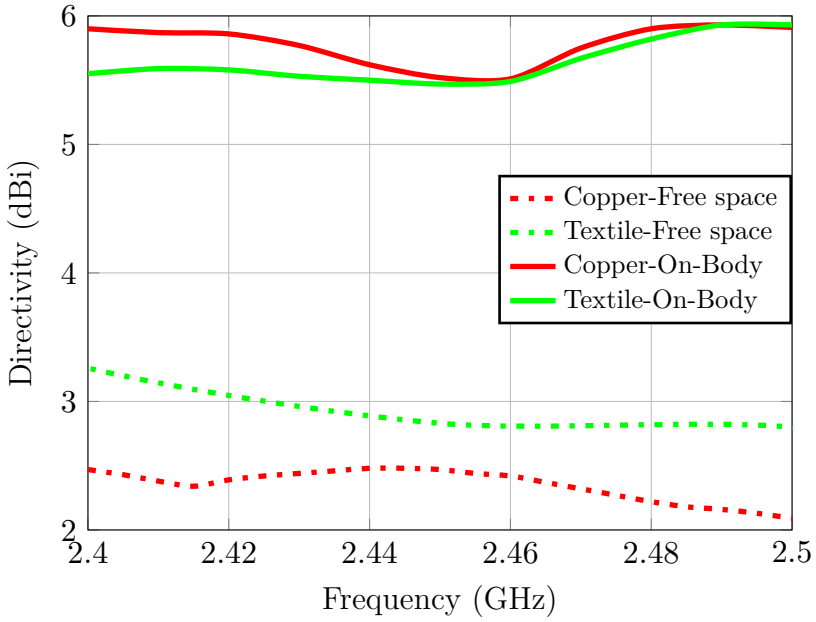

Figure 5.15 Measured directivity of the proposed textile and copper HMMPA antennas.

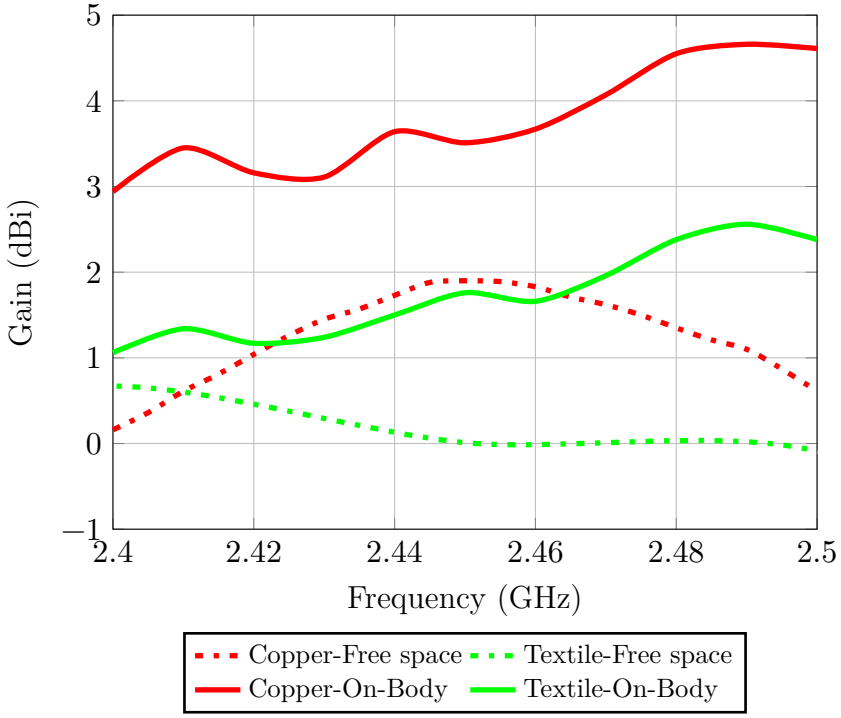

Figure 5.16 Measured radiated (IEEE) gain of the proposed textile and copper HMMPA antennas.

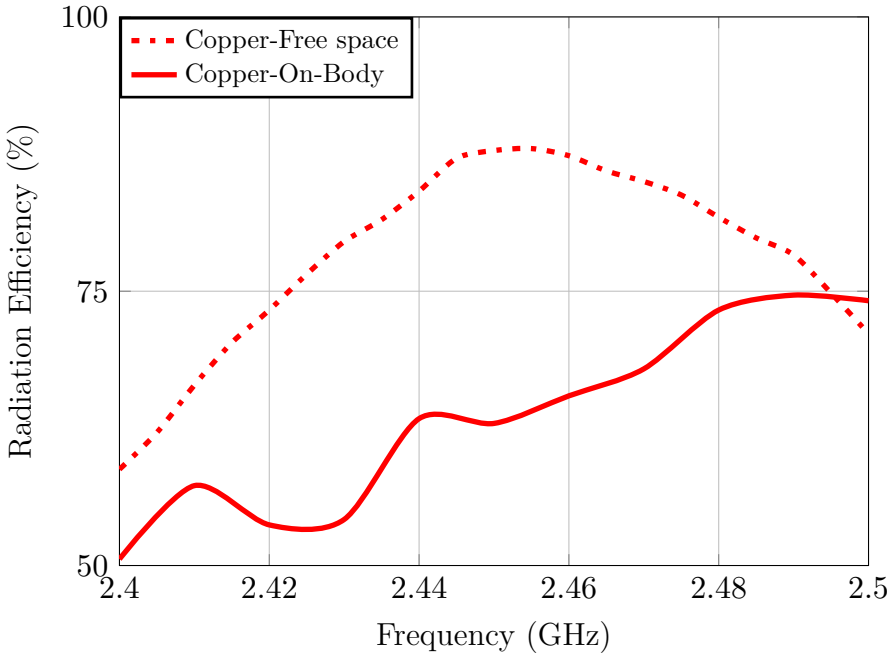

(a)

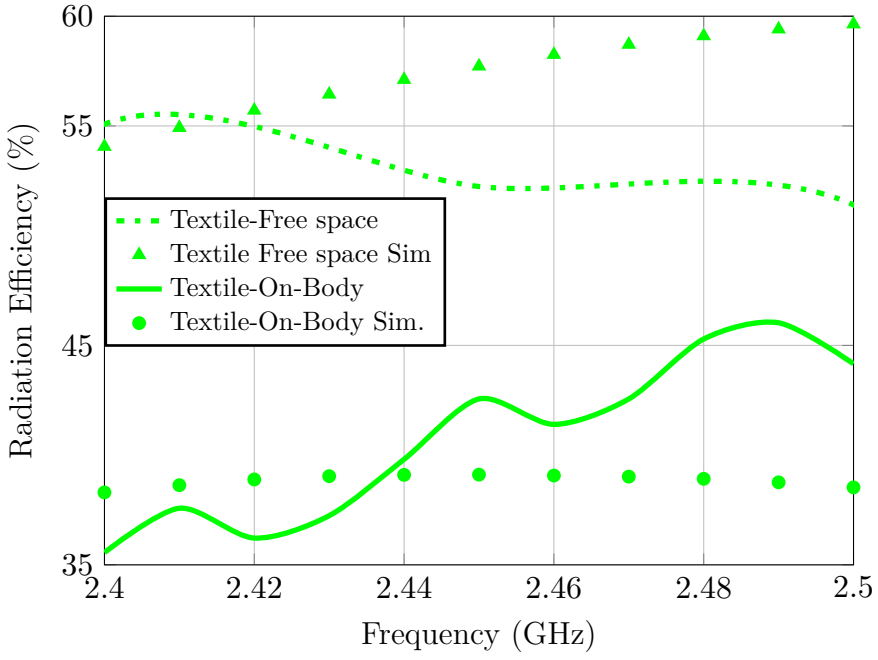

(b)

Figure 5.17 Measured radiation efficiency of (a) copper and (b) textile HMMPA antennas.

After presenting the performance of the proposed textile HMMPA antenna, the question about its practicability arises. It is then compared with a circular patch antenna [34], which employs electromagnetic band-gap structures to generate the on-body propagation. The proposed HMMPA antenna shows an increased fabrication complexity due to the utilisation of the embroidered vias and the multilayer design. However, the increased complexity acts in favour of achieving a smaller size (50mm x 50 mm instead of 136mm x 136mm) and a side-fed design which makes it feasible to be implemented in "smart" clothing. In addition, the proposed HMMPA achieves a better on-body coupling performance since the direction of maximum gain is located closer to the body surface ($\theta = 74^o$ for the HMMPA rather than $\theta = 48^o$ for the EBG antenna).

5.4 Fully-Embroidered Spiral Antenna

An embroidered wearable spiral antenna is presented in this section. The spiral antenna is compact and flexible, yet has a broadband performance over the frequency range from 1 to 3 GHz. It is designed in CST Microwave Studio and is embroidered using the conductive thread Liberator with the embroidery machine at Loughborough University. The antenna is simulated and measured on a SAM torso phantom and on a real person. The far-field performance of the embroidered antenna on the phantom is measured using the CNF measurement method. Due to the broadband performance of the spiral antenna, the interaction with human body is investigated over a wide range of frequencies. The antenna radiation performance including gain, directivity, radiation efficiency, and axial ratio (AR) is presented. The similarity of the simulated and measured results demonstrates the potential of the SAM body phantom as a good alternative to the real human body in wearable antenna testing.

5.4.1 Introduction

Spiral antenna is one of the UWB antennas that exhibits a low profile and a large bandwidth. It provides a broadband performance without suffering from the frequency detuning effect as it happens to narrowband antennas due to the interaction with the human body. One of the key advantages of flexible wearable antennas below 1GHz is that the antenna can be the size of the torso without compromising the user's comfort when the antennas are integrated into clothing. Therefore, the antenna size

is not compromised in terms of size reduction, since it can be hidden inside the inner lining of clothing.

Various embroidered spiral antennas have been considered in the last couple of years [35–37] for wearable applications. The density of the embroidered threads has been increased where the currents were strongest [36]. Different fabrication techniques have been compared in [38]. Spiral antennas have been placed on metallic cylinders [37] and on a small cuboid sponge material [35]. However, none of these works have considered the effect of a realistic human body which is critically important to the behaviour of the antenna, especially at low frequencies where the antenna size is comparable to the body size. Therefore, although similar designs have been previously reported, the effect of the body on the spiral antenna performance has not been properly characterised.

In Section 5.4.2, the simulation of the spiral antenna on the SAM torso phantom is presented. Since the embroidered antenna is flexible which can be tightly attached on the body fitting with the body shape, EM simulations are carried out for planar case as well as considering the effects of bending on the body curvature and the effects of the distance between the antenna and the body. The fabrication of the embroidered spiral antenna is presented in Section 5.4.3. The antenna design is exported as a graphical format to the digital embroidery machine and fabricated at Loughborough University. Section 5.4.4 demonstrates the $|S_{11}|$ measurement of the embroidered antenna on real human and on SAM phantom. The far-field performance including the gain, directivity, radiation efficiency, radiation pattern and axial ratio of the spiral antenna on the SAM torso phantom is measured using the CNF measurement method, which is presented in Section 5.4.5.

5.4.2 Antenna Design

The Archimedean spiral antenna is designed to operate over a wide frequency range from 300 MHz to 3 GHz. The width of each line is 5.8 mm; the spacing between lines is 6.0 mm and the exterior diameter of the whole spiral is 208 mm. In the EM simulation, the two conductive arms of the spiral are modelled as 1 μm thick with the conductivity of silver ($\sigma = 6.21 \times 10^7 S/m$), which emulates the conductive thread Liberator. The antenna design, as modelled in CST Microwave Studio can be seen in Fig. 5.18.

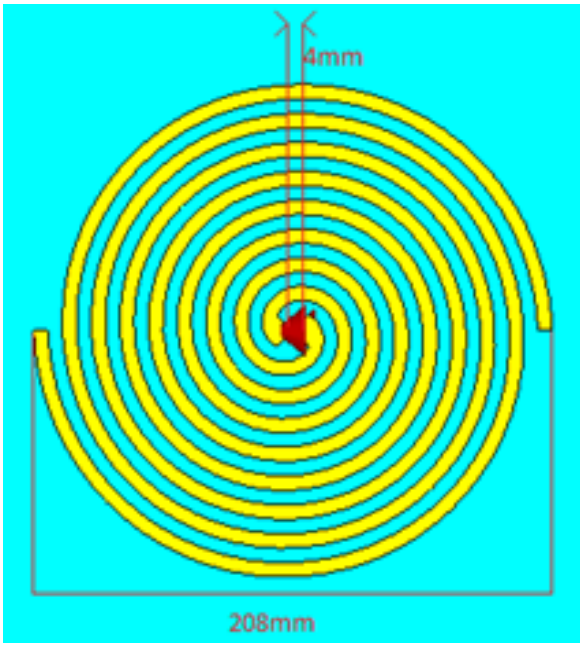

Figure 5.18 Spiral antenna designed in CST Microwave Studio.

5.4.3 EM Simulation of Antenna on the Human Body

The simulation model of the antenna on the body phantom can be seen in Fig. 5.19, where the spiral antenna is slightly curved in order to approximate the placement of the antenna on the real SAM phantom. It is placed on the front side of the SAM phantom covering the entire abdominal area. This location on the SAM body phantom is selected since it is flatter than the chest area and the difference in the local geometry between the numerical and the physical body phantom is negligible. It is noted that the surface of the abdomen of SAM phantom is flatter than the chest area, where the HMMPA antenna was tested previously. This means that the difference in the local geometry of the phantom model between simulations and measurements is negligible.

The simulated $|S_{11}|$ of the antenna on the phantom over the frequency range from 0.3 to 3 GHz for four different spacings (2 mm, 7 mm, 12 mm and 17 mm) between antenna and body is shown in Fig. 5.20a. The 2 mm distance is approximately equal to a layer of T-shirt between the antenna and the human body. All the separations have $|S_{11}|$ generally lower than -5 dB for almost the whole frequency range above 0.5 GHz.

The effect of antenna bending on the Y axis in the $|S_{11}|$ is investigated for 30°,

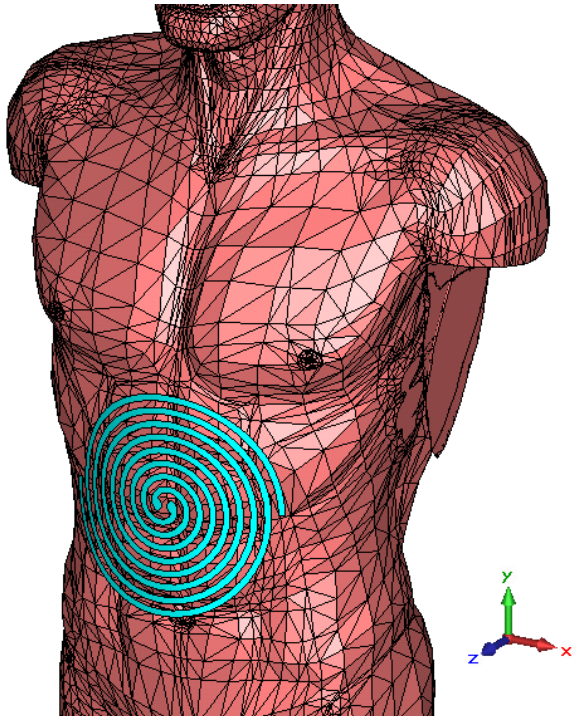

Figure 5.19 Curved spiral antenna simulated on the SAM phantom.

40° and 50° curvature angles respectively. The central point of the antenna with different curving angles remains at the same 2 mm distance from the phantom. Larger curving angles result to the fact that the ends of the two spiral arms come closer to the phantom. Fig. 5.20b shows the simulated $|S_{11}|$ of the curved antenna, compared with this of the planar antenna. The simulated results indicate that the $|S_{11}|$ deteriorates by 0.5 to 1 dB at the frequency ranges of 0.8 to 1.0 GHz and 1.4 to 2.0 GHz, but no significant impact is observed at the rest of the frequency range. In addition, the $|S_{11}|$ discrepancy among the different curvature angles is negligible.

However, a weak impedance matching is observed between the spiral antenna input impedance and the feeding with an SMA cable of 50 Ω input impedance. An 150 Ω (real) input impedance of the spiral antenna is found after simulations. Therefore a 3:1 impedance transformer can be used to improve the impedance matching and move below −10 dB the $|S_{11}|$ of spiral antenna. Simulation results indicate that the radiation efficiency of the spiral antenna is not affected by the transformer. The measurement results of the embroidered spiral antenna with the impedance transformer between the feed cable and the antenna are presented in Section 5.4.5.

The simulated far-field performance of the spiral antenna on phantom at 2.4 GHz,

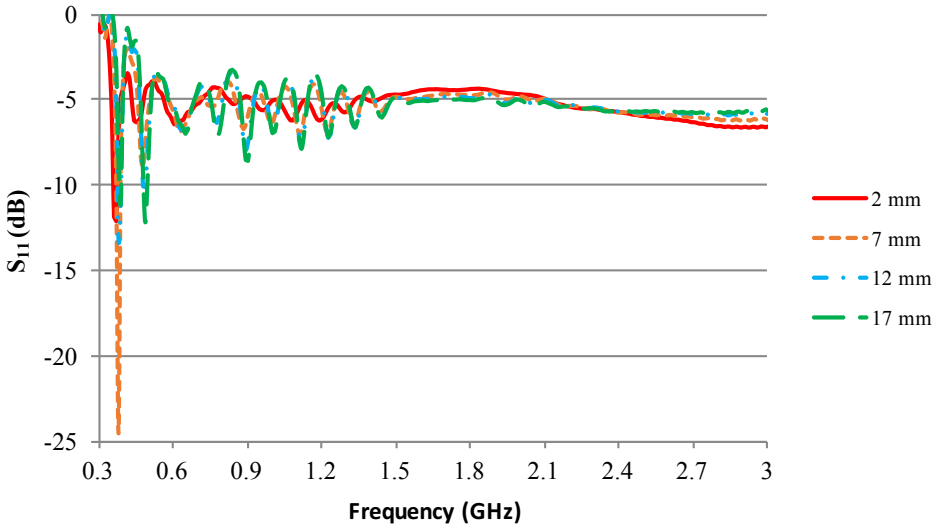

(a)

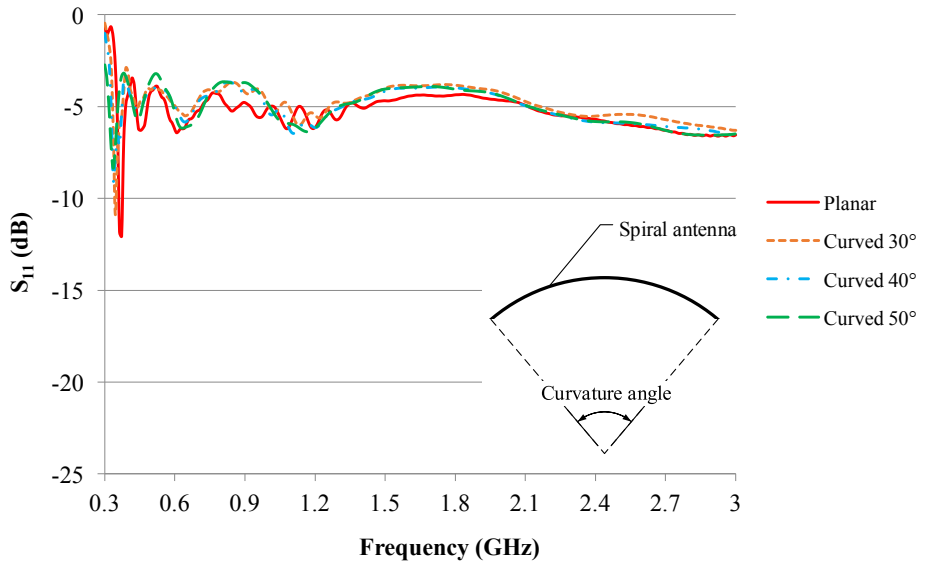

(b)

Figure 5.20 Simulated $|S_{11}|$ of the spiral antenna on the SAM phantom. (a) Planar spiral antenna at different distances from SAM phantom and (b) different curvatures of the spiral antenna on the SAM phantom.

with a curvature of 50° is shown in Fig. 5.21. It is clearly seen that the back side of the radiation pattern ($\theta = 90^o$ to $\theta = 270^o$) is distorted by the phantom which is located behind the antenna and the whole pattern becomes more directional. The spiral antenna is expected to be circularly polarised since the level of E_θ and E_ϕ

components is very similar at the boresight direction ($\theta = 0^o$). The axial ratio (AR) level is used to examine the circular polarization performance of the spiral antenna. The simulated AR at the boresight of the spiral antenna on phantom with 50° curvature at 2.4 GHz is 1.22 dB, which proves that the antenna is circularly polarised even when it is curved and placed close to the phantom.

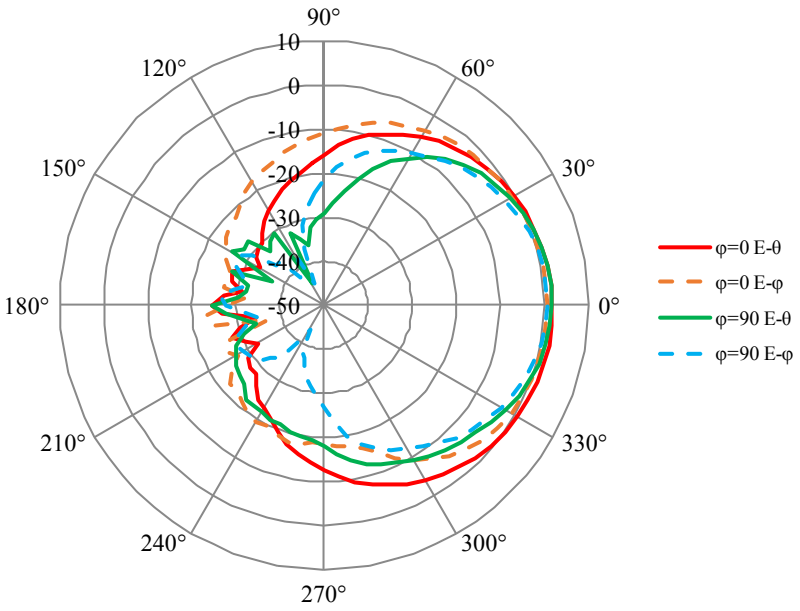

Figure 5.21 Simulated normalised radiation pattern of the 50° curved spiral antenna 2 mm away from SAM phantom at 2.4 GHz. E_θ and E_ϕ components at $\phi = 0^o$ (XZ-plane) and $\phi = 90^o$ (YZ-plane).

The simulated radiation efficiency of the spiral antenna on SAM phantom is shown in Fig. 5.22 for planar and curved cases. It shows a logical trend that with the increased separation distance between the antenna and the body, the efficiency of the antenna is increased. On the other hand, increased curvature decreases the antenna efficiency, but not significantly, (approximately 2% reduction). Since all the curved antennas have the same 2 mm distance from the centre to the phantom, it can be concluded that the distance between the antenna and human body is more important compared with the curving angle of the spiral antenna. The antenna efficiency for different curving angles is very similar, which indicates that this spiral antenna can be tightly fitted on-body and curving does not affect its performance.

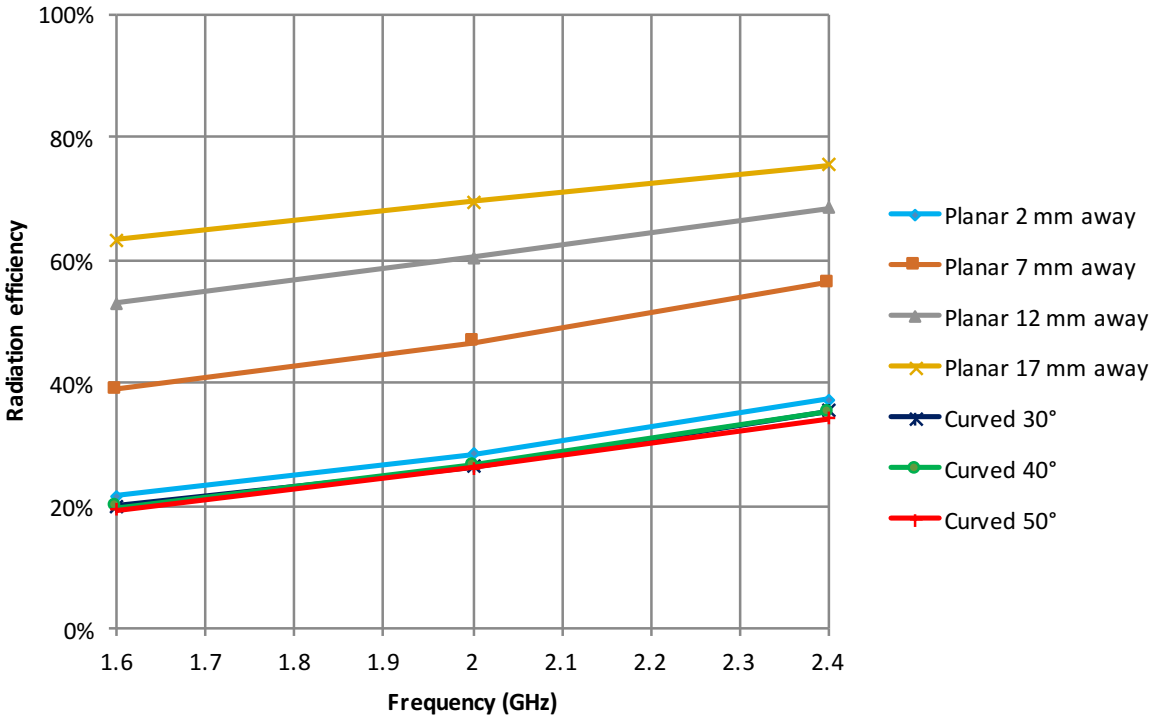

Figure 5.22 Simulated radiation efficiency of the spiral antenna on SAM phantom

5.4.4 Embroidery Process

The spiral antenna design is exported as a graphical format to the digital embroidery machine. A 0.5 mm white cotton fabric is used for the antenna substrate, while the silver coated conducting thread Liberator [13] is used for the embroidery. The stitch direction of the embroidered threads follows the current flow direction for giving the optimal performance. Higher number of stitches, shorter stitch width and closer stitch spacings improve the density and robustness of the embroidered pattern, at the cost of losing flexibility. However, for a medium density embroidery setting, it still requires more than 12000 individual stitches which represents more than 120 meters of thread, to complete the spiral pattern. This makes the fabrication of the spiral antenna time consuming and costly. In order to reduce the expenses of fabrication, 4 mm stitch width is used and each single arm of the spiral is formed by four parallel stitches. The final antenna is consisted of approximately 4500 individual stitches with an approximate length of 45 m of Liberator thread which is the main cost of the design. Meanwhile, the thread tension should also be carefully adjusted to ensure it is suitable for the specialised threads. Tension that is too tight may result to

warping of the base fabric or even breaking of the thread causing discontinuity to the embroidered pattern. On the other hand, tension that is too loose could result in a loosen thread. The final embroidered spiral antenna is shown in Fig. 5.23.

The embroidered spiral antenna is fed by a 50 Ω flexible coaxial cable. The inner probe and outer shield of the coaxial cable are respectively soldered on the two arms of the spiral. A low temperature solder is used to avoid damaging the base fabric (white fabric in Fig. 5.23). The other end of the cable is connected to a Vector Network Analyser to measure its $|S_{11}|$ response on a real human body.

(a) **(b)**

Figure 5.23 Picture of the fabricated spiral antenna operating from 0.3 GHz to 3 GHz. (a) Top view, (b) zoomed view.

5.4.5 On-Body Antenna Performance

The fabricated embroidered spiral antenna is measured on the SAM phantom using the cylindrical near-field measurement technique. The CNF measurement system inside the anechoic chamber is shown in Fig. 5.24a. The axis system is fixed with the Z-axis facing the probe's aperture. The spiral antenna placement on the SAM phantom is shown in Fig. 5.24b.

Before presenting the far-field radiation pattern results, the $|S_{11}|$ of the embroidered spiral antenna is presented, comparing the performance between the SAM phantom and a real human body. The placement of the spiral on the real human body is shown in Fig. 5.25. The difference of the $|S_{11}|$ of the spiral antenna on the SAM phantom and on the real human body (abdomen) is shown in Fig. 5.26. The results

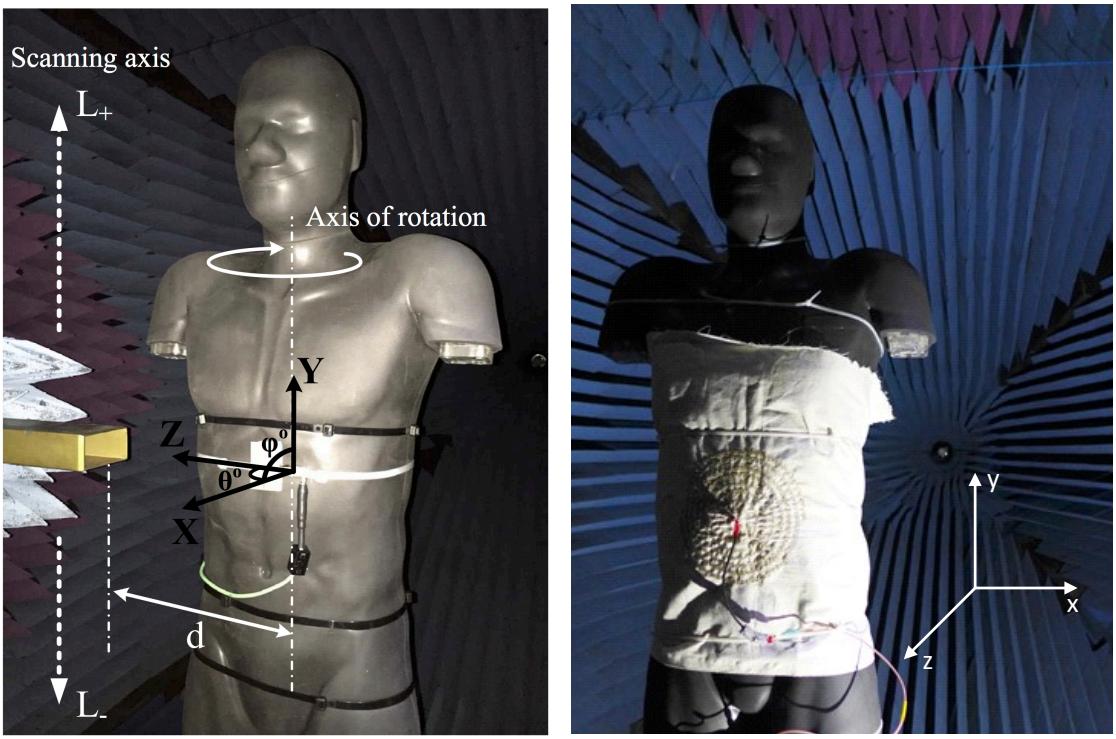

(a) (b)

Figure 5.24 (a) CNF measurement system including the SAM phantom on the turntable and the near field scanning probe, (b) Spiral antenna placed on the SAM phantom's surface.

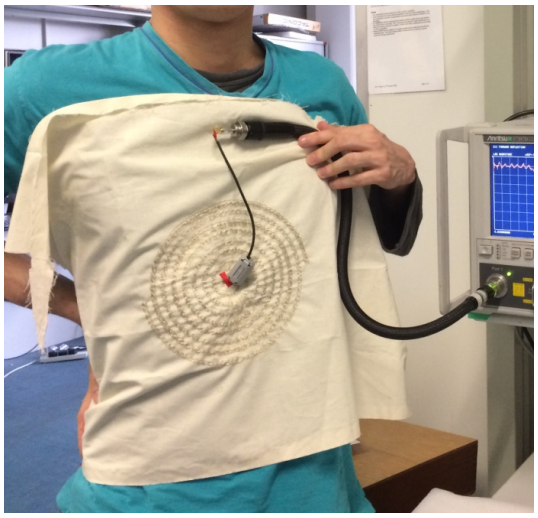

Figure 5.25 Measurement setup of the embroidered spiral antenna on a real human body.

show that the SAM phantom is a very good approximation to the real human body over the considered frequency range. However, the actual $|S_{11}|$ of the spiral antenna shows poor performance creating the need for better impedance matching between the 50 Ω characteristic impedance of the coaxial cable and the roughly 150 Ω input impedance of the spiral.

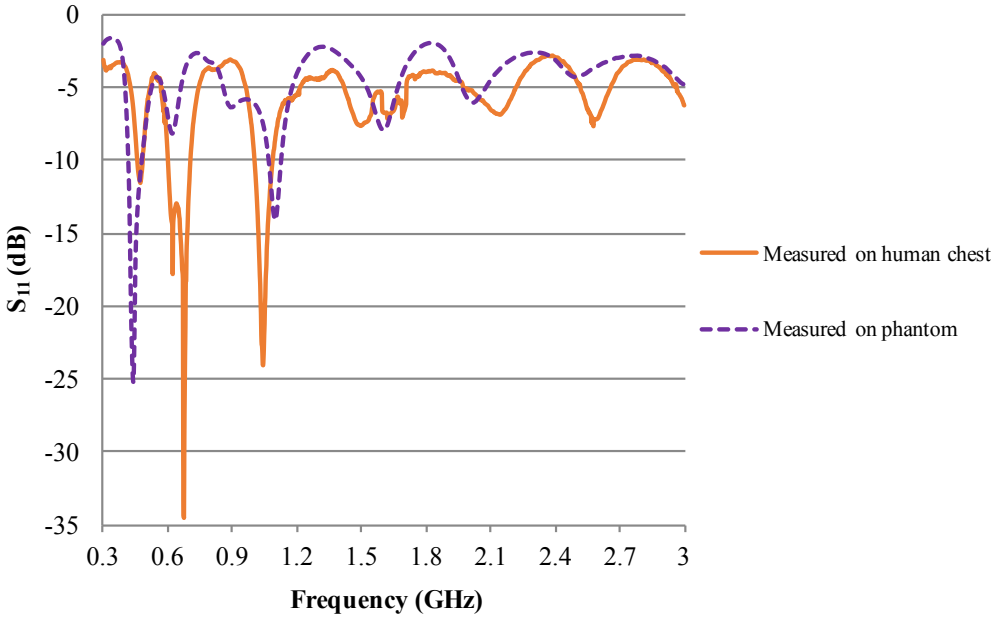

Figure 5.26 Measured $|S_{11}|$ of the embroidered spiral antenna on a real human and on SAM phantom.

A 3:1 impedance transformer is used to transform the 50 Ω input impedance to 150 Ω in order to match the impedance of the spiral antenna. The transformer is soldered to the two arms of the spiral. The embroidered spiral antenna is measured when placed against a real person wearing a jumper. The measured $|S_{11}|$ result is shown in Fig. 5.27. The simulated and measured S_{11} results of the planar antenna with the transformer in free space are included for comparison. The antenna against the human abdomen shows a $|S_{11}|$ below -8 dB between 0.9 to 3 GHz. It can be clearly seen in Fig. 5.23 that the substrate and the antenna has been slightly warped due to the tension of the embroidered threads. The inherent flexibility of wearable antennas inevitably means that there will be discrepancies between simulations and measurements.

The directivity, gain and efficiency of the embroidered spiral antenna on the SAM torso phantom are derived from the CNF measurement after the required NF-FF

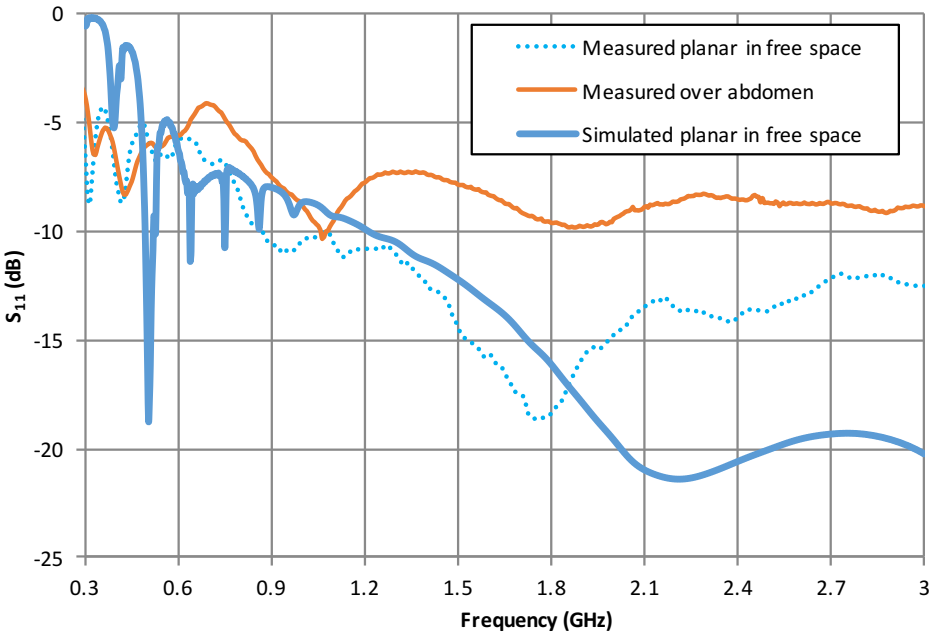

Figure 5.27 Measured $|S_{11}|$ of embroidered spiral antenna in free space and when placed over human abdomen, using a 3:1 impedance transformer.

transformation. The computed far-field characteristics from 1.6 to 2.6 GHz are shown in Table 5.1. Note that the gain and the radiation efficiency do not include the $|S_{11}|$ mismatch. As can be seen from Fig. 5.24b, the antenna has been placed flush against the torso. Therefore, the antenna has been measured in the worst case scenario. Therefore, sections of the conducting thread are less than 2 mm away from the lossy torso. As a comparison, the printed dipole operating at 2.4 GHz, placed flush to the body phantom in the previous chapter, presented a radiation efficiency of 5%.

Table 5.1 Computed far-field characteristics from near-field measurements of the embroidered spiral antenna on the phantom.

Freq. (GHz)	***Directivity (dBi)***	***Rad. Gain (dBi)***	***Rad. Efficiency (%)***
1.6	9.36	0.29	12.4
1.8	9.45	1.69	16.8
2.0	9.57	2.69	20.5
2.2	10.14	3.12	19.9
2.4	9.98	3.00	20.0
2.6	10.12	3.40	21.3

The antenna gain is increased from 0.29 dBi at 1.6 GHz to 3.4 dBi at 2.6 GHz. At higher frequencies, the antenna-phantom separation in terms of wavelength increases, which results in a higher efficiency. Additionally at higher frequencies, the skin depth decreases and therefore the thickness of the metallisation of the conducting thread (in term of skin depths) increases which means the thin (1 micron) conducting thread can better support the currents (reduces the power lost) which leads to higher efficiencies.

The radiation patterns at 1.6, 2.0 and 2.4 GHz of the embroidered spiral antenna on the SAM phantom are shown in Fig. 5.28. The radiation patterns at all the frequencies are distorted between $\theta = 90^o$ and $\theta = 270^o$, which is due to the interaction (power absorption) with the SAM phantom. This effect is in good agreement with the simulation. The radiation pattern becomes more directional at $\theta = 0^o$ degree with the increased frequency. The unavoidable truncation error is also evident in the $\phi = 90^o$ patterns, for angles around $\theta = 90^o$.

The measured and simulated results of the AR level at the boresight ($\theta = 0^o$) from 1.6 to 2.6 GHz of the spiral antenna on the phantom are shown in Fig. 5.29, compared with the simulated AR. The simulation results of the planar spiral antenna in free space and on SAM phantom indicate that the AR of the antenna is increased by approximately 0.5 dB up to 2.2 GHz due to the presence of the phantom. Furthermore, the curving of the spiral antenna does not significantly influence the AR level and all the simulated AR are generally smaller than 1.5 dB from 1.6 to 2.6 GHz at the boresight, which shows all the curved spirals have good wideband circular polarization performance when placed on the body. The wideband performance makes this antenna an ideal candidate for wearable applications. However, the measured AR is generally higher than the simulated, but still AR $<$ 3 dB at 1.8 and 2.4 GHz. The difference between simulated and measured AR is due to imperfection of the embroidered pattern. Since the tension of the threads makes the base fabric warping, it results to the deformation of the spiral arms. This change in the spiral dimension causes the degraded circular polarisation. Meanwhile, the effects of the positioner and the supporting structure of the SAM phantom in the anechoic chamber can also affect the near-field scanning results.

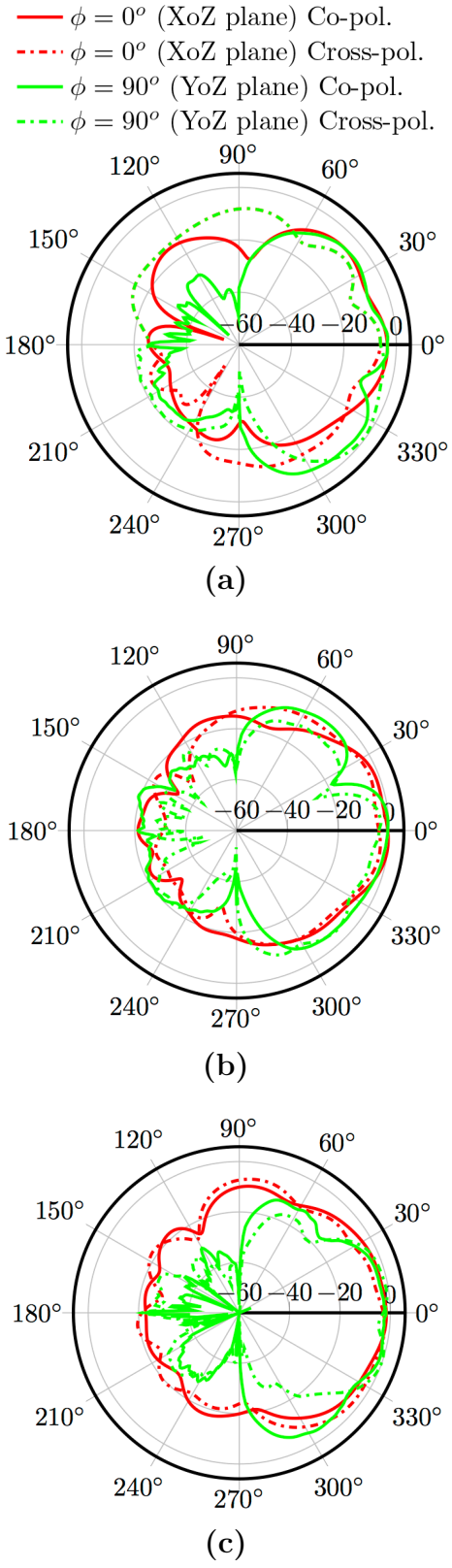

Figure 5.28 Computed gain patterns of the embroidered spiral antenna on SAM phantom for $\phi = 0^o$ (XZ-plane) and $\phi = 90^o$ (YZ-plane) at (a) 1600 MHz, (b) 2000 MHz, and (c) 2400 MHz.

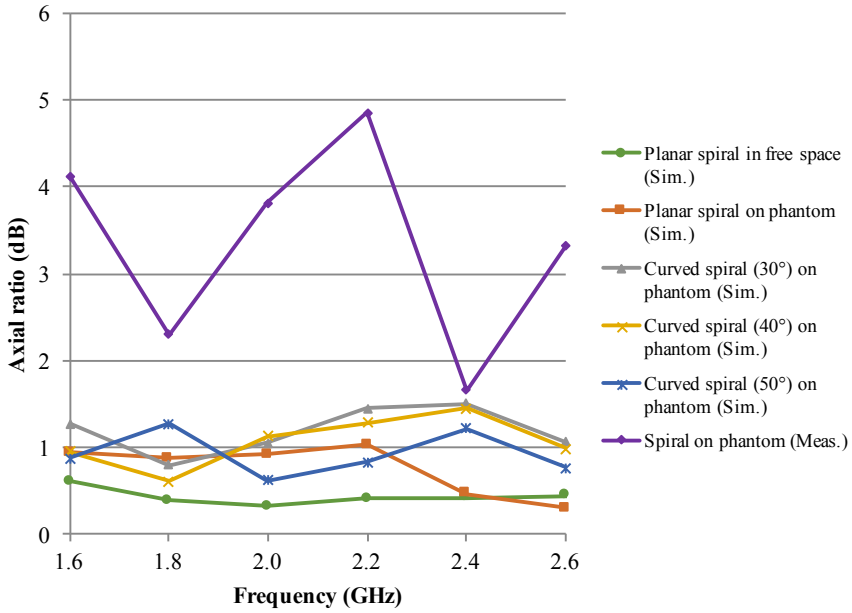

Figure 5.29 Computed axial ratio (AR) at the boresight direction of the spiral antenna on SAM phantom.

5.5 Conclusions

Two novel textile antennas are proposed and developed in this chapter for body-centric wireless communications. The low-profile textile HMMPA antenna can be used for narrowband on-body applications at 2.4 GHz, whereas the textile spiral antenna can utilise the available area of the human torso for off-body wideband applications.

More specifically, an all-textile higher-mode patch antenna (HMMPA) is proposed with embroidered vias that can operate with good efficiency on the human body. It can be easily integrated in smart clothing and work together with on-body communication devices. A perpendicular to the body polarisation is combined with a planar low-profile design. The radiation pattern of the textile antenna is measured in free space and on-body using the cylindrical near-field measurement technique. It is found that the radiation pattern shape is similar to the copper patch antenna, i.e. a monopole-like radiation pattern, meaning that the embroidered vias produce the desired higher mode. A free space radiation efficiency of 55% is achieved while in the on-body case 46% radiation efficiency is measured at 2.4 GHz ISM band. The efficiency reduction of the HMMPA antenna in the on-body case is expected since its maximum radiation is directed along the body surface leading to a stronger interac-

tion with the human body instead of a standard (TM_{01} mode) patch antenna.

Moreover, a fully-embroidered spiral antenna is presented, which can be comfortably worn and embedded in clothing, providing a circular polarisation in a broad range of frequencies. The broadband performance of the spiral antenna is measured and compared to simulated results showing the viability of the antenna to be used on the body surface. Simulated efficiency of up to 75% is obtained with up to 17 mm separation. The efficiency increases with frequency due to the larger antenna-phantom separation and the reduced skin depth effect of the conductive thread. The effect of curving the antenna around the torso compared to the planar antenna is minimal. The stability of the simulated S_{11} and axial ratio with different curvatures and spacings, indicates that the antenna would function on different users.

The fabrication of the embroidered spiral is a challenging process. The tension of the threads causes warping of the substrate and the antenna. The measured $|S_{11}|$ results on the SAM phantom show a good agreement when measured against a real human chest. The results pronounce the viability of using the SAM phantom to emulate the body effects in wearable antenna measurements.

The embroidered spiral shows an improved $|S_{11}|$ when placing a 3:1 impedance transformer that fixes the impedance mismatch with the coaxial cable. The measured radiation efficiency derived from near- field measurements of the embroidered spiral antenna is found approximately 10% to 25% from 1.6 to 2.6 GHz, in the worst case scenario of being placed flush against the torso. These results look reasonable considering the proximity of the antenna to the torso and the finite conductivity of the embroidered thread. The measured and simulated axial ratio of the spiral antenna on the SAM phantom are also compared. The antenna demonstrates a reasonable level of circular polarisation. The measured axial ratio is slightly larger than in the simulations as is often the case with embroidered antennas due to the complex stitch pattern.

References

[1] *Nora Dell-CR Conductive Metallized Nylon Fabric*, Available online: http://www.shieldextrading.net/pdfs/NoraDell%20CR.pdf.

[2] *LessEMF Pure Copper Polyester Taffeta Fabric.*, Available online: http://www.lessemf.com/fabric.html#1212.

[3] *LessEMF Nickel Copper Ripstop Fabric.*, Available online: http://www.lessemf.com/fabric.html#1213.

[4] T. Haagenson, S. Noghanian, P. de Leon, and Y. Chang, "Textile Antennas for Spacesuit Applications: Design, simulation, manufacturing, and testing of textile patch antennas for spacesuit applications.," IEEE Antennas and Propagation Magazine **57(4),** 64–73 (2015).

[5] A. Tsolis, W. Whittow, A. Alexandridis, and J. Vardaxoglou, "Embroidery and Related Manufacturing Techniques for Wearable Antennas: Challenges and Opportunities," Electronics **3(2),** 314–338 (2014).

[6] L. Zhang, Z. Wang, and J. L. Volakis, "Textile Antennas and Sensors for Body-Worn Applications," IEEE Antennas and Wireless Propagation Letters **11,** 1690–1693 (2012).

[7] R. Seager, S. Zhang, A. Chauraya, W. Whittow, Y. Vardaxoglou, T. Acti, and T. Dias, "Effect of the fabrication parameters on the performance of embroidered antennas," IET Microwaves, Antennas Propagation **7(14),** 1174–1181 (2013).

[8] S. Zhang, A. Chauraya, W. Whittow, R. Seager, T. Acti, T. Dias, and Y. Vardaxoglou, "Embroidered wearable antennas using conductive threads with different stitch spacings," In *Antennas and Propagation Conference (LAPC), 2012 Loughborough*, pp. 1–4 (2012).

[9] R. Seager, A. Chauraya, J. Bowman, M. Broughton, R. Philpott, and N. Nimkulrat, "Fabric based frequency selective surfaces using weaving and screen printing," Electronics Letters **49(24),** 1507–1509 (2013).

[10] S. Zhang, A. Chauraya, W. Whittow, R. Seager, T. Acti, T. Dias, and Y. Vardaxoglou, "Repeatability of embroidered patch antennas," In *Antennas and Propagation Conference (LAPC), 2013 Loughborough*, pp. 140–144 (2013).

[11] S. Zhang, R. Seager, A. Chauraya, W. Whittow, and Y. Vardaxoglou, "Non-uniform Meshed Microstrip Antennas for Wearable Applications," In *Antennas and Propagation (EUCAP), 2014 8th European Conference on*, (2014).

[12] Y. Ouyang and W. J. Chappell, "High frequency properties of electro-textiles for wearable antenna applications," IEEE Transactions on Antennas and Propagation **56(2),** 381–389 (2008).

[13] *Liberator™ conductive fiber*, Available online: http://www.metalcladfibers.com/liberator-fiber/.

[14] *AmberStrand™ conductive fiber*, Available online: http://www.metalcladfibers.com/amberstrand-fiber/.

[15] C. Delaveaud, P. Leveque, and B. Jecko, "New kind of microstrip antenna: the monopolar wire-patch antenna," Electronics Letters **30(1),** 1–2 (1994).

[16] G. Conway and W. Scanlon, "Antennas for Over-Body-Surface Communication at 2.45 GHz," IEEE Transactions on Antennas and Propagation **57(4),** 844–855 (2009).

[17] J. Tak, K. Kwon, S. Kim, and J. Choi, "Dual-Band On-Body Repeater Antenna for In-on-On WBAN Applications," International Journal of Antennas and Propagation (2013).

[18] A. Al-Zoubi, F. Yang, and A. Kishk, "A Broadband Center-Fed Circular Patch-Ring Antenna With a Monopole Like Radiation Pattern," IEEE Transactions on Antennas and Propagation **57(3),** 789–792 (2009).

[19] F. Yang, Y. Rahmat-Samii, and A. Kishk, "Low-profile patch-fed surface wave antenna with a monopole-like radiation pattern," IET Microwaves, Antennas Propagation **1(1),** 261–266 (2007).

[20] J. Liu, Q. Xue, H. Wong, H. W. Lai, and Y. Long, "Design and Analysis of a Low-Profile and Broadband Microstrip Monopolar Patch Antenna," IEEE Transactions on Antennas and Propagation **61(1),** 11–18 (2013).

[21] K.-L. Wong and C.-I. Lin, "Characteristics Of a 2.4-GHz Compact Shorted Patch Antenna In Close Proximity To a Lossy Medium," Microwave and Optical Technology Letters **45(6),** 480–483 (2005).

[22] Z. G. Liu and Y. X. Guo, "Dual band low profile antenna for body centric communications," IEEE Transactions on Antennas and Propagation **61(4),** 2282–2285 (2013).

[23] T. Kaufmann and C. Fumeaux, "Wearable Textile Half-Mode Substrate-Integrated Cavity Antenna Using Embroidered Vias," IEEE Antennas and Wireless Propagation Letters **12,** 805–808 (2013).

[24] S. J. Chen, T. Kaufmann, and C. Fumeaux, "Shorting Strategies for a Wearable L-Slot Planar Inverted-F Antenna," International Workshop on Antenna Technology (iWAT) pp. 18–21 (2014).

[25] J. Tak, S. Lee, and J. Choi, "All-textile higher order mode circular patch antenna for on-body to on-body communications," IET Microwaves, Antennas Propagation **9(6),** 576–584 (2015).

[26] H. Giddens, D. L. Paul, G. S. Hilton, and J. P. McGeehan, "Influence of body proximity on the efficiency of a wearable textile patch antenna," 6th European Conference on Antennas and Propagation (EuCAP) pp. 1353–1357 (2012).

[27] T. M. Nguyen, J.-Y. Chung, and B. Lee, "Radiation Characteristics of Woven Patch Antennas," IEEE Transactions on Antennas and Propagation **63(6),** 663–666 (2015).

[28] D. L. Paul, H. Giddens, M. G. Paterson, G. S. Hilton, and J. P. McGeehan, "Impact of Body and Clothing on a Wearable Textile Dual Band Antenna at Digital Television and Wireless Communications Bands," IEEE Transactions on Antennas and Propagation **61(4),** 2188–2194 (2013).

[29] P. J. Soh, G. A. E. Vandenbosch, S. L. Ooi, and N. H. M. Rais, "Design of a broadband all-textile slotted PIFA," IEEE Transactions on Antennas and Propagation **60(1),** 379–384 (2012).

[30] H. Rahim, F. Malek, I. Adam, S. Ahmad, N. Hashim, and P. Hall, "Design and simulation of a wearable textile monopole antenna for body centric wireless communications," PIERS Proceedings pp. 1381–1384 (2012).

[31] P. S. Hall and Y. Hao, *Antennas and Propagation For Body-Centric Wireless Communications*, 2 ed. (Artech House, 2012).

[32] "IEEE Standard Test Procedures for Antennas," ANSI/IEEE Std 149-1979 pp. 1–135 (1979).

[33] W. Leach and D. Paris, "Probe compensated near-field measurements on a cylinder," IEEE Transactions on Antennas and Propagation **21(4),** 435–445 (1973).

[34] R. Khouri, P. Ratajczak, P. Brachat, and R. Staraj, "A thin surface-wave antenna using a via-less EBG structure for 2.45 GHz ON-Body communication systems,"

Antennas and Propagation (EuCAP), 2010 Proceedings of the Fourth European Conference on pp. 3–6 (2010).

[35] H. Abufanas, R. J. Hadi, C. Sandhagen, and A. Bangert, "New approach for design and verification of a wideband Archimedean spiral antenna for radiometric measurement in biomedical applications," In *2015 German Microwave Conference*, pp. 127–130 (2015).

[36] B. Ivsic, A. Galoic, and D. Bonefacic, "Embroidered textile logarithmic spiral antenna and its energy efficiency," In *ELMAR (ELMAR), 2015 57th International Symposium*, pp. 157–160 (2015).

[37] J. Zhong, A. Kiourti, T. Sebastian, Y. Bayram, and J. Volakis, "Conformal Load-Bearing Spiral Antenna on Conductive Textile Threads," IEEE Antennas and Wireless Propagation Letters (2016).

[38] J. Matthews and G. Pettitt, "Development of flexible, wearable antennas," In *Antennas and Propagation, 2009. EuCAP 2009. 3rd European Conference on*, pp. 273–277 (2009).

Chapter 6

Conclusions and Future Work

The objective of this doctoral thesis is to contribute to the available knowledge of body-centric wireless communications. This part of wireless technology is receiving increasing attention in the recent years and it can be found in numerous applications of everyday life. Hence, this research can be found valuable in developing and characterising future efficient wearable antenna systems.

6.1 Summary of Research Novelty

This study provides an insight on the radiation properties of wearable devices on the human body, by developing a cylindrical near-field measurement methodology. A solid full-body SAM phantom is employed to replicate human body dielectric characteristics and minimise the measurement uncertainty. This methodology of qualifying wearable antennas is based on the captured near-field and far-field patterns. Several antenna locations are selected as each body part introduces different dielectric loading and interaction with the antenna, so as to investigate the antenna performance for various possible applications. Two wearable textile antennas, suitable for on-body and off-body communications respectively, are tested in order to show the measurement accuracy in different on-body radiation conditions.

The proposed measuring system offers the full-body characterisation of wearable antennas in contrast to conventional far-field systems that have been proved useful only for small size approximate body phantoms. The measurement time and space of the measurement facility are also reduced. This measurement system can be used as a repeatable test-bed for evaluating the performance of wearable antennas. The

accuracy is retained for any antenna-body tissue separation distance and on-body location. Thus, wearable antenna designs can be optimised for operation on the human body surface with the aim of achieving better impedance matching, less radiation pattern distortion and absorption in the human body by minimising the near-field interaction and increasing the radiation efficiency.

In addition, to cope with the proliferation of "smart" clothing that demands all the RF components incorporated into clothing, two fully-textile wearable antennas are realised in the embroidery machine. It is found that the fabricated textile antennas achieve a comparable performance with the traditional compact antennas, both in free space and on-body, leading to a seamless integration into clothing.

Apart from the antenna perspective, several on-body channel models have been developed using the best-fit statistical distributions of the empirical data derived either from simulations or measurements. The effect of using wearable antennas with different radiation characteristics is also examined on the extracted statistical model. A channel measurements campaign including the user's movement inside an anechoic environment is performed in order to characterise four specific dynamic on-body channels. The specific dynamic channels under investigation are: chest-waist, foot-waist, wrist-waist and back-waist channels.

The contribution of this research work can be briefly found in: the development of a cylindrical near-field measurement methodology for wearable antennas characterisation and evaluation for different antenna types, fabrication of novel textile wearable antennas and, channel modelling for specific dynamic on-body links.

6.2 Summary of Results

In Chapter 2, channel modelling for wearable antennas with different radiation characteristics is implemented via EM simulations and channel measurements. A simulation series of the waist-foot channel in different body postures is created to study the dynamic channel behaviour on the path loss and large-scale fading. Path gain is found similar in the running activity while in walking is found more than 10 dB different between HMMPA and IFA antennas. The best fit for the large-scale fading is obtained with Lognormal distribution for HMMPA antennas, whereas Weibull is found more suitable to characterise body shadowing between IFA antennas. In the channel measurements, four static and dynamic on-body channels are investigated including user's movement in terms of their path gain, large-scale fading caused from

body shadowing and small-scale fading caused from multi path reflections. HMMPA antennas experience lower body shadowing and achieve higher channel path gain up to 20 dB compared with the other two antenna types, owing to the strong surface wave propagation. Small-scale fading is modelled with different (5 in total) statistical distributions, for the three antenna types in the four on-body channels. It is found stronger for the case of dynamic channels where a larger spread from the mean value is spotted.

In Chapter 3, three different wearable antennas are developed from EM simulations that will be used for the validation of the near-field measurement methodology. The development of wearable antennas is thoroughly explained, starting from the materials selection up to the fabrication process and characterisation. The radiation properties of the wearable antennas, suitable either for on-body or for off-body communications, are investigated. The suitability of the SAM homogenous phantom for antenna investigations at 2.4 and 5.8 GHz ISM band is validated by comparing the results with a voxel numerical phantom.

In Chapter 4, the near-field measurement methodology is presented and tested with a printed dipole on a full-body anthropomorphic phantom. It is selected as the worst case wearable antenna that couples strongly with the human body. Three on-body locations are considered, namely on chest, head and shoulder. Near-field distribution of the printed dipole in vertical and horizontal orientation is graphically plotted in an outline of the human body, revealing the on-body propagation and body shadowing mechanisms. After transformation, far-field results are obtained. For both 2.4 and 5.8 GHz, a difference in antenna efficiency of less than 12.2% (or 0.56 dB) is achieved between measurements and simulations, which validates the accuracy of the proposed CNF method in the determination of radiation efficiency. Afterwards, two microstrip wearable antennas, a MPA and a HMMPA, suitable for on-body and off-body communications respectively are investigated on chest at 2.4 and 5.8 GHz ISM band. A minor interaction with body is revealed for the case of MPA antenna, which is slightly increased at the 5.8 GHz, with the main lobe focusing at the front hemisphere. This minor interaction is reflected in the on-body antenna efficiency where a less than 3% drop is spotted. As for the HMMPA antenna, looking at the near-field plots, a full body coverage is observed at both frequencies. The main lobe of the far-field pattern is forced parallel to the body surface while the radiation at the broadside direction is suppressed by almost 20 dB due to the shorting pins at the sides of the radiating patch. However, the enhanced on-body performance of the

HMMPA comes together with an increased body absorption and scattering of a part of the radiated power towards the human body. An efficiency reduction of almost 30% is captured from the free space to the on-body case.

In Chapter 5, the potential of seamless antenna integration in "smart" clothing is demonstrated. A novel fabrication method using the state of the art digital embroidery machine at Loughborough University is used, which creates flexible and light-weight wearable antennas for operation on the human body. Two novel fully textile wearable antennas are realised. A fully-textile HMMPA antenna is realised with textile embroidered vias that provide an enhanced on-body propagation. The radiation pattern shape of the textile antenna is found to be similar to the copper antenna, i.e. a monopole-like radiation pattern, meaning that the embroidered conductive vias produce the desired higher mode. A free space radiation efficiency of 55% is achieved while in the on-body case a 46% radiation efficiency is measured for operation in the 2.4 GHz ISM band. Moreover, an embroidered broadband spiral antenna is realised that achieves a circular polarisation with a low-profile, suitable for off-body communications. A radiation efficiency of around 25% is demonstrated at 1.6-2.6 GHz when attached flush to the body surface, due to an increased antenna-body interaction. This could be a promising starting point in order to gradually replace all the bulky printed antennas with flexible low-profile textile antennas that reach an adequate on-body radiation performance.

6.3 Future Work

The future potential of this research work is based on the profound capability of the developed measurement test-bed for wearable antenna performance characterisation. The cylindrical near-field measurement method can be found useful towards the improvement of wearable antennas that operate individually or cooperatively in the form of an antenna array on the surface of human body. The development of wearable antenna arrays with high gain in millimetre wave frequencies can be seen as a potential research study, meeting the standards for high data rates while achieving wearable antenna miniaturisation.

The randomness of the on-body antenna pattern, caused from the different interactions at each on-body location, can be thoroughly investigated using the rapid CNF measurement technique, extended from the three on-body locations currently investigated in this work to a more detailed on-body map. This investigation can

lead to the creation of a statistical antenna radiation pattern model that can be used to describe universally the antenna performance on the full human body or can be used in combination with specific on-body channel models.

Another future implementation of the CNF measurement method is in the development of diversity wearable antenna systems with the aim of achieving an increased overall channel capacity. To that extend, the on-body performance of diversity antennas can be optimised by minimising the mutual coupling from the amplitude information of the captured near field. From the phase information of the near field, the correlation coefficients of the different on-body channels can be extracted. A 2x2 MIMO wearable antenna system can then be studied with the aid of a 4-port VNA.

Due to the ability of the CNF measurement technique to capture the electric field in close proximity to the body surface, the radiation performance of implanted antennas can be possibly investigated.

Moreover, the installed textile antenna performance integrated in "smart" clothing can be investigated on a full body anthropomorphic phantom. This can lead to "smart" clothes with optimised on-body antenna performance by minimising the radiation towards the human body while maximising the off-body radiation. In combination to this, the utilised embroidery technique for textile antenna fabrication can be further improved in terms of the the stitching quality and the fabric materials used (of higher thread's conductivity and substrate's flexibility) leading to a better antenna performance.

Appendix A

Modelling of the Human Body

In the research of body-centric wireless communications, it is important to understand the electromagnetic properties of human tissue in order to enable the development of antennas and transceivers for such communications systems. Hence, the modelling of the body is required. In this section, the derivation of the dielectric properties of different human body parts is explained, together with the modelling of human body with physical and numerical phantoms.

A.0.1 Dielectric properties of human body

The basic concepts of dielectric spectroscopy and the dielectric spectrum of a biological tissue will be discussed in this section, mainly derived from the studies in [1–3]. Dielectric properties vary significantly with tissue type and frequency. The dielectric properties of materials are obtained from their measured complex relative permittivity ϵ that has no unit as being a relative quantity. It is expressed as:

$$\epsilon_r = \epsilon'_r - j\epsilon''_r \tag{A.1}$$

where ϵ'_r is the relative permittivity, a measure of the charge displacement and consequent energy stored in the material, and ϵ''_r is the out-of-phase loss factor, a measure of the electrical energy dissipated. In a perfect dielectric material, losses are due to the displacement currents and the loss factor ϵ''_r can be expressed in terms of the displacement electrical conductivity σ_d. In a biological material, an external electric field will induce ionic as well as displacement currents, where ionic currents and the corresponding losses are proportionate with the material ionic conductivity σ_i.

The total conductivity of the material σ is given by:

$$\sigma = \sigma_d + \sigma_i \tag{A.2}$$

and is related to the loss factor through the expression:

$$\epsilon_r'' = \frac{\sigma}{\epsilon_0 \omega} \tag{A.3}$$

In practice it is only possible to measure the total conductivity σ. Where present σ_i, which is frequency independent, can only be obtain from dielectric spectral analysis. In the loss factor expression (Eq. A.3), ϵ_0 is the permittivity of free space and ω is the angular frequency of the field. Conductivity is expressed in siemens per metre (S/m), which presumes that, in the above expression, ϵ_0 is given in farads per metre (F/m) and ω in radians per second (rad/s). The dielectric properties are determined from ϵ_r' and ϵ_r'' values, or equivalently ϵ_r' and σ values, as a function of frequency.

The dielectric properties of a biological tissue are a measure of the interaction with electromagnetic radiation and its constituents at the cellular and molecular level. The mechanisms of interaction are well understood and the theory is proved by experimental data. The main features of the dielectric spectrum of a biological tissue are as follows:

- The dielectric properties of tissues are highly frequency and temperature dependent. Their dielectric spectrum consists of three main regions known as α-, β- and γ- dispersions, descriptively referred to as occurring at low, intermediate and high frequencies in the frequency range from hertz to gigahertz.

- The low-frequency α-dispersion in the hertz to kilohertz range is associated with ionic diffusion processes at the site of the cellular membrane. The β-dispersion, extends over 3-4 frequency decades centred in the hundreds of kilohertz region, and is due mainly to the polarisation of cellular membrane and organic macromolecules.

- The γ-dispersion, in the gigahertz region, is due to the molecular polarisation of tissue water. The study of both α- and β-dispersions is outside of the GHz frequencies of interest and as a result only the γ- dispersion would be used.

The γ-dispersion is due to the polarisation and relaxation of the water molecules. High water content tissue exhibits a γ-dispersion similar to that of pure water when

the presence of organic matter is taken into consideration. The frequency dependence of the complex permittivity in the γ-dispersion region as described from a 4-Cole-Cole model is [3]:

$$\epsilon(\omega) = \epsilon_\infty + \sum_{n=1}^{4} \frac{\Delta\epsilon_n}{1 + (j\omega\tau_n)^{(1-\alpha_n)}} + \frac{\sigma_i}{j\omega\epsilon_0} \tag{A.4}$$

where ϵ_∞ is the permittivity in the terahertz frequency range, ϵ_0 is the free space permittivity and σ_i is the conductivity due to ionic drift and lower frequency polarisation mechanisms. For each dispersion region the material parameters are: $\Delta\epsilon_n$ is the variation of permittivity in the frequency range, τ_n is the relaxation time and α is a parameter describing some broadening of the dispersion.

Tissue material parameters have been derived from dielectric measurements carried out in Gabriel et. al [1] using an open-ended coaxial probe together with a computer controlled network analyser. Most of the measurements made on human autopsy material within 48 hours or freshly killed sheep within 2 hours. Measurements on live tissue (*in vivo*) are not realisable since the measuring probe needs to be in contact with the tissue.

The aforementioned 4-Cole-Cole model describes the frequency dependence of the complex permittivity of human tissue in the frequency range from Hz to GHz. It can be used with confidence for frequencies above 1 MHz. With a choice of parameters appropriate to each tissue, this model (A.4) could be used to predict its dielectric behaviour over the desired frequency range.

In Table A.1, the various parameters of muscle tissue are given from [1], which are necessary to find ϵ from equation (A.4) , at any desired frequency.

Table A.1 Muscle tissue parameters for 4-Cole-Cole model [4]

m	**1**	**2**	**3**	**4**
$\Delta\epsilon$	50	7000	$1.2 \cdot 10^6$	$1.2 \cdot 10^6$
$\tau(ps)$	7.234	353	318	2.27
α	0.1	0.1	0.1	0.0
ϵ_∞	4.0			
ϵ_0	$8.854 \cdot 10^{-12}$ F/m			
σ_i	0.2			

The conductivity, relative permittivity, loss tangent, and penetration depth for several human body tissues are listed in Table A.2 at 2.45 GHz, calculated using the

online database [4]. In the online database [4], the parametric model of equation (A.4) is used together with the material parameters measured by Gabriel et al. [1]. This frequency is selected to correspond to the measurement frequency used in Chapter 4 for on-body antenna measurements and Chapter 2 for on-body channel modelling.

In Fig. A.1 and Fig. A.2, muscle and fat tissues are compared and plotted in terms of relative permittivity, conductivity and penetration depth using the same online database [4]. It is seen that the relative permittivity of muscle reduces faster than fat tissue with frequency while the conductivity is increased faster for muscle than fat tissue respectively. Also, in Fig. A.2 the frequency dependence of the penetration depth of both tissues is plotted.

At 100 MHz, penetration depth is significant, thus in this frequency range medical applications that employ communication with medical implants are developed. As the frequency increases, the penetration depth reduces and at 2.45 GHz is 11.3 and 2.1 cm, for fat and muscle respectively. Therefore, penetration at the ISM band is small (not penetrating through the muscle tissue) and propagation around the surface of the body is mostly realised. Some general conclusions can be drawn from all the aforementioned:

- Tissue parameters are well documented [4].
- Tissue parameters change with frequency.
- Tissue parameters change with tissue type.
- Muscle has high ϵ and σ and hence high interface mismatch and loss.
- Fat has low ϵ and σ.

A.0.2 Physical Phantoms

An extensive review of physical phantoms has been done in [5] and presented here. A phantom can be defined as a simulated biological body or as a physical model simulating the characteristics of the biological tissues [5]. The aim of such a phantom is to explore the interaction between the human body and the electromagnetic fields. The use of phantoms can provide a stable, controllable propagation environment that cannot be easily realised with human subjects. For this purpose, phantoms have been used extensively in medical research on the effects of electromagnetic radiation

Table A.2 Dielectric properties of several human body tissue parts at 2.45 GHz [4]

Tissue name	**Relative permittivity**	**Conductivity [S/m]**	**Loss tangent**	***Penetration* depth [m]**
Air	1	0	0	N/A
Aorta	42.53	1.435	0.2476	0.0243
Blood	58.26	2.545	0.3205	0.01612
Bone, cancellous	18.55	0.8052	0.3185	0.02874
Bone, cortical	11.38	0.3943	0.2542	0.04578
Bone, marrow	5.297	0.09504	0.1316	0.1288
Brain, grey matter	48.91	1.808	0.2712	0.02072
Brain, white matter	36.17	1.215	0.2465	0.02647
Breast, fat	5.147	0.137	0.1954	0.0883
Cartilage	38.77	1.756	0.3323	0.01908
Cerebro spinal fluid	66.24	3.458	0.383	0.01272
Cornea	51.62	2.295	0.3263	0.01683
Eye, sclera	52.63	2.033	0.2834	0.01913
Fat	5.28	0.1045	0.1452	0.117
Heart	54.81	2.256	0.302	0.01761
Kidney	52.74	2.429	0.338	0.01609
Liver	43.03	1.686	0.2875	0.02086
Lung, deflated	48.38	1.683	0.2551	0.02212
Lung, inflated	20.48	0.8042	0.2881	0.03018
Muscle	52.73	1.739	0.2419	0.02233
Nail	11.38	0.3943	0.2542	0.04578
Retina	52.63	2.033	0.2834	0.01913
SkinDry	38.01	1.464	0.2826	0.02257
SkinWet	42.85	1.592	0.2726	0.02203
Spinal cord	30.14	1.089	0.2649	0.02701
Spleen	52.45	2.238	0.3131	0.01738
Stomach	62.16	2.211	0.2609	0.01909
Tendon	43.12	1.685	0.2867	0.0209
Testis	57.55	2.168	0.2763	0.01875
Tongue	52.63	1.803	0.2513	0.02153
Tooth	11.38	0.3943	0.2542	0.04578
Trachea	39.73	1.449	0.2675	0.0233

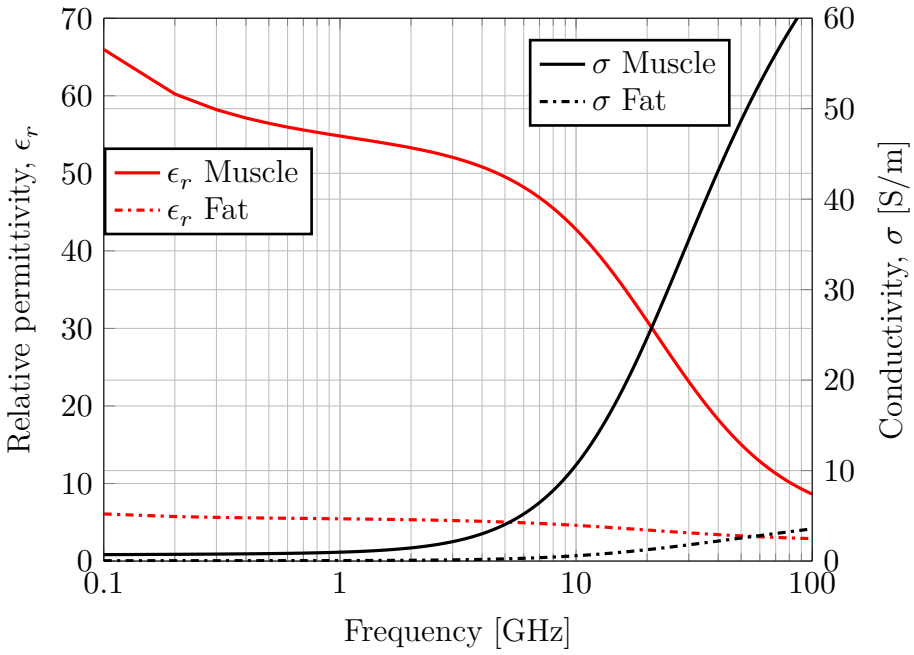

Figure A.1 Relative permittivity, ϵ_r and effective conductivity, σ of muscle and fat tissue from 100 MHz to 100 GHz [4].

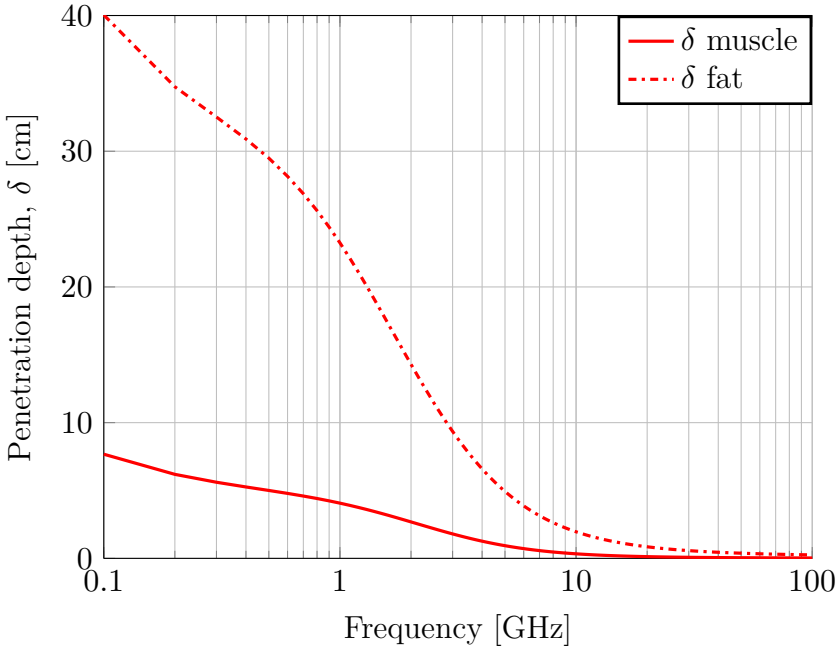

Figure A.2 Penetration depth, δ (in cm) inside muscle and fat tissue from 100 MHz to 100 GHz [4].

on health as well as in development of various methods of medical diagnosis and treatment, such as X-ray, MRI scan, and hyperthermia.

A phantom can be realised with abdomen, torso or full-body models and it can be fabricated in liquid, semisolid (gel), or solid (dry) form.

A.0.2.1 Liquid Phantoms

This type is the first and oldest of all the phantom types. It consists of a liquid filled container that has the same electrical characteristics as the tissues in the human body in the defined range of frequencies. Liquid phantoms are used extensively in SAR studies by direct measurement of the electric fields inside the phantom with a small probe. The phantoms used in this method have a thin shell, usually made of a fibreglass material with small relative permittivity and conductivity.

The relative permittivity of the phantom shell should be less than 5, the loss tangent less than 0.05, and the thickness of the shell should be 2.0 ± 0.2 mm for the frequencies in the range 0.8 to 3 GHz. The shell usually has a shape of a human head, a full body or a simple flat rectangular box, depending on the requirements of the application. Most recipes for the liquid contain either sugar at lower frequencies, or, at higher frequencies, diacetin or diethylene glycol butyl ether (DGBE) in different proportions to control permittivity of the solution, while salt (NaCl) is used to adjust conductivity.

This type of phantom allows for recording the detailed distribution of the fields inside the phantom. In addition, the human body is not represented accurately, as the internal structure is replaced with a homogeneous medium. For studying the propagation around the body, this is not an issue, as long as the losses in the body are large, and thus only a relatively thin external layer of the phantom has a significant effect on the propagation. However, it suffers from some disadvantages such as the limited range of frequencies over which the liquid can simulate the required dielectric properties, the difficulty of handling the container in the test environment, and the container itself having electrical characteristics that should be taken into consideration. However, although liquid phantoms have these disadvantages, they still have the important advantage of being easy to fabricate.

As an example, a liquid phantom head is used at Loughborough University for SAR measurements [6] (Fig.A.3) with the shape based on the SAM phantom. In Fig. A.4, a multi-postural realistic human-torso phantom which size was determined from

the average values of a Japanese male, is composed of a shell filled with liquid.

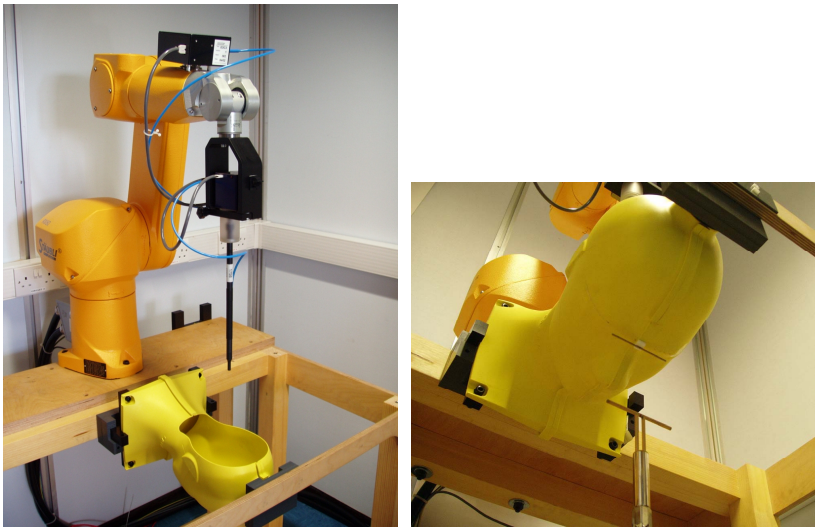

(a) (b)

Figure A.3 A liquid SAM phantom head used in Loughborough University for SAR measurements.

Figure A.4 A multipostural real-shaped liquid body phantom developed by Ogawa in Panasonic, Japan.

A.0.2.2 Semi-solid (Gel) Phantoms

In order to get rid of the outer shell of the phantoms, a solidifying agent has been used to make materials of jelly-like consistency that are capable of self-shaping. Different recipes use TX-151 or agar as the gelling agent, while polyethylene powder and sodium chloride are used to control the permittivity and conductivity of the material respectively. Although this type of phantom is only suitable for simulating high-water content materials (such as muscle, brain, etc.) and offers limited control of the electrical characteristic over a wide frequency range, it has the flexibility to be reshaped and is easy to produce.

Another solid gel phantom material uses polyacrylamide as its main constituent. This type of material is capable of simulating both high- and low-water content materials, depending on the liquid solvent used in its fabrication. The material is transparent and can be used in the wide frequency range, up to 5.5 GHz. All the gel phantom materials degrade over time due to losing water.

Figure A.5 shows a human-torso semi-solid phantom of Japanese male, which is composed of an agar-based phantom [7] to evaluate EM dosimetry, as well as the characteristics of antennas. This phantom, which is called the TX-151 phantom, can simulate the dielectric constants of high-water content tissues at 800 to 2400 MHz [7] and 3.8 to 5.8 GHz [8].

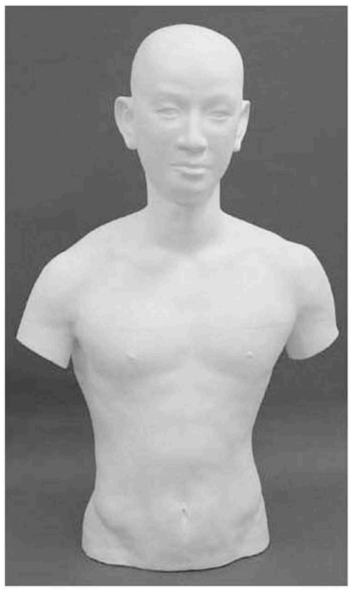

Figure A.5 Realistic human-torso phantom (agar-based solid phantom).

A.0.2.3 Solid (Dry) Phantoms

If the internal structure of the phantom has to be preserved, the use of a solid phantom is a good option. A solid phantom is made of materials capable of keeping their shape for a long period of time. This type of the phantom is mostly suited for propagation studies around, as well as inside, the body, since it can accurately represent the inhomogeneous structure of the human body. The SAR measurements on such phantoms are performed by the method of thermography. Before the measurement, the solid phantom has to be cut along the plane in which the SAR is to be measured. Then, after the solid phantom is illuminated by a radio source, the surface temperature is measured by an infrared sensor. The SAR is then deducted from the temperature rise.

A number of recipes for solid phantoms have been proposed, including a mixture of ceramic and graphite powder, silicone rubber mixed with carbon fibre, and conductive plastic containing carbon black. These phantoms have excellent mechanical and dielectric properties, which do not degrade over a long time because they do not contain water. The main disadvantage of ceramic and graphite phantoms results from the fact that solid phantoms need special and expensive equipment and special procedure in producing the composition, such as very high temperature (260 °C) and high pressure. The other phantoms are easier to fabricate, but it can be difficult to produce large quantities of these materials because of their short curing times.

Kobayashi et al. [9] developed a steady solid phantom, which is called the dry phantom. The dielectric properties of this type are not dependent on time. However, the manufacturing of this phantom is fairly difficult in most conventionally equipped laboratories. Figure A.6a shows an example of a human-head dry phantom. Recently, unlike the dry phantom, lighter and flexible human body-shaped phantoms have been developed. As an example, Fig. A.6b shows the full body "Rubber" phantom that is also used in the scope of this thesis. The "Rubber" phantom is made from silicone rubber and a conductive substance, such as carbon nanotube, is also mixed in to control electrical characteristics.

In order to investigate experimentally dynamic channel characterisation, so-called dynamic phantoms have been studied which can simulate the walking or running actions of a human. Figure A.7 shows an arm-waving dynamic phantom [10], which has unique features in that waving of the right and left arms and the direction and speed of waving can be controlled independently.

(a) (b)

Figure A.6 Example of dry (a) phantom head, and (b) full-body SAM phantom.

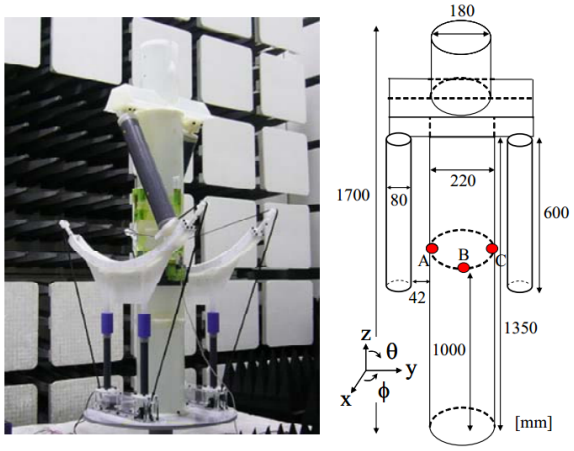

Figure A.7 Arm-waving dynamic phantom [10].

A.0.3 Numerical Phantoms

Many numerical phantoms that can be used in EM simulations have been reported. These are divided in simple-shaped theoretical or more realistic anthropomorphic phantoms. The first type is found useful in theoretical analysis. However, in order to calculate the characteristics of antennas close to the human body in detail, it is necessary to use a more realistic numerical phantom. In this section the different types of numerical phantoms that are used to describe the antenna-body interaction are discussed.

A.0.3.1 Theoretical Phantoms

Theoretical phantoms are the simplest form of numerical phantoms, found in homogeneous, or layered flat geometry that are used to evaluate EM dosimetry and antenna radiation close to human body. Spherical models are mainly used to replicate the human head, while cylindrical phantoms are often used as full-body models.

A.0.3.2 Homogeneous Phantoms

Homogeneous anthropomorphic models are widely used in the literature to describe the far-field antenna performance on the human body. Some homogeneous models (Fig.A.8), such as the specific anthropomorphic mannequin (SAM) phantom, are widely used. These phantoms are fully sufficient for most high frequency applications and can be simulated much faster than voxel models.

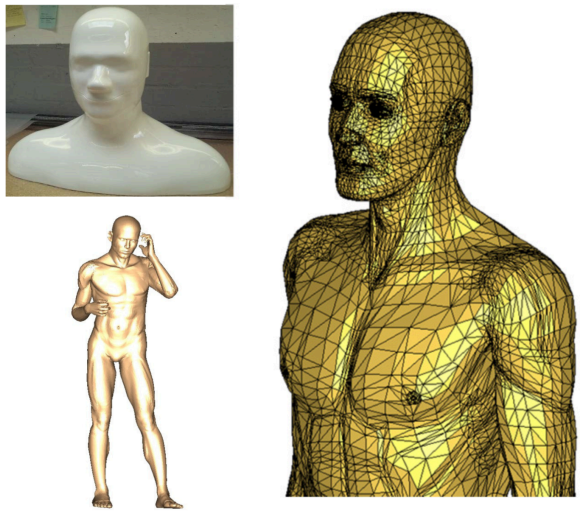

Figure A.8 Homogeneous numerical SAM phantoms.

Posable homogeneous body models can be also realised that incorporate movement like walking or running. These phantoms are created in 3D-CAD software such as POSER and then imported to the EM simulator. The advantages of these phantoms are that they are anthropomorphic and are easy to represent different snapshots of a dynamic scenario with the moving body parts. In [11], the feasibility to replace dynamic channel measurements with posable EM simulations is demonstrated. A male and a female poser phantoms are used to investigate channel gain variations for waist-foot and waist-wrist channels considering the influence of the different body posture. Two pseudo-moving actions of 30 frames are obtained from the animation

software, namely walking and standing up actions. It is proved that a good agreement can be achieved with EM simulation of posable phantoms.

A.0.3.3 Voxel Phantoms

Recently, the progress in medical imaging, such as magnetic resonance imaging (MRI) and x-ray computed tomography (CT), has sparked the development of precise head and full-body voxel models. Human head models are usually used for the evaluation of EM dosimetry (SAR), as well as to examine characteristics of antennas when placed close to the head. Mason et al. [12] proposed a very high spatial resolution full-body human voxel model classifying over 40 different types of tissues, based on photographic male data from the visible human project (VHP) dataset at the US National Library of Medicine [13]. Figure A.9a,b shows the full-body (HUGO) human voxel model [14]. The original data of the VHP was obtained from a 38-year-old male cadaver, 186 cm in height and 90 kg weight, while the voxel model weights 105 kg due to the process of modelling. This model is widely used for the numerical simulation throughout the world.

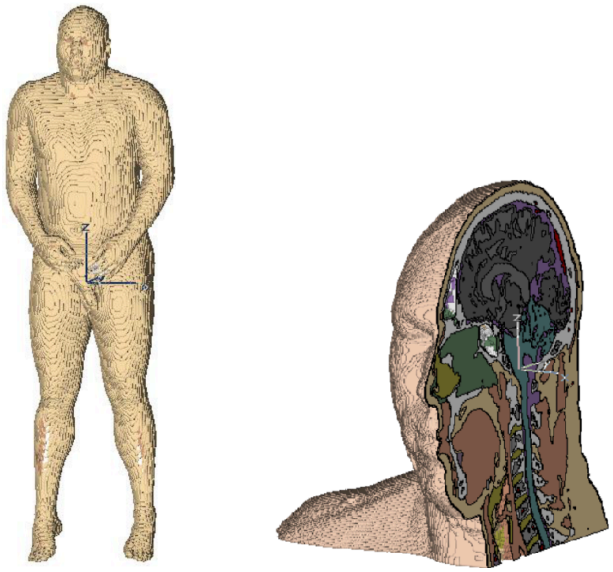

(a) (b)

Figure A.9 HUGO voxel model: (a) full body and (b) detailed cross-sectional view of head.

References

[1] C. Gabriel, "Compilation of the dielectric properties of body tissues at RF and microwave frequencies," Technical report, Brooks Air Force Technical Report (1996) .

[2] C. Gabriel, S. Gabriel, and E. Corthout, "The dielectric properties of biological tissues: I. Literature survey.," Physics in medicine and biology **41(11),** 2231–49 (1996).

[3] A. Peyman, S. Holden, and C. Gabriel, "Dielectric Properties of Tissues at Microwave Frequencies," Mobile Telecommunications and Health Research Programme pp. 1–46 (2000).

[4] D. Andreuccetti, R. Fossi, and C. Petrucci, "An Internet resource for the calculation of the dielectric properties of body tissues in the frequency range 10 Hz - 100 GHz,", Website at http://niremf.ifac.cnr.it/tissprop/. IFAC-CNR, Florence (Italy), 1997. Based on data published by C.Gabriel et al., 1996.

[5] P. S. Hall and Y. Hao, *Antennas and Propagation for Body-Centric Wireless Communications. Second Edition*, 2nd ed. (Artech House, Inc., 2012).

[6] *DASY 4, SPEAG*, Available online: http://www.speag.com/support/dasy-2/dasy4-downloads/.

[7] Y. Okano, "The SAR Evaluation Method by a Combination of Thermographic Experiments and Biological Tissue-Equivalent Phantoms," IEEE Transactions on Microwave Theory and Techniques **48(11),** 2094–2103 (2000).

[8] R. Ishido et al., "A Study on the Solid Phantoms for 3-6 GHz and Evaluation of SAR Distributions Based on the Thermographic Method," In *Proc. 2004 Int. Symp. Electromagnetic Compatibility*, pp. 577–580 (Sendai, Japan, 2004).

[9] T. Kobayashi, T. Nojima, K. Yamada, and S. Uebayashi, "Dry phantom composed of ceramics and its application to SAR estimation," Microwave Theory and Techniques, IEEE Transactions on **41(1),** 136–140 (1993).

[10] K. Ogawa and K. Honda, "BAN shadowing properties of an arm-waving dynamic phantom," In *Proceedings of 6th European Conference on Antennas and Propagation, EuCAP 2012*, pp. 515–519 (2012).

[11] M. Gallo, P. S. Hall, Q. Bai, Y. I. Nechayev, C. C. Constantinou, and M. Bozzetti, "Simulation and Measurement of Dynamic On-Body Communication Channels," IEEE Transactions on Antennas and Propagation **59(2),** 623–630 (2011).

[12] P. A. Mason, W. D. Hurt, T. J. Walters, J. A. D'Andrea, P. Gajsek, K. L. Ryan, D. A. Nelson, K. I. Smith, and J. M. Ziriax, "Effects of Frequency, Permittivity, and Voxel Size on Predicted Specific Absorption Rate Values in Biological Tissue During Electromagnetic-field Exposure.," IEEE Trans. Microwave Theory Tech. **48(11),** 2050–2057 (2002).

[13] *US National Library of Medicine, National Institute of Health, USA, "The Visible Human Project"*, Available online: http://www.nlm.nih.gov/research/visible/visible_human.html.

[14] X. G. Xu, T. C. Chao, and A. Bozkurt, "VIP-man: An Image-based Whole-body Adult Male Model Constructed from Color Photographs of the Visible Human Project for Multiparticle Monte Carlo Calculations," Health Phys. **78,** 476–486 (2000).

Appendix B

Statistical Distribution Models

Distribution	**Expression**
Lognormal	$f(r) = \frac{1}{r\sigma\sqrt{2\pi}} exp(-\frac{(ln(r)-\mu)^2}{2\sigma^2}), \quad r > 0$
Weibull	$f(r) = \frac{b}{a}(\frac{r}{a})^{b-1} exp(-\frac{r}{a})^b, \quad r \geq 0$
Rice	$f(r) = \frac{r}{s^2} exp(-\frac{r^2+c^2}{2s^2}) I_0(\frac{cr}{s^2}), \quad r \geq 0$
Gamma	$f(r) = \frac{1}{b^a \Gamma(a)} r^{a-1} exp(-r/b), \quad r \geq 0, a, b > 0$
$\alpha - \mu$	$f(r) = \frac{\alpha \mu^\mu r^{\alpha\mu-1}}{\hat{r}^{\alpha\mu}\Gamma(\mu)} exp(-\mu\frac{r^\alpha}{\hat{r}^\alpha}), \quad r \geq 0, a > 0$

Appendix C

CDFs of Small-scale Fading for On-Body Channels

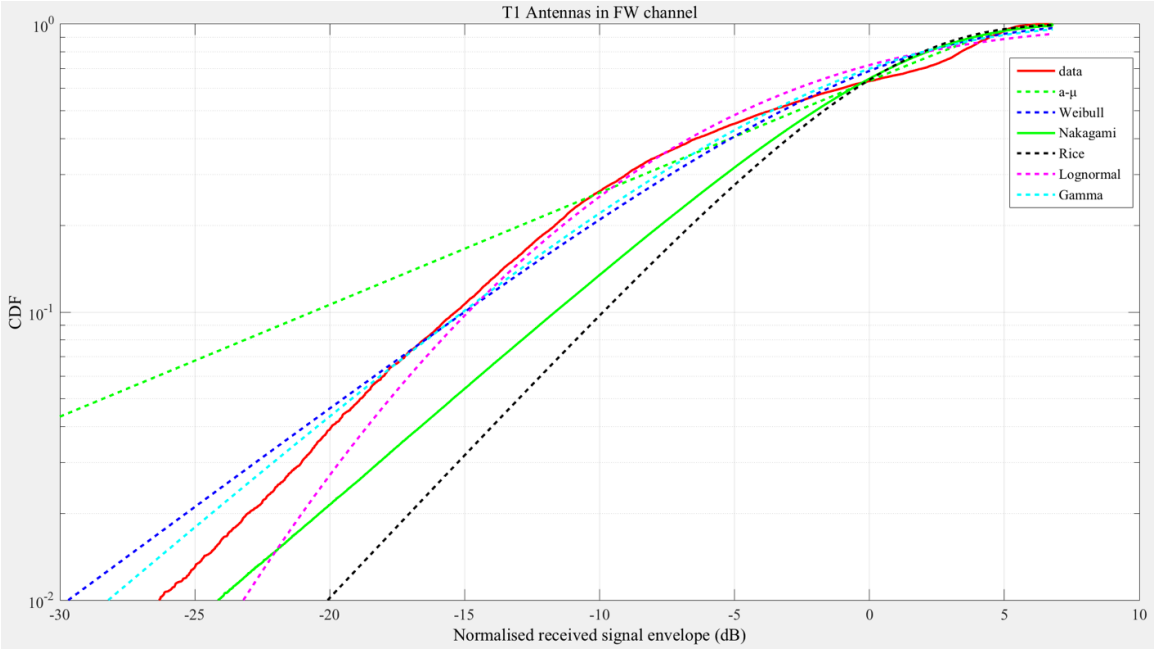
T1 Antennas in FW channel
CDF
Normalised received signal envelope (dB)
data
a-μ
Weibull
Nakagami
Rice
Lognormal
Gamma

(a) T1-FW

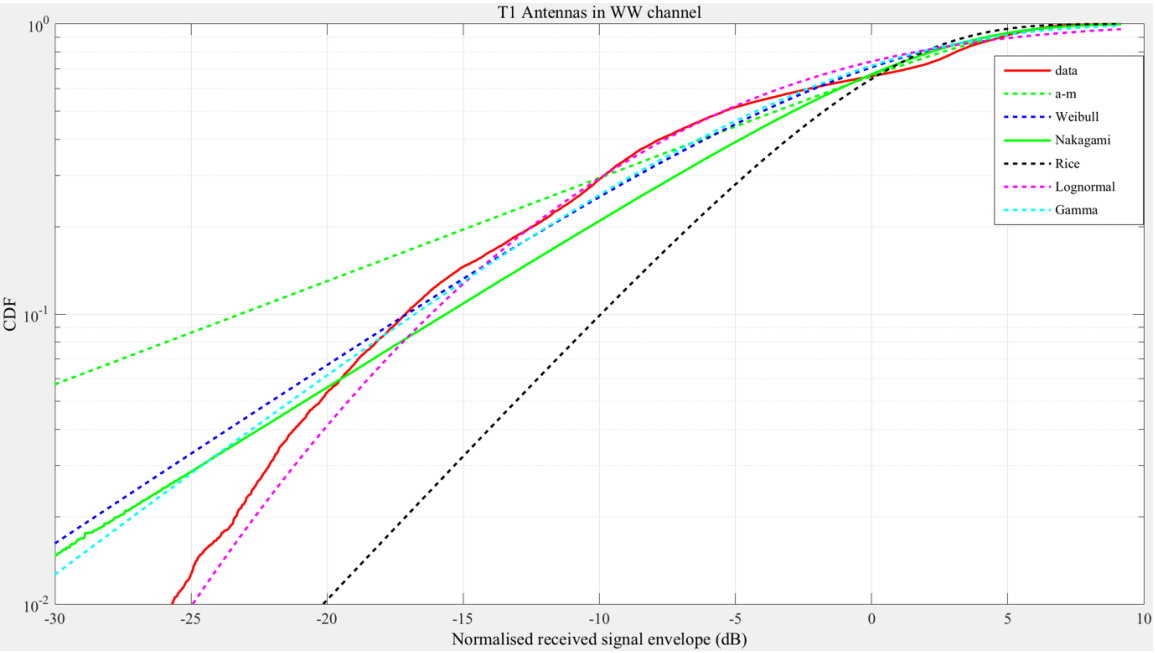
T1 Antennas in WW channel
CDF
Normalised received signal envelope (dB)
data
a-m
Weibull
Nakagami
Rice
Lognormal
Gamma

(b) T1-WW

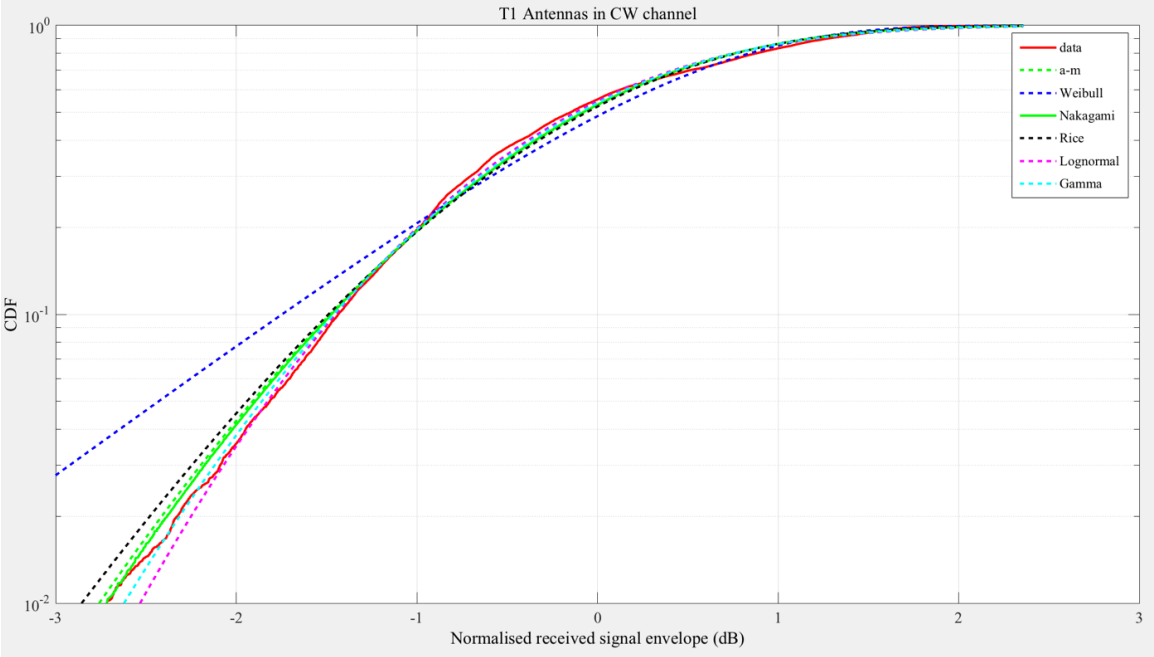

(c) T1-CW

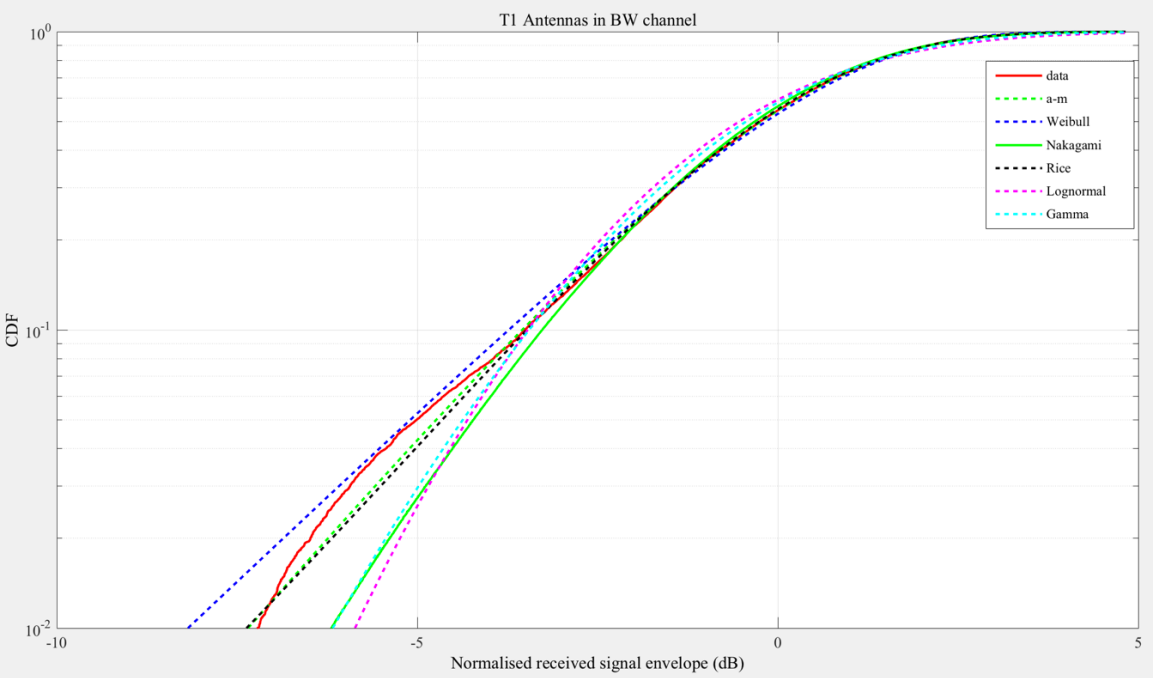

(d) T1-BW

Figure C.0 All the theoretical CDF models of small-scale fading for on-body channels with T1 antennas.

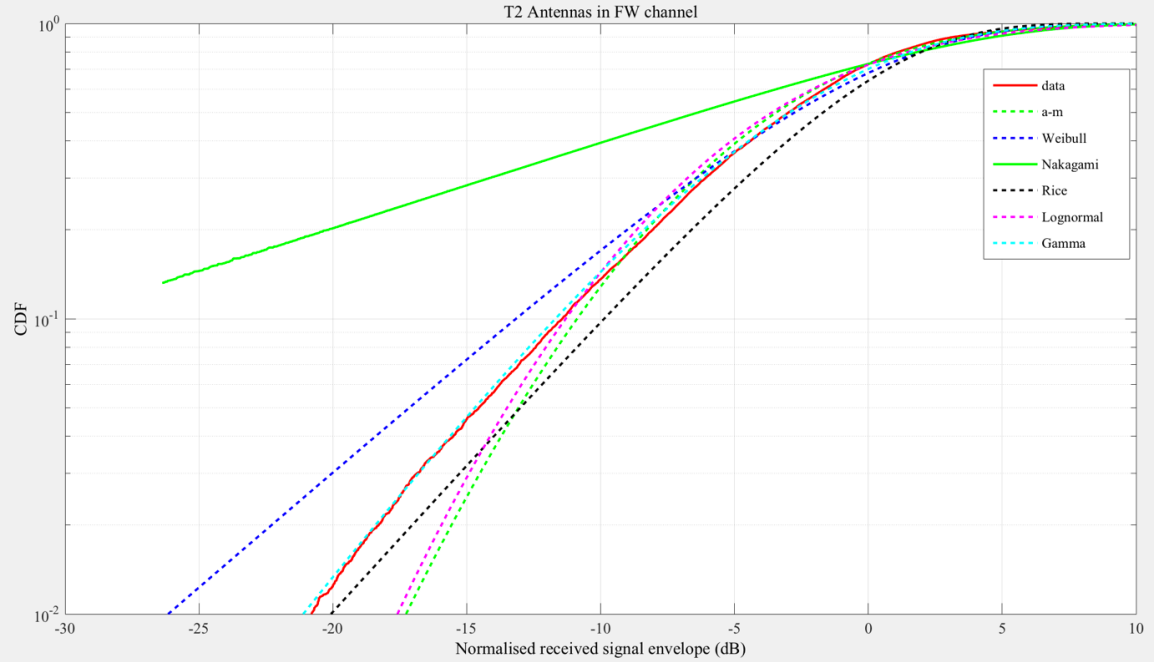
T2 Antennas in FW channel
CDF
Normalised received signal envelope (dB)
data
a-m
Weibull
Nakagami
Rice
Lognormal
Gamma

(a) T2-FW

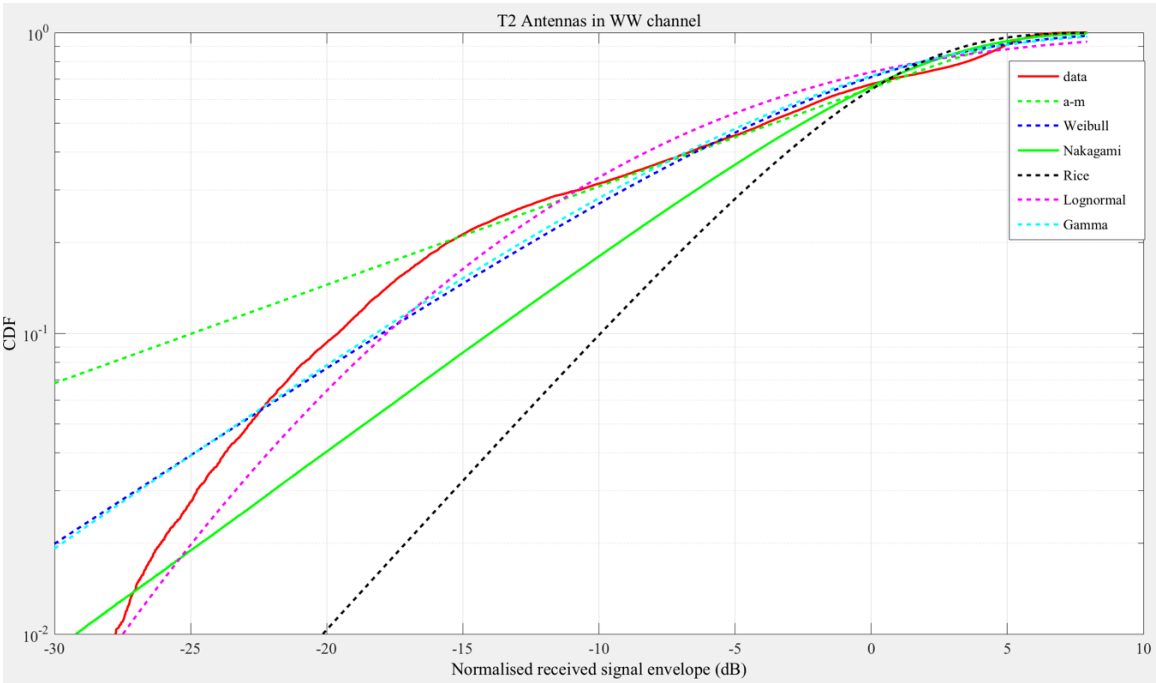
T2 Antennas in WW channel
CDF
Normalised received signal envelope (dB)
data
a-m
Weibull
Nakagami
Rice
Lognormal
Gamma

(b) T2-WW

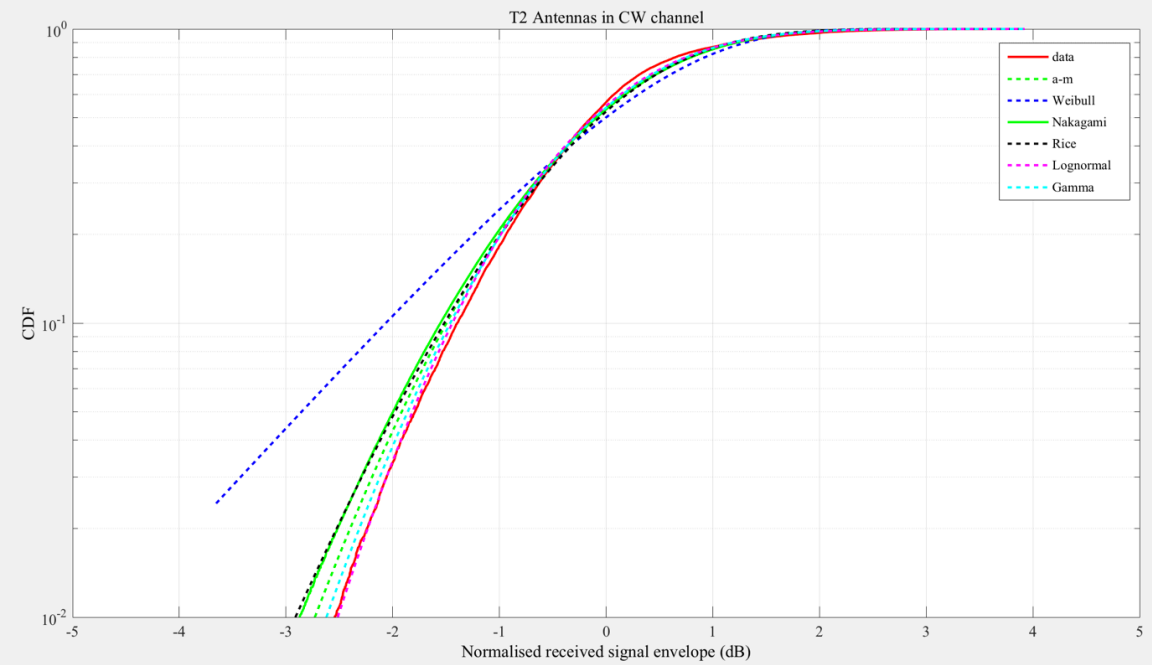

(c) T2-CW

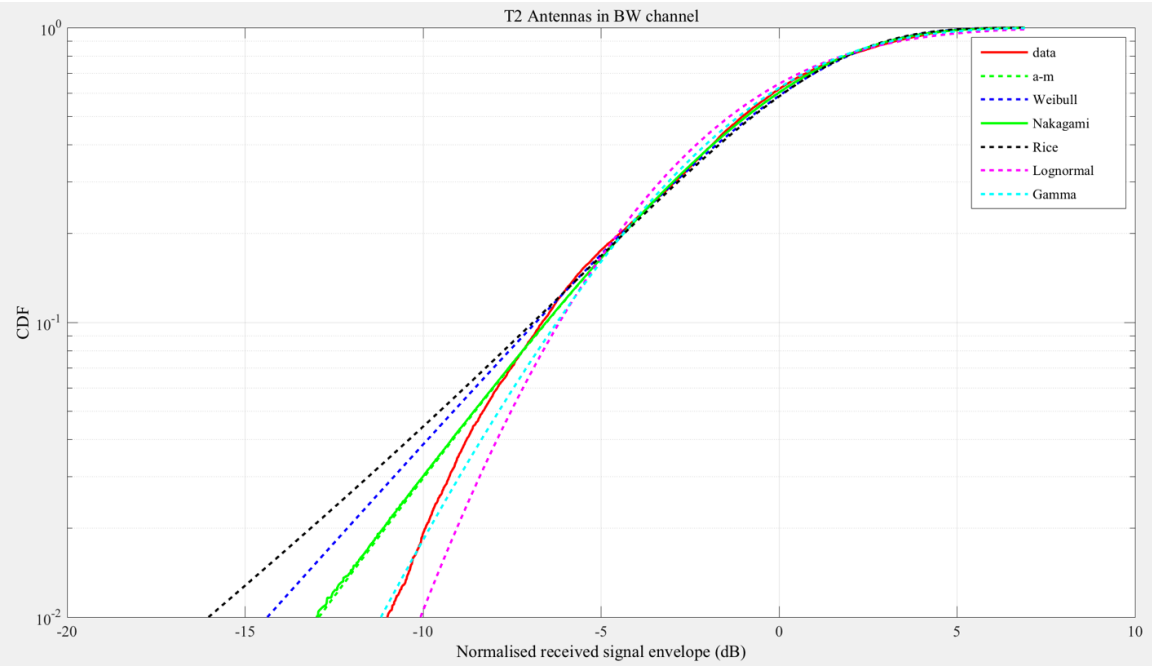

(d) T2-BW

Figure C.0 All the theoretical CDF models of small-scale fading for on-body channels with T2 antennas.

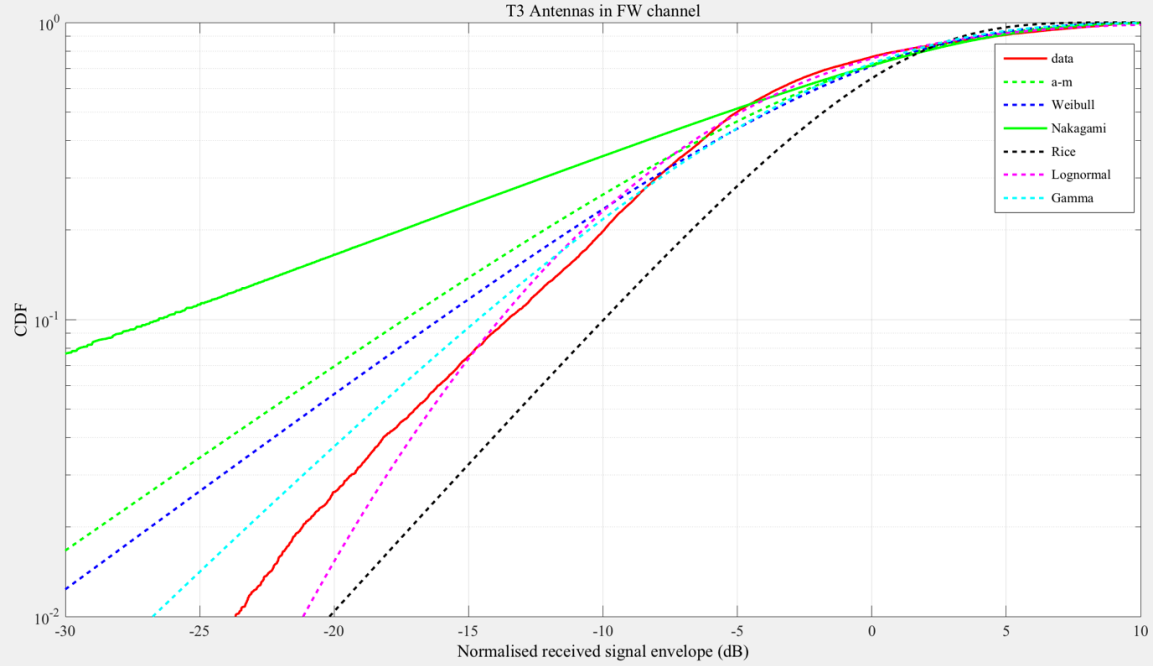
T3 Antennas in FW channel
CDF
Normalised received signal envelope (dB)
data
a-m
Weibull
Nakagami
Rice
Lognormal
Gamma

(a) T3-FW

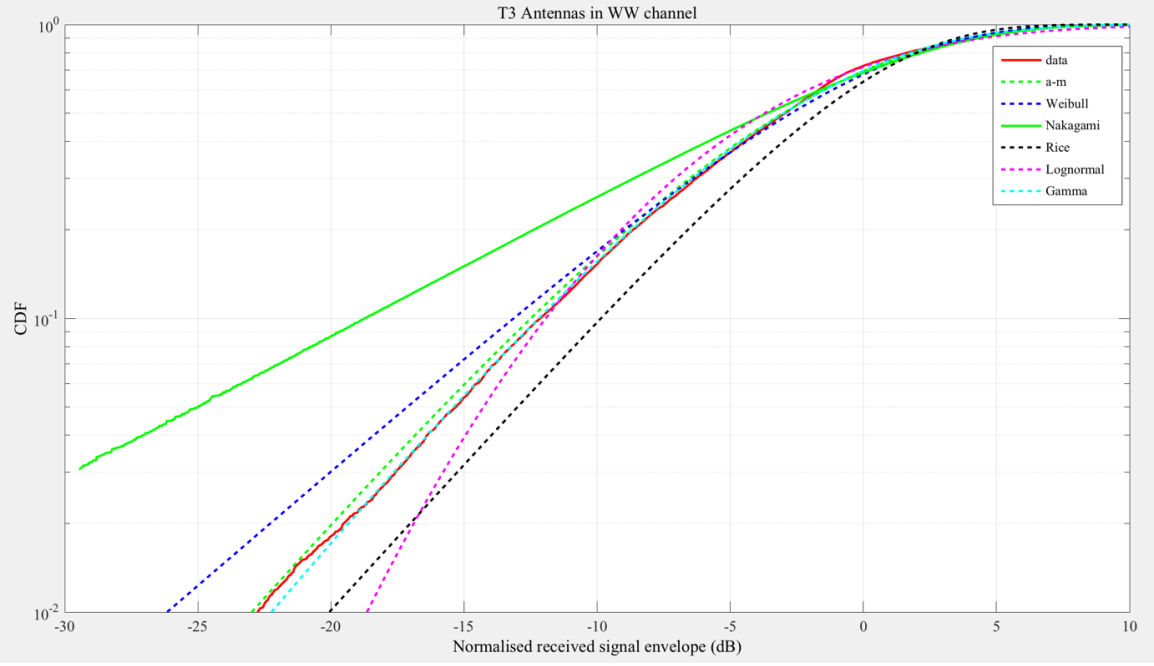
T3 Antennas in WW channel
CDF
Normalised received signal envelope (dB)
data
a-m
Weibull
Nakagami
Rice
Lognormal
Gamma

(b) T3-WW

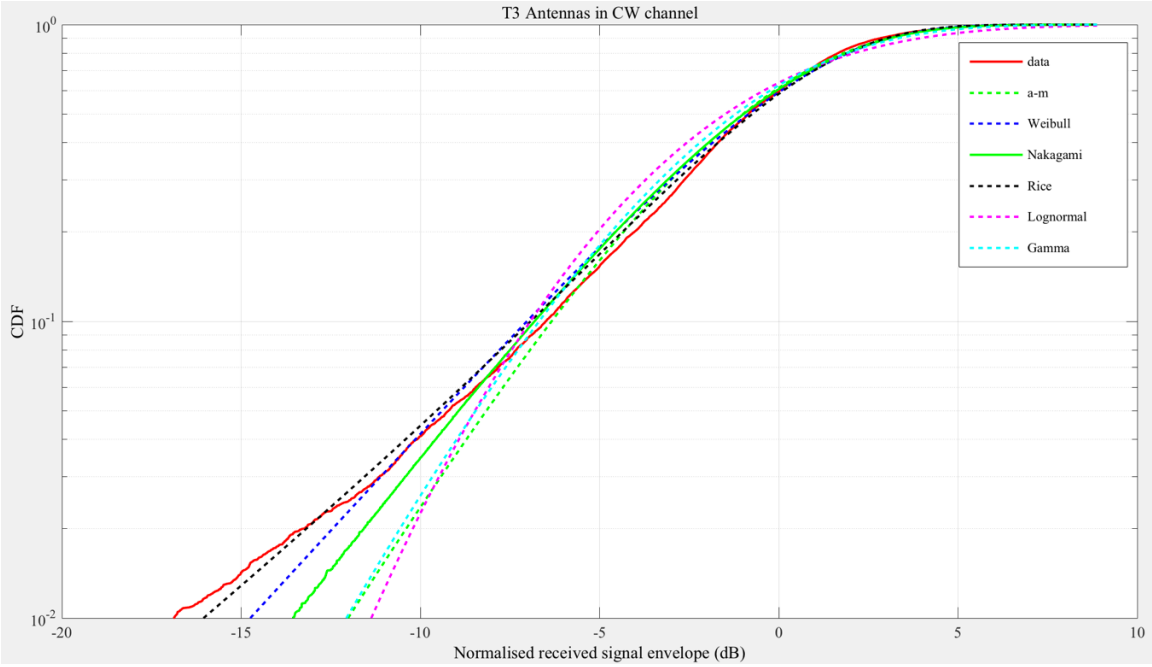

(c) T3-CW

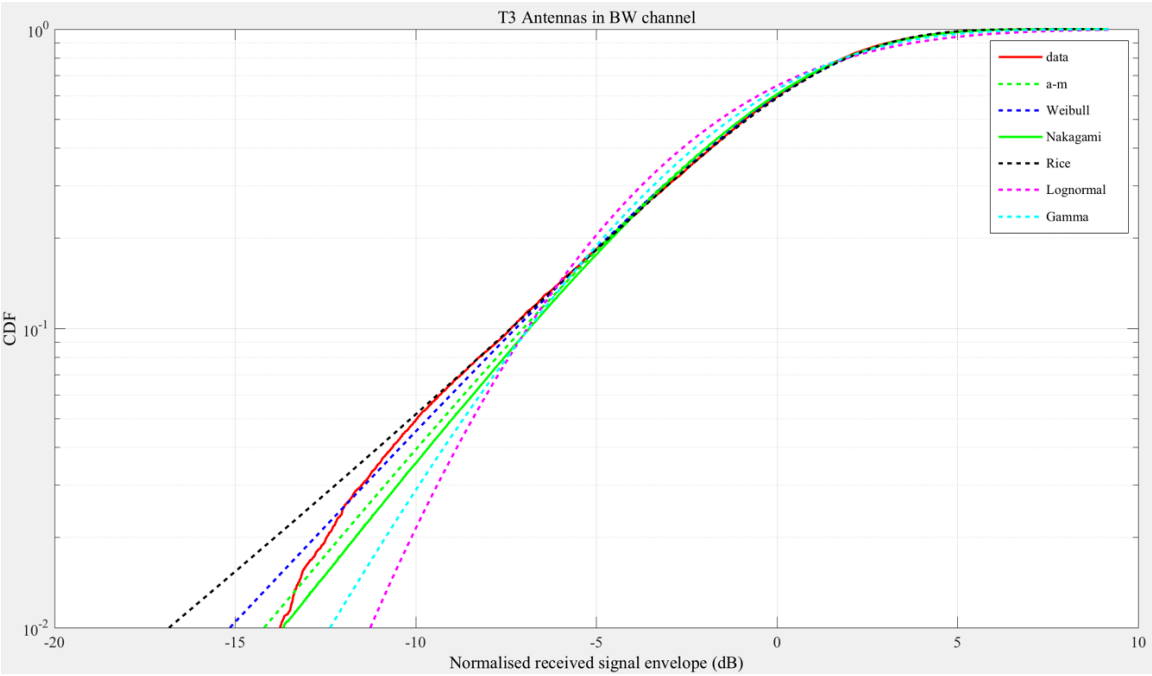

(d) T3-BW

Figure C.0 All the theoretical CDF models of small-scale fading for on-body channels with T3 antennas.

Appendix D

Goodness-of-fit Tests of Statistical Distribution Models

Several goodness-of-fit tests have been used in the literature, the Kolmogorov- Smirnov (KS), the Kullback-Leibler (KL), the Akaike's Information Criterion (AIC), the Bayesian Information Criterion (BIC) and the Anderson-Darling (AD). The first two are employed herein since they can be used for the generic model $\alpha - \mu$. The KS- and KL-statistic values are gathered in Table D.1 and Table D.2 respectively.

The Kolmogorov- Smirnov statistic (D) is defined as the maximum value of the absolute difference between two cumulative distribution functions. Thus, for comparing the cumulative distribution of the measured received signal envelope $F_E(x)$ (empirical CDF) to a known cumulative distribution function $F_X(x)$ (theoretical CDF), the K-S statistic is:

$$D = \max_{-\infty<x<\infty} |F_E(x) - F_X(x)| \tag{D.1}$$

An alternative metric to test distribution fitting is the Kullback-Leibler (KL) divergence, which is based on comparing the relative entropy of the two PDFs. This test introduces entropy as an information criterion in statistics and works by minimizing the lack of information in the sampling model. For large samples, the commonly used Akaike's Information Criterion (AIC) relies on Kullback-Leibler information as averaged entropy. It is defined as,

$$D_K = \int_{-\infty}^{\infty} f_E(x) ln \left(\frac{f_E(x)}{f_X(x)} \right) dx \tag{D.2}$$

where $f_E(x)$ represents the empirical CDF of the measured received signal envelope to a known theoretical PDF $f_X(x)$.

Table D.1 KS statistics for all the theoretical distribution models of the received signal envelope

KS-STAT	Lognormal	Weibull	Gamma	Rice	Nakagami-m	a-m
T1-FW	0.0919	0.0939	0.0961	0.1898	0.1489	0.0650
T1-WW	0.0838	0.0761	0.0811	0.2374	0.1221	0.0765
T1-CW	0.037	0.0606	0.0354	0.0374	0.0347	0.0328
T1-BW	0.0493	0.0156	0.0312	0.0098	0.022	0.0078
T2-FW	0.0373	0.0447	0.0244	0.092	0.2513	0.0294
T2-WW	0.0851	0.0696	0.0664	0.2141	0.138	0.0666
T2-CW	0.0282	0.0942	0.0392	0.0515	0.0513	0.0399
T2-BW	0.0417	0.0275	0.0208	0.0317	0.0141	0.0156
T3-FW	0.031	0.0745	0.0663	0.2179	0.1684	0.0706
T3-WW	0.0493	0.0445	0.0224	0.0976	0.1039	0.0254
T3-CW	0.0876	0.0323	0.0561	0.0225	0.0363	0.0312
T3-BW	0.0708	0.0099	0.0394	0.0118	0.0159	0.0129

Table D.2 KL statistics for all the theoretical distribution models of the received signal envelope

KL-STAT	Lognormal	Weibull	Gamma	Rice	Nakagami	a-m
T1-FW	0.1566	0.1267	0.1272	0.2819	0.2034	0.0913
T1-WW	0.1102	0.0933	0.0934	0.3484	0.1163	0.0884
T1-CW	0.0331	0.0707	0.0327	0.0663	0.0773	0.0693
T1-BW	0.0545	0.0123	0.03	0.0092	0.0206	0.0087
T2-FW	0.0501	0.0408	0.023	0.1389	0.1411	0.0436
T2-WW	0.1578	0.1134	0.1136	0.4361	0.1911	0.051
T2-CW	0.0166	0.1376	0.0216	0.0382	0.0302	0.0255
T2-BW	0.0313	0.0243	0.0154	0.0304	0.0174	0.0171
T3-FW	0.0396	0.069	0.0539	0.2873	0.124	0.0611
T3-WW	0.0511	0.021	0.014	0.099	0.0505	0.0151
T3-CW	0.1498	0.0301	0.061	0.0257	0.032	0.0433
T3-BW	0.0786	0.0135	0.0313	0.0112	0.0147	0.0117

Appendix E

Plot 2D near-field patterns using Matlab

E.1 From cylindrical near-field measurements

```
%Choose to read a near-field measurements file in .xlsx format
%derived from the original Midas .txt format
file=strcat('filepath','.xlsx');
tab=strcat('sheet name');

% Read Y_slide, Azimuth and number of Frequencies
Azim_start=xlsread(file,tab,'B9');
Azim_stop=xlsread(file,tab,'D9');
Azim_step=xlsread(file,tab,'F9');

Y_Slide_start=xlsread(file,tab,'B7');
Y_Slide_stop=xlsread(file,tab,'D7');
Y_Slide_step=xlsread(file,tab,'F7');

Azimuth=[Azim_start:Azim_step:Azim_stop];
Y_slide=[Y_Slide_start:Y_Slide_step:Y_Slide_stop];
Azim=repmat(Azimuth,length(Y_slide),1);
Y_Slide=repmat(Y_slide,length(Azimuth),1);
Y_Slide=Y_Slide';

% Find 5800 MHz value and begin printing after 6 cells
f=xlsread(file,tab,'B:B');
```

```
kk = find(f==2450)+2;

for k=1:length(Azimuth);
i=kk(k)+6;
j=i+length(Y_slide)-1;
start = sprintf('B%i', i);
stop = sprintf('B%i', j);
to=':';
range = strcat(start,to,stop);
Magn_Co(:,k)=xlsread(file,range);
end

for k=length(Azimuth)+1:length(kk);
i=kk(k)+6;
j=i+length(Y_slide)-1;
start = sprintf('B%i', i);
stop = sprintf('B%i', j);
to=':';
range = strcat(start,to,stop);
Magn_Cross(:,k-length(Azimuth))=xlsread(file,range);
end
Magn_Co_true=Magn_Co-max(max(Magn_Co));
Magn_Cross_true=Magn_Cross-max(max(Magn_Co));

%Plot Co- and Cross- polarised near-field components
NF_2D_MAP_Co
NF_2D_MAP_Cross
```

E.2 From EM simulations

```
file=strcat('CST_TO_MATLAB_NF_PLOTS','.xlsx');
%done
% tab=strcat('CPS_Dipole_5.8_V_10mm');
% tab=strcat('CPS_Dipole_5.8_H_10mm');
% tab=strcat('MPA_5.8_10mm');
tab=strcat('HMMPA_5.8GHz_10mm');
% Create azimuth and Y-slide vectors from Cartesian X,Y,Z in CST
i=3;
j=5618;
```

```
% j=8829;
% j=8930;
startX = sprintf('A%i', i);
stopX = sprintf('A%i', j);
to=':';
rangeX = strcat(startX,to,stopX);
X(:,1)=xlsread(file,tab,rangeX);
Xodd(:,1)=X(1:2:end,1);

startY = sprintf('B%i', i);
stopY = sprintf('B%i', j);
to=':';
rangeY = strcat(startY,to,stopY);
Y(:,1)=xlsread(file,tab,rangeY);
Yodd(:,1)=Y(1:2:end,1);

startZ = sprintf('C%i', i);
stopZ = sprintf('C%i', j);
to=':';
rangeZ = strcat(startZ,to,stopZ);
Z(:,1)=xlsread(file,tab,rangeZ);
Zodd(:,1)=Z(1:2:end,1);

startEX = sprintf('D%i', i);
stopEX = sprintf('D%i', j);
to=':';
rangeEX = strcat(startEX,to,stopEX);
EX(:,1)=xlsread(file,tab,rangeEX);
EXodd(:,1)=EX(1:2:end,1);

startEY = sprintf('E%i', i);
stopEY = sprintf('E%i', j);
to=':';
rangeEY = strcat(startEY,to,stopEY);
EY(:,1)=xlsread(file,tab,rangeEY);
EYodd(:,1)=EY(1:2:end,1);

startEZ = sprintf('F%i', i);
stopEZ = sprintf('F%i', j);
to=':';
rangeEZ = strcat(startEZ,to,stopEZ);
EZ(:,1)=xlsread(file,tab,rangeEZ);
```

```
EZodd(:,1)=EZ(1:2:end,1);

startEXI = sprintf('G%i', i);
stopEXI = sprintf('G%i', j);
to=':';
rangeEXI = strcat(startEXI,to,stopEXI);
EXI(:,1)=xlsread(file,tab,rangeEXI);
EXIodd(:,1)=EXI(1:2:end,1);

startEYI = sprintf('H%i', i);
stopEYI = sprintf('H%i', j);
to=':';
rangeEYI = strcat(startEYI,to,stopEYI);
EYI(:,1)=xlsread(file,tab,rangeEYI);
EYIodd(:,1)=EYI(1:2:end,1);

startEZI = sprintf('I%i', i);
stopEZI = sprintf('I%i', j);
to=':';
rangeEZI = strcat(startEZI,to,stopEZI);
EZI(:,1)=xlsread(file,tab,rangeEZI);
EZIodd(:,1)=EZI(1:2:end,1);

% Create matrices for Azim, Y_Slide, Magn_Co and Magn_Cross

[THETA] = 180*cart2pol(Xodd,Yodd)/pi();
Azim=vec2mat(THETA,72);
Y_slide=Zodd(1:72:end,1);
Y_Slide=repmat(Y_slide,1,72);

EX=20.*log10(sqrt(EXodd.^2+EXIodd.^2));
EY=20.*log10(sqrt(EYodd.^2+EYIodd.^2));
EZ=20.*log10(sqrt(EZodd.^2+EZIodd.^2));

%for V-polarised antennas
Magn_Co=EZ;
Magn_Co_true=Magn_Co-max(Magn_Co);
Magn_Co_true=vec2mat(Magn_Co_true,72);


Magn_Cross=20.*log10((sqrt((10.^(EY./20).*cos(pi().*THETA./180)).^2+
(10.^(EX./20).*sin(pi().*THETA./180)).^2)));
```

```
Magn_Cross_true=Magn_Cross-max(Magn_Co);
Magn_Cross_true=vec2mat(Magn_Cross_true,72);

%for H-polarised antennas
Magn_Co=20.*log10((sqrt((10.^(EY./20).*cos(pi().*THETA./180)).^2+
(10.^(EX./20).*sin(pi().*THETA./180)).^2)));
Magn_Co_true=Magn_Co-max(Magn_Co);
Magn_Co_true=vec2mat(Magn_Co_true,72);

Magn_Cross=EZ;
Magn_Cross_true=Magn_Cross-max(Magn_Co);
Magn_Cross_true=vec2mat(Magn_Cross_true,72);



Azim=circshift(Azim,[0 54]);
Y_Slide=circshift(Y_Slide,[0 54]);
Magn_Co_true=circshift(Magn_Co_true,[0 54]);
Magn_Cross_true=circshift(Magn_Cross_true,[0 54]);

NF_2D_MAP_Co_CST_Norm
NF_2D_MAP_Cross_CST_Norm
```